Generating and manipulating entanglement of spins and photons

Dissertation zur Erlangung des
akademischen Grades eines Doktors der
Naturwissenschaften (Dr.rer.nat.)

vorgelegt von
Adrian Auer

an der

Mathematisch-Naturwissenschaftliche Sektion

Fachbereich Physik

Tag der mündlichen Prüfung: 29.06.2015
1. Referent: Prof. Dr. Guido Burkard
2. Referent: Prof. Dr. Wolfgang Belzig

Acknowledgments

The time as a graduate student has been a very exciting period, to which many people have contributed in various ways. First, I would like to thank my doctoral advisor Prof. Dr. Guido Burkard for his excellent guidance within last the four years, not only because of his expertise and continuous helpfulness. I also highly acknowledge his motivation and dedication for a proper education of young scientists, and I very much appreciated all his encouragement for scientific exchange that allowed the participation in many conferences and workshops, and not least a longer research stay at Stanford University.

The visit at Stanford was a great and stimulating experience, and I thank Prof. Dr. Yoshihisa Yamamoto for the hospitality in his research group. Lively discussions were held with Dr. Shruti Puri, Dr. Peter McMahon, and Dr. Cody Jones. I really enjoyed the time we spent together. I also want to mention Prof. Dr. Rupert Huber who wrote a letter of recommendation for a DAAD scholarship (during his vacation), since without this funding the whole project would not have been realizable.

Our research group in Konstanz continuously changed and I am thankful to have met so many great people here. In this context, I would like to mention my colleagues Dr. Matthias Droth, Dr. Marco Hachiya, Dr. Julia Hildmann, Dr. Eleftheria Kavousanaki, Dr. Andor Kormányos, Peter Machon, Prof. Dr. András Pályi, Dr. Alexander Pearce, Dr. Csaba Péterfalvi, Marko Rančić, Dr. Julien Rioux, Niklas Rohling, Maximilian Russ, Heng Wang, Daniel Zeuch, and everybody who I forgot. Furthermore, my thanks go to our secretary Maria Rosner who takes so much care of us, and to Stefan Gerlach who kept our computers running.

Erik and Hugo, you deserve your own paragraph, I guess you know why.

Marcus Beck and Markus Ring proofread the manuscript of this thesis. Additionally, I would like to thank both them as well as Sven Deutschländer for all the support, motivation and recreational activities during the time of the PhD and the whole studies.

My final gratitude goes to my family, to my girlfriend Julia, and all of my friends who always believed in me and kept supporting me whenever they could.

Abstract

Spins in a solid-state environment and photons are both promising physical systems regarding the implementation of qubits. Whereas electron and nuclear spins act very well as localized qubits that are able to store and process quantum information, photons are the primary candidates to transmit quantum information between distant locations. Entanglement, on the other hand, is a fundamental resource of quantum information processing enabling, e.g., secure communication over long distances. The generation and manipulation of entanglement are thus fundamental steps in order to leverage the benefits of quantum information processing. The aim of this dissertation is therefore to theoretically investigate entangling mechanisms for various physical systems.

A functioning source of entangled photons is a basic hardware component required for quantum communication. To this end, we study a system composed of semiconductor quantum wells inside a microcavity, known as intersubband cavity system, in which the interaction of the electronic system with the cavity field can reach the ultrastrong coupling regime. The ground state contains a finite number of photons, and we find that these photons are entangled. The amount of entanglement is quantified analytically, and maximal entanglement is found to be possible.

The technique of entanglement purification allows to restore maximal entanglement that has decreased, e.g. due to decoherence. Purification requires quantum memory, a role for which electron spins in electrically-defined quantum dots are well suited. However, existing purification protocols are rather unpractical in this case. Here, the concept of asymmetric bilateral two-qubit operations is introduced to purify spin entanglement by harnessing the typical interaction between electrons in neighboring quantum dots. As it turns out, this concept can be applied to a variety of qubit systems, e.g. superconducting qubits or spins in nitrogen-vacancy centers in diamond.

The latter example offers several possibilities to implement a qubit, of which the intrinsic nitrogen nuclear spin has proven its viability in many ways. We develop a scheme to deterministically couple two nuclear spin qubits, in which the interaction is mediated by an optical cavity. It is found that an entangling two-qubit gate, also required for universal quantum computation, can be implemented with operation times below 100 nanoseconds, i.e. several orders of magnitude faster compared to the decoherence time of the nuclear spin.

The verification of entanglement, which is required e.g. in entanglement-based quantum communication to detect an eavesdropping attack, typically involves a measurement of qubit states. Using the input-output formalism, we derive a fully quantum-mechanical model of an optical readout scheme to measure the spin state of an electron in a self-assembled quantum dot.

Zusammenfassung

Spins in Festkörpersystemen wie auch Photonen sind beides vielversprechende physikalische Systeme in Bezug auf die Umsetzung von Qubits. Elektronen- und Kernspins werden einerseits als lokalisierte Qubits verwendet, die in der Lage sind, Quanteninformation zu speichern und zu verarbeiten. Um Quanteninformation zwischen verschieden Orten zu übertragen, kommen dagegen hauptsächlich Photonen zum Einsatz. Verschränkung an sich kann als grundlegende Resource der Quanteninformationsverarbeitung angesehen werden, die z. B. sichere Kommunikation über weite Distanzen ermöglicht. Die Erzeugung und Verarbeitung von Verschränkung sind daher grundlegende Vorgänge, um die Vorteile der Quanteninformationsverarbeitung auch tatsächlich nutzen zu können. Eine theoretische Untersuchung von Verschränkungsmechanismen in Bezug auf verschiedene physikalische Systeme ist daher das Ziel dieser Dissertation.

Eine funktionstüchtige Quelle verschränkter Photonen gehört zur Grundausstattung, um Quantenkommunikation zu betreiben. Zu diesem Zweck wird ein System bestehend aus Halbleiter-Quantentöpfen in einem Hohlraumresonator untersucht. Die Wechselwirkung zwischen dem elektronischen System der Quantentöpfe und dem elektromagnetischen Feld im Inneren des Hohlraumresonators kann dabei so stark sein, dass der Bereich der ultrastarken Wechselwirkung erreicht wird. Der Grundzustand enthält dann bereits eine endliche Anzahl Photonen und wird gezeigt, dass diese verschränkt sind. Der Grad der Verschränkung wird analytisch quantitativ bestimmt und es zeigt sich, dass maximale Verschränkung möglich ist.

Das Prinzip der Verschränkungsreinigung ermöglicht es, maximale Verschränkung wiederherzustellen, welche beispielsweise durch Dekohärenz verringert wurde. Die Reinigung an sich benötigt einen Speicher für Quanteninformation, wofür sich Elektronenspins in elektrisch-definierten Quantenpunkten sehr gut eignen. Bestehende Protokolle zur Verschränkungsreinigung sind für solche Systeme allerdings eher unbrauchbar. In dieser Arbeit wird dazu das Konzept asymmetrischer bilateraler Zwei-Qubit Operationen eingeführt, um die Verschränkung zwischen Spins reinigen zu können. Dabei wird lediglich die typische Wechselwirkung zwischen Elektronen in benachbarten Quantentöpfen ausgenutzt. Wie sich hierbei herausstellt, kann das eingeführte Konzept auch für weitere Qubit-Systeme verwendet werden, z. B. für supraleitende Qubits oder Spins in Stickstoff-Fehlstellen-Zentren im Diamanten.

Das letztere Beispiel bietet sogar mehrere Möglichkeiten zur Umsetzung eines Qubits. Darunter befindet sich auch der intrinsische Kernspin des Stickstoffatoms, der sich bereits in vielerlei Hinsicht bewährt hat. In dieser Arbeit wird ein Mechanismus zur kontrollierbaren Kopplung zweier

Kernspin-Qubits entwickelt, bei dem die Wechselwirkung durch einen optischen Hohlraumresonator vermittelt wird. Es wird gezeigt, dass ein verschränkendes Zwei-Qubit Gatter, welches auch zum universellen Quantenrechnen benötigt wird, in unter 100 Nanosekunden ausgeführt werden kann. Dies ist mehrere Größenordnungen schneller als die Dekohärenzzeit des Kernspins.

Der Nachweis von Verschränkung wird beispielsweise dazu benötigt, um einen Lauschangriff in Quantenkommunikationsprotokollen aufzudecken, die auf der Verwendung verschränkter Zustände basieren. Dazu werden typischerweise Messungen von Qubit-Zuständen benötigt. Um den Spinzustand eines Elektrons in einem selbstassemblierten Quantenpunkt zu messen, wird hier ein quantenmechanisches Modell für einen optischen Auslesevorgang mit Hilfe des Input-Output Formalismus entwickelt.

Contents

1

Introduction

Entanglement is a fundamental feature of quantum mechanics that puzzled many of the founders of the theory, including, among others, Albert Einstein and Erwin Schrödinger [1, 2]. Back then it lead rather to a debate on nonlocality and realism within the theory of quantum mechanics itself, while nowadays entanglement can be seen more as a powerful resource in the context of modern technology that may enable perfectly secure communication and quantum computation [3, 4].

Everyday life is influenced more strongly than ever by information technology (IT), e.g. through the use of e-mail, smartphones or social media. Therefore, the development of secure tools and components that can guarantee the protection of information on the private, industrial, and governmental level is a highly desirable aim for future IT security.[1] Whereas present-day encryption methods, especially the RSA cryptosystem [5], rely on computational disadvantages of classical computers and could, in principle, be broken with quantum computers, the field of quantum cryptography provides a means for perfectly secure communication [3, 4]. In general, cryptology describes the process of encrypting (cryptography) and decrypting (cryptanalysis) secret information that is exchanged between two parties. This is a common procedure that is apparently necessary if one thinks, e.g., of financial transactions. The crucial part in cryptographic schemes is the security against any eavesdropping by undesired third parties to obtain the secret information.

As already pointed out, quantum computers are capable of breaking classical encryption schemes. However, quantum mechanics also provides completely secure methods of cryptography, which, in principle, no eavesdropper is able to overcome [6, 7]. One of them is entanglement-based quantum key distribution (QKD) to remotely generate a secret key for secure encryption if the two parties share a maximally entangled two-qubit state [7]. Usually, an eavesdropper has to perform some kind of measurement on a quantum system to gain information about its state.

[1] The German Federal Office for Information Technology registers, e.g., five targeted eavesdropping attacks on the Federal Office of Administration per day and the worldwide economic loss through cyber crime was estimated to amount up to 575 billion dollars in the year 2013. The numbers are taken from a recently published booklet (March 2015) about the "Forschungsrahmenprogramm" *Selbstbestimmt und sicher in der digitalen Welt* of the German Federal Ministry of Education and Research (http://www.bmbf.de/pub/Forschungsrahmenprogramm_IT_Sicherheit.pdf).

However, the quantum state is affected by the measurement, and especially, entanglement is lost. Hence, two communicating parties can reveal the presence of an eavesdropping attack by its unavoidable perturbation of a shared entangled two-qubit state. It is thus a fundamental law of physics that provides security in entanglement-based QKD [7].

For the real-world application of QKD and other quantum communication protocols, the generation of long-distance entanglement is indispensable. For this purpose, one has to counteract the unavoidable signal attenuation due to the interaction of the entangled particles with their environment. Whereas in classical communication technology intermediate repeater stations amplify and restore a signal that has been attenuated during the travel from sender to receiver, a component known as quantum repeater enables the creation of long-range entanglement for the purpose of long-distance quantum communication [8, 9]. The working principle of quantum repeaters essentially requires the ability to establish entanglement between intermediate nodes and subsequently increase the amount of entanglement using purification techniques [10, 11].

Another branch of quantum information processing is quantum computation [3, 4], a technology inspired by the idea of Richard P. Feynman in 1982 who suggested the simulation of a quantum system using an apparatus of quantum-mechanical nature itself instead of classical computers [12]. The first universal quantum computer was described by David Deutsch in 1985 [13], and attention increased further through the development of quantum algorithms that outperform their classical counterparts, e.g. Grover's algorithm to speedup the search in an unsorted database [14] or Shor's algorithm to efficiently find the prime factors of an integer [15]. The implementation of an entangling quantum gate between two qubits is a fundamental requirement for universal quantum computation [3, 16]. Any quantum circuit in the form of a unitary operation on a given number of qubits can be constructed from arbitrary single-qubit operations and the entangling two-qubit controlled-NOT gate, which is then said to be a universal set of quantum gates.

The requirements for a physical system to be of potential use for quantum computation and communication have been summarized by D. P. DiVincenzo in Ref. 17. The first five criteria are:

(i). The system must be scalable and exhibit well characterized qubits.

(ii). The state of the qubits can be initialized to a simple fiducial state.

(iii). The decoherence times of the qubits are much longer than the gate operation time.

(iv). A universal set of quantum gates can be implemented.

(v). The capability to measure the qubits.

These criteria are sufficient for quantum computation. However, in order to be of possible use in quantum communication, a physical system must fulfill the two extra requirements [17]:

(vi). An interface between stationary and flying qubits must be available.

(vii). Flying qubits can be faithfully transmitted between specified locations.

In this thesis, we concentrate on realizations for quantum information processing based on solid-state systems [18–26]. Stationary qubits are thereby typically represented by electron or nuclear spins, which show remarkable coherence properties. Additionally, solid-state systems bear the potential of providing a scalable qubit architecture and some of the required technological resources already exist from conventional electronics. Within this thesis, several different systems are studied with respect to entanglement generation and manipulation, which are separately described in the following chapters. We provide a detailed introduction into the topic and an overview of the actual state of research at the beginning of each of these chapters.

In Chap. 2, we introduce and mathematically define the notion of bipartite entanglement (Secs. 2.1 and 2.2). We describe how to quantify entanglement in terms of the von Neumann entropy for pure states and the entanglement of formation for mixed states (Sec. 2.3), which is required at a later stage to quantify the entanglement of two photons. The subsequent Chap. 3 shall introduce some of the fundamental concepts of quantum information processing that strongly motivate the work of this thesis. After defining the qubit as basic unit of quantum information in Sec. 3.1, we describe the circuit model of quantum computation (Sec. 3.2) and afterwards work step by step towards the quantum repeater protocol in more detail (Secs. 3.3 to 3.6).

Having the basic information at hand that generally motivates the work presented within this thesis, we start with the description of a solid-state based source of entangled photons in Chap. 4. Such a component is required since photons are typically used as a carrier for the transport of quantum information [27]. We propose a scheme to generate entangled photons from the ground state of the intersubband cavity system (Sec. 4.3), which already contains correlated photon pairs if operated in the so-called ultrastrong coupling regime. In Sec. 4.4, we demonstrate how these correlations lead to entanglement (Sec. 4.4.1) and quantify the amount of entanglement in order to estimate the usability for quantum information processing (Sec. 4.4.2).

Chap. 5 deals with a method to restore entanglement, which is known as entanglement purification. It is an indispensable task in realistic scenarios due to the loss of quantum coherence, e.g. through the interaction of quantum systems with their environment. The original task is to develop a purification protocol specifically for electron spin qubits in lateral quantum dots (Sec. 5.2), for which we derive an efficient solution by introducing the concept of asymmetric bilateral operations (Sec. 5.3). However, it turns out that this concept can be applied to a variety of spin-spin interaction types (Sec. 5.4).

We continue in Chap. 6 with another kind of spin that can be utilized as qubit, namely the nitrogen nuclear spin of nitrogen-vacancy (NV) centers in diamond. We begin with a description of the physical properties the NV center (Sec. 6.2) that is followed by a thorough overview of the vast number of experimental and theoretical achievements with respect to quantum information processing (Sec. 6.3). In Sec. 6.4, we then develop a mechanism to couple two distant nuclear spin qubits and eventually implement a two-qubit quantum gate between them.

The last project described in Chap. 7 is about work, which evolved during a research visit at Stanford University. The measurement of a qubit state is a basic step in many quantum communication protocols and in the circuit model of quantum computation. Furthermore, the verification of entanglement typically involves measurements, i.e. a spin readout in the case of spin qubits. Electron spins in self-assembled quantum dots (Sec. 7.2) have also been considered for the realization of qubits and we develop a quantum-mechanical description of a possible qubit readout scheme in Sec. 7.3.

In the final chapter (Chap. 8), we conclude by summarizing our results and giving an outlook based on the concepts developed within this thesis. All technical methods that are required at some stage in this thesis can be found in the appendix (Appendices A to E).

2

Entanglement

2.1 Introduction

A quantum-mechanical phenomenon that does not have a classical analog is the appearance of so-called *entangled states* [28]. Entanglement can arise in composite quantum systems and leads to correlations between the subsystems that cannot be described by any classical formalism. The first descriptions of entanglement were on the one hand given by A. Einstein, B. Podolsky, and N. Rosen in their seminal work on the EPR paradox [1], and on the other hand by E. Schrödinger [2] who also introduced the German word *Verschränkung* to describe the phenomenon, from which the denomination *entanglement* actually originated. Before giving a precise mathematical definition of entanglement, we start with a basic example to point out the quantum correlations mentioned before. Consider a quantum system composed of two subsystems, which are commonly named system A and system B. Each subsystem is a quantum-mechanical two-level system with states $|0\rangle$ and $|1\rangle$, respectively. Quantum mechanics allows the system to be in a superposition state, e.g.

$$|\Psi^-\rangle = \frac{1}{\sqrt{2}} \left(|01\rangle - |10\rangle \right), \tag{2.1}$$

where we used the short-hand notation $|ij\rangle \equiv |i\rangle_\mathrm{A} \otimes |j\rangle_\mathrm{B}$. If one of the two subsystems is measured, it will be in state $|0\rangle$ or $|1\rangle$ with equal probability, and the other system will be projected into a definite state. We therefore do not have any knowledge about the subsystems themselves. However, the total system is in a pure state, i.e. one has maximal knowledge about the whole system.[1] This circumstance has been recognized already by E. Schrödinger in 1935, when he wrote [2]: "So verfügt man vorläufig (bis die Verschränkung durch eine wirkliche Beobachtung gelöst wird) nur über eine *gemeinsame* Beschreibung der beiden in jenem Gebiet von höherer Dimensionszahl. Das ist der Grund, weshalb die Kenntnis der Einzelsysteme auf das Notdürftigste, ja auf Null herabsinken kann, während die des Gesamtsystems dauernd maximal bleibt. Bestmögliche Kenntnis eines Ganzen schließt *nicht* bestmögliche Kenntnis seiner Teile ein – und darauf beruht doch der ganze

[1] This circumstance can also be quantified in terms of the von Neumann entropy, see Sec. 2.3.

Spuk."[2]

The fact that a measurement on one of the subsystems instantaneously affects the other one, no matter how far they are apart, was a puzzling feature of quantum theory at this time. So-called local hidden variable theories (LHVTs) have therefore been introduced and considered as alternative approaches to quantum mechanics in order to resolve this issue [29]. As the terminology already suggests, these theories contain hidden and inaccessible variables that contain deterministic information about future measurement outcomes. Especially, if the locations are space-like separated, the obtained results should be independent. However, J. S. Bell could demonstrate in a seminal article that the assumptions of a LHVT lead to constraints on the correlations of measurement results, which are known as *Bell inequality* [29]. The important point is that the Bell inequality is violated if the total system is described by specific entangled states, e.g. the state $|\Psi^-\rangle$ in Eq. (2.1). This circumstance provides a means to experimentally falsify the concept of local hidden variables. The violation of a generalized version of Bell's inequality, known as the *CHSH inequality* [28], was demonstrated using entangled photon pairs [30, 31] and therefore, LHVTs could be ruled out as alternative theories to quantum mechanics.

But entanglement does not need to be only a mysterious and counterintuitive feature of quantum mechanics. Especially in the context of quantum information processing, entanglement can be viewed as a resource that enables certain tasks. Among these are entanglement-based quantum cryptography [7] and quantum teleportation [32], the latter being described in Sec. 3.4. In the following, we concentrate on bipartite entanglement, which has been the most studied case in the literature and is required in many parts of this thesis, specifically for two-level systems. It is an ongoing challenge to characterize entanglement of mixed bipartite states in multidimensional systems, not to mention entanglement of multipartite systems in general. An overview of these topics can be found in Ref. 28.

2.2 Definition of Bipartite Entanglement

In this section, we give the definitions of bipartite entanglement for pure and mixed states. In both cases, we consider a system that is composed of two quantum-mechanical subsystems. We adapt the commonly used notation in quantum communication and refer to the two entities as subsystem A and subsystem B, which stands for the two communicating parties Alice and Bob, respectively. The states of subsystem A are described by vectors from a Hilbert space $\mathcal{H}_\mathrm{A}$ with dimension d_A, whereas the Hilbert space $\mathcal{H}_\mathrm{B}$ with dimension d_B contains the state vectors of subsystem B. Following the quantum-mechanical formalism for composite systems, the Hilbert space $\mathcal{H}$ of the composite system is given by the tensor product of the Hilbert spaces $\mathcal{H}_\mathrm{A}$ and $\mathcal{H}_\mathrm{B}$,

$$\mathcal{H} = \mathcal{H}_\mathrm{A} \otimes \mathcal{H}_\mathrm{B}. \tag{2.2}$$

[2] An English translation can be found, e.g., in Ref. 28.

If $\{|a_i\rangle_A\}$ is an orthonormal basis of the Hilbert space $\mathcal{H}_A$, and $\{|b_j\rangle_B\}$ of $\mathcal{H}_B$, then a pure state that describes the total system is a vector $|\psi\rangle$ from the product space $\mathcal{H}$ that is generally given by

$$|\psi\rangle = \sum_{i=1}^{d_A} \sum_{j=1}^{d_B} c_{ij} \left| a_i b_j \right\rangle, \tag{2.3}$$

with some complex coefficients c_{ij}, and we again used the abbreviated notation $|a_i b_j\rangle \equiv |a_i\rangle_A \otimes |b_j\rangle_B$. An entangled pure state can be defined in a simple way. If it is possible to find states $|\phi\rangle_A \in \mathcal{H}_A$ and $|\nu\rangle_B \in \mathcal{H}_B$ in such a way that the pure state $|\psi\rangle \in \mathcal{H}_A \otimes \mathcal{H}_B$ can be written as

$$|\psi\rangle = |\phi\rangle_A \otimes |\nu\rangle_B, \tag{2.4}$$

then $|\psi\rangle$ is called a product state or *separable*. Otherwise, the pure state $|\psi\rangle$ is called *entangled* [28]. If $|\psi\rangle$ is a separable state, Alice and Bob have prepared their systems locally and independent of each other in the states $|\phi\rangle_A$ and $|\nu\rangle_B$, respectively. This cannot be done to generate entangled states, for which Alice's and Bob's system need to interact directly or via an ancillary system. A useful tool to decide whether a pure state is entangled or not is the so-called *Schmidt decomposition* [3]. For a given state $|\psi\rangle \in \mathcal{H}_A \otimes \mathcal{H}_B$, there exist orthonormal states $|\alpha_i\rangle_A$ in $\mathcal{H}_A$ and orthonormal states $|\beta_j\rangle_B$ in $\mathcal{H}_B$ such that $|\psi\rangle$ can be decomposed as

$$|\psi\rangle = \sum_{k=1}^{R} \lambda_k |\alpha_k \beta_k\rangle, \tag{2.5}$$

with some positive real numbers λ_k, called the *Schmidt coefficients* that fulfill the relation $\sum_{k=1}^{R} \lambda_k^2 = 1$. The number $R \leq \min\{d_A, d_B\}$ is the so-called *Schmidt rank* of the state $|\psi\rangle$. The numbers λ_k^2 are the eigenvalues of the reduced density matrices of either subsystem A or B [3], which provides a means to calculate the Schmidt rank R. According to the definition of entanglement given above, a pure state is separable if and only if it has a Schmidt rank $R = 1$.

So far, only the definition of separability for pure states has been discussed. However, and this is the more realistic scenario encountered in the laboratory, the bipartite system can be in a mixed state due to a lack of information, described by a density matrix

$$\rho = \sum_i q_i |\phi_i\rangle\langle\phi_i|, \tag{2.6}$$

where the eigenstates of ρ are denoted as $|\phi_i\rangle$, and the real positive eigenvalues q_i satisfy the relation $\sum_i q_i = 1$. The physical motivation for the definition of mixed-state entanglement originates from the type of correlations that a mixed state can exhibit. For the preparation of ρ one could imagine the following situation. Alice prepares a state ρ_i^A with some probability p_i and communicates the information about what state she prepared to Bob over a classical channel.

Depending on which state Alice prepared, Bob will prepare his system in a specific state ρ_i^{B}. In doing so, the total system is prepared in the state

$$\rho = \sum_i p_i \rho_i^{\mathrm{A}} \otimes \rho_i^{\mathrm{B}}, \tag{2.7}$$

which is the most general state that can be prepared by Alice and Bob using only local operations and classical communication (LOCC). The correlations that the state in Eq. (2.7) exhibits arise from the probabilities p_i and thus, they have a purely classical origin. Entanglement of mixed states is therefore defined in the following way. A mixed state ρ of a bipartite system is *separable* if and only if it can be written as a convex combination, i.e. with coefficients $p_i \geq 0$ and $\sum_i p_i = 1$, as given in Eq. (2.7). Otherwise, the mixed state ρ is said to be *entangled* [33]. The number of convex weights p_i in the case of a separable mixed state is constrained by the dimensions of the Hilbert spaces $\mathcal{H}_{\mathrm{A}}$ and $\mathcal{H}_{\mathrm{B}}$ to be maximally $d_{\mathrm{A}}^2 d_{\mathrm{B}}^2$ [28]. An entangled mixed state shows correlations that cannot be produced only by LOCC, but the two subsystems need to interact in some way. Formulated in a more mathematical terminology, this means that an operator describing the unitary evolution of the composite system must act nonlocally, i.e. on states of both Hilbert spaces $\mathcal{H}_{\mathrm{A}}$ and $\mathcal{H}_{\mathrm{B}}$ to entangle an initially separable state.

Whether a pure bipartite state is separable or entangled can easily and with certainty be answered using the Schmidt decomposition [Eq. (2.5)], as described before. However for mixed bipartite states, this question is in general hard to answer and a general criteria for arbitrary dimensions has not yet been developed [28]. As an example, we describe the so-called positive partial transpose (PPT) criterion, also known as Peres-Horodecki criterion, to detect bipartite entanglement of mixed states. A general density matrix of the composite system can be expressed as

$$\rho = \sum_{ij} \sum_{kl} \rho_{ij,kl} \, |i\rangle_{\mathrm{A}} \langle j| \otimes |k\rangle_{\mathrm{B}} \langle l| \,, \tag{2.8}$$

where $\{|i\rangle_{\mathrm{A}}\}$ and $\{|k\rangle_{\mathrm{B}}\}$ are sets of orthonormal vectors in $\mathcal{H}_{\mathrm{A}}$ and $\mathcal{H}_{\mathrm{B}}$, respectively. The partial transpose is defined as the transposition with respect to only one of the two subsystems, e.g. subsystem A,

$$\rho^{\mathrm{T_A}} = \sum_{ij} \sum_{kl} \rho_{ij,kl} \, |j\rangle_{\mathrm{A}} \langle i| \otimes |k\rangle_{\mathrm{B}} \langle l| \,. \tag{2.9}$$

A density matrix ρ is called PPT if the partial transpose is positive semidefinite, $\rho^{\mathrm{T_A}} \geq 0$, i.e. it has no negative eigenvalues. The PPT criterion ensures that if ρ is separable, then $\rho^{\mathrm{T_A}} \geq 0$ or equivalently $\rho^{\mathrm{T_B}} \geq 0$ [34]. Thus, if one eigenvalue of the partial transpose is found to be negative, one can deduce that the state is entangled. The PPT criterion is in general not sufficient for separability, i.e. there exist entangled states that are PPT. However, in the special cases $d_{\mathrm{A}} = 2$ and $d_{\mathrm{B}} = 2$ or 3, PPT does imply that the state ρ is separable [35].

2.3 Entanglement Measures

In the previous section, the concept of entanglement was described for pure and mixed states in the bipartite case. A further interesting question, which is also relevant in Chap. 4 within this thesis, is *how much* a state is entangled. The motivation to quantify entanglement also comes from the distribution of so-called maximally entangled states in quantum communication [28], e.g. in the quantum teleportation protocol (see Sec. 3.4). If the distributed states are not maximally entangled, a faithful teleportation cannot be guaranteed. In the case of pure states, a convenient entanglement measure is the entropy of either subsystem [36], called *entropy of entanglement*,

$$E\left(|\psi\rangle\right) \equiv S(\rho_{\mathrm{A}}) = S(\rho_{\mathrm{B}}). \tag{2.10}$$

Here, $S(\rho) = -\mathrm{Tr}(\rho \log_2 \rho)$ is the von Neumann entropy, and $\rho_{\mathrm{A}} = \mathrm{Tr}_{\mathrm{B}}(|\psi\rangle\langle\psi|)$ and $\rho_{\mathrm{B}} = \mathrm{Tr}_{\mathrm{A}}(|\psi\rangle\langle\psi|)$ are the reduced density matrices of subsystem A and B, respectively. In this sense, one can relate the amount of entanglement to the missing information about the states of the subsystems themselves. From the definition in Eq. (2.10) one can immediately see that if $|\psi\rangle$ is a separable state, then the reduced density matrices describe pure states and hence, the von Neumann entropy is zero. If the reduced density matrices are maximally mixed, i.e.

$$\rho_{\mathrm{A}} = \rho_{\mathrm{B}} = \frac{1}{d}\mathbb{1}, \tag{2.11}$$

in case of two d-dimensional systems, then the total state is *maximally entangled* and the entropy of entanglement is $S(\rho_{\mathrm{A}}) = S(\rho_{\mathrm{B}}) = \log_2 d$. For two-level systems, or qubits (see Sec. 3.1), the maximal amount of entanglement is $E(|\psi\rangle) = 1$. An orthonormal basis of maximally entangled two-qubit states is given by the so-called *Bell states*,

$$|\Phi^{\pm}\rangle = \frac{1}{\sqrt{2}}\left(|00\rangle \pm |11\rangle\right), \tag{2.12}$$

$$|\Psi^{\pm}\rangle = \frac{1}{\sqrt{2}}\left(|01\rangle \pm |10\rangle\right), \tag{2.13}$$

that are required for many purposes in quantum communication, of which some are explained in Chap. 3. Finally, it is worth mentioning that the amount of entanglement cannot be increased by only local operations or by LOCC [28, 36].

Compared to the case of pure states, the quantification of entanglement for mixed states is not as straightforward. Several measures have been proposed in the literature based on some basic requirements that an entanglement measure should have. These are, e.g., that the entanglement must be zero for separable states or that it cannot increase under any LOCC operation. A detailed discussion would exceed the introduction given here, but can be found, e.g., in Ref. 28. We only introduce a measure called *entanglement of formation* [36], for which an analytical solution in

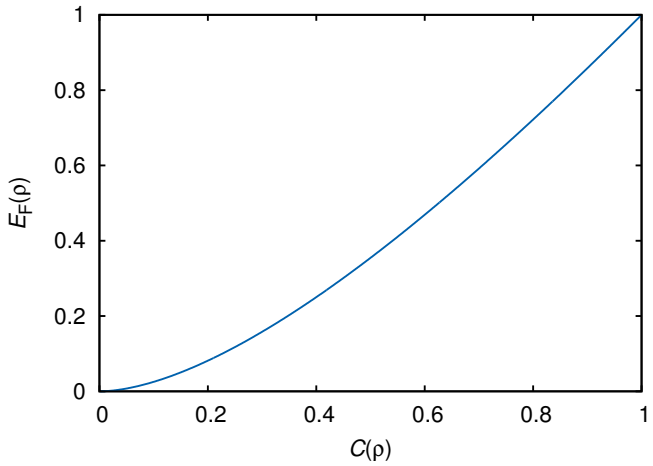

Figure 2.1 – Entanglement and concurrence. Entanglement of formation $E_F(\rho)$ as a function of the concurrence $C(\rho)$ [Eq. (2.17)]. Monotonicity suggests the use of the concurrence itself as a suitable entanglement measure.

the case of two two-level systems has been found [37], and that is used later on in this thesis to quantify the amount of entanglement between two photons. The entanglement of formation is one of the so-called convex roof measures. A general mixed state ρ can be decomposed into pure states $|\psi_i\rangle$, i.e.

$$\rho = \sum_i p_i \, |\psi_i\rangle\langle\psi_i| \,, \tag{2.14}$$

with some convex weights $p_i \geq 0$ that satisfy the relation $\sum_i p_i = 1$. The decomposition in Eq. (2.14) is not unique, and the entanglement of formation $E_F(\rho)$ of a bipartite mixed state ρ is defined as the average entropy of entanglement $E(|\psi_i\rangle)$, minimized over all possible decompositions $\{p_i, |\psi_i\rangle\}$ [36],

$$E_F(\rho) \equiv \min \sum_i p_i E(|\psi_i\rangle). \tag{2.15}$$

The definition of the entanglement of formation is justified by the circumstance that Alice and Bob need to share $E_F(\rho)$ maximally-entangled states to create the state ρ without transferring any quantum information between them [36].[3] It is generally a hard task to compute the entanglement of formation for mixed states because the calculation involves the minimization over all possible ensembles $\{p_i, |\psi_i\rangle\}$. However, in the case of two qubits, the convex roof in Eq. (2.15) can be calculated analytically by means of the so-called *concurrence* [37]. Although it seems to be merely a special case for which the entanglement of formation can be computed analytically, the study of entanglement of two-qubit systems is fundamentally important in the application of quantum information processing. The concurrence can be calculated explicitly from the density matrix ρ,

[3] This statement has to be understood in the asymptotic limit of Alice and Bob sharing n maximally-entangled states, from which they can produce a larger number m of states ρ, and the ratio n/m approaches the entanglement of formation $E_F(\rho)$ in the limit of large n [36].

and is given by the expression

$$C(\rho) = \max\{0, \lambda_1 - \lambda_2 - \lambda_3 - \lambda_4\}. \tag{2.16}$$

Here, the λ_i are the eigenvalues of the Hermitian matrix $R = \sqrt{\sqrt{\rho}\tilde{\rho}\sqrt{\rho}}$ in decreasing order, and the transformed density matrix is $\tilde{\rho} = (\sigma_y \otimes \sigma_y)\rho^*(\sigma_y \otimes \sigma_y)$, where ρ^* denotes complex conjugation of ρ in the basis $\{|0\rangle, |1\rangle\}$. The entanglement of formation and the concurrence are related via the expression [37]

$$E_{\mathrm{F}}(\rho) = h\left(\frac{1 + \sqrt{1 - C^2(\rho)}}{2}\right), \tag{2.17}$$

where $h(x) = -x\log_2(x) - (1-x)\log_2(1-x)$ denotes the binary entropy function. Since the entanglement of formation $E_{\mathrm{F}}(\rho)$ monotonically increases from 0 to 1 as a function of the concurrence $C(\rho)$ in the range from 0 to 1 (Fig. 2.1), the concurrence itself may be used as a suitable entanglement measure [37].

3

Quantum Information Processing

3.1 Quantum Bits

The fundamental unit of quantum information is the quantum bit, usually named *qubit* [3]. The name stems from its classical counterpart, the *bit*, which is the basic unit of classical information and can have one of two values, e.g. represented as 0 and 1. From a physical point of view, the qubit is a quantum-mechanical two-level system. The states representing these two levels are commonly named $|0\rangle$ and $|1\rangle$, which is also referred to as the *computational basis*. The crucial difference between the bit and the qubit originates from a fundamental law of quantum mechanics, namely the superposition principle. Whereas the classical bit is either in state 0 or in state 1, the qubit can be in an arbitrary superposition state $|\psi\rangle$, which is a linear combination of the computational basis states,

$$|\psi\rangle = \alpha\,|0\rangle + \beta\,|1\rangle\,, \tag{3.1}$$

with some complex probability amplitudes α and β. When the qubit is measured in the computational basis, it is only possible to tell with certain probabilities $|\alpha|^2$ and $|\beta|^2$ if the measurement outcome will be that the qubit was in state $|0\rangle$ or $|1\rangle$, respectively. Because the probabilities must sum to one, we have $|\alpha|^2 + |\beta|^2 = 1$. From a more mathematical point of view, the state of a qubit is therefore a unit vector in a two-dimensional complex vector space. Since it is a unit vector, Eq. (3.1) can also be rewritten in the following form,

$$|\psi\rangle = \cos\left(\frac{\theta}{2}\right)|0\rangle + e^{i\phi}\sin\left(\frac{\theta}{2}\right)|1\rangle \tag{3.2}$$

with two real numbers θ ($0 \leq \theta \leq \pi$) and ϕ ($0 \leq \phi \leq 2\pi$).[1] The form in Eq. (3.2) allows for a pictorial geometric representation of the qubit state. The numbers θ and ϕ define points on a three-dimensional unit sphere if they are interpreted as angles, as shown in Fig. 3.1. A point on the surface of this sphere thus corresponds to a specific pure state of the qubit. The sphere of all qubit

[1] Here, a global phase factor of $e^{i\gamma}$ is ignored. However, this factor has no physical effects and can therefore be neglected.

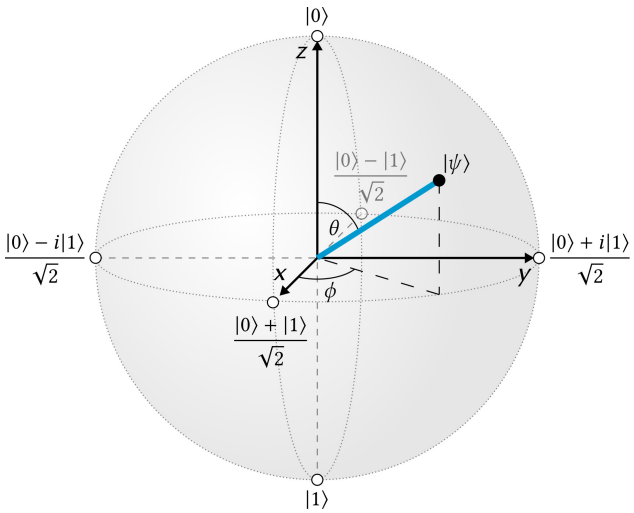

Figure 3.1 – Bloch sphere. The pure state $|\psi\rangle$ of a qubit can be represented by a point on the Bloch sphere, parametrized by the two angles θ and ϕ [Eq. (3.2)]. The poles correspond to the computational basis states $|0\rangle$ and $|1\rangle$. Other superposition states on the equator of the Bloch sphere are indicated.

states is known as the *Bloch sphere*. The poles of the Bloch sphere are the computational basis states $|0\rangle$ and $|1\rangle$, and every other point is a superposition of them. The states in the equatorial plane of the Bloch sphere correspond to superposition states with equal probabilities $|\alpha|^2 = |\beta|^2 = 1/2$.

In reality, qubits always interact with their environment, which can cause changes in the actual qubit state. If there is an energy difference between the computational basis states, unwanted transitions from the state $|0\rangle$ to the state $|1\rangle$ might happen on a characteristic timescale T_1 due to the influence of the environment. (Here, we assume the energy of $|0\rangle$ to be higher compared to $|1\rangle$.) Furthermore, phase coherence is typically lost as well due to uncontrolled interaction with the environment on a timescale T_2 that quantifies a decay of the form $|0\rangle + |1\rangle \rightarrow \{|0\rangle, |1\rangle\}$.

3.2 Elements of Quantum Computation

The manipulation and measurement of a number of qubits in a quantum computer can lead to an immense enhancement of computational power compared to a classical machine for (so far) very specific computational tasks. A first example to be mentioned is Grover's search algorithm [3, 14]. In terms of computational steps, this algorithm provides a quadratic speedup in searching through an unsorted database compared to the best possible classical search algorithm, which proves that a quantum algorithm can outperform a classical one. Another example that even shows an exponential speedup compared to all known classical algorithms, is Shor's algorithm to efficiently find the prime factors of large integer numbers [3, 15].[2] The problem size to factorize an integer

[2]The advantage of using a quantum algorithm to solve a specific task compared to classical computing is proven for Grover's algorithm. However, in case of Shor's algorithm, there is currently no classical algorithm *known* that can

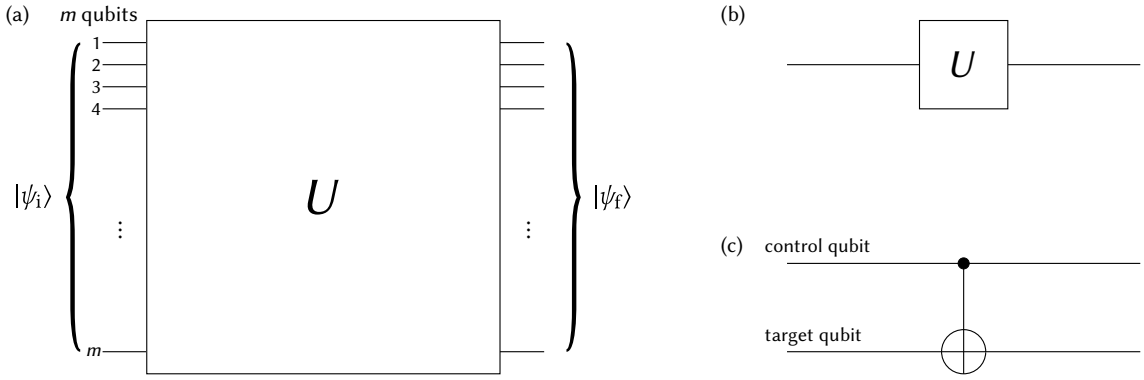

Figure 3.2 – Circuit model of quantum computation. (a) A quantum computation is a unitary operation U on a quantum register composed of m qubits that are initialized to the state $|\psi_i\rangle$. The final state after the computation is given by $|\psi_f\rangle = U|\psi_i\rangle$. (b) Circuit representation of a single-qubit operation U. (c) Circuit representation of the CNOT gate. Control and target qubits are indicated.

N can be quantified by the number of bits required to represent N, which is $n = \lceil \log_2 N \rceil$. The number of operations scales $\sim \exp(cn^{1/3})$ with some constant c for the fastest known classical algorithm. In contrast, the required number of operations to implement Shor's factoring algorithm scales $\sim n^2$. This circumstance received considerable attention since many of the encryption schemes nowadays used in information technology, e.g. the RSA cryptosystem, directly rely on the inability to efficiently factorize large numbers.

In the circuit model of quantum computation, a quantum computer can be thought of a collection of m qubits, which represent a quantum register of size m. The quantum computation itself then consists of quantum circuits, in which a specific sequence of *quantum gates* are applied to one or more qubits (Fig. 3.2). Quantum mechanics requires all these gates to be unitary transformations. Before the computation, the qubits need to be initialized to a certain state, which is the input to the quantum circuit. Due to the superposition principle, a quantum computer can perform the computation for exponentially many input states at once, since the available state space grows exponentially with the number of qubits m. This is also referred to as *quantum parallelism*. After the computational steps in form of unitary transformations have been applied, several qubits may be subject to a measurement in order to obtain some desired result. In analogy to circuits of classical computation, it can be shown that every quantum circuit on any number of qubits can be constructed from a finite set of quantum gates, which is then said to be *universal* [3]. Especially, arbitrary single-qubit rotations together with the two-qubit controlled-NOT gate [see Eq. (3.8) below] are sufficient [16]. In the following, we introduce a number of common single- and two-qubit quantum gates, which are also fundamental building blocks of protocols for quantum communication and are specifically required in some parts of this thesis.

factorize numbers with polynomial effort. The question of finding such an algorithm is related to one of the major unsolved problems in mathematics and computer science, namely the *P versus NP problem* [3].

Single-Qubit Gates

Often used single-qubit operations are given by the Pauli matrices,

$$X \equiv \sigma_x = \begin{pmatrix} 0 & 1 \\ 1 & 0 \end{pmatrix}, \quad Y \equiv \sigma_y = \begin{pmatrix} 0 & -i \\ i & 0 \end{pmatrix}, \quad Z \equiv \sigma_z = \begin{pmatrix} 1 & 0 \\ 0 & -1 \end{pmatrix}. \tag{3.3}$$

Here, and for all further representations of single-qubit gates, the matrix representation is given in the computational basis $\{|0\rangle, |1\rangle\}$. Rotations of an angle φ about the x, y, or z axis on the Bloch sphere can be generated by the Pauli matrices. The corresponding rotation operators are given by

$$R_x(\varphi) \equiv e^{-i\frac{\varphi}{2}\sigma_x} = \begin{pmatrix} \cos\left(\frac{\varphi}{2}\right) & -i\sin\left(\frac{\varphi}{2}\right) \\ -i\sin\left(\frac{\varphi}{2}\right) & \cos\left(\frac{\varphi}{2}\right) \end{pmatrix}, \tag{3.4}$$

$$R_y(\varphi) \equiv e^{-i\frac{\varphi}{2}\sigma_y} = \begin{pmatrix} \cos\left(\frac{\varphi}{2}\right) & -\sin\left(\frac{\varphi}{2}\right) \\ \sin\left(\frac{\varphi}{2}\right) & \cos\left(\frac{\varphi}{2}\right) \end{pmatrix}, \tag{3.5}$$

$$R_z(\varphi) \equiv e^{-i\frac{\varphi}{2}\sigma_z} = \begin{pmatrix} e^{-i\frac{\varphi}{2}} & 0 \\ 0 & e^{i\frac{\varphi}{2}} \end{pmatrix}. \tag{3.6}$$

A rotation about a general axis $\mathbf{n} = (n_x, n_y, n_z)$, where $\mathbf{n}$ is a unit vector, can thus be generated by the operator $R_{\mathbf{n}}(\varphi) = \exp(-i\varphi\mathbf{n}\cdot\boldsymbol{\sigma}/2)$, where $\boldsymbol{\sigma}$ denotes the vector of Pauli matrices. Other useful gates that are required at some point within this thesis are the Hadamard gate H and the phase gate S,[3]

$$\mathrm{H} = \frac{1}{\sqrt{2}}\begin{pmatrix} 1 & 1 \\ 1 & -1 \end{pmatrix}, \quad \mathrm{S} = \begin{pmatrix} 1 & 0 \\ 0 & i \end{pmatrix}. \tag{3.7}$$

Two-Qubit Gates

A universal set of quantum gates is given by arbitrary single-qubit operations together with the two-qubit controlled-NOT (CNOT) gate [16].[4] The CNOT gate has two input qubits, which are commonly referred to as the control and target qubit. The action of CNOT is to flip the state of the target qubit if the control qubit is in state $|1\rangle$, i.e. $|00\rangle \mapsto |00\rangle$, $|01\rangle \mapsto |01\rangle$, $|10\rangle \mapsto |11\rangle$, and $|11\rangle \mapsto |10\rangle$, or in matrix representation

$$U_{\mathrm{CNOT}} = \begin{pmatrix} 1 & 0 & 0 & 0 \\ 0 & 1 & 0 & 0 \\ 0 & 0 & 0 & 1 \\ 0 & 0 & 1 & 0 \end{pmatrix}. \tag{3.8}$$

[3] Here and throughout this thesis, the nomenclature of quantum gates is adopted from Ref. 3.

[4] There are also finite universal sets of quantum gates involving only one two-qubit gate. See e.g. Ref. 3 for more details.

The matrix representation is given in the product basis $\{|00\rangle, |01\rangle, |10\rangle, |11\rangle\}$. Another controlled two-qubit gate is the controlled-Z (CZ) gate, in which the Pauli-Z gate [Eq. (3.3)] is applied to the target qubit if the source qubit is set to $|1\rangle$. In matrix representation, the CZ gate is given by

$$U_{\mathrm{CZ}} = \begin{pmatrix} 1 & 0 & 0 & 0 \\ 0 & 1 & 0 & 0 \\ 0 & 0 & 1 & 0 \\ 0 & 0 & 0 & -1 \end{pmatrix}. \tag{3.9}$$

The CZ gate is also a universal two-qubit quantum gate since the CNOT gate can be constructed by using only additional single-qubit operations,

$$U_{\mathrm{CNOT}} = \mathrm{H}^{(2)} U_{\mathrm{CZ}} \mathrm{H}^{(2)}, \tag{3.10}$$

where the notation is chosen such that the Hadamard gates are applied to the second qubit, which is in this case the target qubit. In Chap. 6, we demonstrate how to implement a CZ gate between two nuclear-spin qubits in diamond. Yet another important two-qubit gate is the SWAP operation that interchanges the states of two qubits,

$$U_{\mathrm{SWAP}} = \begin{pmatrix} 1 & 0 & 0 & 0 \\ 0 & 0 & 1 & 0 \\ 0 & 1 & 0 & 0 \\ 0 & 0 & 0 & 1 \end{pmatrix}. \tag{3.11}$$

This gate, and arbitrary powers of it, are naturally generated by the typical interaction between electron spins in lateral quantum dots, namely an isotropic exchange interaction of Heisenberg type (see Chap. 5 for details). Universal quantum computation with spin qubits in quantum dots is possible since the CNOT gate can be constructed by the root of the SWAP operation using the gate sequence [18]

$$U_{\mathrm{CNOT}} = e^{-i\frac{\pi}{2}} R_y^{(2)}\left(\frac{\pi}{2}\right) R_z^{(1)}\left(-\frac{\pi}{2}\right) R_z^{(2)}\left(\frac{\pi}{2}\right) U_{\sqrt{\mathrm{SWAP}}}\, R_z^{(1)}(-\pi)\, U_{\sqrt{\mathrm{SWAP}}}\, R_y^{(2)}\left(-\frac{\pi}{2}\right), \tag{3.12}$$

where $U_{\sqrt{\mathrm{SWAP}}}$ denotes the so-called $\sqrt{\mathrm{SWAP}}$ gate that fulfills $(U_{\sqrt{\mathrm{SWAP}}})^2 = U_{\mathrm{SWAP}}$,

$$U_{\sqrt{\mathrm{SWAP}}} = \begin{pmatrix} 1 & 0 & 0 & 0 \\ 0 & \frac{1}{2}(1-i) & \frac{1}{2}(1+i) & 0 \\ 0 & \frac{1}{2}(1+i) & \frac{1}{2}(1-i) & 0 \\ 0 & 0 & 0 & 1 \end{pmatrix}. \tag{3.13}$$

3.3 Quantum Networks

A quantum network is a connection of spatially separated quantum systems that are able to exchange quantum information [38]. In such a network structure, the individual systems form the network nodes, also called *quantum nodes*, and the interconnection is established via *quantum channels* (Fig. 3.3). One of the fundamental motivations to establish a quantum network is the possibility for perfectly secure communication, which itself has become a more and more valued task especially over the last few years (see also Footnote 1 in Chap. 1). The field of quantum cryptography [4] provides means to repel any eavesdropping attack by using quantum key distribution [6, 7]. The physical implementation of quantum cryptography requires the communication parties to be able to send, receive, and process quantum information that is stored in qubits. Furthermore, the security of quantum communication can only be guaranteed if quantum information can be processed and transmitted with high fidelity. Therefore, the successful operation of a quantum network requires suitable nodes and channels. The task of a quantum node is to process and store quantum information. Therefore, the quantum systems have to be controllable in a highly accurate way and also need to exhibit a quantum memory with sufficiently long coherence times [39]. On the other hand, these quantum systems have to be able to send and receive quantum information, which requires a functioning interface to the quantum channel. The transport of quantum information is accomplished by so-called flying qubits and is typically carried out with optical photons [27, 38]. Thereby, the state of a qubit can, e.g., be encoded in the polarization degree of freedom. Due to the weak interaction of photons with their environment, they can faithfully carry quantum information over long distances, e.g. through free space or optical fibers. Thus, the coherent mapping of quantum states from photons to matter, and vice versa, is a fundamental procedure for interfacing the quantum nodes with the connecting channels.

However, even the best optical fibers are able to faithfully transmit photons only up to a certain length scale without losing quantum coherence, which is typically on the order of 10 kilometers [9]. Scattering and absorption within the fibers lead to decoherence of the quantum state of a flying qubit and therefore, perfectly secure communication is not possible anymore. Whereas in classical communication, the signal attenuation can be counteracted by intermediate network nodes that consecutively amplify and restore the signal, such a repeater structure is not feasible for quantum communication. The fundamental laws of quantum mechanics forbid to copy quantum states, which is known as the *no-cloning theorem* [40]. Therefore, the production of many copies of a single qubit in order to amplify the signal in a quantum channel is inherently not possible. One way to overcome this limitation is provided by the concept of quantum teleportation, which is described in the next section. Quantum teleportation offers the possibility to transmit qubit states over arbitrary distances if the two communicating network nodes share a maximally entangled state. Of course, the distribution of entanglement over such long distances also requires qubits, or quantum information in general, to be transmitted over these distances. However, provided that

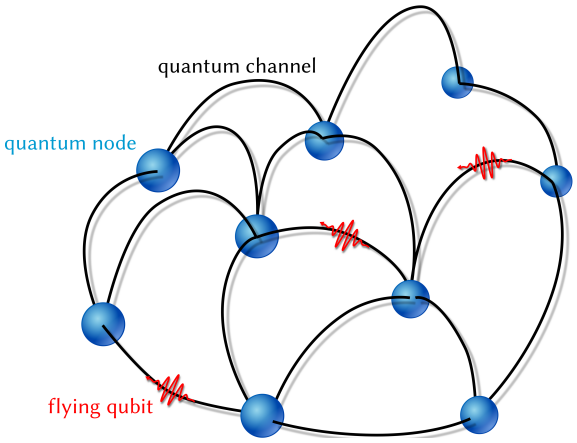

Figure 3.3 – Structure of a quantum network. Quantum networks consist of network nodes that are connected via quantum channels. Quantum information can be exchanged between the nodes using flying qubits. In this way, the nodes can be entangled, which is a fundamental requirement for perfectly secure long-distance communication or distributed quantum computation.

one has access to a source of entangled particles, the concept of a quantum repeater has been established that enables the entangling of distant quantum nodes [8, 9]. The working principle of quantum repeaters will be described in Sec. 3.6.

Quantum networks also offer new opportunities in quantum computation through the distribution of long-distance entanglement between individual quantum processors. For example, if a quantum computational task can be split into several subroutines, it can be efficiently implemented nonlocally via distributed quantum computation [41]. Other purposes are, e.g., the facilitation of large quantum registers from systems that cannot easily be scaled [42] or the simulation of many-body quantum systems by generating effective interactions between the quantum nodes via the quantum channels [38].

3.4 Quantum Teleportation and Entanglement Swapping

Although photons can serve as high-quality carriers of quantum information, the transmission distance is still limited due to absorption and scattering, e.g. within optical fibers. However, the *quantum teleportation protocol* [32] offers the possibility to transmit a quantum state between two communicating parties faithfully over arbitrary distances, provided that Alice and Bob share a maximally entangled state. Thus, the establishment of long-distance entanglement is a fundamental building-block of a quantum network, for which a quantum-repeater architecture is indispensable (see Sec. 3.6). In a slightly modified version of the original quantum teleportation protocol, one can also teleport entanglement itself, which is known as *entanglement swapping* [43]. In the following, we will describe the two mentioned quantum communication protocols.

For quantum teleportation, we consider the following situation. Alice possesses a qubit in an

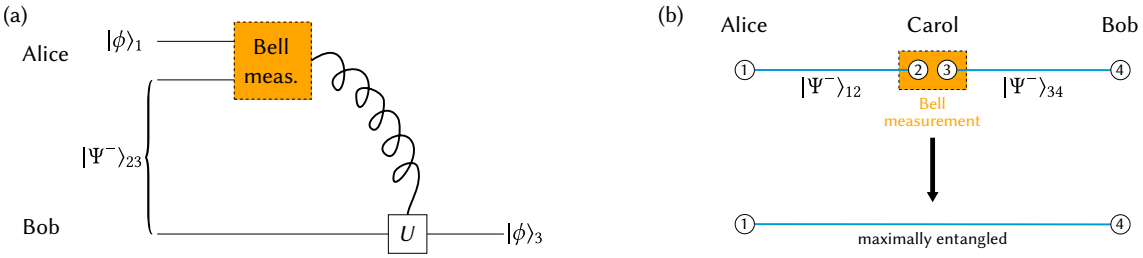

Figure 3.4 – Quantum teleportation and entanglement swapping. (a) Protocol for quantum teleportation. Alice holds qubit 1 in the unknown state $|\phi\rangle_1$ and qubit 2, which itself is entangled with qubit 3 at Bob's site. Alice performs a Bell measurement on qubits 1 and 2, and sends the measurement outcome via a classical channel to Bob. According to this information, Bob can apply a specific unitary transformation U to his qubit to recreate the state $|\phi\rangle_3$ that is identical with Alice's initial state. (b) Protocol for entanglement swapping. Alice's and Bob's qubit, respectively, are entangled with a qubit of a third party, here Carol. A Bell measurement of Carol on qubits 2 and 3 projects qubits 1 and 4 into one of the four Bell states, depending on the measurement outcome.

unknown quantum state $|\phi\rangle = a|0\rangle + b|1\rangle$ with $|a|^2 + |b|^2 = 1$, and she wants to transfer this state to her communication partner Bob. But a faithful direct transmission of the physical qubit is not possible due to a lossy quantum channel connecting both parties. However, if Alice and Bob additionally share a maximally entangled Bell state $|\Psi^-\rangle$, the nonlocal correlations help to transfer the necessary information from Alice to Bob, without knowing anything about the state $|\phi\rangle$. The composite system of the three involved qubits is initially in the state

$$|\psi\rangle_{123} = |\phi\rangle_1 |\Psi^-\rangle_{23}\,, \tag{3.14}$$

where qubit 1 is in the unknown state and qubits 2 and 3 are maximally entangled [Fig. 3.4 (a)]. Qubits 1 and 2 are held by Alice, and qubit 3 belongs to Bob. So far, no correlations exist between the unknown qubit 1 and qubit 3 at Bob's site. However, by performing a joint measurement on the composite system of qubits 1 and 2, Alice can effect Bob's qubit, too. By rewriting the state $|\psi\rangle_{123}$ as a superposition of all four maximally entangled Bell states between qubits 1 and 2 in the following form,

$$\begin{aligned} |\psi\rangle_{123} = \frac{1}{2}\Big(&|\Psi^-\rangle_{12}\,(-a\,|0\rangle_3 - b\,|1\rangle_3) + |\Psi^+\rangle_{12}\,(-a\,|0\rangle_3 + b\,|1\rangle_3) \\ &+ |\Phi^-\rangle_{12}\,(a\,|0\rangle_3 + b\,|1\rangle_3) + |\Phi^+\rangle_{12}\,(a\,|0\rangle_3 - b\,|1\rangle_3)\Big), \end{aligned} \tag{3.15}$$

one can see that a measurement in the Bell basis [Eqs. (2.12) and (2.13)], referred to as Bell measurement in the following, performed by Alice projects Bob's qubit into one of the four superposition states in Eq. (3.15), which are all unitary transformations of the initially unknown state $|\phi\rangle$, namely

$$|\psi\rangle_{123} = \frac{1}{2}\Big(|\Psi^-\rangle_{12}\,(-|\phi\rangle_3) + |\Psi^+\rangle_{12}\,(-\sigma_z\,|\phi\rangle_3) + |\Phi^-\rangle_{12}\,(\sigma_x\,|\phi\rangle_3) + |\Phi^+\rangle_{12}\,(-i\sigma_y\,|\phi\rangle_3)\Big). \tag{3.16}$$

Therefore, to fully recover the state $|\phi\rangle$, Bob can apply the inverse operation of the respective unitary transformation. To know which of the four transformations is the correct one, Alice has to send her measurement result to Bob, which is done via a classical channel.[5]

If Alice and Bob each share an entangled state with a third party, here named Carol, it is possible to create entanglement between Alice's and Bob's qubit without any direct interaction between them. The corresponding quantum protocol is known as entanglement swapping [4, 43]. We consider a situation where Alice and Bob each posses one qubit, and Carol has two qubits [Fig. 3.4 (b)]. Each of Carol's qubits is in a maximally entangled state $|\Psi^-\rangle$ with Alice's and Bob's qubit, respectively, and the state $|\psi\rangle_{1234}$ describing the total system of all four qubits is thus given by the tensor product

$$|\psi\rangle_{1234} = |\Psi^-\rangle_{12}\,|\Psi^-\rangle_{34}\,. \tag{3.17}$$

Here, the notation is chosen such that Alice holds qubit 1, Bob qubit 4, and Carol qubits 2 and 3. At this stage, there exists no entanglement between qubits 1 and 4. However, as we will see below, a joint measurement of Carol on qubits 2 and 3 can project qubits 1 and 4 into a maximally entangled state. The four-qubit state in Eq. (3.17) can be regrouped into the following form,

$$|\psi\rangle_{1234} = \frac{1}{2}\left(|\Psi^+\rangle_{14}\,|\Psi^+\rangle_{23} - |\Psi^-\rangle_{14}\,|\Psi^-\rangle_{23} - |\Phi^+\rangle_{14}\,|\Phi^+\rangle_{23} + |\Phi^-\rangle_{14}\,|\Phi^-\rangle_{23}\right), \tag{3.18}$$

from which it is evident what happens in the case of Carol performing a Bell measurement. Qubits 1 and 4 will be projected into the same Bell state as Carol obtains from her joint measurement and therefore, become maximally entangled although they never directly interacted with each other. If the Bell measurement is imperfect or the input states are not maximally entangled, the entanglement of the two-qubit state of qubits 1 and 4 after the measurement, however, will be smaller than unity [9]. Entanglement swapping itself is a fundamental building block of quantum repeaters to generate long-distance entanglement for quantum communication, which is described in Sec. 3.6.

3.5 Entanglement Purification

It was already mentioned that realistic quantum channels are noisy entities, i.e. the transmission of quantum states is not perfect. If the state to be sent is an entangled state, the amount of entanglement decreases during transportation in a noisy quantum channel. Furthermore, sources of entangled particles are also not perfect and produce two-particle states that have an overlap with a maximally entangled state, which is usually smaller than unity. In the laboratory, one generally deals with mixed states that are not maximally entangled. However, for the utilization

[5] It is worth mentioning that no superluminal information transfer can be achieved by quantum teleportation. The necessity to convey the classical information about the measurement result through a classical channel guarantees that special relativity theory is not violated. It can be shown that without any classical communication, teleportation cannot transmit any information at all [3].

in quantum communication, e.g. for the teleportation protocol, (near-)maximally entangled states have to be available in order to guarantee secure communication. To overcome the problem of noisy channels and imperfect sources, several techniques to increase the amount of entanglement have been developed, one of them being *entanglement purification* [11, 44]. Different methods for entanglement purification exist, e.g. filtering protocols, recurrence protocols, or hashing and breeding protocols. Particularly with regard to the work described in Chap. 5, however, we restrict our description of entanglement purification only to the case of recurrence protocols.

We define the fidelity F of general two-qubit quantum state ρ as the overlap relative with the Bell state $|\Psi^-\rangle$, i.e.

$$F \equiv \langle \Psi^- | \rho | \Psi^- \rangle . \tag{3.19}$$

Recurrence protocols work on two or more qubit pairs of low fidelity as input to create a single qubit pair with higher fidelity as output using only local unitary operations, measurements, and two-way communication of the measurement results via a classical channel. Having initially many copies of the low-fidelity pairs and running the purification protocol iteratively on the output pairs with higher fidelity, one can achieve fidelities arbitrarily close to $F = 1$ and thus, obtain a maximally entangled state (Fig. 3.5). The original idea of entanglement purification goes back to C. H. Bennett *et al.* [10], and will be referred to as the BBPSSW protocol. Initially, the physical setup is such that Alice and Bob have access to mixed two-qubit states ρ_I of fidelity $F = \langle \Psi^- | \rho_I | \Psi^- \rangle < 1$ that can originate from a imperfect source or a noisy quantum channel. To apply the purification protocol, the state ρ_I first needs to be brought into the following form that is diagonal in the Bell basis,

$$\rho_F = F |\Phi^+\rangle\langle\Phi^+| + \frac{1-F}{3}\Big(|\Psi^+\rangle\langle\Psi^+| + |\Psi^-\rangle\langle\Psi^-| + |\Phi^-\rangle\langle\Phi^-| \Big). \tag{3.20}$$

This can be achieved for an arbitrary two-qubit state by a so-called *twirl* operation [10, 36] that retains the component of the rotationally invariant state $|\Psi^-\rangle$, equalizes the components of the other three Bell states, and removes all off-diagonal elements. Thereby Alice and Bob have to implement a random bilateral rotation, i.e. they choose a random SU(2) rotation and apply it locally to each of the qubits, respectively. As an interim result, a so-called Werner state W_F [33] is created,

$$W_F = F |\Psi^-\rangle\langle\Psi^-| + \frac{1-F}{3}\Big(|\Psi^+\rangle\langle\Psi^+| + |\Phi^+\rangle\langle\Phi^+| + |\Phi^-\rangle\langle\Phi^-| \Big), \tag{3.21}$$

that can be brought into the Bell-diagonal form in Eq. (3.20) by performing the rotation $R_y(\pi)$ on one of the two qubits to interchange the $|\Psi^-\rangle$ and $|\Phi^+\rangle$ components. The BBPSSW protocol requires two copies of the state ρ_F as input and the next step is a bilateral CNOT operation [Fig. 3.5 (a)]. Therefore, Alice and Bob each perform a CNOT gate [Eq. (3.8)] between the two qubits they hold, respectively, where the qubits of the first (second) pair serve as control (target) qubit and the target qubit is flipped if the source qubit is in state $|1\rangle$. After this bilateral operation, both target qubits are measured in the computational basis $\{|0\rangle, |1\rangle\}$ and the measurement results are compared. If the outcomes of Alice's and Bob's measurement are the same, they keep the

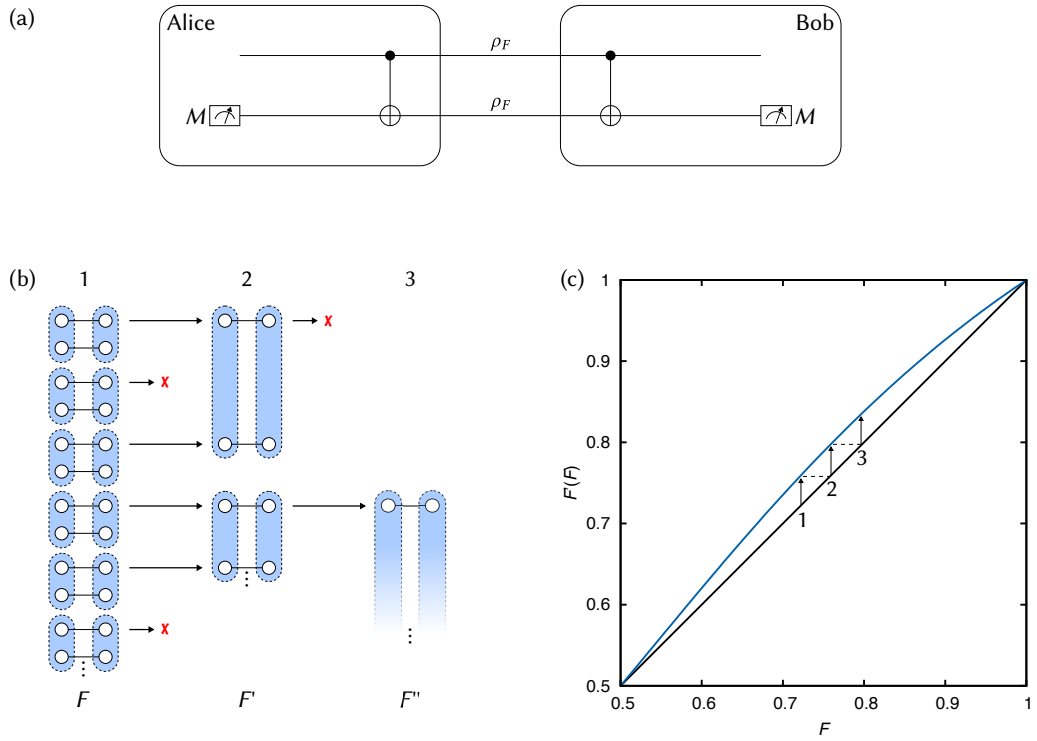

Figure 3.5 – Entanglement purification. (a) Circuit of the BBPSSW protocol. Alice and Bob share two copies of the state ρ_F [Eq. (3.20)], and locally apply a CNOT gate. The target qubits (lower pair) are measured in the computational basis (M) and the results are compared. Purification was successful, i.e. the fidelity of the control qubits (upper pair) has increased, if equal measurement outcomes have been obtained. (b) Iteration of the purification protocol on several input pairs. Purified pairs are used as input for the next round. If purification is not successful, the qubits are discarded (indicated by red crosses). The fidelity increases in each round of purification, $F < F' < F''$. (c) Fidelity $F'(F)$ in Eq. (3.22) (blue). The purification steps from (b) are indicated. Further iteration can increase the fidelity arbitrarily close to 1.

control qubits, otherwise the state is discarded. In the case of obtaining equal measurement results, which is referred to as a successful purification round, the $|\Psi^-\rangle$ and $|\Phi^+\rangle$ components are again interchanged, and the fidelity F' of the remaining source pair is given by [10]

$$F'(F) = \frac{F^2 + \frac{1}{9}(1-F)^2}{F^2 + \frac{2}{3}F(1-F) + \frac{5}{9}(1-F)^2}. \tag{3.22}$$

The fidelity $F'(F)$ is plotted in Fig. 3.5 (c) and turns out to be larger than the initial fidelity F provided that $1/2 < F < 1$. Therefore, iterating the scheme can bring the fidelity arbitrarily close to 1, resulting in a maximally entangled Bell state [Figs. 3.5 (b) and (c)]. Since the state after one purification round is not a Werner state, the unilateral rotation $R_y(\pi)$ in the last step to interchange the $|\Psi^-\rangle$ and $|\Phi^+\rangle$ components is necessary as a prerequisite for the twirl in the subsequent round.

A very similar purification protocol that also makes use of the bilateral CNOT operation and

works on general Bell-diagonal states has been developed by Deutsch *et al.* [11]. This so-called DEJMPS protocol therefore does not need an intermediate twirl operation to come back to Werner form. The protocol initially requires two Bell-diagonal input qubit pairs $\tilde{\rho}$ of the form

$$\tilde{\rho} = A\,|\Phi^+\rangle\langle\Phi^+| + B\,|\Psi^-\rangle\langle\Psi^-| + C\,|\Psi^+\rangle\langle\Psi^+| + D\,|\Phi^-\rangle\langle\Phi^-|\,. \tag{3.23}$$

A purification round begins with Alice performing the single-qubit transformation

$$U = \begin{pmatrix} 1 & -i \\ -i & 1 \end{pmatrix} \tag{3.24}$$

to both of her qubits, and Bob applies the inverse of this operation, U^{-1}. As in the BBPSSW protocol, a bilateral CNOT and the measurement of the target pair follow, keeping the control qubits only if the outcomes are equal. After a successful purification round, the state of the control qubits $\tilde{\rho}'$ is given by [11]

$$\tilde{\rho}' = \left(\frac{A^2+B^2}{N}\,|\Phi^+\rangle\langle\Phi^+| + \frac{2CD}{N}\,|\Psi^-\rangle\langle\Psi^-| + \frac{C^2+D^2}{N}\,|\Psi^+\rangle\langle\Psi^+| + \frac{2AB}{N}\,|\Phi^-\rangle\langle\Phi^-|\right), \tag{3.25}$$

where $N = (A+B)^2 + (C+D)^2$. If the initial $|\Phi^+\rangle$ component $A > 1/2$, the states can be purified to a pure $|\Phi^+\rangle$ state by iterative application [11], but in a more efficient way compared to the BBPSSW protocol.

Both protocols described above require a large amount of local resources to begin with, since in every purification round the target pairs are certainly discarded and the purification is only successful with a certain probability (see Chap. 5 for more details on this probability, e.g. in Fig. 5.5). This need in memory capabilities can be transferred to temporal resources by a method called *entanglement pumping* [45]. Instead of having initially many copies of elementary qubit pairs produced by the source and using purified pairs of a previous round as input states in the subsequent round, only a single qubit pair will be continuously purified with the aid of an elementary pair from the source. For the purification step, either the BBPSSW or the DEJMPS protocol can be used. In this case, one only needs to store a single qubit pair as source state and uses a fresh elementary qubit pair as target state in every purification round. But, in case a purification round is not successful, the whole purification process must be started from the beginning and therefore, the number of repetitions increases compared to the BBPSSW and DEJMPS protocols, in which the purification steps can be implemented in parallel. Furthermore, in general no maximally entangled states can be produced by entanglement pumping. However, the scheme can be improved if not only elementary pairs are used for purification, but prepurified pairs with a larger fidelity. With this *nested entanglement pumping* scheme [45] it is possible to generate maximally entangled states, while the memory requirements remain moderate.

3.6 Quantum Repeater

For the distribution of entanglement over arbitrary distances in a quantum communication network the concept of a *quantum repeater* has been developed [8, 9]. Noisy quantum channels in realistic network scenarios limit the distance over which quantum information can be faithfully transmitted, e.g. by using photons as flying qubits. On the one hand, the number of trials to send a photon between two quantum nodes without absorption increases exponentially with the distance between the two nodes. And in addition, the fidelity of the transmitted state with respect to the initially sent state decreases exponentially with this distance. The idea of classical repeater stations that simply amplify the signal on the way from sender to receiver is not applicable for quantum information since quantum states cannot be cloned [40]. The problem of fidelity loss can be partially solved by using entanglement purification techniques that are described in the previous section. However, entanglement purification requires a minimum initial fidelity F_{min}, which for the BBPSSW and the DEJMPS protocol is $F_{\text{min}} = 1/2$ in case all operations are perfect. If the measurements and CNOT gates are erroneous, the minimum fidelity to operate purification becomes larger than 1/2 [8]. Thus, if the channel length is too large, the fidelity of an entangled qubit pair drops below the value F_{min}, such that entanglement purification cannot be applied to create high-fidelity entangled qubit pairs. Nevertheless, maximally-entangled qubit pairs can be created between nodes of arbitrary distance by a nested entanglement purification scheme, which is a combination of entanglement purification and entanglement swapping, known as quantum repeater [8, 9]. The distant entangled qubits can then be used to transfer quantum information via teleportation.

We consider the scenario where entanglement should be established between two quantum nodes A and B (Fig. 3.6). The idea is the following: The quantum channel connecting the two nodes A and B is divided into smaller segments, between which entangled qubit pairs can be distributed with some fidelity F_1 (top part in Fig. 3.6). A Bell measurement at site C_i connects the two involved qubit pairs through entanglement swapping and thus, eventually connects the qubits of nodes A and B if this is performed at each intermediate node. However, the fidelity of a qubit pair that emerged from entanglement swapping is reduced compared to the fidelity F_1 of the initial pairs if $F_1 < 1$. The final fidelity F_N of the pair between A and B also decreases exponentially with the number of intermediate nodes N and hence, might eventually become smaller than F_{min}. Merely inserting intermediate nodes and using entanglement swapping to connect them therefore does not help in generating long-distance entanglement. However, intermediate purification steps of only a fraction of the segments permits the establishment of high-fidelity entanglement between nodes A and B. The number of segments that can be connected via entanglement swapping, and still be purified afterwards, is called L. Typically, this number is much smaller than the total number of segments N. By definition, the fidelity F_L of a connected segment of length L has to be larger than the minimum fidelity required for purification, $F_L > F_{\text{min}}$. For simplicity, one can assume

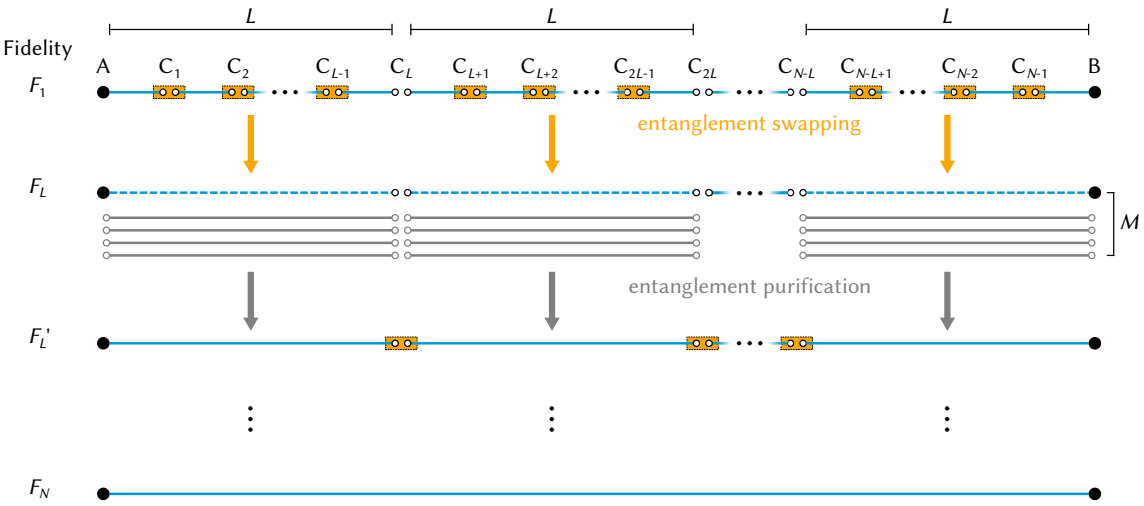

Figure 3.6 – Working principle of a quantum repeater. The channel between nodes A and B is split into N segments by introducing intermediate nodes C_1 to C_{N-1}. Entangled qubit pairs can be distributed between the nodes with a fidelity F_1 (blue lines in top row). Bell measurements (orange boxes) at intermediate nodes (except at $C_L, C_{2L}, \ldots$) create entangled qubit pairs of distance L with a smaller fidelity (indicated by dashed lines) through entanglement swapping. M additional copies can be used to subsequently purify the pairs of length L, and create a single pair with fidelity $F_L' \geq F_1$. Iteration of this scheme creates a single entangled qubit pair between the distant nodes A and B with fidelity $F_N \geq F_1$.

that the whole channel is divided into $N = L^n$ segments, with n being an integer. Beginning at node A, as a first step one connects L subsequent qubit pairs via entanglement swapping to obtain entangled qubit pairs of fidelity F_L between nodes A and C_L, C_L and C_{2L}, ..., and C_{N-L} and B (see Fig. 3.6). In total, this yields N/L qubit pairs of distance L. The remaining qubit pairs can now be purified with M additional copies (second step in Fig. 3.6) that were generated in parallel, up to a fidelity $F_L' \geq F_1$, which is also the condition that determines the number M. The next level in the repeater scheme is simply a repetition of the first step on the new qubit pairs. In doing so, one now obtains qubit pairs that are separated by L^2, which can be purified afterwards. Therefore, n iterations of this scheme will connect nodes A and B with a final fidelity larger than F_1. Subsequent purification steps can be applied to bring the fidelity close to unity. To create a qubit pair that is separated by a longer distance, LM elementary qubit pairs are required in every iteration round. The total number of elementary pairs is $(LM)^n = N^{\log_L M+1}$ [8, 9]. Thus, the resources only grow polynomially with the length of the channel, i.e. the number of segments N. Taking faulty operations into account that exhibit errors of 0.5 %, the required time to create an entangled qubit pair on the global scale is estimated to be a few seconds [9].[6]

[6] The exact value depends on various parameters, such as the probabilities for single-qubit and two-qubit gate errors, measurement errors, the initial fidelity, the kind of loss within the optical fiber, and especially the purification technique. A detailed discussion would exceed this introductory chapter, but can be found in Ref. 9.

4

Entangled Photons in the Polariton Vacuum

4.1 Introduction

Many protocols for quantum communication require the transfer of quantum information that is stored in qubits. E.g. in quantum key distribution [6], single qubits have to be sent from one participant to the other to remotely generate a secret key for encrypted communication. Furthermore, as described in Chap. 3, the distribution of entangled qubits is indispensable to assemble a large-scale quantum network for secure communication eventually over global distances. Photons are the primary physical candidate to take on the role of flying qubits [27], whose task is to faithfully transmit quantum information over long distances. Therefore, highly functioning single- and entangled-photon sources need to be developed. Other hardware components, such as controllable stationary qubit registers including a quantum memory as well as interfaces between stationary and flying qubits (see, e.g., [39, 47–52]), become more and more established, which makes the development of a proper photon source a very timely task. The work presented in this chapter is focused on the generation of entangled photon pairs.

A source of entangled photons must fulfill several basic requirements such that it can be utilized for quantum information processing:

(i). The amount of entanglement has to be sufficiently large. The fidelity during transmission will be decreased, but entanglement-based protocols for quantum information processing require maximally entangled states (see, e.g., Secs. 3.4 and 3.6) and purification requires a minimum fidelity to work (see Sec. 3.5).

(ii). The production of the photon pairs has to be deterministic, i.e. the release of the photons can be triggered by some external control parameter.

(iii). The source has to be efficient, i.e. the probability for the emission of two entangled photons should be large enough to keep the temporal resources in terms of photon production moderate.

Various different approaches for the production of bipartite entangled-photon states have been developed [53]. Perhaps the most prominent examples that were also put into practice are type-II spontaneous parametric down-conversion [54] and the biexciton-recombination cascade in a quantum dot (QD) [55], which are described in Sec. 4.2. However, existing proposals still exhibit drawbacks regarding their practical use. For this reason, the question appears of relevant interest, whether other physical systems might be suitable for entangled-photon production.

In particular, we study the intersubband cavity (ISC) system (Sec. 4.3), for which the emission of correlated photon pairs was predicted theoretically [56]. The emission can be triggered by modulating the light-matter interaction between microcavity photons and electronic intersubband excitations in quantum wells (QWs). Intersubband transitions are mainly used in quantum well infrared photodetectors [57] and quantum cascade lasers [58–61]. Embedded in a microcavity, it is possible to reach a regime of ultrastrong light-matter coupling [62–65], in which the vacuum-field Rabi frequency can be on the order of the intersubband transition frequency. In this regime, the ground state of the system, i.e. a squeezed vacuum, already contains a nonzero number of photons. Other systems that can reach the ultrastrong coupling regime are superconducting circuits [66–68], where the emission of quantum vacuum radiation was recently demonstrated [69].

In our work, we analyze the ground state of the ISC system, i.e. the so-called polariton vacuum, related to two-photon entanglement (Sec. 4.4). For this purpose, we use an explicit expression for the polariton vacuum that is given in terms of photonic Fock states. After postselecting certain photonic states and tracing out all electronic degrees of freedom, the photonic two-qubit system will be in a mixed state. As an entanglement measure, we therefore use the concurrence to quantify the mode entanglement between two photons and find that, in principle, maximally entangled states can be generated, depending on the photon energies.

4.2 Sources of Entangled Photons

Photons are the standard medium to transfer quantum information due to their weak interaction with the environment. Such flying qubits are especially used to distribute entanglement, e.g. in a quantum communication network [38], and thus, need to be produced in a highly accurate way. Various physical approaches for the generation of entangled photon pairs have been suggested and to some extend also been implemented, see e.g. Ref. 53. In this section, we describe the two main techniques, namely the generation with type-II parametric down-conversion in birefringent crystals and the biexciton-recombination cascade in semiconductor QDs. It is worth mentioning that the first experiments regarding the generation of entangled photon pairs utilized atomic radiative decays, culminating in the milestone experiments that demonstrate the violation of Bell's inequality and thus, could rule out physical theories of local hidden variables [30, 31]. However, these approaches have several drawbacks regarding their usability for quantum information

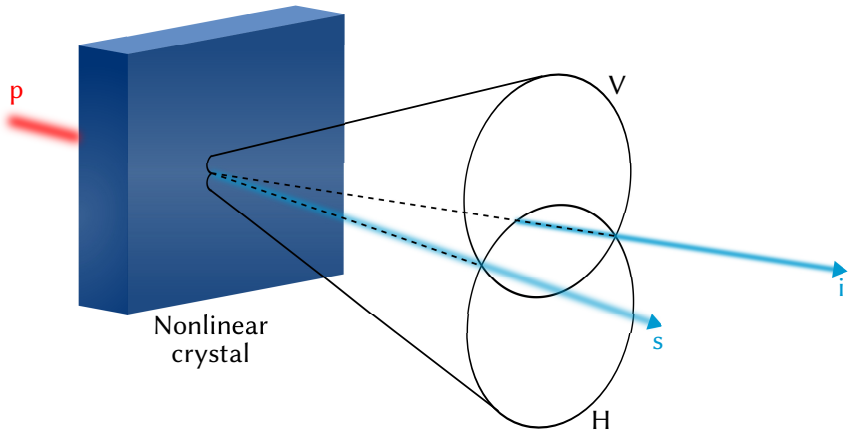

Figure 4.1 – Spontaneous parametric down-conversion. Type-II parametric down-conversion of a pump (p) photon into two photons in a nonlinear crystal. The two generated photons, denoted as signal (s) and idler (i), have orthogonal polarization and are emitted along cones with different symmetry axes for the horizontal (H) and vertical (V) polarization, respectively. Emission along the intersection lines yields the polarization-entangled state in Eq. (4.3).

processing, like the collection efficiency of the photons is too low and the handling of single atoms challenging, but it was neither intended to develop an applicable source of entangled photon pairs in these experiments.

4.2.1 Type-II Parametric Down-Conversion

Polarization-entangled photons can be generated by a nonlinear optical process in birefringent crystals with $\chi^{(2)}$ optical nonlinearity, in which a pump (p) photon incident on the crystal is converted into two photons, commonly named the signal (s) and the idler (i) photon (see Fig. 4.1). This effect is known as parametric down-conversion (PDC). Two kinds of PDC exist that differ in the polarizations of the two generated photons that can either be parallel (type-I) or orthogonal (type-II). Whereas type-I PDC in a single crystal requires post-selection techniques to create entanglement between the two photons, type-II PDC can directly generate entangled photons, which is the scenario described here. Because of energy and momentum conservation in the photon conversion process described above, the so-called phase matching conditions

$$\omega_\mathrm{p} = \omega_\mathrm{s} + \omega_\mathrm{i}, \tag{4.1}$$

$$\mathbf{k}_\mathrm{p} = \mathbf{k}_\mathrm{s} + \mathbf{k}_\mathrm{i}, \tag{4.2}$$

have to be fulfilled, where ω_j and $\mathbf{k}_j$ ($j = \mathrm{p}, \mathrm{s}, \mathrm{i}$) are the photon frequency and wave vector, respectively. Due to the phase matching conditions, the signal and the idler photon are emitted along cones which do not necessarily have a common axis [54]. As one can see from Fig. 4.1, the cones intersect along two lines. If photon emission occurs in direction of the intersection lines, one cannot distinguish to which cone each photon belongs to, although it is known that both

photons have orthogonal polarizations. Thus, the two photons can be described by the entangled state [54]

$$|\psi\rangle = \frac{1}{\sqrt{2}}\left(|V\rangle_s |H\rangle_i + e^{i\alpha} |H\rangle_s |V\rangle_i\right). \tag{4.3}$$

Here, $|V\rangle$ and $|H\rangle$ denote the vertical and horizontal polarization states of the photons, respectively, and the relative phase α can be changed by additional birefringent crystals. Type-II PDC has been used to demonstrate, e.g., the first verification of quantum teleportation [70]. A requirement for the generation of exactly the two-photon state $|\psi\rangle$ in Eq. (4.3) is that the photons need to be indistinguishable except for the polarization degree of freedom. Therefore, the spatiotemporal profile of the photon modes have to be the same. A drawback of PDC for entangled-photon generation is the low conversion efficiency. More than 10^{10} pump photons are required to generate a single photon pair [54], which is too low for practical application. This rate could be increased by a factor of 10 using a modified setup of two lined up nonlinear crystals and type-I PDC [71]. Furthermore, the photon production is a random process, whereas on-demand generation is needed in view of applicability.

4.2.2 Biexciton Decay Cascade

A semiconductor-based approach for the generation of polarization-entangled photon pairs is provided by the radiative decay of the biexciton state in a QD and has been proposed in Ref. 55. The biexciton consists of two bound electron-hole pairs that are created, e.g., by electrical pumping of an electron from the valence band to the conduction band, thus creating a hole in the valence band. Electron and hole reside in a bound state due to Coulomb interaction, which is called an exciton. Angular momentum conservation determines the selection rules for the optical excitation and hence, the spin of the exciton depends on the polarization of the exciting photon, which is either σ^+ or σ^- circularly polarized. In the biexciton state, the constituting electrons have opposite spin projections due to the Pauli principle. The probability for the first recombination in the biexciton is the same for both spin states and hence, a photon is emitted having σ^+ or σ^- circular polarization with equal probability (Fig. 4.2). However, the subsequently emitted photon from the recombination of the remaining electron-hole pair definitely has orthogonal polarization, such that both photons form the maximally entangled Bell state $|\Psi^+\rangle$ [55],

$$|\Psi^+\rangle = \frac{1}{\sqrt{2}}\left(|\sigma^+\rangle_1 |\sigma^-\rangle_2 + |\sigma^-\rangle_1 |\sigma^+\rangle_2\right). \tag{4.4}$$

Here, the indices denote in which recombination process the photon is created. An advantage of this scheme compared to the PDC approach described above is the on-demand production of the photons that can be triggered by electrical pumping. However, for the generation of the state in Eq. (4.4), the intermediate exciton level has to be degenerate for both spin states (Fig. 4.2). Otherwise, the photon polarization can be determined by its energy. This which-path information

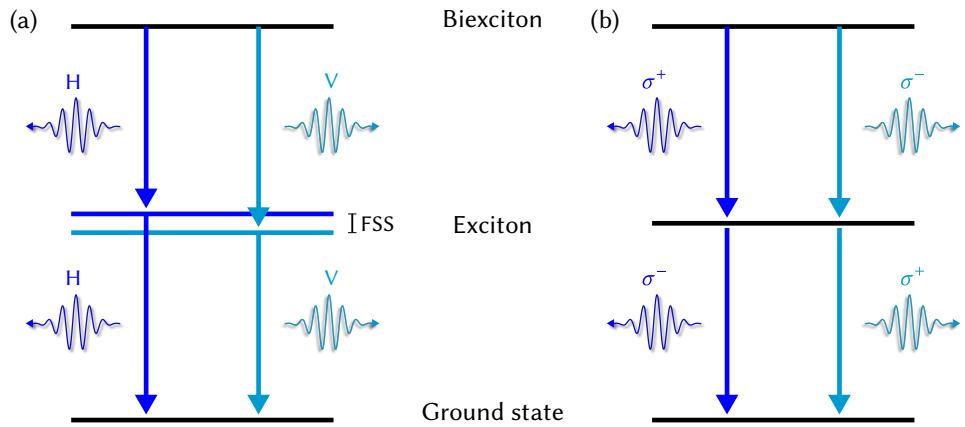

Figure 4.2 – Biexciton-recombination cascade. (a) The biexciton state can decay to the ground state via the intermediate exciton state by the emission of two photons. If the fine-structure splitting (FSS) is larger than the exciton line widths, the frequency of the emitted photons in both recombination processes is different for horizontal (H) and vertical (V) polarization, respectively. Hence, an energy measurement can disclose the which-path information, i.e. through which recombination path the biexciton decayed to the ground state. The photons are therefore not entangled. (b) For degenerate exciton levels, the which-path information is erased and the both polarizations, σ^+ and σ^-, have the same frequency. (Note that in the degenerate case, the description in the circular polarization basis is equivalent to linear polarization.)

destroys the polarization entanglement of the photons. The fine-structure splitting of the exciton states, which can be on the order of 1 μeV [72], is caused by an anisotropic electron-hole exchange interaction and also depends on structural asymmetries of the QD (see e.g. Ref. 73). External magnetic fields can be used to reduce and eventually cancel the fine-structure splitting, enabling entanglement generation in form of the state $|\Psi^+\rangle$ in Eq. (4.4) with a fidelity of 70 % [74]. In different approaches, entangled photons from the biexciton cascade have been generated by erasing the which-path information with spectral filtering [75] or canceling the fine-structure splitting with electric fields [76]. The efficiency of such a semiconductor-based source can be several orders of magnitude larger compared to PDC, creating up to 0.12 photon pairs per excitation pulse [77].

4.3 Intersubband Cavity System

4.3.1 Physical Structure

The intersubband cavity (ISC) system is formed by semiconductor quantum wells (QWs) that are stacked inside a microcavity. The QWs are composed of layers of semiconducting materials with different band gaps, such that a real-space energy structure as depicted in Fig. 4.3 (a) is created. The potential well confines the electronic motion along the growth direction, which is here chosen to be the z axis. In the lateral plane, electrons can freely move inside the semiconducting material. This gives rise to a parabolic dispersion for the motion within the plane normal to the growth axis. An electronic system that can effectively move in only two dimensions is named two-dimensional

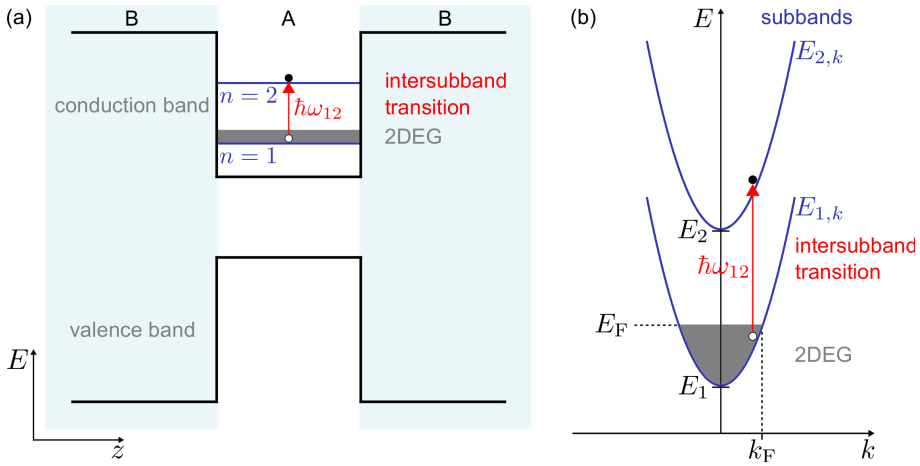

Figure 4.3 – Subband energy structure of a quantum well (QW) formed in a semiconductor heterostructure. (a) In real space, along the growth direction (z) of the structure. The semiconductors forming the QW are denoted as A and B. The QW contains a two-dimensional electron gas (2DEG). Here, we study intersubband transitions between the first two subbands $n = 1$ and $n = 2$ with transition energy $\hbar\omega_{12}$. (b) Same situation in k space, where k is the electronic in-plane momentum perpendicular to the growth axis. The 2DEG populates states up to the Fermi energy E_F, with a corresponding wave vector k_F. The energy dispersion of subband n is denoted as $E_{n,k}$. E_n is the subband energy for zero in-plane momentum.

electron gas (2DEG). Due to the confinement potential, the electronic states in the conduction band are quantized along the z axis, which leads to the formation of parabolic energy bands in the reciprocal in-plane momentum space, the so-called *subbands*.[1] Electronic excitations within the conduction band are thus named *intersubband transitions*. The transition energy does not depend on the band gap of the semiconductor, and can be adjusted by the width and depth of the QW.[2] For our considerations, we assume the 2DEG to only populate the first subband ($n = 1$), such that the Fermi energy is below the energy of the second subband ($n = 2$) for zero in-plane momentum [Fig. 4.3 (b)]. Typically, the energies of intersubband transitions are in the mid-infrared regime [62] and the selection rules require the exciting radiation field to have transverse-magnetic (TM) polarization (Fig. 4.4), since the dipole matrix element is proportional to the z component of the electric field [57]. The excitation of an intersubband transition is a collective effect. All electrons within the 2DEG take part in the interaction with the electromagnetic field, which significantly increases the coupling strength and enables to reach a regime of ultrastrong light-matter interaction. In this regime, the ground state of the ISC system exhibits particular properties that are harnessed for photon generation and are described in the next section.

[1] An equivalent energy structure exists for holes in the valence band of semiconductor A (Fig. 4.3), which is, however, not relevant for the work presented here.

[2] For excitation of an intersubband transition with electromagnetic radiation, the transition energy ω_{nm} between two subbands n and m can be assumed to be dispersionless, since the momentum of the exciting photon is small compared to the in-plane momentum of an electron.

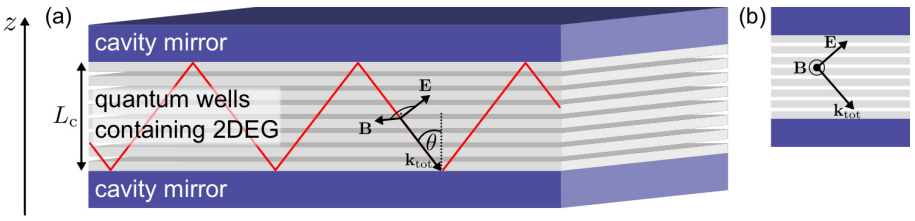

Figure 4.4 – Intersubband cavity system. (a) A sequence of doped quantum wells (gray) inside a microcavity of length L_c (cavity mirrors in blue) forms the intersubband cavity system. The light-matter interaction in such a system depends on the propagation angle θ of the cavity photons. The transverse-magnetic (TM) polarization is indicated by the electric and magnetic field vectors. The electric field **E** lies in the plane of incidence and the magnetic field **B** is perpendicular to it, and both are perpendicular to the photon wave vector $\mathbf{k}_{tot}$. (b) The plane of incidence to better demonstrate the TM-polarization of the photons.

4.3.2 Model

The first theoretical description of the intersubband cavity system (ISC) has been given in Ref. 78 in the context of optical absorption. It was suggested that the interaction between intersubband transitions in quantum wells and microcavity photons can reach the strong coupling regime of cavity QED, forming so-called polariton states. The electromagnetic cavity field can create a material excitation, which itself decays under the emission of a photon into the cavity mode. This interplay inherently couples the dynamics of both the cavity field and the embedded emitter, such that the fundamental excitations of the combined system are composed of a solid-state excitation and a microcavity photon, which is the polariton. The intersubband cavity system was further studied theoretically, see e.g. Ref. 56. It consists of n_{QW} identical quantum wells embedded inside a semiconductor microcavity (Fig. 4.4). The quantum wells are assumed to be negatively charged with a 2DEG of density N_{2DEG} that populates the first subband (Fig. 4.3). We consider the interaction of intersubband excitations between the two lowest subbands and photons of the fundamental cavity mode. The full light-matter interaction Hamiltonian in the Coulomb gauge describing the ISC has the form [56]

$$\begin{aligned} H = &\sum_{\mathbf{k}} \hbar\omega_c(k) \left(a_{\mathbf{k}}^\dagger a_{\mathbf{k}} + \frac{1}{2}\right) + \sum_{\mathbf{k}} \hbar\bar{\omega}_{12}(k) b_{\mathbf{k}}^\dagger b_{\mathbf{k}} \\ &+ \sum_{\mathbf{k}} i\hbar\Omega_R(k) \left(a_{\mathbf{k}}^\dagger + a_{-\mathbf{k}}\right)\left(b_{\mathbf{k}} - b_{-\mathbf{k}}^\dagger\right) + \sum_{\mathbf{k}} \hbar D(k) \left(a_{\mathbf{k}}^\dagger + a_{-\mathbf{k}}\right)\left(a_{-\mathbf{k}}^\dagger + a_{\mathbf{k}}\right). \end{aligned} \tag{4.5}$$

The operator $a_{\mathbf{k}}^{(\dagger)}$ annihilates (creates) a cavity photon with in-plane wave vector $\mathbf{k} = (k_x, k_y)$ and transverse-magnetic (TM) polarization. Photon polarizations other than TM are excluded due to the selection rules for intersubband transitions [57]. Since the dipole moment is oriented along the growth (z) direction, the exciting radiation must have a finite electric field component in z direction. As shown in Fig. 4.4, the magnetic field for TM-polarized light is perpendicular to the plane of incidence, whereas the electric field has a finite z-component if the total wave

vector $\mathbf{k}_{\text{tot}}$ encloses a finite angle θ with the normal to the cavity mirror. Our analysis also applies to the case where the polarization is not purely TM, because only the TM-polarized part of the radiation couples to intersubband transitions. The dispersion of the fundamental cavity mode $\omega_{\text{c}}(k)$ is given by

$$\omega_{\text{c}}(k) = \frac{c}{\sqrt{\varepsilon}}\sqrt{k^2 + k_z^2}, \tag{4.6}$$

where c is the speed of light, ε is the dielectric constant of the material used as cavity spacer and the quantization of k_z depends on the boundary conditions of the electromagnetic field. In the following, $k = |\mathbf{k}|$ is the length of the in-plane wave vector.

The operator $b_{\mathbf{k}}^{(\dagger)}$ annihilates (creates) an electronic intersubband excitation. For the generation of entangled photon pairs, the ISC has to be operated in the so-called *ultrastrong coupling regime*, in which the vacuum-field Rabi splitting $\Omega_{\text{R}}(k)$ is of the order of the transition energy of the emitter that is coupled to the cavity. The ultrastrong coupling regime can only be reached if the electron density N_{2DEG} is sufficiently large, i.e. about 10^{12} cm^{-2}, since the Rabi frequency scales as $\Omega_{\text{R}}(k) \propto \sqrt{N_{\text{2DEG}}}$ [see Eq. (4.11) below]. For such high densities, the renormalization of the intersubband energy due to Coulomb interaction between the electrons within the 2DEG,

$$\bar{\omega}_{12}^2(k) = \omega_{12}^2\Big(1 + \delta(k)\Big), \tag{4.7}$$

can in general not be neglected. The so-called depolarization shift $\delta(k)$ [57] is found to be [79, 80]

$$\delta(k) = \frac{N_{\text{2DEG}} e^2 I(k)}{\varepsilon_0 \varepsilon \omega_{12} k}, \tag{4.8}$$

where e is the elementary charge, ε_0 is the vacuum permittivity and ω_{12} is the transition energy between the subbands 1 and 2, which in the absence of Coulomb interaction determines the absorption maximum. The function $I(k)$ originates from the two-dimensional Coulomb integral,

$$I(k) = \int \mathrm{d}z\, \mathrm{d}z'\, \varphi_1(z)\varphi_2(z)\varphi_2(z')\varphi_1(z') e^{-k|z-z'|}, \tag{4.9}$$

where $\varphi_{1,2}(z)$ are the z dependent parts of the (real) QW wave functions of subband 1 and 2, respectively. By using proper matching conditions at the semiconductor interfaces [57], the wave functions are obtained by solving the Schrödinger equation. The integral $I(k)$ can then be solved analytically. The depolarization shift itself describes the change in spatial charge distribution within the 2DEG, i.e a plasmonic excitation, due to the excitation of an electron from subband 1 to subband 2, which accompanies a single-particle excitation. Hence, the operators $b_{\mathbf{k}}^{(\dagger)}$ in Eq. (4.5) are plasmonic operators describing collective electronic excitations. They can be obtained from a Bogoliubov transformation of the single-particle operators $\tilde{b}_{\mathbf{k}}^{(\dagger)}$ [81] that describe the only bright, i.e. optically active, intersubband excitation and that are given by the completely symmetric

superposition [56, 82]

$$\tilde{b}_{\mathbf{k}} = \frac{1}{\sqrt{n_{\mathrm{QW}} N_{\mathrm{2DEG}} A}} \sum_{m=1}^{n_{\mathrm{QW}}} \sum_{q<k_{\mathrm{F}}} c_{2,\mathbf{q}+\mathbf{k}}^{(m)\dagger} c_{1,\mathbf{q}}^{(m)}. \tag{4.10}$$

Here, A is the sample are, the operator $c_{i,\mathbf{q}}^{(m)\dagger}$ creates an electron in subband i of QW m with in-plane wave vector $\mathbf{q}$, and k_{F} is the Fermi wave vector. The operators $b_{\mathbf{k}}^{(\dagger)}$ fulfill Bose commutation relations $[b_{\mathbf{k}}, b_{\mathbf{k}'}^{\dagger}] \simeq \delta_{\mathbf{k},\mathbf{k}'}$ in the weak excitation regime, i.e. when the number of intersubband excitations is much less than the number of electrons forming the 2DEG [56, 83].

The vacuum Rabi frequency $\Omega_{\mathrm{R}}(k)$ for the intersubband cavity system is given by [56, 84]

$$\Omega_{\mathrm{R}}(k) = \sqrt{\frac{e^2 N_{\mathrm{2DEG}} n_{\mathrm{QW}}^{\mathrm{eff}} f_{12} \bar{\omega}_{12}(k)}{2\varepsilon_0 \varepsilon m^* L_{\mathrm{c}}^{\mathrm{eff}} \omega_{\mathrm{c}}(k)} \sin^2\theta(k)}, \tag{4.11}$$

where $n_{\mathrm{QW}}^{\mathrm{eff}}$ is an effective number of embedded quantum wells since not all quantum wells are equally coupled to the photon field, $L_{\mathrm{c}}^{\mathrm{eff}}$ denotes an effective cavity thickness that depends on the type of cavity mirrors, and f_{12} is the oscillator strength of the subband transition. For a deep rectangular well as considered here, $f_{12} \simeq 1$ [57]. Finally, $\theta(k)$ is the propagation angle of a cavity photon, $\sin\theta(k) = k/\sqrt{k^2 + k_z^2}$. The dispersive coupling parameter $D(k)$ arises from the squared electromagnetic vector potential and can be approximated by $D(k) \simeq \Omega_{\mathrm{R}}^2(k)/\bar{\omega}_{12}$, which is valid for deep rectangular wells and exact for parabolic well potentials [56, 65]. As it has been predicted in the primary work of C. Ciuti *et al.* in Ref. 56, a regime of ultrastrong light-matter interaction can be reached in the ISC system. The commonly applied rotating-wave approximation, in which the antiresonant terms in the interaction Hamiltonian containing either two annihilation or two creation operators can be neglected, is not valid anymore. From a perturbative perspective, the contribution of the antiresonant terms scales as $\Omega_{\mathrm{R}}(k)/\bar{\omega}_{12}(k)$. Due to the large dipole moment of intersubband transitions and the collective coupling to all electrons in the 2DEG, the Rabi frequency [Eq. (4.11)] can become a significant fraction of the transition frequency $\bar{\omega}_{12}(k)$ [62–65]. Additionally, the contribution $D(k)$ from the squared electromagnetic potential is also not negligible. The contribution of the above mentioned terms has been verified experimentally [63] and has to be incorporated as given in the Hamiltonian description above.

4.3.3 Polariton Vacuum

The Hamiltonian in Eq. (4.5) can be diagonalized with an extended Bogoliubov transformation [85], also known as Hopfield transformation, where new bosonic operators

$$p_{j,\mathbf{k}} = w_j(k) a_{\mathbf{k}} + x_j(k) b_{\mathbf{k}} + y_j(k) a_{-\mathbf{k}}^{\dagger} + z_j(k) b_{-\mathbf{k}}^{\dagger} \tag{4.12}$$

are introduced that describe a quasiparticle of combined light-matter excitation, called intersubband cavity polariton [86]. Here, j indicates whether it belongs to the lower (j = LP) or upper

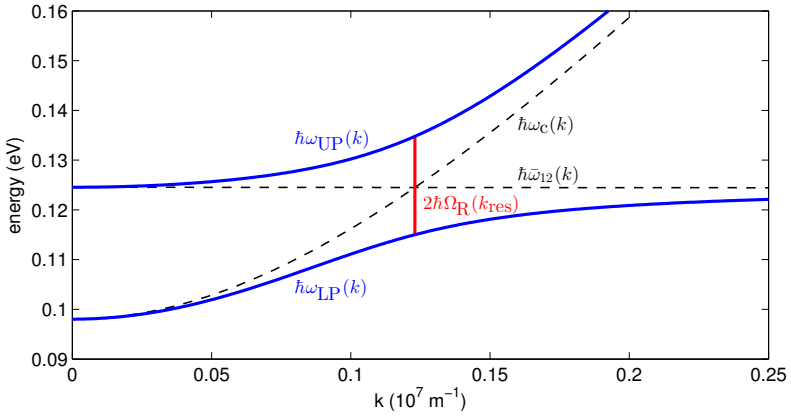

Figure 4.5 – Polariton dispersions. Lower and upper polariton energy dispersions $\hbar\omega_{\mathrm{LP}}(k)$ and $\hbar\omega_{\mathrm{UP}}(k)$ as a function of the absolute value of the in-plane wave vector k. Here, $n_{\mathrm{QW}}^{\mathrm{eff}} = 50$ GaAs/AlGaAs ($\varepsilon = 10.0$, $m^* = 0.067\, m_0$) QWs are assumed to be located inside a cavity of length $L_{\mathrm{c}}^{\mathrm{eff}} = 2\,\mu$m and doped with a two-dimensional electron gas density of $N_{\mathrm{2DEG}} = 10^{12}$ cm^{-2}. The plot shows the anticrossing region where the dotted lines are the bare cavity photon dispersion $\hbar\omega_{\mathrm{c}}(k)$ and the constant intersubband transition energy $\hbar\omega_{12} = 113$ meV [62]. The vacuum-field Rabi splitting is $2\hbar\Omega_{\mathrm{R}}(k_{\mathrm{res}})$. This plot takes into account the depolarization shift, $\bar{\omega}_{12}(k) = \omega_{12}\sqrt{1+\delta(k)}$.

(j = UP) polariton branch and again, the wave vectors $\mathbf{k}$ are in-plane. The aim is to choose the Hopfield coefficients $w_j(k)$, $x_j(k)$, $y_j(k)$ and $z_j(k)$ appropriately, such that the Hamiltonian becomes diagonal in the basis of polariton Fock states,

$$H = E_{\mathrm{G}} + \sum_{j\in\{\mathrm{LP,UP}\}} \sum_{\mathbf{k}} \hbar\omega_j(k) p_{j,\mathbf{k}}^{\dagger} p_{j,\mathbf{k}}. \tag{4.13}$$

Here, E_{G} denotes a constant ground state energy and $\omega_j(k)$ are the resulting lower and upper polariton dispersion, shown in Fig. 4.5. The Hopfield coefficients can be determined by the bosonic commutator relations

$$\left[p_{j,\mathbf{k}}^{(\dagger)}, p_{j',\mathbf{k}'}^{(\dagger)}\right] = 0, \tag{4.14}$$

$$\left[p_{j,\mathbf{k}}, p_{j',\mathbf{k}'}^{\dagger}\right] = \delta_{j,j'}\delta_{\mathbf{k},\mathbf{k}'}, \tag{4.15}$$

and furthermore, the following relation must hold [56],

$$\left[p_{j,\mathbf{k}}, H\right] = \hbar\omega_j(k) p_{j,\mathbf{k}}. \tag{4.16}$$

Here, as well as for all further quantitative results, we assume GaAs/AlGaAs quantum wells, which have been commonly used experimentally [62, 86–88]. The material-dependent parameters are $m^* = 0.067\, m_0$ and $\varepsilon = 10$. The number of embedded quantum wells n_{QW}, the length of the microcavity L_{c} and the subband level spacing ω_{12}, which is determined by the quantum well depth and thickness, can be adjusted during the manufacturing process. The density of

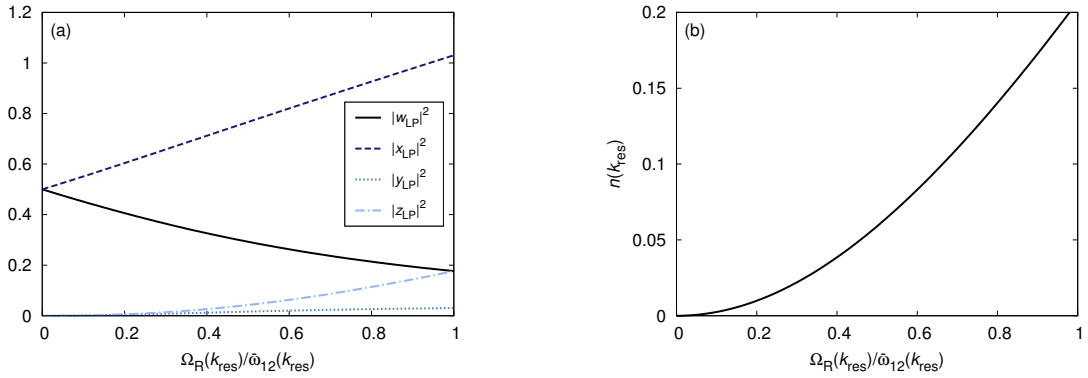

Figure 4.6 – Hopfield coefficients and photon number. (a) Hopfield coefficients for the lower polariton in the resonant case, i.e., for an in-plane wave vector k_{res} such that $\bar{\omega}_{12}(k_{\mathrm{res}}) = \omega_c(k_{\mathrm{res}})$, as a function of the ratio $\Omega_R(k_{\mathrm{res}})/\bar{\omega}_{12}(k_{\mathrm{res}})$. (b) Photon number $n(k_{\mathrm{res}})$[Eq. (4.19)] in the resonant case, as a function of $\Omega_R(k_{\mathrm{res}})/\bar{\omega}_{12}(k_{\mathrm{res}})$.

the two-dimensional electron gas can be varied experimentally. To obtain the results of Fig. 4.5, we chose $n_{\mathrm{QW}}^{\mathrm{eff}} = 50$, $L_c^{\mathrm{eff}} = 2\,\mu$m, $\hbar\omega_{12} = 113\,$meV and $N_{2\mathrm{DEG}} = 10^{12}\,\mathrm{cm}^{-2}$ as one particular set of experimentally reasonable values of the parameters mentioned above, on the basis of the experimental work done in Ref. 62.

Compared to many other cavity QED systems that can be described by a Jaynes-Cummings-type Hamiltonian where the rotating-wave approximation has been applied [89], the ground state of the intersubband cavity system operated in the ultrastrong coupling regime is not the ordinary vacuum $|0\rangle$ that contains no cavity photons and no intersubband excitations,

$$a_{\mathbf{k}}\,|\,0\,\rangle = b_{\mathbf{k}}\,|\,0\,\rangle = 0, \tag{4.17}$$

but a state $|G\rangle$ that exhibits no intersubband cavity polaritons, i.e.

$$p_{j,\mathbf{k}}\,|\,G\,\rangle = 0, \quad j \in \{\mathrm{LP},\mathrm{UP}\}. \tag{4.18}$$

From Fig. 4.6 (a), we see that in the *ordinary case* $\Omega_R(k)/\bar{\omega}_{12}(k) \ll 1$, the Hopfield coefficients $y_j(k)$ and $z_j(k)$ are negligibly small, such that the conditions in Eqs. (4.17) and (4.18) are actually equal. The ground state $|G\rangle$ significantly differs from the vacuum state $|0\rangle$. The ISC system has some peculiar properties in the ultrastrong coupling regime that were worked out in Ref. 56, whereof the essential ones are that it contains a finite number of photons,

$$n(k) \equiv \langle\,G\,|\,a_{\mathbf{k}}^{\dagger}a_{\mathbf{k}}\,|\,G\,\rangle = |y_{\mathrm{LP}}(k)|^2 + |y_{\mathrm{UP}}(k)|^2\,, \tag{4.19}$$

and photons with opposite in-plane wave vectors $\mathbf{k}$ and $-\mathbf{k}$ are correlated, i.e.

$$\langle\,G\,|\,a_{\mathbf{k}}a_{-\mathbf{k}}\,|\,G\,\rangle = -w_{\mathrm{LP}}^{*}(k)y_{\mathrm{LP}}(k) - w_{\mathrm{UP}}^{*}(k)y_{\mathrm{UP}}(k). \tag{4.20}$$

Only if the light-matter interaction is so strong that the Rabi frequency $\Omega_R(k)$ becomes comparable to the transition frequency $\bar{\omega}_{12}(k)$ of the emitter itself, the Hopfield coefficients $y_j(k)$ are reasonably large, $|y_j(k)|^2 \approx 0.1$, such that the polariton vacuum $|G\rangle$ exhibits the properties in Eqs. (4.19) and (4.20), and therefore significantly differs from the ordinary ground state $|0\rangle$. It is the antiresonant terms in the light-matter interaction Hamiltonian [Eq. (4.5)] that cause the aforementioned anomalous properties and their physical relevance has been verified experimentally [63].

The exact solution for the ground state $|G\rangle$ of the Hamiltonian H in Eq. (4.19) has been derived in Ref. 90 for bulk exciton-polaritons and a detailed derivation for the ISC system can be found in Ref. 91. The polariton vacuum $|G\rangle$ is given by independent photon and intersubband polarization states, and can be written in the form

$$|G\rangle = \frac{1}{N} e^{\frac{1}{2}\sum_{\mathbf{k}} G(k)\left(a^\dagger_{\mathbf{k}} a^\dagger_{-\mathbf{k}} + b^\dagger_{\mathbf{k}} b^\dagger_{-\mathbf{k}}\right) + F(k)\left(a^\dagger_{\mathbf{k}} b^\dagger_{-\mathbf{k}} + b^\dagger_{\mathbf{k}} a^\dagger_{-\mathbf{k}}\right)} |0\rangle . \tag{4.21}$$

The expansion coefficients $G(k)$ and $F(k)$ are determined by Eq. (4.18) and are given by

$$G(k) = \frac{\bar{\omega}_{12}(k) + \omega_c(k) - \omega_{LP}(k) - \omega_{UP}(k)}{\bar{\omega}_{12}(k) - \omega_c(k) - \omega_{LP}(k) - \omega_{UP}(k)}, \tag{4.22}$$

$$F(k) = -i\frac{\bar{\omega}_{12}(k)}{\Omega_R(k)} G(k). \tag{4.23}$$

The normalization constant N can be calculated to be

$$N = \prod_{\mathbf{k}} \sqrt{|w_{LP}(k)|^2 + |x_{LP}(k)|^2} \tag{4.24}$$

In Fig. 4.7, we plot the expansion coefficients $G(k)$ and $|F(k)|$. One can see that $|F(k)|$ is about one order of magnitude larger than $G(k)$ and

$$G(k) \approx |F(k)|^2 \ll 1, \tag{4.25}$$

which was checked for a wide range of experimentally acceptable values of the parameters n_{QW}, L_c, ω_{12}, and N_{2DEG}. Therefore, the polariton vacuum state $|G\rangle$ will be expanded in a Taylor series to second order in the expansion coefficients. If the light-matter interaction is turned off, i.e. $\Omega_R(k) = 0$, we obtain $G(k) = F(k) = 0$ and hence, the ground state is simply given by the ordinary vacuum $|0\rangle$ as expected.

4.3.4 Photon Generation

The fundamental idea, from which the work of this chapter emerged, is that the correlations in Eq. (4.20) might lead to entanglement of two photons propagating in opposite directions. These photons are, however, virtual excitations, but it is conjectured [56, 92, 93] that they can be released by a nonadiabatic switch-off (quench) of the vacuum Rabi frequency $\Omega_R(k)$. An experimental

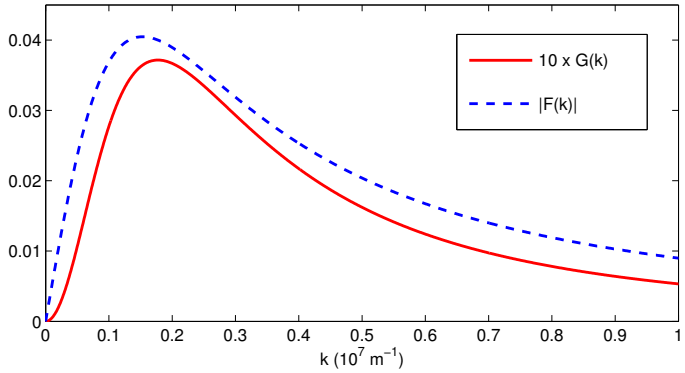

Figure 4.7 – Expansion coefficients. Absolute values of the expansion coefficients $G(k)$ and $F(k)$ as a function of the length k of the in-plane wave vector. Parameter values: $\varepsilon = 10$, $m^* = 0.067\, m_0$, $n_{\mathrm{QW}}^{\mathrm{eff}} = 50$, $L_{\mathrm{c}}^{\mathrm{eff}} = 2\ \mu$m, $\hbar\omega_{12} = 113$ meV, $N_{\mathrm{2DEG}} = 10^{12}$ cm^{-2}. Here, the depolarization shift is taken into account.

approach to this scenario is an ultrafast change of the 2DEG density N_{2DEG} [62, 87, 88]. One mechanism to achieve a modulation of the parameter N_{2DEG} is a gate voltage that depletes the QWs [87]. However, the rapidity is restricted by the capacitance of the electric gates. Another implementation uses two asymmetrically coupled QWs, in which one QW can be charged by electron tunneling and this process can happen on the picosecond time scale or faster [88]. A promising idea to achieve an ultrafast modulation of the coupling strength is an all-optical control scheme [62], in which electrons from the valence band are resonantly excited to the first subband by a femtosecond laser pulse. In this manner, it could be demonstrated experimentally that the coupling between the cavity photon field and intersubband transitions in the QWs can be switched on in a time shorter than a cycle of light in the microcavity. Since then, further progress has been made in the field of ultrafast switching of the light-matter interaction strength, experimentally [94, 95] and theoretically [96]. In Refs. 92 and 93 the spectrum of the radiation emitted from the cavity was derived in more detailed calculations, when a time-dependent coupling $\Omega_{\mathrm{R}}(k,t)$ is predominant in the system and it is predicted that the vacuum radiation rises above the black body radiation.

4.4 Photon Entanglement

In Chap. 2, an entangled pure state $|\psi\rangle$ describing two subsystems A and B was defined by the impossibility of preparing it as a product state $|\psi\rangle = |\phi\rangle_{\mathrm{A}} \otimes |\nu\rangle_{\mathrm{B}}$, in which $|\phi\rangle_{\mathrm{A}}$ and $|\nu\rangle_{\mathrm{B}}$ are states solely of the subsystems A and B, respectively. Furthermore, a mixed state ρ is entangled if it cannot be written as a convex combination $\rho = \sum_{i=1} p_i \rho_i^{\mathrm{A}} \otimes \rho_i^{\mathrm{B}}$ with coefficients $0 \leq p_i \leq 1$ and $\sum_i p_i = 1$, and again ρ_i^{A} and ρ_i^{B} describe the subsystems [cf. Eq. (2.7)]. Many protocols in quantum information processing [7, 8, 32, 97] require the distribution of maximally entangled Bell states. The reliability of a quantum communication protocol depends on the amount of entanglement of

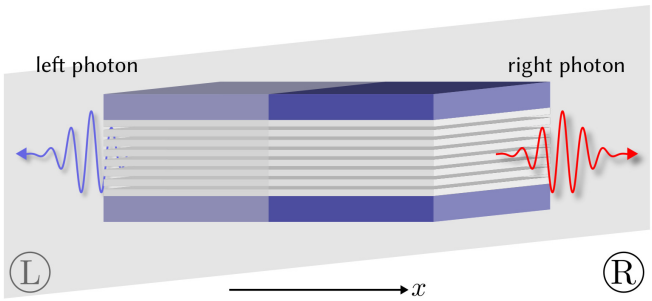

Figure 4.8 – Mode entanglement. Two photons with different frequencies (colors) leaving the cavity in opposite directions. The two subsystems left (L) and right (R) are defined via the sign of k_x. Since there is a difference in frequency, the photons have different in-plane wave vectors.

the distributed two-qubit state. Thus, for practical reasons it is important to quantify the amount of entanglement. For pure bipartite states, the entanglement measure is the von Neumann entropy of one of the subsystems [Eq. (2.10)] [36]. As will be discussed below (Sec. 4.4.2), we deal with mixed two-photon states, where the entanglement can be quantified by the concurrence [Eq. (2.16)] [37].

4.4.1 Mode Entanglement

We first define the type of photon entanglement. Since the transverse-magnetic polarization of the interacting photons is fixed by the selection rules for intersubband transitions [57], polarization entanglement cannot be generated, as it is achieved with PDC or from the biexciton-recombination cascade. But there exist anomalous correlations between two photons with opposite in-plane momentum [Eq. (4.20)],

$$\langle G | \, a_{\mathbf{k}} a_{-\mathbf{k}} \, | G \rangle = -w^*_{\mathrm{LP}}(k) y_{\mathrm{LP}}(k) - w^*_{\mathrm{UP}}(k) y_{\mathrm{UP}}(k). \tag{4.26}$$

Our idea is to test the photonic states in $|G\rangle$ for mode or frequency entanglement [4]. In the following, we limit the treatment to only one spatial direction, since the correlations in Eq. (4.26) occur only for photons with exactly opposite in-plane wave vectors. This direction is chosen to be the x direction. This is schematically shown in Fig. 4.8. Photons with a negative (positive) x component of the wave vector belong to subsystem L (R). $|G\rangle$ itself is a vector from a Hilbert space $\mathcal{H}$, which is a tensor product

$$\mathcal{H} = \mathcal{F}^a \otimes \mathcal{F}^b, \tag{4.27}$$

where $\mathcal{F}^a$ and $\mathcal{F}^b$ denote the Fock spaces of the photons and intersubband excitations, respectively. The situation depicted in Fig. 4.8 is described by vectors in a subspace $\mathcal{H}_{\mathrm{LR}} \subset \mathcal{H}$, which is itself a tensor product of $\mathcal{H}_{\mathrm{L}}$ and $\mathcal{H}_{\mathrm{R}}$, the Hilbert spaces of the subsystems L and R,

$$\mathcal{H}_{\mathrm{LR}} = \mathcal{H}_{\mathrm{L}} \otimes \mathcal{H}_{\mathrm{R}}. \tag{4.28}$$

Since $|G\rangle$ contains states from outside $\mathcal{H}_{\mathrm{LR}}$, we project onto $\mathcal{H}_{\mathrm{LR}}$ with an appropriate projection operator, which could be realized experimentally by a post-selective measurement.

The post-selection needs to fulfill the following requirements: First, we only allow for states in which two photons with opposite in-plane wave vectors appear. In addition, the post-selection is even more restrictive in terms of allowed modes. We only consider two different modes in each subsystem L and R, respectively, that have the same absolute value of the in-plane wave vector. I.e. we choose k and q, with $k \neq q$, and consider the modes $\mathbf{k} = (k, 0)$ and $-\mathbf{k} = (-k, 0)$ and accordingly $\mathbf{q} = (q, 0)$ and $-\mathbf{q} = (-q, 0)$, where all the wave vectors point along the x-direction. Hence, the basis $\{|\mathbf{k}\rangle_{\mathrm{L}}, |\mathbf{q}\rangle_{\mathrm{L}}\}$ and $\{|\mathbf{k}\rangle_{\mathrm{R}}, |\mathbf{q}\rangle_{\mathrm{R}}\}$ of the two Hilbert spaces $\mathcal{H}_{\mathrm{L}}$ and $\mathcal{H}_{\mathrm{R}}$ are given by

$$|\mathbf{k}\rangle_{\mathrm{L}} = a^{\dagger}_{-\mathbf{k}}\,|0\rangle_a\,, \tag{4.29}$$

$$|\mathbf{q}\rangle_{\mathrm{L}} = a^{\dagger}_{-\mathbf{q}}\,|0\rangle_a\,, \tag{4.30}$$

$$|\mathbf{k}\rangle_{\mathrm{R}} = a^{\dagger}_{\mathbf{k}}\,|0\rangle_a\,, \tag{4.31}$$

$$|\mathbf{q}\rangle_{\mathrm{R}} = a^{\dagger}_{\mathbf{q}}\,|0\rangle_a\,, \tag{4.32}$$

where $|0\rangle_a$ denotes the photon vacuum. Since one chooses the modes $\mathbf{k}$ and $-\mathbf{k}$, and accordingly $\mathbf{q}$ and $-\mathbf{q}$, via the post-selection, the photons effectively form a two-qubit system. Our goal is to quantify the entanglement in exactly this two-qubit system. For all further calculations, the polariton vacuum $|G\rangle$ is expanded to second order in the small expansion coefficient $G(k)$,

$$\begin{aligned}
|G\rangle &= \frac{1}{N} e^{\frac{1}{2}\sum_{\mathbf{k}} G(k)\left(a^{\dagger}_{\mathbf{k}}a^{\dagger}_{-\mathbf{k}} + b^{\dagger}_{\mathbf{k}}b^{\dagger}_{-\mathbf{k}}\right) + F(k)\left(a^{\dagger}_{\mathbf{k}}b^{\dagger}_{-\mathbf{k}} + b^{\dagger}_{\mathbf{k}}a^{\dagger}_{-\mathbf{k}}\right)}\,|0\rangle \\
&\approx \frac{1}{\widetilde{N}}\left[1 + \frac{1}{2}\sum_{\mathbf{k}} G(k)\mathcal{T}_{\mathbf{k}}^{\dagger} + \frac{1}{8}\left(\sum_{\mathbf{k}} G(k)\mathcal{T}_{\mathbf{k}}^{\dagger}\right)^2\right]|0\rangle \\
&\equiv \left|G^{(2)}\right\rangle,
\end{aligned} \tag{4.33}$$

where $\widetilde{N}$ is a new normalization constant to preserve $\langle G^{(2)}|G^{(2)}\rangle = 1$ and the operator $\mathcal{T}_{\mathbf{k}}^{\dagger}$ is defined as

$$\mathcal{T}_{\mathbf{k}}^{\dagger} = a^{\dagger}_{\mathbf{k}}a^{\dagger}_{-\mathbf{k}} + b^{\dagger}_{\mathbf{k}}b^{\dagger}_{-\mathbf{k}} - 2i\frac{\bar{\omega}_{12}(k)}{\Omega_{\mathrm{R}}(k)}a^{\dagger}_{\mathbf{k}}b^{\dagger}_{-\boldsymbol{k}}. \tag{4.34}$$

The two-photon states with opposite in-plane wave vectors, which fulfill the post-selection requirements, are in linear order[3]

$$a^{\dagger}_{\mathbf{k}}a^{\dagger}_{-\mathbf{k}}\,|0\rangle_a = |\mathbf{k}\rangle_{\mathrm{L}}\,|\mathbf{k}\rangle_{\mathrm{R}}\,, \tag{4.35}$$

$$a^{\dagger}_{\mathbf{q}}a^{\dagger}_{-\mathbf{q}}\,|0\rangle_a = |\mathbf{q}\rangle_{\mathrm{L}}\,|\mathbf{q}\rangle_{\mathrm{R}}\,, \tag{4.36}$$

and in second order also the following four-particle states containing two photons with opposite in-

[3]For the sake of convenience, we omitted the tensor product sign here, i.e. $|\mathbf{k}\rangle_{\mathrm{L}}\,|\mathbf{k}\rangle_{\mathrm{R}} \equiv |\mathbf{k}\rangle_{\mathrm{L}} \otimes |\mathbf{k}\rangle_{\mathrm{R}}$, and will only use it explicitly to denote the tensor-product structure of the total Hilbert space $\mathcal{H}$ [Eq. (4.27)] in the following.

plane wave vectors and two additional intersubband excitations have an equally large contribution in $|G^{(2)}\rangle$ as the linear order,

$$a^\dagger_{\mathbf{k}} a^\dagger_{-\mathbf{k}} b^\dagger_{\mathbf{k}'} b^\dagger_{-\mathbf{k}'} |0\rangle = |\mathbf{k}\rangle_{\mathrm{L}} |\mathbf{k}\rangle_{\mathrm{R}} \otimes b^\dagger_{\mathbf{k}'} b^\dagger_{-\mathbf{k}'} |0\rangle_b , \tag{4.37}$$

$$a^\dagger_{\mathbf{q}} a^\dagger_{-\mathbf{q}} b^\dagger_{\mathbf{k}'} b^\dagger_{-\mathbf{k}'} |0\rangle = |\mathbf{q}\rangle_{\mathrm{L}} |\mathbf{q}\rangle_{\mathrm{R}} \otimes b^\dagger_{\mathbf{k}'} b^\dagger_{-\mathbf{k}'} |0\rangle_b , \tag{4.38}$$

$$a^\dagger_{\mathbf{k}} a^\dagger_{-\mathbf{q}} b^\dagger_{-\mathbf{k}} b^\dagger_{\mathbf{q}} |0\rangle = |\mathbf{q}\rangle_{\mathrm{L}} |\mathbf{k}\rangle_{\mathrm{R}} \otimes b^\dagger_{-\mathbf{k}} b^\dagger_{\mathbf{q}} |0\rangle_b , \tag{4.39}$$

$$a^\dagger_{\mathbf{q}} a^\dagger_{-\mathbf{k}} b^\dagger_{-\mathbf{q}} b^\dagger_{\mathbf{k}} |0\rangle = |\mathbf{k}\rangle_{\mathrm{L}} |\mathbf{q}\rangle_{\mathrm{R}} \otimes b^\dagger_{-\mathbf{q}} b^\dagger_{\mathbf{k}} |0\rangle_b , \tag{4.40}$$

which follows from Eq. (4.25). Here, the explicit expression of the tensor product $|0\rangle = |0\rangle_a \otimes |0\rangle_b$ of the individual vacuum states for photons and intersubband excitations is used and $\mathbf{k}'$ can be an arbitrary in-plane wave vector. We carry out the post-selection by projecting onto these states with a projection operator $\mathcal{P}_{\mathrm{LR}}$,

$$|\psi_{\mathrm{LR}}\rangle = \frac{\widetilde{N}}{N_{\mathrm{LR}}} \mathcal{P}_{\mathrm{LR}} \left| G^{(2)} \right\rangle , \tag{4.41}$$

with N_{LR} being a necessary normalization constant since the operation is a projection. As an intermediate result, we obtain the pure state $|\psi_{\mathrm{LR}}\rangle$ in which all the two-photon states that fulfill the conditions of the post-selection are extracted. This state is given by

$$\begin{aligned}
|\psi_{\mathrm{LR}}\rangle &= \frac{\widetilde{N}}{N_{\mathrm{LR}}} \mathcal{P}_{\mathrm{LR}} \left| G^{(2)} \right\rangle \\
&= \frac{1}{N_{\mathrm{LR}}} \Bigg[\left(G(k) |\mathbf{k}\rangle_{\mathrm{L}} |\mathbf{k}\rangle_{\mathrm{R}} + G(q) |\mathbf{q}\rangle_{\mathrm{L}} |\mathbf{q}\rangle_{\mathrm{R}} \right) \otimes \left(|0\rangle_b + \frac{1}{2} \sum_{\mathbf{k}'} G(k') b^\dagger_{\mathbf{k}'} b^\dagger_{-\mathbf{k}'} |0\rangle_b \right) \\
&\quad + F^2(k) |\mathbf{k}\rangle_{\mathrm{L}} |\mathbf{k}\rangle_{\mathrm{R}} \otimes b^\dagger_{-\mathbf{k}} b^\dagger_{\boldsymbol{k}} |0\rangle_b + F^2(q) |\mathbf{q}\rangle_{\mathrm{L}} |\mathbf{q}\rangle_{\mathrm{R}} \otimes b^\dagger_{-\mathbf{q}} b^\dagger_{\boldsymbol{q}} |0\rangle_b \\
&\quad + F(k)F(q) |\mathbf{q}\rangle_{\mathrm{L}} |\mathbf{k}\rangle_{\mathrm{R}} \otimes b^\dagger_{-\mathbf{k}} b^\dagger_{\boldsymbol{q}} |0\rangle_b + F(k)F(q) |\mathbf{k}\rangle_{\mathrm{L}} |\mathbf{q}\rangle_{\mathrm{R}} \otimes b^\dagger_{-\mathbf{q}} b^\dagger_{\boldsymbol{k}} |0\rangle_b \Bigg],
\end{aligned} \tag{4.42}$$

and the normalization constant N_{LR} is calculated to be

$$N^2_{\mathrm{LR}} = \left(G^2(k) + G^2(q) \right) \left(1 + \frac{1}{2} S \right) + \left(|F(k)|^2 + |F(q)|^2 \right)^2 - 2G^2(k)|F(k)|^2 - 2G^2(q)|F(q)|^2 . \tag{4.43}$$

In Eq. (4.43), we defined the sum S over all squared expansion coefficients,

$$S = \sum_{\mathbf{k}'} G^2(k') . \tag{4.44}$$

The value of S depends on the number of available states, i.e. the wave vectors over which the sum runs. The density of states increases with the sample area A and hence, the value of S depends on A. The evaluation of the sum S, which is required below to quantify the photon entanglement, is explicitly described in Appendix A.

4.4.2 Measure of Entanglement

In Eq. (4.42), we extracted the part of the polariton vacuum, which contains all photonic states that are allowed by the post-selection. But it is not a bare two-photon state and correlations with intersubband excitations with respective in-plane momenta are still present. However, if we consider to use the photons as an entanglement resource, we are only interested in the photonic correlations and do not infer any information about the electronic states. In general, the photons will therefore be in a mixed quantum state, which is described by a reduced density matrix ρ^a obtained from the pure state $|\psi_{\mathrm{LR}}\rangle$. We compute ρ^a by tracing out the electronic degrees of freedom, i.e. the intersubband excitations, which yields

$$\rho^a = \mathrm{Tr}_b\left(|\psi_{\mathrm{LR}}\rangle\langle\psi_{\mathrm{LR}}|\right) = \frac{1}{N_{\mathrm{LR}}^2}\begin{pmatrix} Z(k) & 0 & 0 & Y(k,q) \\ 0 & X(k,q) & 0 & 0 \\ 0 & 0 & X(k,q) & 0 \\ Y(k,q) & 0 & 0 & Z(q) \end{pmatrix}. \tag{4.45}$$

Here, the matrix representation is given in the product basis $\{(|\mathbf{k}\rangle_{\mathrm{L}}, |\mathbf{q}\rangle_{\mathrm{L}}) \otimes (|\mathbf{k}\rangle_{\mathrm{R}}, |\mathbf{q}\rangle_{\mathrm{R}})\}$ and the following abbreviations have been introduced,

$$X(k,q) = |F(k)|^2|F(q)|^2, \tag{4.46}$$

$$Y(k,q) = G(k)G(q)\left[\left(1+\frac{1}{2}S\right) - |F(k)|^2 - |F(q)|^2\right], \tag{4.47}$$

$$Z(k) = X(k,k) + Y(k,k), \tag{4.48}$$

In the limit of large sample areas, i.e. $A \gg 2\pi c^2/(\mathcal{I}\,\omega_{12}^2)$ (see Appendix A for a definition of the dimensionless integral $\mathcal{I}$), one can take the limit $S \to \infty$ to obtain

$$\rho^a \overset{S\to\infty}{=} \frac{1}{G^2(k)+G^2(q)}\begin{pmatrix} G^2(k) & 0 & 0 & G(k)G(q) \\ 0 & 0 & 0 & 0 \\ 0 & 0 & 0 & 0 \\ G(k)G(q) & 0 & 0 & G^2(q) \end{pmatrix}, \tag{4.49}$$

which corresponds to the pure photon state

$$|\psi^a\rangle = \frac{1}{\sqrt{G^2(k)+G^2(q)}}\left(G(k)\,|\mathbf{k}\rangle_{\mathrm{L}}\,|\mathbf{k}\rangle_{\mathrm{R}} + G(q)\,|\mathbf{q}\rangle_{\mathrm{L}}\,|\mathbf{q}\rangle_{\mathrm{R}}\right). \tag{4.50}$$

The state ρ^a, which we derived from $|G^{(2)}\rangle$, describes two photons that propagate with opposite in-plane wave vectors in the microcavity and that can potentially be released by an appropriate time-modulation of the Rabi frequency $\Omega_{\mathrm{R}}(k)$. As explained above, the photons effectively form a two-qubit system, for which the entanglement of formation can be calculated analytically from

the density matrix using the concurrence $C(\rho^a)$ [37]. The relation between the concurrence and the entanglement of formation can be found in Eq. (2.17) of Sec. 2.3. The concurrence itself is given in Eq. (2.16),

$$C(\rho^a) = \max\{0, \lambda_1 - \lambda_2 - \lambda_3 - \lambda_4\}, \tag{4.51}$$

where the λ_i are the eigenvalues of the matrix $R = \sqrt{\sqrt{\rho^a}\tilde{\rho}^a\sqrt{\rho^a}}$ in decreasing order. The matrix $\tilde{\rho}^a$ is obtained by the transformation $\tilde{\rho}^a = (\sigma_y \otimes \sigma_y)\,(\rho^a)^*\,(\sigma_y \otimes \sigma_y)$, where σ_y is a Pauli matrix [Eq. (3.3)] and $(\rho^a)^*$ contains the complex conjugated matrix elements of ρ^a. For the photonic state ρ^a in Eq. (4.45), the parameters λ_1 to λ_4 are found to be

$$\lambda_1 = \frac{1}{N_{\mathrm{LR}}^2}\left(\sqrt{Z(k)Z(q)} + Y(k,q)\right), \tag{4.52}$$

$$\lambda_2 = \frac{1}{N_{\mathrm{LR}}^2}\left(\sqrt{Z(k)Z(q)} - Y(k,q)\right), \tag{4.53}$$

$$\lambda_{3,4} = \frac{1}{N_{\mathrm{LR}}^2}X(k,q). \tag{4.54}$$

In connection with Eqs. (4.46) – (4.48), we can calculate the concurrence and obtain

$$C(\rho^a) \equiv C(k,q) = \frac{2}{N_{\mathrm{LR}}^2}\left(G(k)G(q)\left[1 + \frac{1}{2}S - |F(k)|^2 - |F(q)|^2\right] - |F(k)|^2|F(q)|^2\right), \tag{4.55}$$

which only depends on the absolute values k and q via the expansion coefficients that are given in Eqs. (4.22) and (4.23),

$$G(k) = \frac{\bar{\omega}_{12}(k) + \omega_{\mathrm{c}}(k) - \omega_{\mathrm{LP}}(k) - \omega_{\mathrm{UP}}(k)}{\bar{\omega}_{12}(k) - \omega_{\mathrm{c}}(k) - \omega_{\mathrm{LP}}(k) - \omega_{\mathrm{UP}}(k)}, \tag{4.56}$$

$$|F(k)| = \frac{\bar{\omega}_{12}(k)}{\Omega_{\mathrm{R}}(k)}G(k). \tag{4.57}$$

We have investigated the role of Coulomb interactions for the concurrence that enter via the depolarization shift in the renormalized intersubband transition frequency $\bar{\omega}_{12}(k)$ [Eq. (4.7)]. In doing so, we find that Coulomb corrections are on the order of 5 % or less for our choice of parameters.[4] The further analysis of the concurrence $C(k,q)$ is thus performed without Coulomb corrections.

To show the dependance of the concurrence on k and q, we have to evaluate the sum S explicitly (see Appendix A). Using a sample area $A = (200\,\mu\mathrm{m})^2$, we find $S = 0.857$. The result is presented in Fig. 4.9, where $C(k,q)$ is shown in a density plot as a function of the modes k and q. Additionally, we show cuts through the density plot for fixed values of q to better illustrate the behavior of the concurrence. One can observe two branches of high entanglement that appear for large values of

[4] For our choice of parameters, the depolarization shift $\delta(k)$ [Eq. (4.8)] is less than 10 %. Expanding the concurrence $\bar{C}(k,q)$ including Coulomb interactions to first order in $\delta(k)$ leads us to $\bar{C}(k,q) \approx C(k,q)(1 + \delta(k)\alpha(k,q) + \delta(q)\alpha(q,k))$ with $|\delta(k)\alpha(k,q) + \delta(q)\alpha(q,k)| < 0.05$, where $\alpha(k,q)$ is an expansion coefficient.

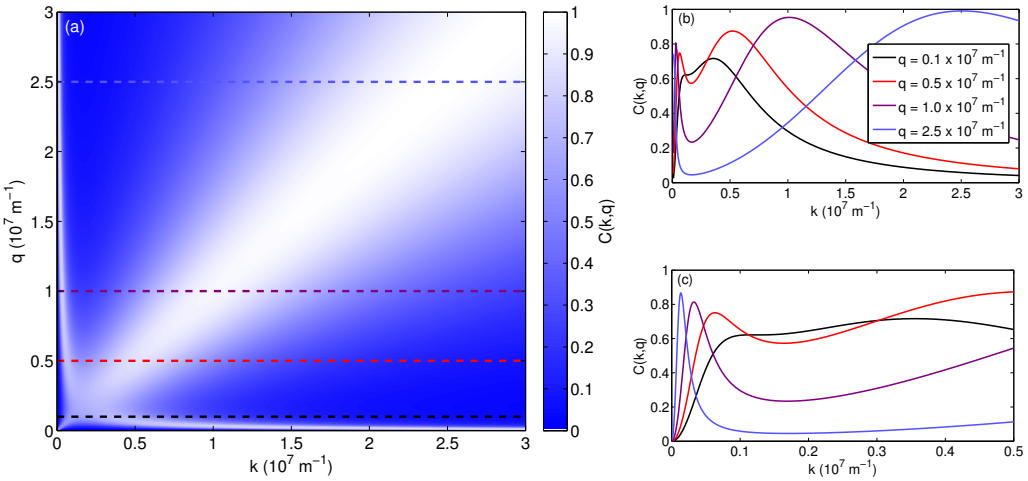

Figure 4.9 – Quantification of photon entanglement. (a) Concurrence $C(k,q)$ as a function of k and q for GaAs/AlGaAs quantum wells. (Parameter values: $\varepsilon = 10$, $m^* = 0.067$, $n_{\mathrm{QW}}^{\mathrm{eff}} = 50$, $L_{\mathrm{c}}^{\mathrm{eff}} = 2$ μm, $\hbar\omega_{12} = 113$ meV, $N_{\mathrm{2DEG}} = 10^{12}$ cm^{-2}.) In (b), we plot $C(k,q)$ for fixed values of q (given in the respective legend) and for a large range of k from 0 to 3×10^7 m^{-1}, which corresponds to a photon energy of 1.9 eV (450 THz, red). (c) Zoom in the range only up to $k = 0.5 \times 10^7$ m^{-1} (320 meV, 80 THz, mid infrared).

k and/or q. Their appearance can be explained by the characteristics of the expansion coefficient $G(k)$ for large k. We find that $G(k)$ tends to zero as k^{-2} and $|F(k)|^2$ scales as k^{-3} for large in-plane wave vectors. Hence, for the diagonal branch, i.e. for $k \approx q$, the terms that are proportional to $|F(k)|^2$ and $|F(q)|^2$ in Eqs. (4.43) and (4.55) can be neglected and we obtain

$$C(k,q) \overset{k,q\to\infty}{\approx} \frac{2G(k)G(q)}{G^2(k)+G^2(q)} \overset{k\approx q}{\approx} 1. \tag{4.58}$$

Accordingly, photons are almost maximally entangled if their wave numbers are of the same size. The other branch appears for $G(k) \approx G(q)$, however when the modes are energetically far from each other. We give a more precise analysis of the expression in Eq. (4.58) below, where the limit of large sample areas is worked out. In Fig. 4.10, we present the concurrence for two other values of ω_{12}, namely $\hbar\omega_{12} = 50$ meV and $\hbar\omega_{12} = 150$ meV. Qualitatively, the concurrence $C(k,q)$ shows the two characteristic branches of high entanglement that were mentioned before, therefore maximally entangled photons are present for a wide range of intersubband transition energies $\hbar\omega_{12}$. The position of the side branch however shifts due to changes in the expansion coefficient $G(k)$.

The case of a large cavity, i.e. a large sample area A, is described by the limit $S \to \infty$ (see Appendix A). In this case, the concurrence is calculated to be

$$C(k,q) = \frac{2G(k)G(q)}{G^2(k)+G^2(q)}. \tag{4.59}$$

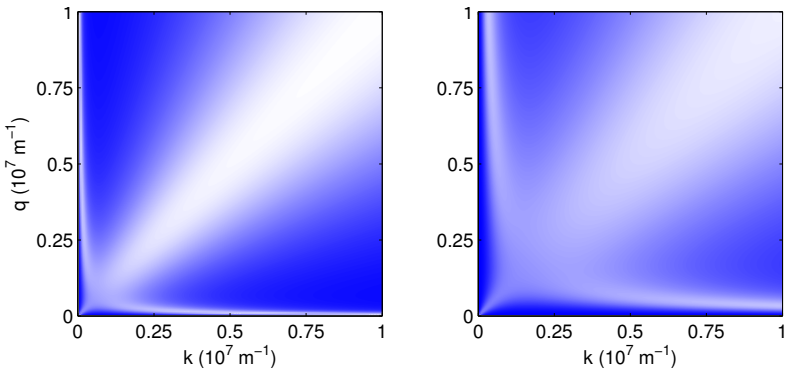

Figure 4.10 – Entanglement for different intersubband transition frequencies. Concurrence $C(k, q)$ for intersubband transition energies of (a) $\hbar\omega_{12} = 50$ meV and (b) $\hbar\omega_{12} = 150$ meV. [Color scale and other parameters values are the same as in Fig. 4.9, besides $L_c^{\text{eff}} = 5$ μm in (a).]

In this limit, the sample area A drops out so that the concurrence $C(k, q)$ becomes independent of A. We show the result in Fig. 4.11. The concurrence has always two maxima if q is kept constant. The two maxima appear for $G(k) = G(q)$, where the photons are maximally entangled since we have $C(k, q) = 1$. One maximum appears for $k \neq q$, which is sharply peaked. If one realizes the post-selection experimentally by choosing a certain finite k range, the entanglement will therefore most likely be reduced. The other maximum appears for $k = q$, which seems to be an artifact of the calculation since this specific point is excluded in the derivation before. The reason for the exclusion is that the two-photon states are separable for $k = q$ and hence, they are not entangled. However, all the states with $k \approx q$ in the vicinity of this point are allowed by the post-selection. Therefore, one can see from the broad shape of this second maximum that for a given q there exists a wide range of corresponding modes k, for which the two photons are almost maximally entangled. The only request for k and q is that the difference between them can be resolved experimentally. In Fig. 4.11 (b), we show a magnification for wave vectors up to 0.5×10^7 m^{-1} to show the dependance of $C(k, q)$ on k clearer around the first maximum, which is not visible in the previous plot. In particular at the intersubband resonance, which is around 0.1×10^7 m^{-1}, the two maxima approach each other so that by selecting different modes around the resonance, the entanglement of the photons can be made almost maximal. The photon energies are about 100–150 meV, which corresponds to the mid infrared.

4.5 Conclusions

An efficient and deterministic source of highly-entangled photons is needed in quantum information processing [see (i).–(iii). in Sec. 4.1]. In this chapter, we examined a new scheme of entangled photon production, based on the emission of quantum vacuum radiation from the intersubband cavity system. The emission of photon pairs can be triggered by a nonadiabatic modulation of the ground state of the system, enabling deterministic photon generation. The ground state consists

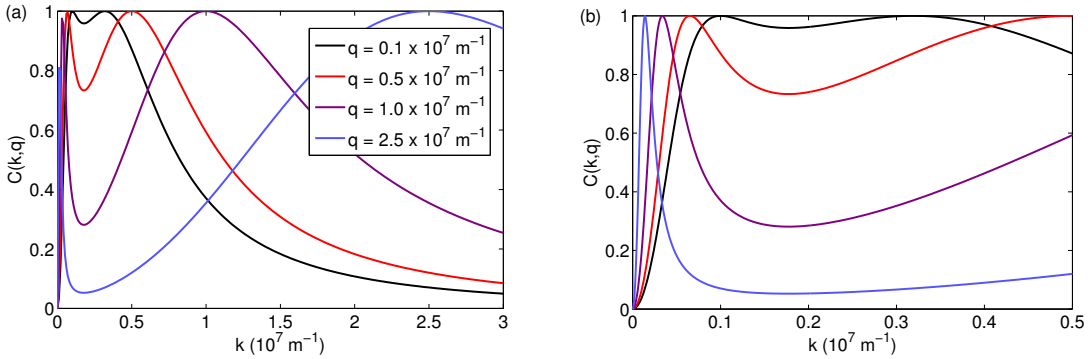

Figure 4.11 – Photon entanglement in the limit of a large cavity. (a) Concurrence $C(k,q)$ in the case of large sample areas for GaAs/AlGaAs quantum wells. (Parameter values: $\varepsilon = 10$, $m^* = 0.067$, $n_{\mathrm{QW}}^{\mathrm{eff}} = 50$, $L_{\mathrm{c}}^{\mathrm{eff}} = 2\ \mu$m, $\hbar\omega_{12} = 113$ meV, $N_{\mathrm{2DEG}} = 10^{12}$ cm^{-2}.) (b) Zoom in the range only up to $k = 0.5 \times 10^7$ m^{-1}.

of an infinite number of photonic and electronic states, and we propose a post-selective measurement to reduce the photonic system to an effective two-qubit system. Thereby, the computational basis is defined as two different in-plane wave vectors. We find an analytical expression for the concurrence to quantify the so-called mode entanglement of the photons, which depends on the absolute values of the chosen wave vectors. The concurrence, and thus the entanglement of the post-selected photons, is nonzero. In the limiting case of large sample areas, there exists a continuous set of mode pairs for which the concurrence is 1, i.e. the photons are maximally entangled. Furthermore, it turns out that for photon energies around the intersubband resonance, which is in the mid infrared of the electromagnetic spectrum, the photons are as well almost maximally entangled, the concurrence being close to unity. This is fundamentally important for the possible use in quantum information processing, e.g. to implement quantum teleportation. A high degree of entanglement can also be reached if the modes chosen in the post-selection are close to each other.

We also want to comment on the possibility of triggering the photon-pair emission by a systematic quench of the light-matter interaction in the microcavity and give a rough estimate on the efficiency of the source. The repetition rate for the photon production is limited by the switching times, which have to be fast enough to perturb the system nonadiabatically. The experiments today achieved switch-on times of the ultrastrong coupling regime of about 10 fs by ultrashort laser pulses [62, 94, 95]. The switch-off process, which is the relevant operation related to photon emission, has to be as fast as this timescale. This gives a rough estimate for a repetition rate of $10^{13} - 10^{14}$ full cycles (switch-on and switch-off) per second. The probability to really measure a desired two-photon state is given by the probability of a successful post-selection $p(k,q)$, which depends on the chosen modes and is given by the expectation value of the projector $\mathcal{P}_{\mathrm{LR}}$, i.e. $p(k,q) = \langle G^{(2)}|\mathcal{P}_{\mathrm{LR}}|G^{(2)}\rangle = \widetilde{N}/N_{\mathrm{LR}}$. The probability is largest for wave vectors corresponding to the resonance frequency of the intersubband transition and is on the order of 10^{-9}. This value

can be significantly increased if not only single modes are allowed by the post-selection, but the photons can have energies within a predefined frequency range. However, the effect on the entanglement still needs to be worked out for this case.

Further studies are also required to model noninstantaneous switch-off processes, presumably using a time-dependent perturbation theory approach. Another open issue is the simultaneous emission of black body radiation at finite temperature, an effect which is expected to be small compared to the vacuum radiation [93], but which will to some extent reduce the average entanglement of the emitted photons.

5

Entanglement Purification with the Exchange Interaction

5.1 Introduction

A fundamental resource for the implementation of large-scale quantum communication networks [38] is the generation of long-distance entanglement between the network nodes. However, due to imperfect sources and the inevitable interaction of the entangled particles with their environment the degree of entanglement decreases. To overcome this issue, the concept of a quantum repeater was established for the practical generation of long-distance entanglement [8, 9], as we describe in Sec. 3.6. The centerpiece of such a device is entanglement purification [10, 11], for which a quantum memory [39] is indispensable. The working principle of the quantum repeater is to divide the distance between the network nodes into smaller segments, create entangled states between them, and sequentially generate high-fidelity entanglement between the nodes through alternating purification and entanglement-swapping steps (Fig. 3.6). Ideal candidates for the realization of stationary qubits acting as quantum memory are spins in solid-state systems, like electron spins in semiconductor quantum dots (QDs) [18] and nitrogen-vacancy centers in diamond [23] (see also Chap. 6). Due to their long coherence times, their complete controllability by electrical or optical means [19, 23, 99], and the possibility of interfacing them with photons [100], the considerable potential of spins as quantum memory has been demonstrated. The main focus of this chapter is devoted to electron-spin qubits that are coupled by an isotropic Heisenberg-type interaction, which is the case, e.g., for spin qubits in lateral QDs [19] (Sec. 5.2). The idea of recurrence protocols for entanglement purification is to use two or more imperfectly entangled qubit pairs to purify one of them with respect to a maximally entangled state. Using existing recurrence protocols involving symmetric local two-qubit operations, such as the BBPSSW or the DEJMPS protocol (see Sec. 3.5), turns out to be rather unpractical for spin qubits since an efficient implementation of the required CNOT gates is challenging. Hence, we concentrate on an open problem in the development of quantum repeaters based on spin qubits, which is the lack of an efficient scheme for entanglement

purification.

Pioneering experiments of entanglement purification have been performed using photonic qubits [101–104]. Limitations of these schemes are the destructive measurements of the purified pairs and the requirement for pure input states [44, 105], besides the impracticality of using photons as quantum memory. The original BBPSSW protocol of C. H. Bennett *et al.* [10] based on CNOT gates has been implemented with atomic qubits, but only locally in the same optical trap [106]. Previous theoretical proposals have demonstrated purification schemes for spin qubits, e.g. by replacing the CNOT in the bilateral operation by the gate sequence that uses two-qubit gates directly generated from the interaction Hamiltonian [107], requiring additional single-qubit operations. Other procedures use three input pairs [108–110] or specifically work for two-spin singlet-triplet qubits [111]. The aim of our study is therefore to examine whether entanglement purification is feasible for characteristic coupling types of spin qubits, however, without single-qubit manipulation, which is too slow for the realization of a quantum repeater.

We present a simple purification protocol based solely on the one-time activation of a Heisenberg exchange interaction leading to the $\sqrt{\text{SWAP}}$ gate (Sec. 5.3). The exchange interaction is readily available in many spin-based qubits systems, such as quantum dots [18]. Following the same approach, we also find a similar result for qubits coupled via a XY-type interaction, which happens to be the interaction between superconducting qubits [112] as well as between optically coupled spin qubits [113], or for qubits coupled via magnetic dipole-dipole interaction (Sec. 5.4). Our proposal works with two input pairs of spin-1/2 qubits and only requires a single two-qubit interaction. In comparison with existing protocols, we achieve an advantage by allowing for *different* two-qubit manipulations locally in the bilateral operation. For a single purification step, the derived protocol requires no extra single-spin operations, making it much faster and less susceptible to gate errors. The only needed operation, the $\sqrt{\text{SWAP}}$ gate, has been implemented experimentally, with a gate time below 0.2 ns [114] (see also [48]), making the implementation of our proposal within reach of current technology. Furthermore, the required single-shot measurement of an electron spin state has also been successfully performed [115, 116].

5.2 Spin Qubits in Lateral Quantum Dots

The spin of an electron is a two-level system and presents a natural platform to implement a qubit. Single or few electrons can be trapped and confined in all three spatial dimensions utilizing quantum dots (QDs). If the extent of the confinement is comparable to the de Broglie wavelength of the electron (tens of nanometers in a typical semiconductor structure), the orbital energy levels are quantized; thus, QDs are also named *artificial atoms*. Many types of QDs exist, with variations, e.g., in size and material composition. In this section, we concentrate on the description of electron spins in lateral QDs [19], which have been extensively studied in the context of quantum information processing [18, 20, 24].

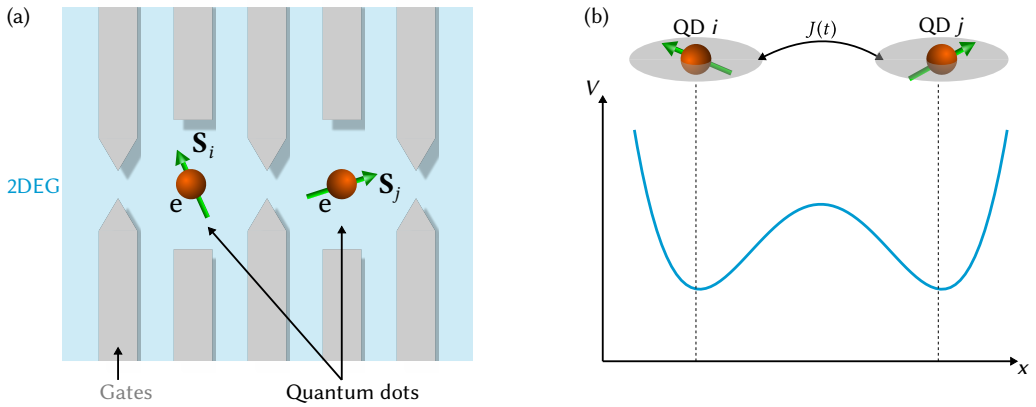

Figure 5.1 – Spin qubits in lateral quantum dots. (a) Part of a quantum register composed of two electrons (e) with spins $\mathbf{S}_i$ and $\mathbf{S}_j$, confined in gate-defined quantum dots. The electrons stem from a two-dimensional electron gas (2DEG) that is created in a semiconductor heterostructure beneath the gates and that confines electrons in the drawing plane. (b) Typical interaction potential V between two electrons in adjacent quantum dots (QDs) i and j [118] along one lateral direction (here the x axis).

Lateral QDs are formed from a two-dimensional electron gas (2DEG), in which electrons are confined in one spatial direction and still able to move in the remaining two. A 2DEG can be formed in a semiconductor heterostructure, such as AlGaAs/GaAs, where due to a band-gap mismatch of the two materials, the electrons are confined to the GaAs layer in this case. In the following, we concentrate on AlGaAs/GaAs heterostructures, unless otherwise stated. Confinement in the lateral direction, i.e. within the plane of the 2DEG, can be achieved by metallic surface gates above the electron layer. The electric field of the electrodes generates an approximately parabolic potential that localizes the electrons within 100 nm [117]. A schematic depiction is given in Fig. 5.1. Capacitive coupling to a source and drain reservoir allows to change the charge state of the QD. In this fashion, a lateral QD can be filled with exactly one electron that can be coherently manipulated for quantum information purposes.

Various ideas emerged of how to encode a qubit in the spin state of one or several electrons confined in electrically-defined QDs. In the original idea [18], also known as the *Loss-DiVincenzo proposal*, the spin eigenstates of a single electron in a QD define the computational basis,

$$|0\rangle \equiv |\uparrow\rangle \equiv \left| m_S = +\frac{1}{2} \right\rangle, \tag{5.1}$$

$$|1\rangle \equiv |\downarrow\rangle \equiv \left| m_S = -\frac{1}{2} \right\rangle, \tag{5.2}$$

also referred to as *spin up* ($|\uparrow\rangle$) and *spin down* ($|\downarrow\rangle$). Here, we denote the electron spin by $\mathbf{S}$ and the S_z eigenstates by $|m_S = \pm 1/2\rangle$. The growth direction of the heterostructure defines the spin quantization axis z, i.e. the direction normal to the 2DEG plane. Other proposals suggested two-electron spin states [119, 120] and three-electron spin states [121] of multiple quantum dots

as computational basis. And also the charge degree of freedom can be exploited as qubit [122]. Substantial progress has been made in the fields of multi-electron spin qubits and charge qubits; however, we were interested in entanglement purification schemes for single spins and therefore focus on single-spin qubits in the following. We present how individual spins can be initialized, manipulated and measured, and how two qubits can be coupled.

An external magnetic field $\mathbf{B}$ is coupled to the electron spin according to the Zeeman Hamiltonian

$$H_z = g\mu_B \mathbf{B} \cdot \mathbf{S}, \tag{5.3}$$

where g is the effective g-factor and μ_B is the Bohr magneton. The spin states $|\uparrow\rangle$ and $|\downarrow\rangle$ can be split by a constant magnetic field component B_z along the z axis by the Zeeman energy $g\mu_B B_z$. Due to the energy separation, the states $|\uparrow\rangle$ and $|\downarrow\rangle$ acquire different phases during the time evolution generated by H_z, corresponding to rotations on the Bloch sphere around the z axis (cf. Fig. 3.1). Transitions between the two spin states can be driven by an ac magnetic field $B_x(t) = B_\perp \cos(\omega t)$ perpendicular to the quantization axis, known as *electron spin resonance* (ESR). In the resonant case, i.e. for $g\mu_B B_z = \omega$, the probability of a spin flip oscillates in time between 0 and 1. The probability is less than 1 in the case of nonresonant driving. Using ESR, coherent oscillations between the states $|\uparrow\rangle$ and $|\downarrow\rangle$ with a Rabi period of 108 ns have been reported, reaching a gate fidelity of 73 % [123]. Although electric fields do not couple directly to the electron spin, they can still be used to drive spin transitions. Due to spin-orbit interaction, an oscillating electric field generated through the metallic gates creates an effective magnetic field that oscillates with the same frequency, which in turn drives Rabi oscillations between the two spin states. This so-called *electric-dipole-induced spin resonance* (EDSR) therefore allows spin rotations about the x axis of the Bloch sphere by purely electrical means with Rabi periods of about 220 ns [124]. The fastest gate time could be reached by utilizing yet another mechanism to create an effective magnetic field from an electric field, i.e. by the application of a slanted magnetic field, achieving a spin-flip time of 20 ns [125].

Because of the small magnetic moment associated with the electron spin, the information about the spin state needs to be transferred to a different measurable quantity in order to read out the qubit. One idea is to convert the information into a charge signal that depends on the spin state of the electron. An example of such a spin-to-charge conversion process is the spin-dependent tunneling of the QD electron into a proximate ancilla dot. The presence or absence of an electron in the ancilla can be detected by a quantum point contact, because the electric field of the electron changes its conductance [18, 126]. This technique enabled single-shot readout of the electron spin state with average fidelities of up to 86 % [115, 116, 127]. Qubit initialization can work in principle in the same fashion, i.e. the measurement projects the spin into a definite state, and has been demonstrated for silicon-based spin qubits [128].

In order to perform quantum computation, two-qubit operations have to be implemented.

Therefore, two such gate-controlled qubits must be coupled. If two QDs are so close to each other that the electronic wave functions overlap, tunneling events between the two dots become possible. This gives rise to an exchange interaction of the two electrons described by the Heisenberg Hamiltonian [18, 118]

$$H_{ij}(t) = J(t)\mathbf{S}_i \cdot \mathbf{S}_j = \frac{1}{4}J(t)\boldsymbol{\sigma}_i \cdot \boldsymbol{\sigma}_j, \tag{5.4}$$

where $\mathbf{S}_i = \boldsymbol{\sigma}_i/2$ is the spin operator of the electron in QD i and $\boldsymbol{\sigma}_i$ is the vector of Pauli matrices. The spin state of the two electrons is either a spin singlet $|S\rangle$, or one of the spin triplet states $|T_+\rangle$, $|T_0\rangle$ and $|T_-\rangle$, that are given by

$$|S\rangle = \frac{1}{\sqrt{2}}\left(|\uparrow\downarrow\rangle - |\downarrow\uparrow\rangle\right) \equiv |\Psi^-\rangle, \tag{5.5}$$

$$|T_+\rangle = |\uparrow\uparrow\rangle, \tag{5.6}$$

$$|T_0\rangle = \frac{1}{\sqrt{2}}\left(|\uparrow\downarrow\rangle + |\downarrow\uparrow\rangle\right) \equiv |\Psi^+\rangle, \tag{5.7}$$

$$|T_-\rangle = |\downarrow\downarrow\rangle. \tag{5.8}$$

The effective exchange coupling $J(t)$ splits the spin triplets from the spin singlet due to a virtual electron exchange between the two dots, which is only possible for the singlet state. Therefore, the energy of the singlet state is lowered by the exchange interaction. One can also see this by rewriting the Hamiltonian $H_{ij}(t)$ for the exchange interaction between the electrons in QD i and j [Eq. (5.4)] in the form

$$H_{ij}(t) = J(t)\left(\frac{1}{4}\mathbb{1} - P_{\Psi^-}\right), \tag{5.9}$$

where $P_{\Psi^-} = |\Psi^-\rangle\langle\Psi^-|$ is the projector onto the singlet subspace. A quantitative description of the exchange coupling $J(t)$ has been derived in Ref. 118. The coupling can be controlled via the gate voltages, thus effectively changing the tunnel barrier between the two dots. In this fashion, specific two-qubit operations necessary for quantum information processing can be implemented. As we describe below, arbitrary powers of the two-qubit SWAP gate [Eq. 3.11] are generated depending on the strength and temporal shape of the exchange interaction $J(t)$. The time evolution of the two-electron spin state coupled via $H_{ij}(t)$ is given by[1,2]

$$\begin{aligned} U_{ij}(\alpha) &= e^{-i\int_0^t \mathrm{d}t' H_{ij}(t')} = e^{-i\alpha/4}\left(\mathbb{1} + \left(e^{i\alpha} - 1\right)P_{\Psi^-}\right) \\ &= \begin{pmatrix} e^{-i\frac{\alpha}{4}} & 0 & 0 & 0 \\ 0 & e^{i\frac{\alpha}{4}}\cos\left(\frac{\alpha}{2}\right) & -ie^{i\frac{\alpha}{4}}\sin\left(\frac{\alpha}{2}\right) & 0 \\ 0 & -ie^{i\frac{\alpha}{4}}\sin\left(\frac{\alpha}{2}\right) & e^{i\frac{\alpha}{4}}\sin\left(\frac{\alpha}{2}\right) & 0 \\ 0 & 0 & 0 & e^{-i\frac{\alpha}{4}} \end{pmatrix}. \end{aligned} \tag{5.10}$$

[1] Time-ordering in Eq. (5.10) is not necessary since $[H_{ij}(t), H_{ij}(t')] = 0$ for all t and t'.
[2] Here, we set $\hbar = 1$.

The matrix representation is in the product basis $\{|\uparrow\uparrow\rangle, |\uparrow\downarrow\rangle, |\downarrow\uparrow\rangle, |\downarrow\downarrow\rangle\}$ and we set the initial time $t_0 = 0$. We parametrize the time evolution by the so-called *pulse area* $\alpha = \int_0^t \mathrm{d}t'\, J(t')$. Here, we see that the temporal shape of the exchange coupling determines the two-qubit evolution. Exchange interaction is commonly applied for some finite time t, which we will refer to as an exchange pulse. If we, e.g., assume a constant exchange coupling J, the pulse area is simply given by $\alpha = Jt$. For an exchange pulse with $\alpha = \pi$, the SWAP operation is implemented,

$$U_{ij}(\pi) = e^{-i\frac{\pi}{4}} U_{\mathrm{SWAP}} = e^{-i\frac{\pi}{4}} \begin{pmatrix} 1 & 0 & 0 & 0 \\ 0 & 0 & 1 & 0 \\ 0 & 1 & 0 & 0 \\ 0 & 0 & 0 & 1 \end{pmatrix}, \tag{5.11}$$

up to an irrelevant global phase factor of $\exp(-i\pi/4)$. If an exchange pulse with a pulse area of $\alpha = \pi/2$ is applied, two spins can be entangled via Heisenberg exchange interaction, and the corresponding quantum gate is the $\sqrt{\mathrm{SWAP}}$ gate [Eq. (3.13)],

$$U_{ij}\left(\frac{\pi}{2}\right) = e^{-i\frac{\pi}{8}} U_{\sqrt{\mathrm{SWAP}}} = e^{-i\frac{\pi}{8}} \begin{pmatrix} 1 & 0 & 0 & 0 \\ 0 & \frac{1}{2}(1-i) & \frac{1}{2}(1+i) & 0 \\ 0 & \frac{1}{2}(1+i) & \frac{1}{2}(1-i) & 0 \\ 0 & 0 & 0 & 1 \end{pmatrix}, \tag{5.12}$$

which is a universal two-qubit gate [18]. In a register composed of several gate-controlled qubits, an elementary quantum gate between spins in dots i and j, e.g., is implemented by turning on the exchange interaction between these dots for a specific time and leaving all other couplings turned off. Thereby, only the state of the intended qubit pair is changed. However, the CNOT gate required for several quantum information protocols [3] is not directly generated by the Heisenberg exchange interaction. As shown in Sec. 3.2, additional single-qubit rotations are required to construct a CNOT gate between qubit i and j from $\sqrt{\mathrm{SWAP}}$,

$$U_{\mathrm{CNOT}} = e^{-i\frac{\pi}{2}} R_y^{(j)}\left(\frac{\pi}{2}\right) R_z^{(i)}\left(-\frac{\pi}{2}\right) R_z^{(j)}\left(\frac{\pi}{2}\right) U_{\sqrt{\mathrm{SWAP}}}\, R_z^{(i)}(-\pi)\, U_{\sqrt{\mathrm{SWAP}}}\, R_y^{(j)}\left(-\frac{\pi}{2}\right). \tag{5.13}$$

Since single-spin rotations on the order of 100 ns are much slower than exchange-based two-qubit operations (see below), such an implementation is challenging. It is this fact, which motivates the development of protocols that can be directly implemented by the Heisenberg exchange interaction, such as the entanglement purification scheme derived in Sec. 5.3.

The coupling of two electron spins via Heisenberg exchange interaction has been successfully demonstrated in AlGaAs/GaAs [48, 114, 129, 130] and Si/SiGe QDs [131]. In the seminal work of Ref. 114, J. R. Petta *et al.* demonstrated electrical control of the exchange interaction between two QDs and the implementation of a $\sqrt{\mathrm{SWAP}}$ gate within 180 ps. Further developments included the demonstration of an exchange-based two-qubit coupling together with independent single-qubit

operations by EDSR in a double QD system, thus obtaining all-electrical control of small spin-qubit processor [48], and the pairwise control of exchange interaction for three spins in a triple QD [130].

Finally, we want to comment on the relaxation and decoherence times for single-spin qubits in electrically-defined QDs, which are limited by the coupling to environmental degrees of freedom. The spin relaxation time T_1 is dominated by spin-orbit interaction combined with phonon emission [20, 24] and can reach values longer than 1 s [132]. The coherence of the spin state, on the other hand, is mainly affected by the nuclear spin bath of the host material that comprises 10^4–10^6 nuclei. The field of all nuclear spins, known as the Overhauser field, fluctuates in time and thus, can randomize the phase of the spin state. A dephasing time of 37 ns has been reported [133]. In the same work, a decoherence time $T_2 = 0.44\ \mu$s could be achieved by using a spin echo, which is suggested to be mainly influenced by hyperfine-mediated flip-flop processes with the nuclear-spin bath.

5.3 Entanglement Purification with the Heisenberg Exchange Interaction

As described in Sec. 3.5, the original BBPSSW protocol for entanglement purification requires the application of a bilateral CNOT gate. For spin qubits coupled via Heisenberg exchange interaction, however, we saw that the implementation of CNOT is a rather challenging task. In this section, we develop a method to purify entanglement directly using Heisenberg exchange interaction. The protocol has a similar structure to the original recurrence protocols of Refs. 10 and 11, the crucial difference being that the bilateral operation is *asymmetric*, meaning that *different* two-qubit gates are applied on each communication side, respectively.

5.3.1 Generic Purification Protocol

We consider the scenario depicted in Fig. 5.2. Two parties, conveniently named Alice and Bob, want to implement a certain task that explicitly requires to share a maximally entangled state. This is a standard job in quantum communication networks where, e.g., the teleportation of an unknown quantum state is based on the distribution of the maximally entangled Bell state $|\Psi^-\rangle$ [32, 38]. However, Alice and Bob only have access to two-qubit states ρ_I that are initially not maximally entangled, which can be caused by different physical effects. The source producing the correlated qubits might be imperfect and as well the transmission of the qubits from the source to Alice and Bob usually does not preserve coherence very well. The initial state ρ_I can be a general mixed two-qubit state with some initial fidelity F,

$$F = \langle \Psi^- | \rho_I | \Psi^- \rangle \tag{5.14}$$

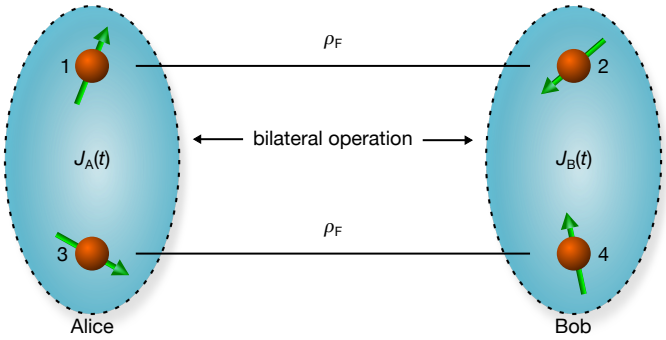

Figure 5.2 – Entanglement purification with Heisenberg exchange. Alice and Bob share two imperfectly entangled spin-qubit pairs ρ_F, Alice holds qubits 1 and 3, Bob has qubits 2 and 4. An asymmetric bilateral operation is implemented if Alice and Bob locally apply different exchange pulses generated by the respective exchange couplings $J_A(t)$ and $J_B(t)$.

relative to the Bell state $|\Psi^-\rangle$. For the purification protocol to be applicable, the state ρ_I has to be brought into the form ρ_F of Eq. (3.20). First, Alice and Bob need to twirl the state ρ_I [10, 36], which yields a Werner state W_F [33],

$$W_F = F\,|\Psi^-\rangle\langle\Psi^-| + \frac{1-F}{3}\Big(|\Psi^+\rangle\langle\Psi^+| + |\Phi^+\rangle\langle\Phi^+| + |\Phi^-\rangle\langle\Phi^-|\Big). \tag{5.15}$$

The twirl operation does not change the $|\Psi^-\rangle$ component, equalizes the components of the other three Bell states, and averages out the off-diagonal elements, resulting in the rotationally symmetric mixture W_F. Afterwards, one of the parties performs the rotation $R_y(\pi)$ of its qubit to interchange the $|\Psi^-\rangle$ and $|\Phi^+\rangle$ components and eventually obtain the state ρ_F,

$$\rho_F = F\,|\Phi^+\rangle\langle\Phi^+| + \frac{1-F}{3}\Big(|\Psi^+\rangle\langle\Psi^+| + |\Psi^-\rangle\langle\Psi^-| + |\Phi^-\rangle\langle\Phi^-|\Big). \tag{5.16}$$

For the purification of the initial state produced by the source and transmitted to Alice and Bob, two copies of the state ρ_F can be used. Hence, Alice and Bob each have two qubits at hand. We label the qubits of Alice 1 and 3, Bob has qubits 2 and 4 (see Fig. 5.2). The four-qubit state ρ describing the actual system is thus given by

$$\rho = \rho_F^{(12)} \otimes \rho_F^{(34)}, \tag{5.17}$$

where $\rho_F^{(ij)}$ denotes the state of qubits i and j. Alice and Bob each continue by the application of an exchange pulse between their respective qubits, which is described the unitary transformation

$$U(\alpha,\beta) = U_{13}(\alpha) \otimes U_{24}(\beta). \tag{5.18}$$

Here, U_{ij} describes the time evolution of qubits i and j coupled via Heisenberg exchange that is

given in Eq. (5.10).[3] If we denote the exchange couplings in Alice's and Bob's spin register as $J_A(t)$ and $J_B(t)$, then the pulse areas α and β are given by

$$\alpha = \int_0^{t_A} \mathrm{d}t' J_A(t'), \tag{5.19}$$

$$\beta = \int_0^{t_B} \mathrm{d}t' J_B(t'), \tag{5.20}$$

where $t_{A/B}$ are the lengths of the pulses. The crucial difference to other entanglement purification protocols [107–111, 134] is that Alice and Bob are allowed to choose different pulse areas and thus, apply different bilateral two-qubit operations. It is exactly this asymmetric bilateral operation that makes entanglement purification via Heisenberg interaction feasible *at all*. The exchange pulses transform the four-qubit state ρ like

$$\rho \mapsto U(\alpha, \beta)\rho U(\alpha, \beta)^\dagger. \tag{5.21}$$

In analogy to the original publication (Ref. 10) where the effect of a bilateral CNOT was explicitly given, we show how the unitary transformation $U(\alpha, \beta)$ acts on combinations of Bell states in Appendix B. After this unitary transformation, the two parties continue like in the original BBPSSW protocol. Although we do not use any conditional quantum operations here, we still denote qubits 1 and 2 as control qubits, and qubits 3 and 4 as target qubits, following the notation in Sec. 3.5 where the CNOT-based purification protocol was described. Alice and Bob measure the target qubits 3 and 4 in the computational basis $\{|\uparrow\rangle, |\downarrow\rangle\}$ and compare the measurement results afterwards. This is done by classical two-way communication. If Alice and Bob obtain equal measurement results, i.e. either both spins are pointing up or both are pointing down, they will keep the control qubits. Otherwise, the state is discarded. The quantum circuit for the purification protocol is shown in Fig. 5.3. As we derive below, in case of keeping the control pair, the fidelity of precisely this state can become larger than the initial fidelity F by the above transformation and measurement, depending on the applied exchange pulses.

Mathematically, we describe a successful measurement by a projection $\mathcal{P}$ onto the subspace spanned by the states in which the spins of qubits 3 and 4 point in the same direction,

$$\mathcal{P} = \mathbb{1}_{12} \otimes \left(|\uparrow\uparrow\rangle_{34} \langle\uparrow\uparrow| + |\downarrow\downarrow\rangle_{34} \langle\downarrow\downarrow| \right). \tag{5.22}$$

Here, $\mathbb{1}_{12}$ is the identity operation on the control qubits 1 and 2, and for a two-qubit state we choose the notation $|\uparrow\uparrow\rangle_{ij} \equiv |\uparrow\rangle_i |\uparrow\rangle_j$ with analogue expression for other combinations. Thus, the normalized four-qubit state ρ' after a successful measurement can be obtained through the

[3] We can separate the time evolution of the four-particle system in Eq. (5.18) into the two-particle propagators $U_{13}(\alpha)$ and $U_{24}(\beta)$ because the Hamiltonians describing each exchange interaction commute, i.e. $[H_{13}(t), H_{24}(t')] = 0$ for all t and t', with $H_{ij}(t)$ given in Eq. (5.4).

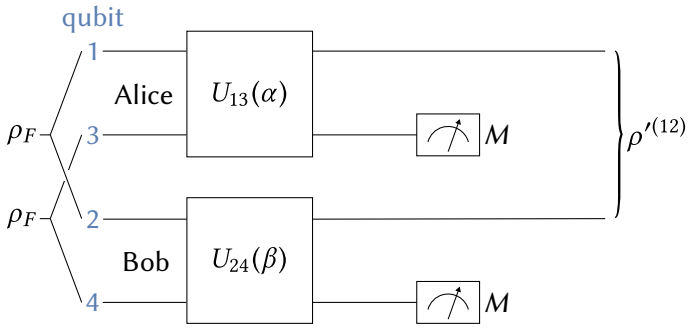

Figure 5.3 – Circuit diagram of the purification protocol. Alice and Bob start with two copies of the state ρ_F. Alice applies the unitary transformation $U_{13}(\alpha)$ to qubits 1 and 3, Bob $U_{24}(\beta)$ to qubits 2 and 4. Subsequent measurements (M) of the target qubits 3 and 4 follow. The state of the control qubits after the transformation becomes $\rho'^{(12)}$. The fidelity of the control state is larger than the initial fidelity for a successful purification round.

operation

$$\rho' = \frac{1}{\mathrm{Tr}(\mathcal{P}U(\alpha,\beta)\rho U(\alpha,\beta)^\dagger\mathcal{P})}\mathcal{P}U(\alpha,\beta)\rho U(\alpha,\beta)^\dagger\mathcal{P}, \tag{5.23}$$

where the trace is taken over the four-qubit Hilbert space. Finally, the state $\rho'^{(12)}$ of the control qubits 1 and 2 is obtained by tracing out the target qubits,

$$\rho'^{(12)} = \mathrm{Tr}_{34}(\rho'). \tag{5.24}$$

The overlap $F'(F,\alpha,\beta) = \langle\Phi^+|\rho'^{(12)}|\Phi^+\rangle$ that equals the fidelity if the $|\Psi^-\rangle$ and $|\Phi^+\rangle$ components are interchanged again, is found to be

$$F'(F,\alpha,\beta) = \frac{(4F-1)(4F+5)\cos\alpha\cos\beta - (4F-1)(8F+1)\sin\alpha\sin\beta + 8F(4F+1) + 5}{6(4F-1)\cos\alpha\cos\beta - 2(4F-1)^2\sin\alpha\sin\beta + 6(4F+5)}, \tag{5.25}$$

which is the main result of this chapter. The fidelity $F'(F,\alpha,\beta)$ depends on the initial fidelity F and on the applied exchange pulses via the pulse areas α and β. The state $\rho'^{(12)}$ is diagonal in the Bell basis, and for the sake of completeness, the remaining diagonal elements are

$$\langle\Phi^-|\rho'^{(12)}|\Phi^-\rangle = \frac{3(1-4F)\sin\alpha\sin\beta + (1-4F)^2\cos\alpha\cos\beta - 9}{2(1-4F)^2\sin\alpha\sin\beta + 6(1-4F)\cos\alpha\cos\beta - 6(4F+5)}, \tag{5.26}$$

$$\langle\Psi^+|\rho'^{(12)}|\Psi^+\rangle = \frac{4(F-1)(2F+1)}{(1-4F)^2\sin\alpha\sin\beta + 3(1-4F)\cos\alpha\cos\beta - 3(4F+5)}, \tag{5.27}$$

$$\langle\Psi^-|\rho'^{(12)}|\Psi^-\rangle = \frac{4(F-1)(2F+1)}{(1-4F)^2\sin\alpha\sin\beta + 3(1-4F)\cos\alpha\cos\beta - 3(4F+5)}. \tag{5.28}$$

From Eq. (5.25), the effect of the *asymmetric* bilateral operation becomes apparent. For a symmetric

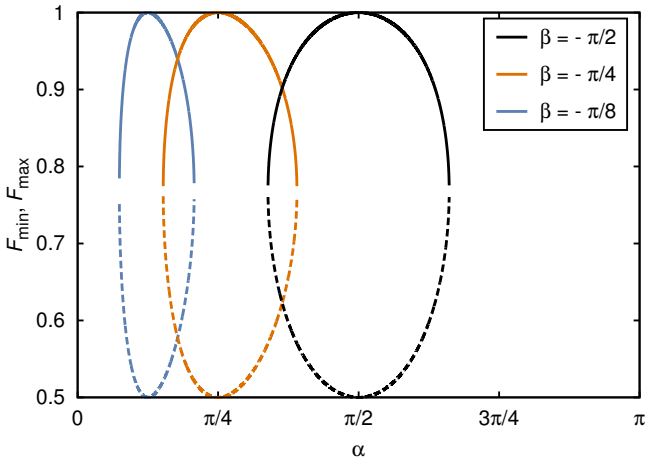

Figure 5.4 – Fixed points of purification protocol. The minimum required initial fidelity F_{min} (dashed lines) for the entanglement purification to work and the maximally attainable fidelity F_{max} (solid lines) when iteratively applying the purification protocol that generates the map in Eq. (5.25) as a function of the pulse area α and for different pulse areas β.

bilateral operation, i.e. for $\alpha = \beta$, the relation $F'(F, \alpha, \alpha) \leq F$ holds in the range $1/2 < F < 1$. Hence, no purification is possible if Alice and Bob apply the same exchange pulses to their qubit pairs. This case has been studied before in Ref. 108 and explained by analyzing the time evolution in the Bell-product basis. However, we want to point out that the requirement of equal operations by Alice and Bob is a dispensable assumption, which prohibits purification if it is not discarded. To show the feasibility of the derived protocol for entanglement purification, the three fixed points of the map in Eq. (5.25) can be found analytically. Except for the case $\alpha = n\pi$, $\beta = m\pi$, and $\alpha - \beta = 2\pi k$ (n, m, k integers), where $F' \equiv F$, a constant fixed point is given by $F_{\text{c}} = 1/4$. The values of the two remaining (possibly complex) fixed points F_{min} and F_{max} depend on α and β, as illustrated in Fig. 5.4 within the physically relevant regime $1/2 \leq F_{\text{min}} \leq F_{\text{max}} \leq 1$. While the fixed points F_{max} and F_{c} are attractive, F_{min} is repulsive. Thus, if the qubit pairs have an initial fidelity $F > F_{\text{min}} \geq 1/2$, iterative application of the described scheme can purify them up to a fidelity F_{max}. If $\alpha = -\beta$, we find $F_{\text{min}} = 1/2$ and $F_{\text{max}} = 1$, which are the same fixed points as in the original BBPSSW protocol. In this case, also the increase in fidelity is maximal, which is investigated more carefully below. Furthermore, one can see from Fig. 5.4 that the robustness of our scheme is largest in the case $\alpha = -\beta = \pi/2$ since deviations from perfectly applied operations have the least effect on the values of F_{min} and F_{max}. If Alice applies a rectangular pulse with an exchange interaction of $J_{\text{A}} = 1\,\mu\text{eV}$ [114], the deviation $\Delta\tau$ from the optimal case must not exceed 100 ps to still achieve a maximum fidelity of 0.99, assuming Bob generates a perfect pulse. Such accuracies can be obtained experimentally [114].

As we can see from Eqs. (5.26) – (5.28), the output state $\rho'^{(12)}$ generally does not have the Bell-diagonal form of ρ_F in Eq. (5.16) with equal components of the states $|\Phi^-\rangle$, $|\Psi^+\rangle$ and $|\Psi^-\rangle$.

A subsequent purification round, however, requires the input states to have the same structure as ρ_F. Therefore, between two purification rounds, another twirl operation needs to be applied that creates the state $\rho_{F'}$ from $\rho'^{(12)}$ with F' given in Eq. (5.25). Since twirling requires a random single-qubit rotation [10, 36], the purification scheme we develop here so far does not get rid of all single-qubit operations. Nevertheless, a purification round still takes substantially less time than the single-qubit gates that would be required for the realization of the standard CNOT sequence [Eq. (5.13)]. On the other hand, the DEJMPS protocol works for general Bell-diagonal two-qubit states and does not need the twirl. By replacing the bilateral CNOT in the DEJMPS protocol by the asymmetric operation described above, we can also establish a working purification method, which is demonstrated below. A deterministic single-qubit rotation between subsequent purification rounds is still required. However, the total number of slow single-qubit rotations is significantly reduced.

5.3.2 Optimal Purification Protocol

The minimal and maximal values of the fixed points $F_{\min} = 1/2$ and $F_{\max} = 1$ are obtained in the case $\alpha = -\beta$. This implies that in principle maximally entangled states can be created using our protocol if Alice and Bob perform mutually inverse operations. Practically, this could be achieved in several ways. Alice and Bob could, e.g., use ferro- and antiferromagnetic exchange couplings $J_A(t) > 0$ and $J_B(t) < 0$, or vice versa. If both parties operate with equal physical setups, the sign of the exchange interaction could be changed using a magnetic field [118, 135]. In the case of equal coupling types, one can use the fact that the propagator $U_{ij}(t)$ is 2π periodic (omitting overall phases). Alice and Bob could choose exchange pulses with, e.g., $0 < \alpha < \pi$ and $\beta = 2\pi - \alpha > 0$ in the case of ferromagnetic coupling to generate inverse operations as well. The fidelity is then given by

$$F'(F, \alpha, -\alpha) = \frac{1}{2} + \frac{3 - 12F^2}{(F-1)(4F-1)\cos(2\alpha) - F(4F+7) - 7}, \tag{5.29}$$

which is plotted in Fig. 5.5 for several values of α and compared to the result of the original BBPSSW proposal. We also show the probability $p(F, \alpha)$ for a successful purification step, i.e. the probability that Alice and Bob obtain equal measurement results,

$$p(F, \alpha) = \frac{1}{18}\Big(7 + F(4F+7) - (F-1)(4F-1)\cos(2\alpha)\Big). \tag{5.30}$$

This probability is given by the expectation value of the projection operator $\mathcal{P}$ [Eq. (5.22)], which is equal to the normalization of the density matrix ρ' [Eq. (5.23)],

$$p(F, \alpha) = \langle \mathcal{P} \rangle = \mathrm{Tr}(\mathcal{P} U(\alpha, \alpha) \rho U(\alpha, \alpha)^\dagger) = \mathrm{Tr}(\mathcal{P} U(\alpha, \alpha) \rho U(\alpha, \alpha)^\dagger \mathcal{P}), \tag{5.31}$$

where we used $\mathcal{P}^2 = \mathcal{P}$ and the cyclic property of the trace.

From Eq. (5.29), we can deduce that the maximal increase in fidelity in the relevant range

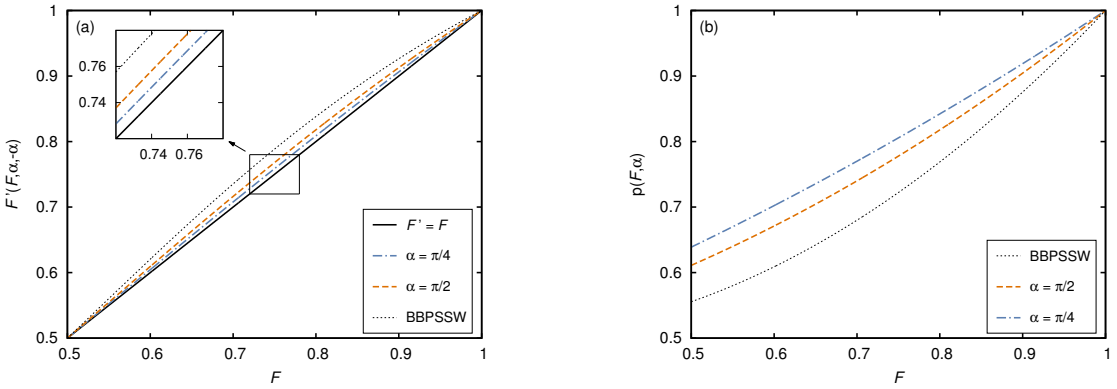

Figure 5.5 – Fidelity increase and measurement probability. (a) Fidelity $F'(F, \alpha, -\alpha)$ of the control state after a purification step as a function of the initial fidelity F, shown for different pulse areas α and compared to the original BBPSSW protocol. (b) Probability $p(F, \alpha)$ for a successful measurement with equal outcomes as a function of the initial fidelity F, also shown for different pulse areas α and compared to the probability in the original BBPSSW protocol.

$1/2 < F < 1$ is given for $\alpha = \pi/2 + 2\pi n$ (n integer). We refer to this case as the *optimal purification protocol* and find for the increase in fidelity

$$F'\left(F, \frac{\pi}{2} + 2\pi n, -\frac{\pi}{2} + 2\pi m\right) = \frac{16F^2 + F + 1}{8F^2 + 2F + 8}, \tag{5.32}$$

where the integers n and m can be chosen independently by Alice and Bob. The optimal value is therefore achieved if Alice applies a $\sqrt{\text{SWAP}}$ gate to her qubits and Bob performs the inverse $\sqrt{\text{SWAP}}$ gate, $\sqrt{\text{SWAP}}^{-1}$.[4]

The described protocol can be slightly improved in terms of resources needed to achieve a specific fidelity. In analogy to the DEJMPS protocol, Alice can begin each purification step with the local operations [Eq. (3.24)]

$$|0\rangle \mapsto \frac{1}{\sqrt{2}}\left(|0\rangle - i\,|1\rangle\right), \quad |1\rangle \mapsto \frac{1}{\sqrt{2}}\left(|1\rangle - i\,|0\rangle\right), \tag{5.33}$$

and Bob performs the inverse operation. The bilateral CNOT is replaced by the asymmetric operation used in the optimal purification protocol. The protocol works for general Bell-diagonal states and does not need the twirl in between subsequent purification steps. The gain in fidelity can be slightly increased [Fig. 5.6 (a)] and thus, the number of purification steps is reduced [Fig. 5.6 (b)].

5.4 Entanglement Purification with other Interaction Types

For the initial situation of two input pairs ρ_F, the concept of asymmetric bilateral two-qubit operations enabled entanglement purification directly from the Heisenberg exchange interaction,

[4] The square of $\sqrt{\text{SWAP}}^{-1}$ is also the SWAP operation and it can be understood as another root of SWAP.

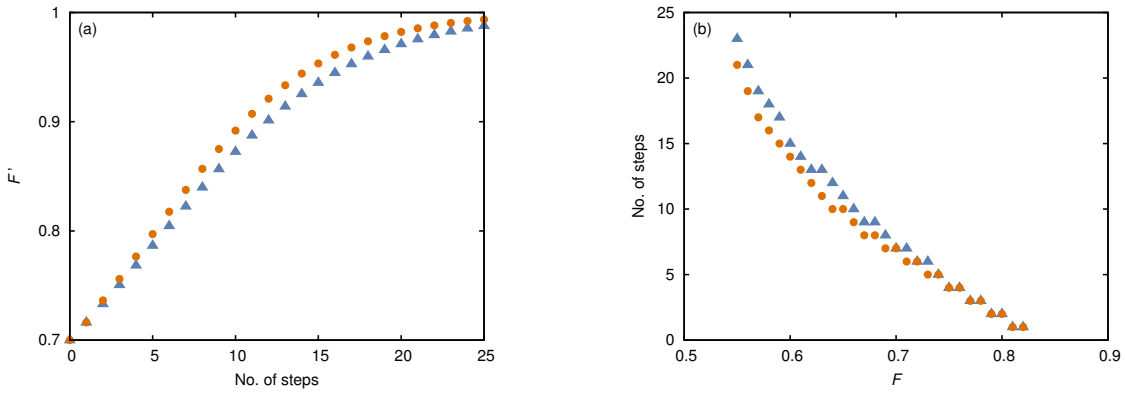

Figure 5.6 – Iteration of purification protocol. (a) Stepwise fidelity increase for an initial fidelity $F = 0.7$ and (b) number (No.) of purification steps needed to achieve a fidelity $F' > 0.82$ (above threshold fidelity of hashing method introduced in [36]) starting from qubit pairs with a fidelity F. Data is shown for the described optimal purification protocol (triangles) [Eq. (5.32)] that requires twirling, and in a more efficient way for a version analogue to the DEJMPS protocol (dots) without twirling, but instead requiring the single-qubit operation in Eq. (5.33).

which is not possible if Alice and Bob apply the same local operations [108]. In this section, we demonstrate that this is also true for other qubit coupling types, such as the XY interaction or magnetic dipole coupling. The calculations are performed in analogy to the previous section.

5.4.1 XY Interaction

The Hamiltonian describing XY-type interaction between two qubits i and j is given by

$$H_{ij}^{\mathrm{XY}}(t) = \frac{1}{4} J^{\mathrm{XY}}(t) \left(\sigma_i^x \sigma_j^x + \sigma_i^y \sigma_j^y \right). \tag{5.34}$$

Compared to the Heisenberg Hamiltonian [Eq. (5.4)], only the x and y components of the spins are coupled, and we denote the coupling constant by $J^{\mathrm{XY}}(t)$. This kind of interaction appears, e.g., in all-optical cavity-coupled QD electron spins [113] or superconducting qubits [112]. For a pulse area $\int_0^\tau \mathrm{d}t' J^{\mathrm{XY}}(t') = -\pi$, the Hamiltonian $H_{ij}^{\mathrm{XY}}(t)$ generates the ISWAP gate,

$$U_{\mathrm{ISWAP}} = U_{ij}^{\mathrm{XY}}(-\pi) = e^{-i(-\pi)\left(\sigma_i^x \sigma_j^x + \sigma_i^y \sigma_j^y\right)} = \begin{pmatrix} 1 & 0 & 0 & 0 \\ 0 & 0 & i & 0 \\ 0 & i & 0 & 0 \\ 0 & 0 & 0 & 1 \end{pmatrix}. \tag{5.35}$$

For purification, Alice and Bob follow the scheme described in Sec. 5.3, i.e. they start with two qubit pairs $\rho = \rho_F \otimes \rho_F$ and apply the XY interaction with pulse areas α and β to their respective qubit pairs. After a subsequent measurement of the target qubits, Alice and Bob keep the control pair if they obtain equal measurement results. As a result, the fidelity $F'_{\mathrm{XY}}(F, \alpha, \beta)$ of the source

state can be increased depending on the pulse areas α and β. A formula for $F'_{\mathrm{XY}}(F,\alpha,\beta)$ can be found in Eq. (8) of Ref. 98. In the case $\alpha = -\beta$, i.e. when both parties apply mutually inverse operations, the result coincides with Eq. (5.29),

$$F'_{\mathrm{XY}}(F,\alpha,-\alpha) = F'(F,\alpha,-\alpha), \tag{5.36}$$

and the gain in fidelity is thus maximal for $\alpha = \pi/2$. In the optimal case, the different qubit interactions correspond to gates whose double application result in the iSWAP gate.

5.4.2 Magnetic Dipole-Dipole Interaction

The dipole-dipole coupling between two magnetic moments $\boldsymbol{\mu}_i = \gamma \mathbf{S}_i$ and $\boldsymbol{\mu}_j = \gamma \mathbf{S}_j$, separated by a distance r, is described by the Hamiltonian [136]

$$H_{\mathrm{dd}} = \frac{\mu_0 \gamma^2}{4\pi r^3} \left(\mathbf{S}_i \cdot \mathbf{S}_j - 3 \left(\mathbf{S}_i \cdot \mathbf{e}_r\right) \left(\mathbf{S}_j \cdot \mathbf{e}_r\right) \right). \tag{5.37}$$

Here $\mathbf{e}_r$ is a unit vector pointing along the connecting line between the two identical magnetic moments with gyromagnetic ratio γ and μ_0 is the vacuum permeability. For example, the electron spins of two nitrogen-vacancy centers in diamond (Chap. 6) that were close enough to each other could be coupled via the interaction of the associated magnetic moments and entangled in this way [137]. Without loss of generality, we can assume the connecting line to define the z axis and thus, obtain

$$H_{\mathrm{dd}} = \frac{\mu_0 \gamma^2}{16\pi r^3} \left(\sigma_i^x \sigma_j^x + \sigma_i^y \sigma_j^y - 2\sigma_i^z \sigma_j^z \right), \tag{5.38}$$

where we assume spin-1/2 systems that are magnetically coupled. The strength of the interaction could in principle be varied by changing the distance r between the qubits, which might not be a trivial task. However, as proof of principle of our developed concept and to demonstrate that it works for a variety of Hamiltonians, we apply the asymmetric purification scheme developed above as well to qubits coupled via H_{dd}. We define the pulse area as $\alpha = \int_0^t \mathrm{d}t' \mu_0 \gamma^2 / (16\pi r(t')^3)$ and assume a time-dependent distance $r(t)$. The fidelity $F'_{\mathrm{dd}}(F,\alpha,\beta)$ after one purification round with initial fidelity F is calculated to be

$$F'_{\mathrm{dd}}(F,\alpha,\beta) = \frac{\Gamma(F,\alpha,\beta)}{6(4F-1)\cos\alpha\cos\beta - 2(4F-1)^2 \sin\alpha \sin\beta + 6(4F+5)}, \tag{5.39}$$

and the numerator $\Gamma(F,\alpha,\beta)$ is given by the expression

$$\begin{aligned} \Gamma(F,\alpha,\beta) = {} & (2F(4F+1)-1)(2\cos(2(\alpha+\beta)) + \cos(4(\alpha+\beta)) + 2\cos(6(\alpha+\beta))) \\ & - 2(F-1)(4F-1)\cos(4(\alpha-\beta)) + 4F(4F+1) + 7. \end{aligned} \tag{5.40}$$

We also find that the minimal and maximal values of the fixed points $F_{\min}$ and $F_{\max}$, respectively are obtained if Alice and Bob apply mutually inverse operations, since

$$F'_{\mathrm{dd}}\left(F, \frac{\alpha}{4}, -\frac{\alpha}{4}\right) = F'(F, \alpha, -\alpha), \tag{5.41}$$

and therefore the discussion of Sec. 5.3.2 also applies for entanglement purification in case of qubits coupled via magnetic dipole-dipole interaction, with the optimal purification achieved for a pulse area of $\alpha = \pi/8$.

5.5 Conclusions

An open problem in the development of quantum repeaters had been the lack of a scheme for entanglement purification directly with the exchange interaction. For this purpose, we developed the concept of asymmetric bilateral two-qubit operations for entanglement purification that, to the best of our knowledge, has not been studied before in the literature. This concept can be applied to a very broad range of solid-state spin qubits, e.g., electron spins in QDs, nitrogen-vacancy centers in diamond, or superconducting qubits. Thus, the development of this concept could be a significant step towards large-scale quantum communication.

By the use of asymmetric operations, we designed an entanglement purification protocol, in which the bilateral two-qubit operation is directly generated from the one-time activation of a Heisenberg-type spin-spin interaction. We have shown that an asymmetric unitary evolution of Alice's and Bob's qubits, respectively, can lead to an increased fidelity of one of the shared qubit pairs with respect to the Bell state $|\Phi^+\rangle$ if the initial fidelity was larger than a given minimal value. In the special case where Alice and Bob apply mutually inverse operations, the maximally obtainable fidelity by iterative application of our protocol is $F = 1$; i.e., in principle maximally entangled states can be generated. We found that the optimal case is when the two communicating parties apply the $\sqrt{\mathrm{SWAP}}$ and the $\sqrt{\mathrm{SWAP}}^{-1}$ gates locally on their qubits. Since the coupling of electron spins in gate-controlled QDs is well described by an exchange interaction of Heisenberg type, the protocol is particularly suitable for spin qubits. In terms of operation times, the presented protocol is much faster than protocols based on CNOT applied to spin qubits. The reason is that single-qubit gates needed in constructing the CNOT need operation times on the order of 100 nanoseconds [124] whereas the $\sqrt{\mathrm{SWAP}}$ can be generated two orders of magnitude faster in about 0.2 nanoseconds [114]. Therefore, besides the smaller error-proneness due to the smaller number of gate operations, a much faster iteration of the protocol is possible. Even higher iteration rates would be achieved if the intermediate twirl operation could be implemented through the exchange interaction, e.g. by exchange-controlled single-spin rotations with predicted gating times of about 1 nanosecond [138]. The feasibility of this idea should be the aim of further studies. At this stage, we point out that fast single-qubit gates on the picosecond timescale have been demonstrated for

charge qubits in gate-controlled QDs [139] and for spin qubits in self-assembled QDs [99, 140]. However, two-qubit gates have not yet been demonstrated for spin qubits in self-assembled QDs and, moreover, charge qubits have coherence times in the range of nanoseconds and are therefore not suitable as quantum memory.

In addition, we showed that our purification method of applying an asymmetric bilateral operation works as well for qubits coupled via a XY-type or magnetic dipole-dipole interaction and is therefore suitable for cavity-coupled spin qubits, superconducting qubits, and nitrogen-vacancy centers in diamond. The interaction types investigated in our studies are special cases of a general spin-spin interaction of the form $\mathbf{S}_i^T \cdot \overleftrightarrow{\mathbf{J}} \cdot \mathbf{S}_j$, with some coupling tensor $\overleftrightarrow{\mathbf{J}}$. Therefore, further investigation on entanglement purification from this general interaction Hamiltonian needs to take place.

6

Long-Range Two-Qubit Gate between Nuclear Spins in Diamond

6.1 Introduction

Point defects in a crystalline solid-state environment offer several possibilities for the physical implementation of a qubit including, e.g., spins of donor atoms in silicon [141–143] and defects in silicon carbide [144, 145]. Among those crystal defects, the perhaps most prominent example is the nitrogen-vacancy color center in diamond [20, 23, 25], which comprises a substitutional nitrogen atom in the diamond lattice and a missing carbon atom at a neighboring site (Fig. 6.1). Several seminal experiments could demonstrate its functionality as qubit and it has since then evolved to be a major research branch of quantum information processing. Today, it is known that the orbitals of the NV center are highly localized states. The ground state of the NV center is an electronic spin-1 system, and it features an excited state manifold that can be optically excited, in which the transition lies within the 5.5 eV band gap of diamond. Therefore, such defects are sometimes seen as "trapped atoms" [23]. The electron spin can be initialized by optical spin polarization, coherently manipulated, e.g., by microwave pulses, and read out with a high accuracy. Furthermore, the electron spin shows coherence times of milliseconds at room temperature, which made the NV center a highly promising candidate to be utilized as qubit in a quantum computer or quantum network. An overview can be found in recent reviews [20, 21, 23]. The NV center also finds application in various other fields, e.g., as single-photon source [146], highly sensitive nanoscale sensor for magnetometry [147], or in bioimaging [148], to name only a few of them.

But it is not only the electron spin that can be useful for quantum information processing. Nuclear spins weakly interact with their environment and are less susceptible to effects that can destroy their quantum state. Hence, nuclear spins in diamond show even better coherence properties than the NV electron spin and are likewise prospective candidates for the physical realization of a qubit [49, 149–152]. There are three types of nuclear spins that play a role with respect to quantum information processing. First of all, the NV center by definition comprises a

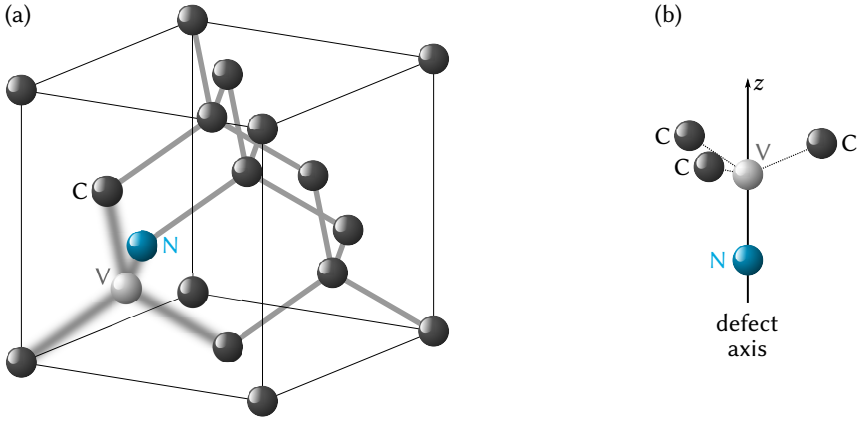

Figure 6.1 – Atomic structure of the nitrogen-vacancy center. (a) Diamond lattice formed by carbon (C) atoms. A point defect in the lattice of C_{3v} symmetry is created by a substitutional nitrogen (N) atom next to a vacancy (V) where an atom is missing in the lattice. (b) Spin quantization axis (z axis) given by the connecting line between the nitrogen atom and the vacancy.

nitrogen atom that possesses a nuclear spin, which can either be a ^{14}N or ^{15}N isotope. Carbon is mainly occurring as ^{12}C isotope that has no nuclear spin. On the other hand, ^{13}C has a nuclear spin and can be coincidently located at proximate lattice sites since it appears with a small natural abundance of 1.1 %. However, our work is focussed on the intrinsic nitrogen nuclear spins.

Being either used for quantum computation or as node in a quantum communication network (see Chap. 3), it is indispensable to deterministically entangle two distant nuclear spin qubits. A mechanism to implement an entangling two-qubit operation has to be available that is fast enough compared to the timescale set by the nuclear-spin decoherence time, and couples nuclear spins over long distances. The generation of entanglement between nuclear spins in diamond has been studied before, including both experimental [47, 50, 153–155] and theoretical work [156–159]. Previous theoretical proposals addressing nuclear spin entanglement in diamond considered, e.g., an effective coupling between two ^{14}N nuclear spins via magnetically coupled electron spins [158]. Such a scheme limits the maximal distance between the two qubits to about 50 nm. In a quantum repeater protocol specified for network nodes that possess two internal degrees of freedom, like the NV center with its electron and nuclear spin, the entangling of two nuclear spins was proposed by also utilizing prior electron entanglement [156, 157, 159]. Therefore, a deterministic long-distance entangling scheme between nuclear spin qubits should have been developed, and the results are presented in this chapter.

In our work, we develop a mechanism to deterministically implement a controlled quantum gate between two distant nitrogen nuclear spin qubits in diamond, and thus, generate long-range entanglement that can be used, e.g., in quantum networks (see Chap. 3 for details). The coupling between the nuclear spins is achieved by virtual excitation of an optical cavity, to which both NV centers are coupled. External laser photons incident on each NV center can be scattered into the cavity mode by exciting electronic Raman-type transitions between the ground and excited state,

and thereby mediating an effective interaction between the two NV centers. We find that the scattering process depends on the nitrogen nuclear-spin state. The scattering can be completely suppressed for a specific nuclear spin configuration by properly tuning the laser frequency, which eventually leads to the implementation of a controlled-Z (cz) gate (Sec. 3.2). Quantitative analysis of our proposed mechanism yields fast gate operation times below 100 nanoseconds, which is a few orders of magnitude faster than the decoherence time of about a millisecond for the nitrogen nuclear spin. Cavity-mediated coupling between NV *electron* spins has been studied before, see Ref. 160.

This chapter is organized in the following way. First, in Sec. 6.2 we describe the physical system to be studied, namely the NV color center in diamond including electronic structure and spin properties, and the hyperfine interaction between the NV electron spin and the respective nuclear spins. It follows a detailed overview about spin qubits in diamond in Sec. 6.3, where we try to emphasize the usability of the NV center for quantum information processing. We describe major achievements regarding single- and multi-qubit control for both, the electron and nuclear spins. Sec. 6.4 is devoted to our own work, in which we describe the coupling of a NV center to an optical cavity (Sec. 6.4.1), afterwards how the scattering of an external laser photon into the cavity mode depends on the nitrogen nuclear-spin state (Sec. 6.4.2), and finally how to implement a universal two-qubit gate (Sec. 6.4.3).

6.2 The Nitrogen-Vacancy Center

6.2.1 Properties of the Nitrogen-Vacancy Center

The nitrogen-vacancy (NV) color center is a paramagnetic point defect in the diamond lattice, in which a substitutional nitrogen (N) atom is located adjacent to a vacancy where a carbon (C) atom is missing (see Fig. 6.1). Such a defect often occurs naturally and can also be formed during the diamond synthesis process [161] or be produced by ion implantation [162]. Depending on the nitrogen isotope, the NV center can comprise either a ^{14}N or ^{15}N nucleus, which affects the hyperfine interaction. The connecting line between the nitrogen atom and the vacancy is called the defect axis and it determines the spin quantization axis, which is defined to be the z direction.

The NV center can occur in a negative (NV^-) or neutral (NV^0) charge configuration. The negatively charged system has been studied experimentally and theoretically in great detail, and important milestones regarding its feasibility for quantum information processing could be achieved that include, e.g., coherent qubit manipulation and two-qubit entanglement.[1] An overview about the latest achievements can be found in recent reviews [20, 23, 163] and is partially given in Chap. 6.3. The defect (in the negatively charge state) incorporates six electrons, of which five are unpaired electrons occupying the dangling bonds of the nitrogen and the three carbon

[1] Our work only concentrates on the negatively charged configuration NV^-, which we simply refer to as "NV center" in the following.

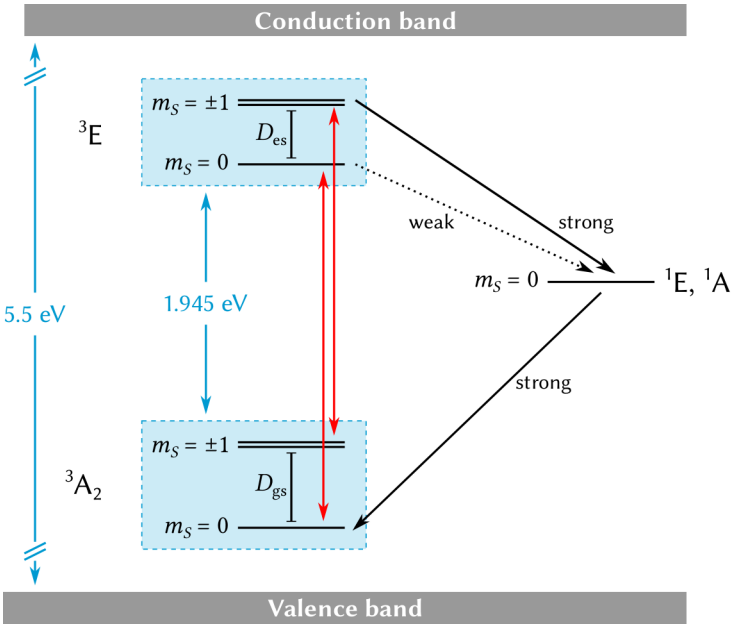

Figure 6.2 – Energy-level diagram of the NV center. Electronic states localized to the NV center lie within the 5.5 eV band gap of diamond (not to scale). The transition energy between the ground (^{3}A$_2$) and excited (^{3}E) state is 1.945 eV, and both states are spin triplets. Optical transitions are spin conserving, indicated by red arrows. Spin states $m_S = 0$ and $m_S = \pm 1$ are separated by the zero-field splitting D_{gs} (D_{es}) in the ground (excited) state. (No external magnetic field considered here; excited-state fine structure omitted.) On the right, the relaxation process through an intersystem crossing via the intermediate, metastable singlet states ^{1}E and ^{1}A is depicted, as will be described in Sec. 6.2.2. Nonradiative decay from ^{3}E into the singlets is stronger for the $m_S = \pm 1$ sublevels, allowing for optical spin polarization.

atoms. The additional sixth electron is captured from the lattice, possibly from nearby nitrogen donors [164]. The symmetry of the diamond lattice is reduced due to the formation of the point defect, which in this case has C_{3v} symmetry; i.e. the system is invariant under rotations about the defect axis by multiples of 120°, and there exist three mirror planes spanned by the defect axis and one of the three nearest-neighbor carbon atoms, respectively. The loss in translational symmetry generates electronic states that are localized around the defect. These localized states are energetically located within the diamond bandgap as schematically depicted in Fig. 6.2. A strong optical zero-phonon line (ZPL) between ground and excited state can be observed that has a transition energy of 1.945 eV (637 nm). 95 % of the optical emission goes into the phonon-assisted sideband. *Ab initio* calculations show that around 70 % of the electron density in the ground state is localized to the three C atoms [165]. In the excited states, the electron density is larger at the nitrogen site, which causes the hyperfine interaction to be approximately 20 times larger compared to the ground state. This fact is harnessed in our mechanism to couple two nuclear spin qubits, as will be described below in Sec. 6.4.

6.2.2 Electronic Structure and Spin Hamiltonian

A detailed understanding of the electronic structure of NV centers has been developed only recently using a group-theoretical approach in combination with *ab initio* calculations [166, 167]. The electronic properties are determined by the six constituting electrons, and can be either deduced from a six-electron [166] or two-hole [167] model. The electronic system has integer spin due to the even number of electrons, and both the orbital ground and excited state are $S = 1$ spin triplets, which was also confirmed experimentally [168, 169].

The ground state is an orbital singlet and transforms according to the A_2 representation of the C_{3v} group. Since it is a spin triplet, it is denoted as $^3A_2$. The excited state transforms as E, which is an orbital doublet. Hence, the excited state is ^3E. The NV center can be optically excited from the ground state to the excited state with a transition energy of 1.945 eV (637 nm). The optical transition is spin conserving and even preserves spin coherence [170, 171]. Furthermore, optical excitation to the excited state can be harnessed to initialize the spin state of the NV center. Being in the excited state ^3E, the system can relax back to ground state $^3A_2$ either by spontaneous emission of a photon, or via a nonradiative and not spin-conserving intersystem crossing (ISC) through the intermediate singlet states ^1A and ^1E. The electronic structure including the radiative and nonradiative decay channels are depicted in Fig. 6.2. Whereas the excited state has a short lifetime of about 10 nanoseconds [172], relaxation via the ISC traps the electronic system in the singlet states for about 300 ns [170]. Furthermore, the relaxation process via the ISC is spin selective and favors the states with spin projection $m_S = \pm 1$ compared to the $m_S = 0$ state. However, the decay through the ISC does not conserve the spin state and ends up in the ground state $^3A_2$ with spin projection $m_S = 0$ (see Fig. 6.2). On the other hand, the decay rates of the spin-conserving radiative relaxation processes are the same for every spin state. In general, the NV center can be in some mixed state of S_z eigenstates. If the system is optically illuminated, every spin state is equally excited. But the relaxation is an asymmetric process, due to the ISC, which opens an additional decay channel for the $m_S = \pm 1$ components. Since the decay via the ISC ends in the $m_S = 0$ state, a net increase in $m_S = 0$ population is achieved. Continuous optical pumping thus initializes the electron spin to the $m_S = 0$ state, a mechanism known as *optical spin polarization* that can also be exploited to measure the electron spin state [173]. If the electron spin is in the $m_S = 0$ state, optical pumping will lead to many subsequent relaxation events, resulting in a large signal in case the fluorescence is measured. In contrast, if the spin state is either $m_S = 1$ or $m_S = -1$, there exists the possibility that the system gets trapped in the long-lived singlet states, which in turn reduces the measurement signal. A measurement of the contrast in fluorescence therefore implements a measurement of the NV spin state. In Sec. 6.3, an overview about the NV center in the context of quantum information processing will be given. The ability to optically initialize and measure to electron spin state of a NV center, nowadays with very high accuracies, is one of the main reasons to utilize the NV center for this purpose. In a majority of the undermentioned works, optical spin polarization has been employed, even in the case of nuclear spins.

One exceptional property of the NV center that distinguishes it from many other qubit proposals, is the appearance of room-temperature spin coherence in the ground state spin triplet. Decoherence times (T_2) up to 1.8 ms for NV centers formed with ^{14}N isotopes [174] and 2 ms for ^{15}N isotopes [175] at room temperature have been observed using spin-echo techniques. These values can be significantly increased if the system is cooled down to cryogenic temperatures and T_2 can reach up to 0.6 s at 77 K [176]. The relaxation time (T_1) also depends crucially on the temperature and ranges from milliseconds to minutes [177]. The main reason for a loss of spin coherence is the interaction of the electron spin with other magnetic moments surrounding the defect. Such additional magnetic moments can be either ^{13}C isotopes [178, 179], or single nitrogen atoms also embedded in the diamond lattice, so-called P1 centers [180]. The ^{13}C isotope has nuclear spin $I = 1/2$ and exists with natural abundance of 1.1 %. ^{13}C nuclear spins are weakly coupled to the electron spin via hyperfine interaction. Uncontrolled interaction with the ^{13}C nuclear spin bath can be suppressed by using isotopically ultrapure diamond samples, in which the appearance of ^{13}C isotopes is strongly reduced. The presence of nearby electron spins, stemming from nitrogen impurities, can have a significant effect on the electron spin coherence due to the electron's large magnetic moment. A spin bath comprised of several nitrogen atoms generates an additional magnetic field, which is, however, not static and changes in time because of spin flips within the bath. Application of an external magnetic field can counteract this effect. If the Zeeman energy becomes larger than the magnetic coupling between the nitrogen spins, the dynamics within the bath freezes out and fluctuations can be suppressed [180].

Ground-State Spin Hamiltonian

In the absence of a magnetic field, the $m_S = \pm 1$ spin sublevels are split from the $m_S = 0$ sublevel by a zero-field splitting that is present in the ground and the excited state. The physical origin of the zero-field splittings are magnetically-induced spin-spin interactions [see also Eq. (5.37)] among the electrons that are localized to the defect [166, 167]. In the presence of an external magnetic field $\mathbf{B}$, the ground state Hamiltonian of the NV center has the form

$$H_{\mathrm{gs}} = D_{\mathrm{gs}} S_z^2 + \gamma_{\mathrm{e}} \mathbf{B} \cdot \mathbf{S}, \tag{6.1}$$

where $\mathbf{S}$ denotes the NV center spin, and spin-spin interactions are included via the zero-field splitting of $D_{\mathrm{gs}}/2\pi = 2.88$ GHz [25]. A static magnetic field applied along the defect axis, $\mathbf{B} = B\mathbf{e}_z$, further splits the $m_S = 1$ and $m_S = -1$ states by the Zeeman energy $2\gamma_{\mathrm{e}} B$. The electron gyromagnetic ratio is $\gamma_{\mathrm{e}}/2\pi = g_{\mathrm{e}}\mu_{\mathrm{B}}/2\pi = 2.803$ MHz/G, with an isotropic g-factor of the electron spin of $g_{\mathrm{e}} = 2.0029$ and small anisotropies are neglected. At the ground-state level anticrossing (GSLAC), the $m_S = 0$ and $m_S = -1$ states become degenerate, which happens at a magnetic field strength of about 1028 G (Fig. 6.3). At the same time, the $m_S = 1$ state is split off by approximately $2D_{\mathrm{gs}}$, which creates a well-isolated two-level system. Therefore, the two spin sublevels $m_S = 0$

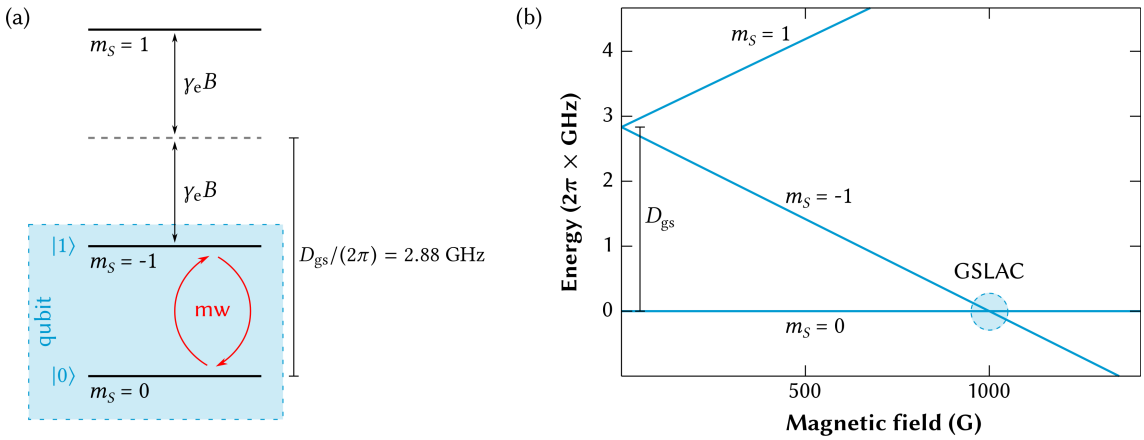

Figure 6.3 – Ground-state fine structure in a magnetic field. (a) Spin sublevels are split by the ground-state zero-field splitting D_{gs} and the Zeeman energy $\gamma_e B$. The $m_S = 0$ and $m_S = -1$ states are typically used to implement the qubit states $|0\rangle$ and $|1\rangle$. Transitions between the qubit states can be driven by microwave (mw) pulses. (b) Magnetic-field dependence of ground-state spin sublevels, originating from Hamiltonian H_{gs} [Eq. (6.1)]. At = 1028 G, the $m_S = 0$ and $m_S = -1$ states are degenerate. As will be discussed below, hyperfine interaction couples the $m_S = 0$ and $m_S = -1$ spin states, leading to a ground-state level anticrossing (GSLAC).

and $m_S = -1$ can serve as the computational basis states $|0\rangle$ and $|1\rangle$. If a magnetic field strength is chosen such that there is an energy difference between the $m_S = 0$ and $m_S = -1$ states, the relative phase between the two qubit states changes over time. This corresponds to a rotation about the z axis on the Bloch sphere [cf. Fig. 3.1]. Usually, the energy splitting is adjusted to be in the microwave regime. An oscillating magnetic field of frequency ω along the x axis, $\mathbf{B}_x(t) = B_x \cos(\omega t)\mathbf{e}_x$, changes the population of these two states via the term $\gamma_e B_x \cos(\omega t) S_x$ in the Hamiltonian H_{gs} [Eq. (6.1)]. If the frequency ω is resonant to the transition frequency between the $m_S = 0$ and $m_S = -1$ levels, the qubit sinusoidally changes between the states $|0\rangle$ and $|1\rangle$. A rotation of the qubit state about the x axis on Bloch sphere can therefore be achieved by the application of microwave pulses.

Excited-State Spin Hamiltonian

The ^{3}E excited state has a more complex fine structure compared to the $^3A_2$ ground state because the orbital doublet is, e.g., more susceptible to strain. Moreover, it shows a pronounced temperature dependence due to phonon-induced orbital averaging [181, 182]. The two quasi-degenerate orbital branches of the ^{3}E excited state are denoted as E_x and E_y. At low temperatures, spin-orbit coupling, spin-spin interaction and local nonaxial strain, however, lift the degeneracy and create a sublevel structure in the excited state [181, 183–185]. In the limit of low-strain, the excited-state spin Hamiltonian is nearly diagonal in the eigenbasis of the spin-orbit Hamiltonian, in which the spin-orbit coupling strength has a magnitude of 5.3 GHz [181, 186]. The eigenstates, thus, have mixed orbital and spin character. In a typical sample, however, impurities in the diamond lattice produce

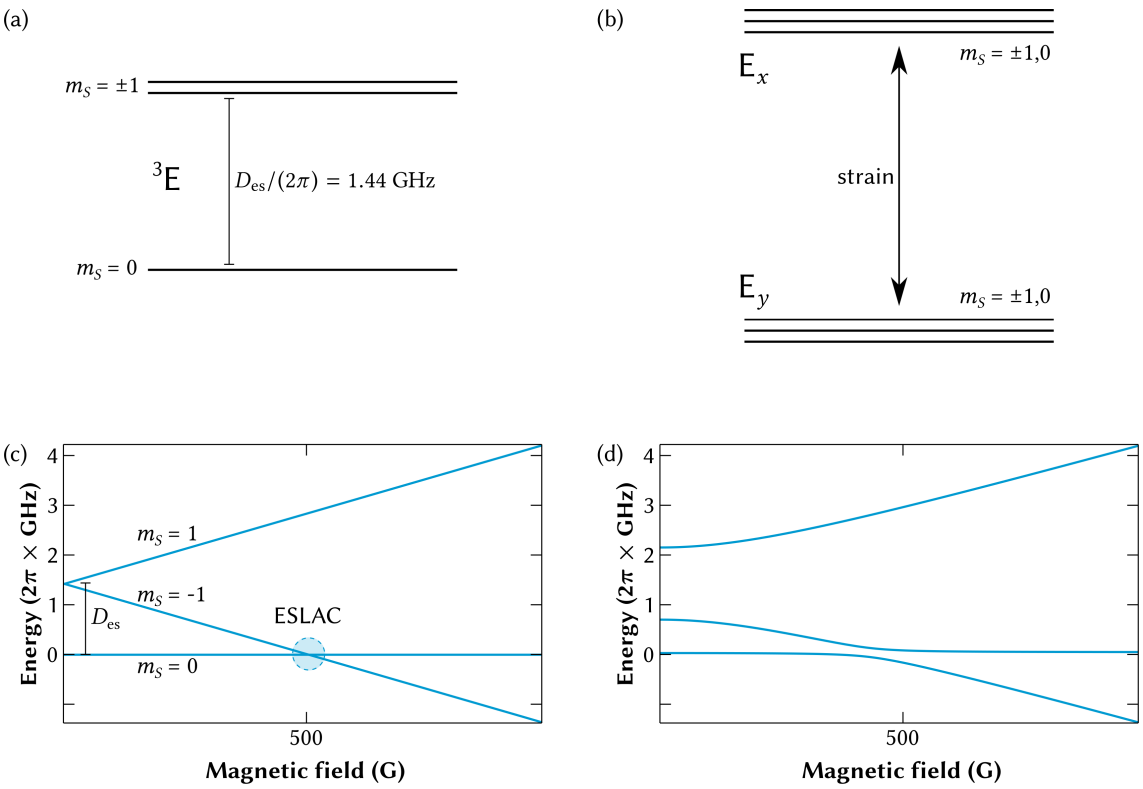

Figure 6.4 – Excited-state level structure at room and low temperature. (a) Room-temperature level spacing of the ^{3}E excited orbital state at zero magnetic field. The $m_S = \pm 1$ spin states are separated from the $m_S = 0$ state by the excited-state zero-field splitting D_{es}. (b) At low temperatures and strain fields larger than 10 GHz, the orbital doublet splits into two branches, E_x and E_y. Both manifolds consist of three spin sublevels with quantum numbers $m_S = \pm 1, 0$. (c) Magnetic-field dependence of the room-temperature spin states. A magnetic field along the defect axis splits the $m_S = \pm 1$ states by the Zeeman energy. The $m_S = 0$ and $m_S = -1$ spin states become degenerate at around 507 G, giving rise to an excited-state level anticrossing (ESLAC) originating from hyperfine interaction. (d) Low-temperature energy dependence of the E_y orbital branch, where spin-spin interaction according to H_{es} [Eq. (6.2)] mixes the spin sublevels.

strain fields of 10 GHz and more [23]. In this case, the E_x and E_y state split into well-separated orbital branches, and each of them consists of three spin sublevels (Fig. 6.4). Spin-orbit coupling, spin-spin interaction and strain fields can induce transitions between the two orbital branches, which are energetically suppressed if the strain fields are large enough, i.e. above 10 GHz. In the following, we restrict our considerations to the limit of large strain and include only one of the two excited-state orbital branches in our description, namely E_y. Spin-spin interaction within the

lower branch is still present and the excited-state spin Hamiltonian H_{es} is given by [25, 166, 186][2]

$$H_{\text{es}} = D_{\text{es}} S_z^2 + \frac{\Delta_1}{2}\left(S_x^2 - S_y^2\right) - \frac{\Delta_2}{\sqrt{2}}\left(S_x S_z + S_z S_x\right) + \gamma_{\text{e}}^{(\text{es})} \mathbf{B} \cdot \mathbf{S}. \tag{6.2}$$

Spin-spin interaction gives rise to a zero-field splitting of $D_{\text{es}}/2\pi = 1.44$ GHz, and to the transversal couplings $\Delta_1/2\pi = 1.54$ GHz and $\Delta_2/2\pi = 0.154$ GHz [186]. The gyromagnetic ratio $\gamma_{\text{e}}^{(\text{es})}$ of the excited state is slightly larger compared to the ground state due to a larger g-factor of $g_{\text{e}}^{(\text{es})} = 2.15$ [186].

Under ambient conditions, the excited state fine structure changes and only a single electron-spin resonance around 1.4 GHz is measured [181, 184, 185] if no external magnetic field is applied (Fig. 6.4). In a magnetic field, three fine structure levels are observed compared to six at low temperature. This effect is ascribed to an orbital averaging due to lattice vibrations that interact with the orbital degree of freedom, but not with the electron spin [182]. The room-temperature Hamiltonian $H_{\text{es}}^{\text{RT}}$ of the excited state has the form [184, 185]

$$H_{\text{es}}^{\text{RT}} = D_{\text{es}} S_z^2 + E_{\text{es}}\left(S_x^2 - S_y^2\right) + \gamma_{\text{e}}^{(\text{es})} \mathbf{B} \cdot \mathbf{S}, \tag{6.3}$$

where the parameter $E_{\text{es}}/2\pi = 70 \pm 30$ MHz has been related to strain. In Sec. 6.4, we develop a mechanism to couple to NV-based qubits that requires very narrow line widths, which is only possible at cryogenic temperatures. Therefore, we choose to work with the low-temperature Hamiltonian given in Eq. (6.2).

6.2.3 Hyperfine Interaction

So far, only the fine structure of the energy levels has been described by considering electronic spin interactions, comprising magnetically-induced spin-spin interactions and the interaction with an external magnetic field $\mathbf{B}$. In this section, we include the hyperfine interaction of the electron spin with the intrinsic nitrogen nuclear spin (Fig. 6.5) that gives rise to additional level splittings, the so-called hyperfine structure. We will not go into the details of hyperfine interactions with randomly occurring proximate ^{13}C nuclear spins since we explicitly want to make use of properties intrinsic to every NV center. Hence, we are able to derive a generic scheme to couple two nuclear spin qubits in diamond that depends less on the local environment of the NV center.

Hyperfine interaction (hf) between an electron spin $\mathbf{S}$ and a nuclear spin $\mathbf{I}$ has the form [187]

$$H_{\text{hf}} = \mathbf{S}^T \cdot \overleftrightarrow{\mathbf{A}} \cdot \mathbf{I}, \tag{6.4}$$

[2] Although Refs. 25 and 166 have been published by the same authors, we found discrepancies in the expressions given for H_{es} (Eq. (3) in [25] and Tab. 3 in [166], respectively). An inconsistency was also found by Bassett *et al.* in Ref. 186 by independently deriving H_{es}. We use the expression given in 25 and 186, which is consistent with measurement results also performed by Bassett *et al.* using time-dependent quantum tomography.

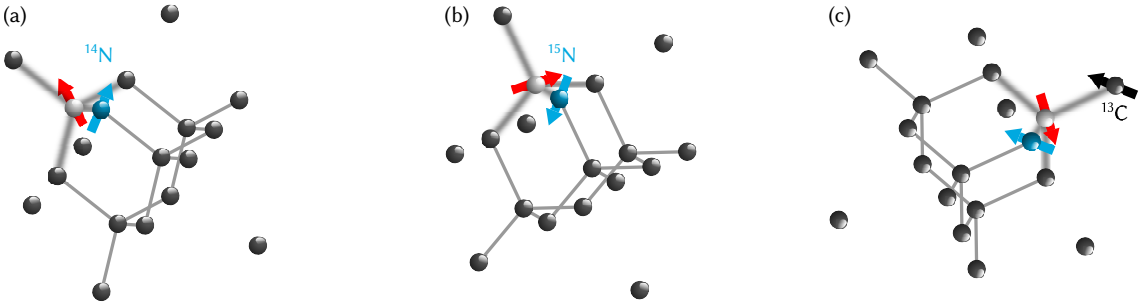

Figure 6.5 – Possible hyperfine interactions. The NV electron spin (red arrow) interacts with the intrinsic nitrogen nuclear spin (blue arrow) that is either (a) $I = 1$ for the ^{14}N isotope or (b) $I = 1/2$ for the ^{15}N isotope. (c) Additional hyperfine interaction can occur if a ^{13}C nuclear spin (black arrow) is located close to the NV center.

where the hyperfine tensor $\overleftrightarrow{\mathbf{A}}$ fully describes the interaction between the two spins including Fermi contact interaction and magnetic dipole-dipole coupling. The Fermi contact interaction is isotropic and present for orbitals that have a nonzero electron density at the position of the nucleus. Anisotropy in the hyperfine tensor comes from the dipole-dipole coupling. For the NV center, the hyperfine tensor describing the interaction with the intrinsic nuclear spin is diagonal and anisotropic [25, 188, 189],

$$\overleftrightarrow{\mathbf{A}} = \begin{pmatrix} A_\perp & 0 & 0 \\ 0 & A_\perp & 0 \\ 0 & 0 & A_\parallel \end{pmatrix}, \tag{6.5}$$

leading to a hyperfine-interaction Hamiltonian of the form

$$H_{\mathrm{hf}} = A_\perp S_x I_x + A_\perp S_y I_y + A_\parallel S_z I_z = \frac{A_\perp}{2}\left(S_+ I_- + S_- I_+\right) + A_\parallel S_z I_z. \tag{6.6}$$

Here, the electron spin raising (+) and lowering (−) operators are defined as $S_\pm = S_x \pm iS_y$, and analogue expressions hold for the nuclear spin. If it is energetically allowed, the terms proportional to $S_+ I_-$ and $S_- I_+$ can induce flip-flop processes between the electron and nuclear spin. The flip-flop terms induce significant effects only when spin states are nearly degenerate, whose magnetic quantum numbers m_S that differ by ±1. This happens at the GSLAC around 1028 G (Fig. 6.3), or at the excited-state level anticrossing around 507 G (ESLAC, Fig. 6.4). *Ab initio* studies of the electronic structure showed that the electron density in the excited state is significantly larger at the position of the nitrogen nucleus compared to the orbital ground state [165]. The hyperfine coupling constants in the excited state are therefore about 20 times larger compared to the coupling constants in ground state for both nitrogen isotopes, ^{14}N and ^{15}N (see Tab. 6.1).

The total ground state Hamiltonian is obtained by adding nuclear-spin dependent interactions

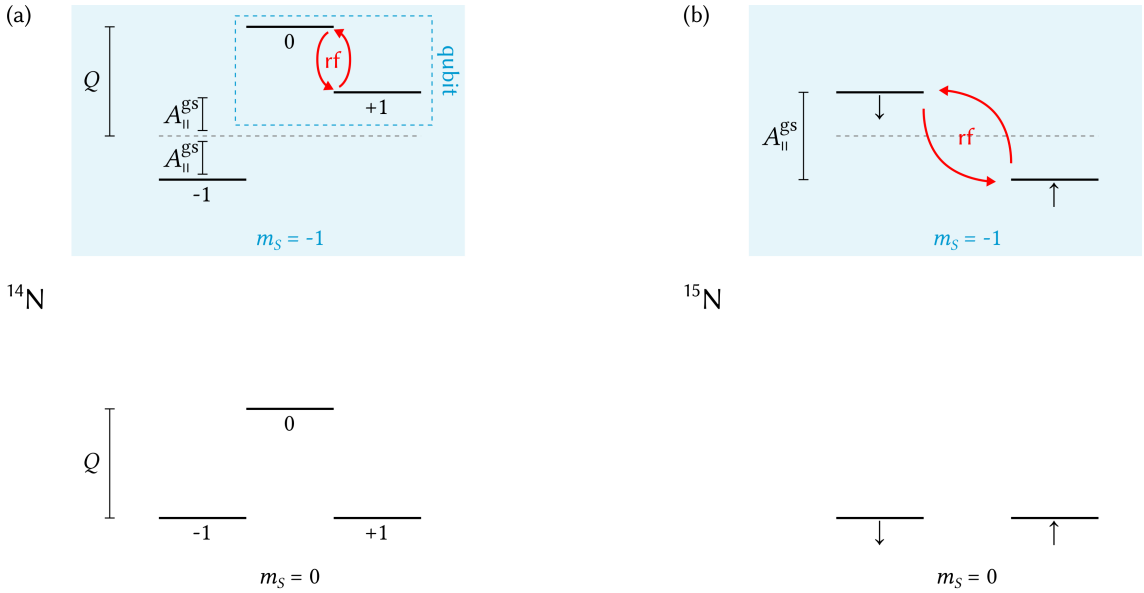

Figure 6.6 – Ground-state hyperfine structure of the NV center. (a) NV hyperfine structure with ^{14}N nuclear spin ($I = 1$) according to H_{gs} [Eq. (6.7)]. Spin manifolds are split into three sublevels with quantum numbers $m_I = \pm 1, 0$. Only the $m_S = 0$ and $m_S = -1$ (blue shaded) are depicted, $m_S = 1$ states are split off by a magnetic field. The nuclear electric quadrupole moment Q splits the hyperfine level with $m_I = 0$ from the $m_I = \pm 1$ levels. For $m_S = -1$, hyperfine interaction further splits the levels with quantum numbers $m_I = -1$ and $m_I = 1$ by $2A_{\parallel}^{\text{gs}}$. Hyperfine levels $|m_S, m_I\rangle = |-1, 0\rangle$ and $|-1, +1\rangle$ will be selected as computational basis $|0\rangle$ and $|1\rangle$. Transitions between the qubit states can be driven by radio frequency (rf) pulses. (b) Analogue to (a) with ^{15}N nuclear spin ($I = 1/2$) exhibiting no electric quadrupole moment. Spin manifolds are split into two sublevels with quantum numbers $m_I = +1/2$ (↑) and $m_I = -1/2$ (↓).

to the Hamiltonian in Eq. (6.1),[3]

$$H_{\text{gs}} = D_{\text{gs}} S_z^2 + \gamma_{\text{e}} \mathbf{B} \cdot \mathbf{S} + \frac{A_{\perp}^{\text{gs}}}{2} (S_+ I_- + S_- I_+) + A_{\parallel}^{\text{gs}} S_z I_z + Q I_z^2 - \gamma_{\text{n}} \mathbf{B} \cdot \mathbf{I}. \tag{6.7}$$

$A_{\parallel}^{\text{gs}}$ and $A_{\perp}^{\text{gs}}$ denote the longitudinal and transversal hyperfine coupling constants, respectively. Nuclear spins with $I > 1/2$ also exhibit an electric quadrupole moment Q, which is on the order of a few MHz. Furthermore, the nuclear spin also couples to the external magnetic field and γ_{n} denotes the nuclear gyromagnetic ratio. For a magnetic field B along the defect axis, the nuclear spin states with different quantum numbers m_I are split by the nuclear Zeeman energy $\gamma_{\text{n}} B$. The hyperfine structure of the ground state originating from Hamiltonian H_{gs} in Eq. (6.7) is depicted in Fig. 6.6. All relevant parameters values for ^{14}N and ^{15}N nuclear spins can be found in Tab. 6.1.

Hyperfine interaction in the NV center excited state has so far been mainly analyzed under ambient conditions [184, 191]. The experimental observations fit well to a room-temperature

[3] In the following, H_{gs} and H_{es} denote the spin Hamiltonians *including* hyperfine interaction.

Table 6.1 – Relevant nuclear-spin parameters for the NV center. (^{15}N nuclear spin does not have an electrical quadrupole moment.)

Parameter	Description	^{14}N	^{15}N
I	Nuclear spin	1	1/2
$\gamma_n/2\pi$	Nuclear gyromagnetic ratio	0.308 kHz/G [190]	−0.432 kHz/G [190]
$A_{\parallel}^{gs}/2\pi$	Longitudinal hf coupling (gs)	−2.2 MHz [150, 151, 188, 191]	3.0 MHz [184, 188]
$A_{\parallel}^{es}/2\pi$	Longitudinal hf coupling (es)	≈ 40 MHz [191]	61 MHz [184]
$A_{\perp}^{gs}/2\pi$	Transversal hf coupling (gs)	−2.7 MHz [188]	3.65 MHz [188]
$A_{\perp}^{es}/2\pi$	Transversal hf coupling (es)	≈ 40 MHz [191]	61 MHz [184]
$Q/2\pi$	Nuclear quadrupole coupling	−5 MHz [150, 188, 191]	–

Hamiltonian that has the same structure as H_{gs} in Eq. (6.7),

$$H_{es}^{RT} = D_{es}S_z^2 + E_{es}\left(S_x^2 - S_y^2\right) + \gamma_e^{(es)}\mathbf{B}\cdot\mathbf{S} + \frac{A_{\perp}^{es}}{2}\left(S_+I_- + S_-I_+\right) + A_{\parallel}^{es}S_zI_z + QI_z^2 - \gamma_n\mathbf{B}\cdot\mathbf{I}, \quad (6.8)$$

with excited-state hyperfine coupling constants $A_{\parallel}^{es}$ and $A_{\perp}^{es}$. The measurements did not show any anisotropy, which was found in *ab initio* calculations for ^{15}N nuclear spins [189]. For low temperature, we model hyperfine interaction in the excited state using a diagonal and anisotropic hyperfine tensor. By adding the nuclear-spin terms to Eq. (6.2), we obtain

$$\begin{aligned} H_{es} = {} & D_{es}S_z^2 + \frac{\Delta_1}{2}\left(S_x^2 - S_y^2\right) - \frac{\Delta_2}{\sqrt{2}}\left(S_xS_z + S_xS_x\right) + \gamma_e^{(es)}\mathbf{B}\cdot\mathbf{S} \\ & + \frac{A_{\perp}^{es}}{2}\left(S_+I_- + S_-I_+\right) + A_{\parallel}^{es}S_zI_z + QI_z^2 - \gamma_n\mathbf{B}\cdot\mathbf{I}. \end{aligned} \quad (6.9)$$

In further discussions, we use the room-temperature values for the hyperfine constants $A_{\parallel}^{es}$ and $A_{\perp}^{es}$. The physical mechanism we exploit in the two-qubit gate scheme derived below only depends on the difference between the ground- and excited-state hyperfine constants; qualitatively, it is therefore rather insensitive to actual parameter values.

6.3 Spin Qubits in Diamond

6.3.1 Electron Spin Qubits

Not only the coherence times have to be long enough for a desired system to be of use in quantum information processing. The ability to initialize, manipulate and readout the state of the qubit with sufficiently high accuracy have to be demonstrated as well (see the criteria on p. 2).

Qubit initialization and readout can be achieved via optical spin polarization [173], which is described in more detail in the Sec. 6.2.2. When the NV center is optically excited resonant to the $m_S = 0$ transition, the fluorescence signal crucially depends on the electron spin state. If the

system is in the $m_S = 0$ state, a finite number of photons will be detected, whereas no signal is expected for $m_S = \pm 1$. Hence, the presence or absence of fluorescence will give information about the electron spin state. First studies of single defect centers have been performed in Ref. 192 and improved experimental work demonstrated projective single-shot readout with an average fidelity of about 93 % [193]. Even better results for spin readout can be achieved by exploiting coherent hyperfine interactions with nearby nuclear spins, as demonstrated using a ^{13}C [194] or a ^{14}N [191] nuclear spin as an ancilla. Initialization of the electron spin to the $m_S = 0$ state was also implemented using optical spin polarization with fidelities above 99 % at cryogenic temperature [193, 195–197].

An external magnetic field $\mathbf{B}$ splits spin states with different quantum numbers m_S by the Zeeman energy according to the Hamiltonian $H = \gamma_e \mathbf{B} \cdot \mathbf{S}$. Coherent rotations of the NV electron spin state about the x axis on the Bloch sphere can be achieved using microwave radiation (see Sec. 6.2.2) [195, 198]. Using this method, the implementation of a spin flip or Pauli-X gate [Eq. (3.3)], also known as a π pulse, could be achieved with a gate time below 1 nanosecond [199] and with gate fidelities reaching 99 % [154]. By a combination of two microwave pulses, a refined version of the Deutsch-Josza quantum algorithm has been experimentally implemented [200]. Rotations about the polar axis have been achieved using various methods, e.g. by utilizing the optical Stark effect with fidelities of 89 % [201]. In a more recent experiment, qubit rotations in the equatorial plane of the Bloch sphere were demonstrated by harnessing the excited state manifold [202]. In a Λ configuration, coherent population trapping [203] can be exploited to all-optically control the electron spin state. If the two transitions in the Λ configuration are excited by lasers with Rabi frequencies Ω_0 and Ω_1, respectively, a ground-state superposition $|D\rangle$ of the form

$$|D\rangle = \frac{1}{\sqrt{\Omega_0^2 + \Omega_1^2}} \left(\Omega_1 |m_S = 0\rangle - \Omega_0 |m_S = +1\rangle\right) \tag{6.10}$$

cannot be further excited by the optical means due to destructive interference between the two transitions [23, 202]. The state $|D\rangle$ is therefore called dark state. If the system decays from the excited state (see Fig. 6.2) into the dark state $|D\rangle$, it will be trapped in this superposition. A proper adjustment of the Rabi frequencies Ω_0 and Ω_1 allows the preparation of any superposition of the $m_S = 0$ and $m_S = +1$ spin states. Initialization of the spin state to arbitrary positions on the Bloch sphere, readout in an arbitrary basis, and single-spin rotations about arbitrary axes could be demonstrated using this technique [202]. Especially the ultrafast implementation of a Pauli-Z gate [Eq. (3.3)] within 160 ps with a fidelity of 77 % [186]. The devices for optical manipulation have smaller dimensions, which makes this scheme very promising for large-scale application. Yet another approach enabled high-fidelity single qubits gates with fidelities around 98 % using holonomic transformations [204], but with slower gate times of 160 ns when compared to the all-optical realization mentioned above.

An open issue in the development of diamond-based quantum information processing is

scalability. As explained in Sec. 3.2, qubits must be coupled to eventually perform universal quantum computation. This means, individual NV centers have to interact with each other in a highly controllable fashion. An ongoing challenge to develop coupling mechanisms between two distant NV center spins, in which the interaction can be arbitrarily turned on and off, and is strong enough to implement quantum gates much faster than the decoherence time. Some of the proposed interaction mechanisms and proof-of-principles experiments are described below.

One of these ideas is to use the of magnetic dipolar coupling between two magnetic moments [see e.g. Eq. (5.37)]. The generation of an entangled state between two electron spins and fidelities of up to 82 % with respect to a maximally entangled state, has been reported for NV centers separated by roughly 10–25 nm and coupled via magnetic dipole-dipole interaction [137, 153, 154]. A drawback of such a scheme is the random distribution of NV centers in naturally occurring diamond or the lack of positioning accuracy for implanted NV centers, although there has been a lot of progress related to nitrogen-ion implantation in diamond (see e.g. Refs. 205 and 206). The locations of the defects have to be close enough to achieve large enough coupling strengths via the dipolar coupling [cf. Eq. (5.37)]. The maximal displacement is set by the decoherence time T_2 and amounts to roughly 30–50 nm [153, 154]. The interaction with proximate nitrogen atoms, that do not form a NV defect, has also been observed [196, 207, 208]. However, there shouldn't be any unwanted and disturbing interactions with other defects or nuclear spins present in the vicinity of the system of coupled NV centers. There is thus a piece of randomness left in this scheme. On the other hand, entanglement purification can be directly achieved with magnetic dipolar coupling as developed in Sec. 5.4.2, which plays a key role in quantum repeater protocols [8, 9, 156, 157].

Besides the aforementioned works addressing single- and two-qubit controllability, groundbreaking results could also be achieved regarding the feasibility for quantum communication. It was pointed out in Ref. 17 that a physical apparatus must have "The ability to interconnect stationary and flying qubits …" and "…faithfully to transmit flying qubits between specified locations …" [cf. criteria (vi.) and (vii.) on p. 2]. A first step towards diamond-based quantum communication networks was the demonstration of entanglement between the NV center electron spin and an optical photon [209]. The NV center is excited to a state that decays with equal probability to one of the ground states with spin projection $m_S = +1$ or $m_S = -1$. This can be achieved for an equal superposition of the spin states, because the optical transition is spin-conserving. Due to the associated orbital angular momentum, the polarization of the emitted photon depends on the spin state to which the system decayed, and is either σ^+ or σ^- circular polarization. Therefore, the NV center and the emitted photon reside in the entangled state [209]

$$|\psi\rangle = \frac{1}{\sqrt{2}}(|\sigma^-\rangle\,|m_S = +1\rangle + |\sigma^+\rangle\,|m_S = -1\rangle), \tag{6.11}$$

where $|\sigma^\pm\rangle$ denote the polarization state of the photon. Since the NV center level structure depends

on parameters like strain, magnetic and electric fields, the energy of the emitted photon varies from defect to defect. However, using dc Stark tuning [210], the emission lines between different NV centers can be brought into resonance, rendering the emitted photons indistinguishable. In doing so, two-photon quantum interference between photons that originate from dissimilar NV centers could be observed [211, 212]. Going one step further, the combination of spin-photon entanglement and two-photon interference offers the possibility for measurement-based long-distance entanglement generation. In a modified experiment [51], two-photon interference on a beam splitter and a subsequent photon measurement projected the spin qubits onto the maximally entangled states $|\Psi^{\pm}\rangle$ [Eq. (2.13)], where the sign depends on the specific measurement outcome. The fidelity of the experimentally realized entangled state was around 70 %, and even more impressing, the two entangled NV centers were separated by 3 m [51]. The quantum teleportation protocol, described in Sec. 3.4, was implemented in a follow-up experiment [52]. An entangled electron-spin state between distant NV centers was used to unconditionally teleport an arbitrary state of a ^{14}N nuclear spin of one NV center onto the electron spin of another NV center, again separated by 3 m. Thus, the demonstration of spin-photon entanglement, the heralded entanglement generation between electron spins, and the teleportation of a qubit state make the NV center a highly promising candidate for the realization stationary qubits in quantum communication networks.

The electronic NV spin has also been part of several quantum register architectures that contain one [197, 213] or more nuclear spin qubits [47, 154, 155, 214]. Harnessing hyperfine interaction, the electron spin is thereby either utilized to initialize, manipulate and readout the nuclear spin qubits as an ancilla spin, or is part of the quantum register itself. Furthermore, the NV spin was used as ancilla to generate nuclear spin entanglement (see Sec. 6.3.2).

6.3.2 Nuclear Spin Qubits

Nuclear spins surrounding the NV center need to act not only as a source of decoherence. As already mentioned in Sec. 6.3.1, hyperfine interaction with nuclear spins can, e.g., increase the spin-readout fidelity [191, 194]. Another possibility is to directly utilize the nuclear spin as qubit and define the computational basis as nuclear spin eigenstates. Since nuclear spins weakly interact with their environment, coherence times can reach one second at room temperature [149]. These remarkable coherence properties have strongly motivated the idea to use nuclear spins as high-fidelity quantum memory [39], e.g. in quantum repeaters [156, 157].

Two types of nuclear spins influence the NV center in the diamond crystal, see Fig. 6.5. First, there is a 1.1 % abundance of ^{13}C isotopes naturally occurring in diamond, which have nuclear spin $I = 1/2$. However, their appearance in the lattice is random. If a ^{13}C spin is located in close vicinity to the NV center, hyperfine interaction can be strong enough (about 100 MHz) to achieve coherent coupling to the electron spin. The second type originates from the nitrogen atom that is by definition intrinsic to every NV center. It usually occurs as ^{14}N isotope with nuclear spin $I = 1$,

or as ^{15}N for implanted samples having nuclear spin $I = 1/2$.

In the following, we describe the progress made towards nuclear-spin based quantum information processing in diamond for both types of nuclear spin qubits, which strongly motivates our work on long-distance nuclear spin coupling.

Intrinsic Nitrogen Nuclear Spin Qubits

The electron spin of a NV center is coherently coupled to at least one nuclear spin, which belongs to the intrinsic nitrogen atom forming the defect itself. The small gyromagnetic ratio of the nitrogen nuclear spin makes it less susceptible to its magnetic environment. Hence, nitrogen nuclear spins exhibit decoherence times T_2 up to 1.3 ms at room temperature [49], which suggests to use the nuclear spin itself as qubit, especially to store quantum information. Whereas the ^{15}N isotope has nuclear spin $I = 1/2$ and naturally forms a qubit, in the case of the ^{14}N isotope ($I = 1$), two of the three nuclear spin sublevels are chosen as computational basis. The nuclear spin levels are split by the hyperfine interaction with the electron spin, and for the ^{14}N nucleus as well by the nuclear quadrupole coupling as depicted in Fig. 6.6 (a). The longitudinal and transversal hyperfine-coupling constants in the ground state are on the order of a few MHz for both nitrogen isotopes. In the excited state, the interaction strength is approximately 20 times larger compared to the ground states because the electron density is substantially larger close to the lattice site of the nitrogen nucleus [165]. The literature values determined by experiments can be found in Tab. 6.1.

Coherent control of a nuclear spin can be achieved by radio frequency (rf) pulses [150, 191]. Rabi frequencies of 25–30 kHz make the direct implementation of nuclear-spin rotations in such a fashion rather slow and a π rotation takes about 30–40 μs [150, 151]. However, exploiting electron spin dynamics during a strong off-resonant microwave driving pulse, a fast phase gate of the form

$$U = \begin{pmatrix} 1 & 0 \\ 0 & e^{i\Delta\phi} \end{pmatrix} \tag{6.12}$$

can be implemented, where the phase $\Delta\phi = A_{\parallel}^{\mathrm{gs}} t/2$ depends on the longitudinal hyperfine coupling $A_{\parallel}^{\mathrm{gs}}$ and the pulse duration t [151]. In doing so, the implementation of a Pauli-Z gate takes approximately 500 ns.

Because of the small magnetic moment of atomic nuclei, it is difficult to measure the nuclear spin state directly. For this purpose, the interaction with the electron spin can be exploited once more. At the ESLAC, the method of optical spin polarization can also be utilized to initialize the nuclear-spin state. The $m_S = 0$ and $m_S = -1$ nuclear-spin states become degenerate near the ESLAC and hyperfine-induced electron-nuclear-spin flip-flop processes start to become effective. These processes can be harnessed to initialize the nuclear spin state, which we first describe for the ^{14}N nuclear spin. Before nuclear spin initialization, the electron spin can be polarized to the

$m_S = 0$ state by optical spin polarization (see Sec. 6.3.1), independent of the nuclear spin state. Subsequent optical pumping to the excited state is a nuclear-spin-conserving process. Hyperfine interaction in the excited state can cause transitions between nearly-degenerate states, i.e. between the states $|0, 0\rangle$ and $|-1, +1\rangle$, and between the states $|0, -1\rangle$ and $|-1, 0\rangle$.[4] The state $|0, +1\rangle$ will not be affected by this scheme since the excited states with quantum number $m_S = 1$ are more than 1 GHz in energy away from the ESLAC, which is several orders of magnitude larger than the transversal hyperfine coupling. Flipping the electron spin from $|m_S = 0\rangle$ to $|m_S = -1\rangle$ opens a decay channel via the ISC that ends in the $m_S = 0$ ground state, bringing the system into either $|0, +1\rangle$ or $|0, 0\rangle$, respectively. Additional optical pumping cycles will further increase the fraction of state $|0, +1\rangle$ and eventually polarize the ^{14}N nuclear spin to the state $|m_I = +1\rangle$. The first experimental implementations of the described procedure have been reported in Refs. 150 and 191. In a different approach [152, 193], the ^{14}N nuclear spin was initialized by application of a CNOT gate between electron and nuclear spin, followed by an optical electron-spin measurement that also determines the nuclear spin. This method can also be used to measure the nuclear-spin state in a single shot with readout fidelities reaching 92 % [152].

Compared to the two-step process required for the initialization of a ^{14}N nuclear spin, one optical pumping cycle is sufficient to increase the fraction of the state $|0, +1/2\rangle$ in the case of a ^{15}N nuclear-spin qubit [215]. Hyperfine-induced transitions from of this state are energetically suppressed, whereas the state $|0, -1/2\rangle$ couples to the state $|-1, +1/2\rangle$. This transition creates some probability for the system to relax through the ISC to the ground state $|0, +1/2\rangle$, which gradually polarizes the ^{15}N nuclear spin to $|m_I = +1/2\rangle$ by repeated optical pumping.

That the ^{14}N nuclear spin is an excellent candidate to serve as quantum memory has been demonstrated in Ref. 49. Using Landau-Zener transitions through the GSLAC, the eigenstates of all Pauli matrices could be mapped from the electron spin to the nuclear spin within 120 ns using magnetic field sweeps, thereby achieving an average storage fidelity of 88 %. The ability to store the electron spin state coherently in the intrinsic nitrogen nuclear spin offers the possibility to realize a quantum memory that comes along with every NV center. The coupled entity of electron and ^{14}N nuclear spin forms a small quantum register containing two qubits. Such a register could be initialized, coherently manipulated, and read out afterwards in a single experiment [193], and it was possible to implement Grover's search algorithm [213].

There has also been previous work that is closely related to the topic of this chapter, i.e. the coupling of distant nuclear spin qubits. This is a necessary requirement for a scalable quantum computer or a large-scale quantum communication network where distant network nodes have to be entangled. We described above that it is possible to swap the electron-spin state onto the nuclear spin. One possibility to entangle two nuclear spins is thus to swap an entangled state of two electron spins onto the two intrinsic nuclear spins intrinsic. The electron spins must be

[4] For the sake of clarity, we use the notation $|m_S, m_I\rangle$ to denote the NV center hyperfine levels in this section, since the electron spin and the nuclear spin have to be considered.

entangled beforehand, e.g. by magnetic dipole-dipole interaction or by two-photon interference on a beam splitter (see Sec. 6.3.1). Two ^{15}N nuclear spins, separated by 25 nm, could be entangled exploiting the dipole interaction between two electron spins, with a transfer efficiency of almost 90 % [153, 154]. The entanglement of the electron spins could be stored in such a way for over 1 ms. However, the disadvantage of dipole-induced entanglement generation is still the limitation on the maximal distance between the NV centers, which inhibits scalability.

Proximal Carbon Nuclear Spin Qubits

Whereas most of the ^{13}C isotopes in the diamond lattice serve as a nuclear spin bath and lead to the decoherence of the electron spin, proximate ^{13}C nuclei in the first and second coordination cell around the defect coherently interact with the NV spin [178]. In this way, it is rather the electron spin that serves as an ancilla system to initialize, manipulate, and readout the spin state of the ^{13}C nuclear spin. The relaxation time T_1 of the ^{13}C nuclear spin state is about 2 s, and the decoherence time could be increased to above 1 s at room temperature using a specific technique to decouple the nuclear spin from its environment [149, 216]. The nuclear spin levels are mostly split by the hyperfine interaction with the NV electron spin comparable to the case of a ^{15}N nuclear spin that is depicted in Fig. 6.6 (b). The interaction strength, and therefore the splitting, depends on the distance between the NV center and the ^{13}C nucleus, and is typically on the order of 10–150 MHz [150, 194, 217]. Hence, direct driving of nuclear spin transitions can also be achieved using rf pulses. The speed of nuclear-spin Rabi oscillations is limited by the nuclear-spin Rabi frequency of about 100 kHz and a π rotation takes several microseconds [150, 194, 217]. High-fidelity initialization and single-shot readout of the ^{13}C nuclear spin state can be achieved in the same fashion as for the nitrogen nucleus, i.e. by optical pumping at the ESLAC [215] or by applying a CNOT gate between NV spin and nuclear spin [149, 216].

The system comprised of a NV center and proximal ^{13}C nuclear spins naturally forms a small quantum register containing two or more qubits [47, 155, 193, 194, 197]. In such a register, it is possible to map an arbitrary electron-spin state to the ^{13}C the nuclear spin that acts as quantum memory, by selectively driving electron spin transitions conditioned on the nuclear spin state [197]. Exploiting the long nuclear-spin coherence time, the electron spin can be stored for several microseconds and retrieved afterwards. Furthermore, it is also possible to initialize the coupled electron-nuclear-spin system to a specific quantum state. Subsequent frequency-selective rf pulses can entangle two ^{13}C nuclear spins and generate all four Bell states $|\Phi^{\pm}\rangle$ and $|\Psi^{\pm}\rangle$ [Eqs. (2.12) and (2.13)] [47]. In addition, multipartite entanglement between two ^{13}C nuclear spins and an electron spin was reported n Refs. 194 and 47. In a hybrid quantum register, in which additionally to the two ^{13}C nuclear spins the intrinsic ^{14}N nuclear spin was used as qubit, high-fidelity initialization of the whole register with fidelities of 99 % and single-shot readout of a ^{13}C nuclear spin with 99.6 % fidelity were achieved [214]. Together with high-fidelity quantum gates, such high accuracies come close to the threshold values required for fault-tolerant quantum computation [3]. Finally, it

is also worth mentioning that it was a hybrid ^{14}N–^{13}C system, in which the first experimental violation of Bell's inequality with solid-state spins was demonstrated [50]. Besides the strong coupling to nearby ^{13}C nuclear spins, even the detection and manipulation of weakly coupled (20–80 kHz) nuclei from the spin bath has been achieved, thereby increasing the number of qubits in a local register to six nuclear spins [218].

6.4 Controlled Quantum Gate between Nuclear Spins

In this section, we give a detailed description of a method to effectively couple two distant nuclear spin qubits. We use the method of quasi-degenerate perturbation theory in terms of Schrieffer-Wolff transformations to derive an effective interaction between two nitrogen nuclear spins. Supplemental information about Schrieffer-Wolff transformations can be found in Appendix C.

6.4.1 Model

The model considered here consists of two distinct NV centers that are both coupled to the same mode of an optical cavity. In the end, the goal is couple both NV centers due to their mutual interaction with the quantized cavity field. However, it is more instructive to start by describing the coupling of a single NV center to an optical cavity. After developing the formalism to describe this system, it will be straightforward to add the second NV center and afterwards derive an effective interaction between them. A single NV center is described by the ground and excited state Hamiltonians H_{gs} [Eq. (6.7)] and H_{es} [Eq. (6.9)],

$$H_{\mathrm{gs}} = D_{\mathrm{gs}} S_z^2 + \gamma_{\mathrm{e}} \mathbf{B}\cdot\mathbf{S} + \frac{A_{\perp}^{\mathrm{gs}}}{2}\left(S_+ I_- + S_- I_+\right) + A_{\parallel}^{\mathrm{gs}} S_z I_z + Q I_z^2 - \gamma_{\mathrm{n}} \mathbf{B}\cdot\mathbf{I}, \tag{6.13}$$

$$\begin{aligned} H_{\mathrm{es}} = {} & D_{\mathrm{es}} S_z^2 + \frac{\Delta_1}{2}\left(S_x^2 - S_y^2\right) - \frac{\Delta_2}{\sqrt{2}}\left(S_x S_z + S_z S_x\right) + \gamma_{\mathrm{e}} \mathbf{B}\cdot\mathbf{S} \\ & + \frac{A_{\perp}^{\mathrm{es}}}{2}\left(S_+ I_- + S_- I_+\right) + A_{\parallel}^{\mathrm{es}} S_z I_z + Q I_z^2 - \gamma_{\mathrm{n}} \mathbf{B}\cdot\mathbf{I}, \end{aligned} \tag{6.14}$$

where we used the same electron gyromagnetic ratio for both orbitals. To use a single Hamiltonian for the NV center, we introduce Pauli matrices τ_i $(i = x, y, z)$ that operate on the orbital degree of freedom, i.e.

$$\tau_z \left|\mathrm{es}\right\rangle = \left|\mathrm{es}\right\rangle, \tag{6.15}$$

$$\tau_z \left|\mathrm{gs}\right\rangle = -\left|\mathrm{gs}\right\rangle, \tag{6.16}$$

and $\left|\mathrm{gs}\right\rangle$ ($\left|\mathrm{es}\right\rangle$) denotes the electronic orbital ground (excited) state. The resulting Hamiltonian of a single NV center is given by

$$H_{\mathrm{NV}} = \frac{1}{2}(1-\tau_z) H_{\mathrm{gs}} + \frac{1}{2}(1+\tau_z)\left(H_{\mathrm{es}} + E_{\mathrm{g}}\right) = H_{\mathrm{e}} + H_{\mathrm{n}} + H_{\mathrm{hf}} + \frac{1}{2} E_{\mathrm{g}}. \tag{6.17}$$

Here, $E_g = 1.945$ eV denotes the transition energy between the $^3A_2$ ground and ^3E excited state (see Fig. 6.2). For later purposes, we subdivide the Hamiltonian H_{NV} into an electronic part (e), a nuclear-spin dependent part (n), and a hyperfine-interaction part (hf) according to

$$H_e = \gamma_e B S_z + D S_z^2 - \frac{1}{2}\Delta\tau_z S_z^2 + \frac{1}{2}E_g\tau_z + \frac{1}{2}(1+\tau_z)\left(\frac{\Delta_1}{2}\left(S_x^2 - S_y^2\right) - \frac{\Delta_2}{\sqrt{2}}\left(S_x S_z + S_z S_x\right)\right), \tag{6.18}$$

$$H_n = -\gamma_n B I_z + Q I_z^2, \tag{6.19}$$

$$H_{hf} = D_{hf} S_z I_z + \frac{1}{2}\Delta_{hf}\tau_z S_z I_z, \tag{6.20}$$

with the following abbreviations

$$D = \frac{D_{gs} + D_{es}}{2}, \qquad \Delta = D_{gs} - D_{es}, \tag{6.21}$$

$$D_{hf} = \frac{A_\parallel^{gs} + A_\parallel^{es}}{2}, \qquad \Delta_{hf} = A_\parallel^{es} - A_\parallel^{gs}. \tag{6.22}$$

In deriving Eqs. (6.18) – (6.20) we assumed that the field direction is parallel to the defect axis, i.e. $\mathbf{B} = B\mathbf{e}_z$, and the field strength is sufficiently far away from the GSLAC and ESLAC such that the energy splitting of the electron-spin states is much larger than the transversal components of the hyperfine tensors, i.e. $A_\perp^{gs}$ and $A_\perp^{es}$. In this case, flip-flop processes between the electron and nuclear spin are energetically suppressed and we therefore neglect the flip-flop terms $S_+I_- + S_-I_+$ in the hyperfine interaction (secular approximation). The eigenstates of the Hamiltonian H_{es} including the transversal hyperfine coupling are plotted in Fig. 6.7 For magnetic fields in the range of $90 < B < 120$ G, the eigenstates have well defined quantum number m_I, which justifies the secular approximation.

We now describe the coupling of a single NV center to an optical cavity. The physical situation is depicted in Fig. 6.8. The quantized cavity field is described by bosonic operators a and $a^\dagger$ that annihilate or create a cavity photon of frequency ω_c, respectively. The NV center in the excited state can emit a photon into the cavity mode when it relaxes to the ground state, and vice versa. Such an interaction of a single bosonic mode with a two-level system is well described by the *Jaynes-Cummings Hamiltonian* [89],

$$H_c = \omega_c a^\dagger a + g\left(\tau_+ a + \tau_- a^\dagger\right). \tag{6.23}$$

In the interaction part of the Hamiltonian H_c, the operators $\tau_\pm = (\tau_x \pm i\tau_y)/2$ create transitions between the orbital states, i.e. $\tau_+ |gs\rangle = |es\rangle$ and $\tau_- |es\rangle = |gs\rangle$, and the coupling strength g is assumed to be real. The rotating-wave approximation in the Hamiltonian H_c is valid since the coupling strengths are far below the transition energy of almost 2 eV. The interaction of NV centers with optical cavities was demonstrated experimentally using whispering gallery mode cavities [219] or photonic crystal cavities [220], reaching coupling strengths of about 50 MHz.

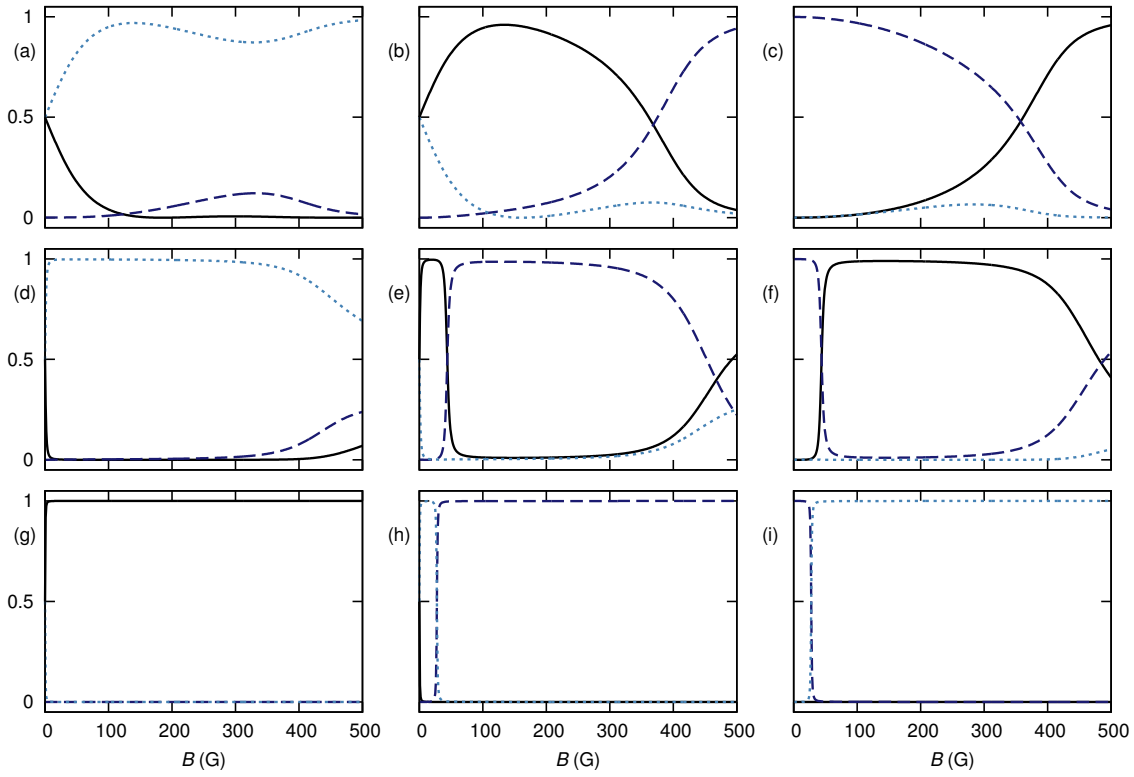

Figure 6.7 – Eigenstates of excited state Hamiltonian. Projection $|\langle\psi_{\text{es}}|m_I\rangle|^2$ of eigenstates $|\psi_{\text{es}}\rangle$ of H_{es} [Eq. (6.14)] in energetically decreasing order from (a) to (i) for $m_I = +1$ (solid), $m_I = 0$ (dashed), and $m_I = -1$ (dotted), as function of the magnetic field B. (a) – (c) correspond to hyperfine levels of the $m_S = +1$ state, (d) – (f) correspond to the hyperfine levels of $m_S = -1$ that are utilized for the proposed gate scheme below, and (g) – (i) analog for $m_S = 0$. For $90 < B < 120$ G, the eigenstates are approximate nuclear-spin eigenstates with well defined quantum number m_I.

In addition to the optical cavity, we assume an external laser field is applied to the NV center (see Fig. 6.8) that can also drive transitions between the ground and the excited state. The laser is modeled by a classical radiation field of frequency ω_{L} and the interaction with a two-level system can be described by a time-dependent Hamiltonian [89],

$$H_{\text{L}}(t) = \Omega e^{-i\omega_{\text{L}}t}\tau_+ + \Omega^* e^{i\omega_{\text{L}}t}\tau_-. \tag{6.24}$$

The complex Rabi frequency Ω depends on the intensity and phase of the laser field. The laser provides a controllable entity in our model that can trigger an effective interaction of two NV centers, as shown below.

The total Hamiltonian $H_1(t)$ that describes the situation depicted in Fig. 6.8 comprises the NV center, the cavity and the laser field, is thus given by

$$H_1(t) = H_{\text{NV}} + H_{\text{c}} + H_{\text{L}}(t). \tag{6.25}$$

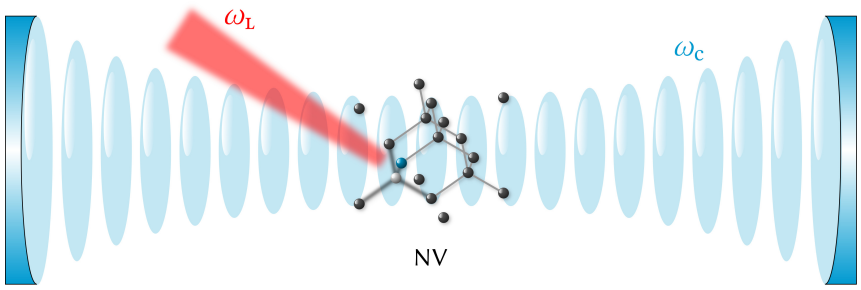

Figure 6.8 – NV center coupled to an optical cavity. A single NV center, placed inside an optical cavity, is coupled to a cavity mode of frequency ω_c. The cavity field is schematically depicted in blue. The NV center orbital transition is off-resonantly driven by an external laser of frequency ω_L.

A transformation into a frame rotating with the frequency of the laser field makes the Hamiltonian $H_1(t)$ time-independent. The technical details of the transformation can be found in Appendix D. We apply the transformation

$$H_1' = e^{i\xi_1 t} H_1(t) e^{-i\xi_1 t} - \xi_1, \tag{6.26}$$

and choose $\xi_1 = \omega_L(a^\dagger a + \tau_z/2)$. After the transformation, the time-independent Hamiltonian H_1' has an analogue structure as the original Hamiltonian $H_1(t)$ [Eq. 6.25] and can be written as[5]

$$H_1' = H_e' + H_n + H_{hf} + H_c' + H_L', \tag{6.27}$$

where the interaction with the external laser field is now given by the time-independent Hamiltonian

$$H_L' = \Omega\tau_+ + \Omega^*\tau_-. \tag{6.28}$$

The transformation into the rotating frame also changes the electronic Hamiltonian [Eq. (6.18)] to

$$H_e' = \gamma_e B S_z + D S_z^2 - \frac{1}{2}\Delta\tau_z S_z^2 + \frac{1}{2}\delta\tau_z + \frac{1}{2}(1+\tau_z)\left(\frac{\Delta_1}{2}\left(S_x^2 - S_y^2\right) - \frac{\Delta_2}{\sqrt{2}}\left(S_x S_z + S_z S_x\right)\right), \tag{6.29}$$

where the transition energy E_g is shifted by ω_L to the detuning $\delta = E_g - \omega_L$. In the Hamiltonian H_c [Eq. (6.23)], the transformation causes a shift of the cavity frequency ω_c to $\delta_c = \omega_c - \omega_L$, which is the detuning of the laser frequency from the cavity mode,

$$H_c' = \delta_c a^\dagger a + g\left(\tau_+ a + \tau_- a^\dagger\right). \tag{6.30}$$

6.4.2 Nuclear-Spin Dependent Photon Scattering

Excluding the NV center, the external laser field and the optical cavity are independent objects that do not interact with each other. However, the situation significantly changes if an absorber that interacts with both fields is located inside the cavity. One can imagine, e.g., a scenario in which

[5] The constant term $E_g/2$ in Eq. (6.17) will be omitted from now on.

a photon from the laser field[6] is absorbed by the NV center, which is thereby excited from the ground to the excited state described by the Hamiltonian H'_{L} [Eq. (6.28)]. Due to the coupling to the cavity via H'_{c} [Eq. (6.30)], the NV center itself can now emit a photon into the cavity mode. This two-step process can also be seen as scattering of a laser photon into the cavity mode, however mediated by an intermediate excitation of the NV center. As we demonstrate below, the rate of such scattering process depends on the nitrogen nuclear-spin state.

We assume the laser frequency to be sufficiently detuned from any optical transition such that the NV center is only excited virtually. Any real population of the excited state offers the possibility of spontaneous decay, making the whole process incoherent. For the case of only virtual excitation, one can use the technique of quasi-degenerate perturbation theory in the framework of Schrieffer-Wolff (SW) transformations [221, 222] to effectively decouple the low- and high-energy subspaces of the Hamiltonian H'_1 in Eq. (6.27). Here, the high-energy subspace is the orbital excited-state manifold. The effects of the coupling between the two subspaces is incorporated in the structure of the transformed states. The Hamiltonian H'_1 can be separated into a block-diagonal part $H_1^{(0)}$ that only acts within the low- and high-energy subspace, respectively,

$$H_1^{(0)} = H'_{\mathrm{e}} + H_{\mathrm{n}} + H_{\mathrm{hf}} + \delta_{\mathrm{c}} a^\dagger a, \tag{6.31}$$

and an off-diagonal part V_1 that connects the two subspaces of the total Hilbert space,

$$V_1 = \Omega\tau_+ + \Omega^*\tau_- + g\left(\tau_+ a + \tau_- a^\dagger\right), \tag{6.32}$$

i.e. $H'_1 = H_1^{(0)} + V_1$. For the SW transformation, we construct an anti-Hermitian operator S_1 that is defined by the condition $[S_1, H_1^{(0)}] = V_1$, and apply the unitary transformation of the Hamiltonian H'_1 according to

$$\widetilde{H}_1 = e^{-S_1} H'_1 e^{S_1} \approx H_1^{(0)} + \frac{1}{2}\left[V_1, S_1\right], \tag{6.33}$$

keeping only the lowest-order contribution of the off-diagonal interaction part V_1 (see Appendix C). The approximation made here is justified if the off-diagonal elements are small compared to the energy gap between the low- and high-energy subspace. The transformed Hamiltonian $\widetilde{H}_1$ is block-diagonal and only acts within the low- and high-energy subspace, respectively.

For the time being, we neglect the contributions proportional to the transversal spin-spin couplings Δ_1 and Δ_2 in Eq. (6.29). The physics behind the scattering process can be more illustratively depicted in this case and do not change qualitatively. Furthermore, one can write down the SW transformation explicitly. To eventually obtain quantitative results, the spin-spin contributions will be included again. The anti-Hermitian operator S_1, that is determined by the

[6] Although we describe the laser as a classical radiation field, we use the term *photon* in the context of NV center optical excitation.

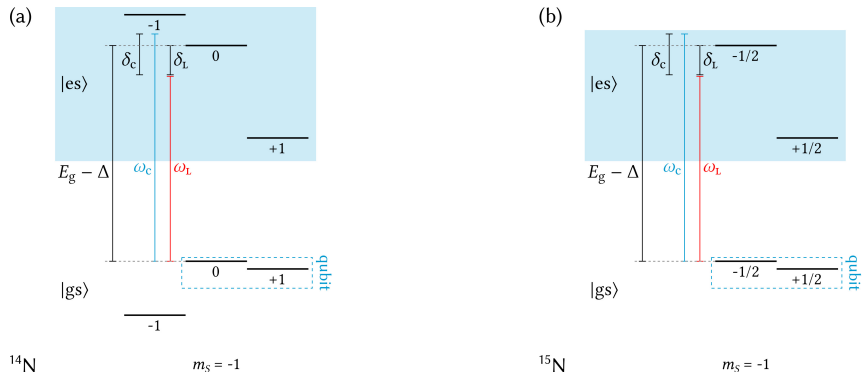

Figure 6.9 – NV center energy level diagram with involved frequencies. (a) Hyperfine levels of the $m_S = -1$ manifolds in the ground ($|\mathrm{gs}\rangle$) and excited ($|\mathrm{es}\rangle$) state (blue shading) for a ^{14}N nuclear spin. The energy difference between the $m_I = 0$ states is $E_g - \Delta$. The laser of frequency ω_L is detuned from the $m_I = 0$ optical transition by δ_L. The difference between the cavity and the laser frequency is δ_c. Also indicated are the computational basis states $|0\rangle = |m_S = -1, m_I = 0\rangle$ and $|1\rangle = |m_S = -1, m_I = +1\rangle$ in the ground state. (b) Equivalent level diagram for a ^{15}N nuclear spin. Computational basis chosen as $|0\rangle = |m_S = -1, m_I = -1/2\rangle$ and $|1\rangle = |m_S = -1, m_I = +1/2\rangle$.

condition $[S_1, H_1^{(0)}] = V_1$, is calculated to be

$$S_1 = \left[\Omega \left(\Delta S_z^2 - \Delta_{\mathrm{hf}} S_z I_z - \delta\right)^{-1} \tau_+ + g \left(\Delta S_z^2 - \Delta_{\mathrm{hf}} S_z I_z + \delta_c - \delta\right)^{-1} \tau_+ a\right] - \mathrm{h.c.} \tag{6.34}$$

At this point, we can fully decouple the orbital ground and excited state by calculating $\widetilde{H}_1$ in Eq. (6.33). We are only interested in the low-energy dynamics of the system and therefore restrict our considerations to the respective subspace of the total Hilbert space. The dimension of the Hilbert space is further reduced by taking only the $m_S = -1$ subspace into account and neglecting the spin states with $m_S = 0$ and $m_S = +1$. This restriction is justified since a magnetic field is chosen that separates the spin states with different quantum number m_S well in energy. In doing so, we can replace the spin operator S_z by its eigenvalue $m_S = -1$ in the following. The effective low-energy part of $\widetilde{H}_1$ acting on the orbital ground state with $m_S = -1$ is given by

$$\begin{aligned} \widetilde{H}_1^{(\mathrm{gs})} &= -\left(A_{\parallel}^{\mathrm{gs}} + \gamma_n B\right) I_z + Q I_z^2 + \delta_c a^\dagger a \\ &\quad + \frac{1}{2}\left(g\Omega \left((\Delta_{\mathrm{hf}} I_z - \delta_L)^{-1} + (\Delta_{\mathrm{hf}} I_z + \delta_c - \delta_L)^{-1}\right) a^\dagger + \mathrm{h.c.}\right), \end{aligned} \tag{6.35}$$

where we define the laser detuning $\delta_L = \delta - \Delta$ from the $m_I = 0$ orbital transition. An overview about the involved energies is shown in Fig. 6.9. In Eq. (6.35) we omit all constant terms and neglect small energy shifts proportional to g^2 (Lamb shift) and $|\Omega|^2$ (Stark shift).

On the basis of previous experimental work [49, 50, 151], in which the nitrogen nuclear spin

has been utilized as qubit, we choose the computational basis as

$$|0\rangle = |m_S = -1, m_I = 0\rangle, \tag{6.36}$$

$$|1\rangle = |m_S = -1, m_I = +1\rangle, \tag{6.37}$$

and neglect the $m_I = -1$ state from now on. We can use the spectral representation $I_z = |1\rangle\langle 1|$ and the completeness relation $\mathbb{1} = |1\rangle\langle 1| + |0\rangle\langle 0|$, and perform the inversion in Eq. (6.35) to obtain

$$\begin{aligned}\widetilde{H}_1^{(\mathrm{gs})} = \left(Q - A_{\parallel}^{\mathrm{gs}} + \gamma_{\mathrm{n}} B\right)|1\rangle\langle 1| + \delta_{\mathrm{c}} a^\dagger a - \frac{1}{2}\left(g\Omega\left(\frac{1}{\delta_{\mathrm{L}} - \Delta_{\mathrm{hf}}} + \frac{1}{\delta_{\mathrm{L}} - \Delta_{\mathrm{hf}} - \delta_{\mathrm{c}}}\right)|1\rangle\langle 1| a^\dagger + \mathrm{h.c.}\right) \\ - \frac{1}{2}\left(g\Omega\left(\frac{1}{\delta_{\mathrm{L}}} + \frac{1}{\delta_{\mathrm{L}} - \delta_{\mathrm{c}}}\right)|0\rangle\langle 0| a^\dagger + \mathrm{h.c.}\right).\end{aligned} \tag{6.38}$$

In this form, we see that the cavity excitation and disexcitation crucially depends on the laser detuning δ_{L} and the nuclear-spin state of the nitrogen atom. The scattering into and out of the cavity can especially be completely suppressed for one of the two nuclear-spin states, e.g., if the laser frequency is chosen such that $\delta_{\mathrm{L}} = \delta_{\mathrm{c}}/2$. In this case, a laser photon can only be scattered if the nitrogen nuclear spin is in state $m_I = +1$, i.e. in the qubit state $|1\rangle$. The effective Hamiltonian describing this situation, also referred to as $m_I = +1$-scattering, is

$$\widetilde{H}_1^{(\mathrm{gs})} = \left(Q - A_{\parallel}^{\mathrm{gs}} + \gamma_{\mathrm{n}} B\right)|1\rangle\langle 1| + \delta_{\mathrm{c}} a^\dagger a + g'|1\rangle\langle 1| a^\dagger + (g')^*|1\rangle\langle 1| a. \tag{6.39}$$

For the process that a photon is scattered into the cavity or vice versa, we thus obtain an effective coupling strength

$$g' = g\Omega \frac{\Delta_{\mathrm{hf}}}{\Delta_{\mathrm{hf}}^2 - \left(\frac{\delta_{\mathrm{c}}}{2}\right)^2}. \tag{6.40}$$

The second possibility is to suppress the scattering mechanism if the NV nuclear spin is in the qubit state $|0\rangle$. This can be achieved by adjusting the laser frequency to a detuning of $\delta_{\mathrm{L}} = \Delta_{\mathrm{hf}} + \delta_{\mathrm{c}}/2$. We find the same effective scattering rate g' [Eq. (6.40)] for this case. However, we concentrate on the first case in the following, where the detuning allows scattering only if the qubit is state $|1\rangle$.

The transversal spin-spin interaction terms proportional to Δ_1 and Δ_2 have so far not been included in the derivation of the effective low-energy Hamiltonian $\widetilde{H}_1^{(\mathrm{gs})}$. Quantitative predictions regarding the developed scattering mechanism can only be made if these terms are taken into account. We can perform the SW transformation in a similar fashion as described in above, determining the anti-Hermitian matrix S_1 from the full Hamiltonian H_1' in Eq. (6.27). In doing so, we have to assume sufficiently large detunings $|\delta_{\mathrm{L}}| > |\Omega|$ and $|\delta_{\mathrm{L}} - \delta_{\mathrm{c}}| > g$ such that the off-diagonal terms in V_1 are small compared to the energy gap between the low- and high-energy subspace. We therefore assume an initially empty cavity that is maximally populated by one photon, and only if the NV center is in the ground state. In the excited state, we need to include the $m_S = 0$ and $m_S = +1$ spin states, giving a 10-dimensional Hilbert space. We consider the scenario

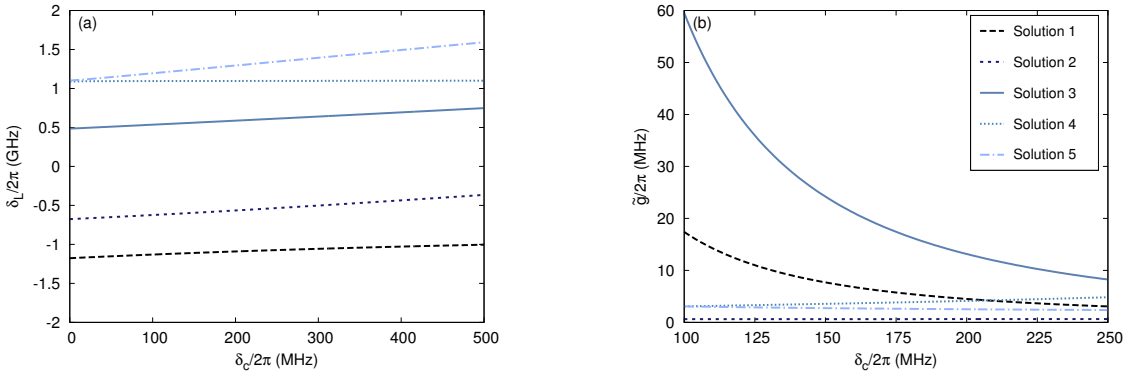

Figure 6.10 – Laser detunings enabling scattering only from the state $|1\rangle$. (a) Five solutions of δ_L, for which the matrix element for scattering of a laser photon from the $m_I = 0$ state is zero, as a function of δ_c. (b) Effective coupling strength $\tilde{g} = g\Omega f(\delta_c)$ for the solutions δ_L shown in (a). Solution 3 (solid line) is used for further calculations.

when scattering is only possible if the nuclear spin qubit is in state $|1\rangle$. Compared to the unique solution for the laser detuning δ_L previously, we find five solutions such that the scattering matrix element for the $m_I = 0$ state is zero, shown in Fig. 6.10. For all solutions, the effective ground state Hamiltonian in the case of $m_I = +1$ scattering has the same form as given in Eq. (6.39),

$$\widetilde{H}_1^{(\mathrm{gs})} = \left(Q - A_{\parallel}^{\mathrm{gs}} + \gamma_n B\right) |1\rangle\langle 1| + \delta_c a^\dagger a + \tilde{g}\,|1\rangle\langle 1|\,a^\dagger + (\tilde{g})^*\,|1\rangle\langle 1|\,a, \tag{6.41}$$

however with a different effective coupling strength $\tilde{g} = g\Omega f(\delta_c)$, where $\Delta_{\mathrm{hf}}/(\Delta_{\mathrm{hf}}^2 - (\delta_c/2)^2)$ is replaced by a different detuning-dependent part $f(\delta_c)$. In the following derivation, we choose the solution gives rise to the largest value of $\tilde{g}$ (solution 3 in Fig. 6.10), and eventually minimizes the two-qubit gate time in the following.

6.4.3 Controlled Quantum Gate

In this section, we derive the main result of this project, which is the coupling of two nitrogen nuclear spins via an optical cavity and the fast implementation of a two-qubit quantum gate below 100 nanoseconds. Compared to the physical setting before, a second NV center (NV 2 in Fig. 6.11) is placed inside the optical cavity and coupled to the same optical mode. An additional external laser drives optical transitions in NV 2, which can lead to the scattering of laser photons into the cavity by the mechanism described in Sec. 6.4.2. The total system is described by the Hamiltonian[7]

$$H_2(t) = \omega_c a^\dagger a + \sum_{i=1}^{2} H_{\mathrm{NV}}^{(i)} + g_i\left(\tau_{+,i}a + \tau_{-,i}a^\dagger\right) + H_L^{(i)}(t), \tag{6.42}$$

[7] For clarity, the notation is chosen in such a way that all operators and parameters that appeared before in the case of a single NV center and are associated now to one of the two NV centers, are indicated by an index i.

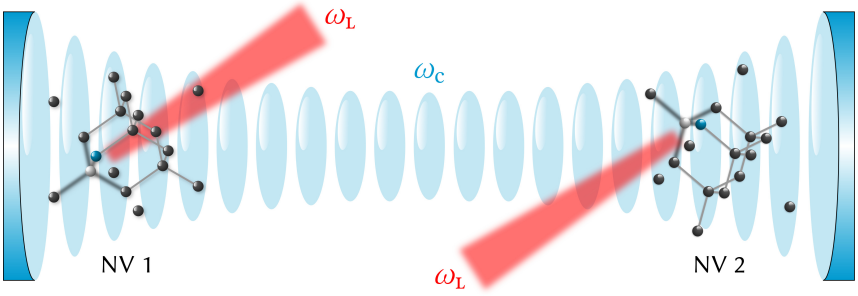

Figure 6.11 – Schematic setup to couple two nitrogen nuclear spins. Two NV centers (NV 1 and NV 2) are coupled to a common mode ω_c of an optical cavity. Photons from the external lasers of frequency ω_L can be scattered into the cavity, as described in Sec. 6.4.2. This mechanism effectively couples the two nitrogen nuclear spins intrinsic to each NV center, which can be harnessed to implement a two-qubit quantum gate.

where $H_{NV}^{(i)}$ is the Hamiltonian of NV center i ($i = 1, 2$) [Eq. (6.17)], g_i and $\tau_{\pm,i}$ are the couplings to the cavity and the optical transition operators of NV center i, respectively, and $H_L^{(i)}(t)$ describes the laser excites NV center i. To develop a formal description of the scattering processes of the two lasers, we proceed in a similar way as in Secs. 6.4.1 and 6.4.2. At first, $H_2(t)$ is made time-independent by applying the transformation $H_2' = \exp(i\xi_2 t)H_2(t)\exp(-i\xi_2 t) - \xi_2$ with

$$\xi_2 = \omega_L\left(a^\dagger a + \sum_{i=1}^{2}\frac{\tau_{z,i}}{2}\right). \tag{6.43}$$

Afterwards, we eliminate the excited states of each NV center by applying the SW transformation $\widetilde{H}_2 = \exp(-S_2)H_2'\exp(S_2)$. The anti-Hermitian matrix $S_2 = \sum_i S_1^{(i)}$ can be constructed from the single-NV matrices S_1 that were derived above, including spin-spin interactions. In analogy to Eq. (6.41), the effective ground state Hamiltonian for scattering only if both nuclear spins are in state $m_I = +1$ is given by

$$\widetilde{H}_2^{(gs)} = \delta_c a^\dagger a + \sum_{i=1}^{2}\left(Q - A_\parallel^{gs} + \gamma_n B\right)|1\rangle_i\langle 1| + \tilde{g}^{(i)}|1\rangle_i\langle 1|a^\dagger + \left(\tilde{g}^{(i)}\right)^*|1\rangle_i\langle 1|a. \tag{6.44}$$

The Hamiltonian $\widetilde{H}_2^{(gs)}$ will be the basis for the derivation of an effective interaction between the nitrogen nuclear spins of the NV centers. One can imagine, e.g., the situation where NV 1 scatters a laser photon into the cavity, which can be subsequently scattered by NV 2 into exciting the laser field. If we assume a sufficiently large detuning δ_c, the cavity field is only virtually excited in the intermediate step of the process described above. We demonstrate below that the exchange of a virtual cavity photon creates a conditioned phase shift on the state of both nuclear spins because such a process is only possible if both nuclear spins are in the $m_I = +1$ state. To derive an effective interaction between the two nuclear spin qubits, we again use the method of a SW transformation and decouple the subspaces containing zero and one cavity photon in the Hamiltonian $\widetilde{H}_2^{(gs)}$. We

construct an anti-Hermitian matrix S,

$$S = -\sum_{i=1}^{2}\left[\frac{\tilde{g}^{(i)}}{\delta_c}\,|1\rangle_i\langle 1|\,a^\dagger - \text{h.c.}\right], \tag{6.45}$$

that fulfills the condition $[S, H_2^{(0)}] = V_2$, where

$$H_2^{(0)} = \delta_c a^\dagger a + \sum_{i=1}^{2}\left(Q - A_{\shortparallel}^{gs} + \gamma_n B\right)|1\rangle_i\langle 1|, \tag{6.46}$$

$$V_2 = \sum_{i=1}^{2}\tilde{g}^{(i)}\,|1\rangle_i\langle 1|\,a^\dagger + \left(\tilde{g}^{(i)}\right)^*|1\rangle_i\langle 1|\,a, \tag{6.47}$$

are the block-diagonal and off-diagonal parts of $\widetilde{H}_2^{(gs)}$, respectively. We then apply the unitary transformation

$$H_{eff} = e^{-S}\widetilde{H}_2^{(gs)}e^{S} \approx H_2^{(0)} + \frac{1}{2}[V_2, S] = \sum_{i=1}^{2}H_{eff}^{(i)} + H_{int} + \delta_c a^\dagger a. \tag{6.48}$$

As it was the case for the first SW transformation, we only keep terms up to the lowest order in the interaction Hamiltonian V_2. In Eq. (6.48), the Hamiltonian H_{eff} contains terms that only act on a single nuclear spin i ($H_{eff}^{(i)}$), and a term that couples both nuclear spins (H_{int}). The hyperfine levels of each NV center are slightly shifted by $|\tilde{g}^{(i)}|^2/\delta_c$ due to the interaction with the cavity field,

$$H_{eff}^{(i)} = \left(Q - A_{\shortparallel}^{gs} + \gamma_n B - \frac{|\tilde{g}^{(i)}|^2}{\delta_c}\right)|1\rangle_i\langle 1|. \tag{6.49}$$

The more interesting part of H_{eff} is the interaction term H_{int} that effectively couples the two nuclear-spin qubits. It can be written as

$$H_{int} = -g_{12}\,|11\rangle\langle 11|, \tag{6.50}$$

where $|11\rangle = |1\rangle_1|1\rangle_2$ denotes the product state of both nuclear spin qubits being in the $m_I = +1$ state. The effective two-qubit coupling constant g_{12} is given by

$$g_{12} = 2\frac{|\tilde{g}^{(1)}||\tilde{g}^{(2)}|}{\delta_c}\cos(\phi_1 - \phi_2), \tag{6.51}$$

where ϕ_i is the phase of the ith laser, $\Omega_i = |\Omega_i|e^{i\phi_i}$. From Eq. (6.51), we see that the coupling between both nuclear spins can be maximized by adjusting the phases ϕ_i to be equal or differ by multiples of π. The lasers offer the possibility to externally adjust the interaction between the two qubits. The interaction can be switched on and off by turning the lasers on or off, and therefore, the quantum gate can be implemented in a highly controllable manner. The value of g_{12}

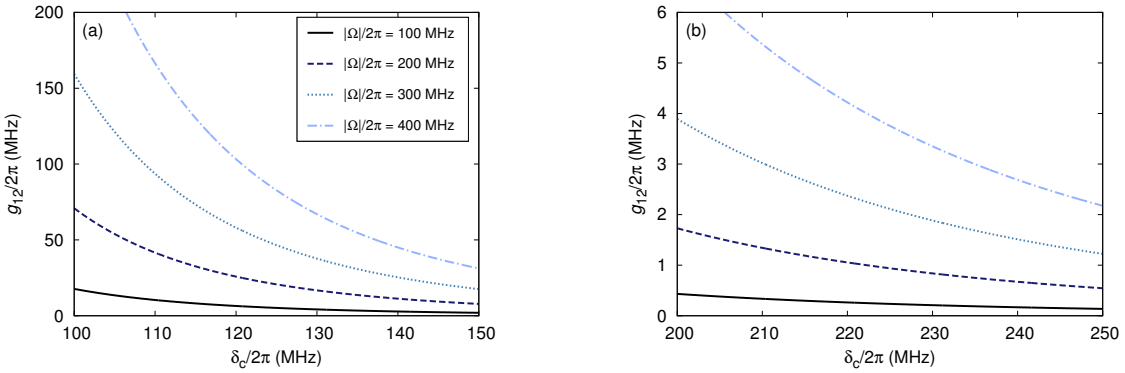

Figure 6.12 – Effective two-qubit coupling strength. (a) Effective two-qubit coupling strength g_{12} as a function of the cavity detuning δ_c for different values of the laser Rabi frequency $\Omega_1 = \Omega_2 \equiv \Omega$ (see legend, valid for both figures) and $g_1/2\pi = g_2/2\pi = 50$ MHz. (b) Equivalent to the left plot, but for $g_1/2\pi = g_2/2\pi = 200$ MHz. All calculations performed for $B = 120$ G.

is analyzed in Figs. 6.12 (a) and (b) for different adjustable parameters. For equivalent couplings $g_1/2\pi = g_2/2\pi = 50$ MHz and $\Omega_1 = \Omega_2 \equiv \Omega$ with $|\Omega|/2\pi = 300$ MHz, e.g., the effective two-qubit coupling strength can reach 100 MHz and more [Fig. 6.12 (a)]. For larger values of g_i, the detuning δ_c must be chosen sufficiently large to ensure only virtual excitation of the cavity. This effectively decreases the coupling strength g_{12} [Fig. 6.12 (b)].

We now analyze the time evolution $U(t)$ of the two-qubit system composed of the two nuclear spins, that is generated by the Hamiltonian H_{eff} in Eq. (6.48). The single- and two-qubit parts in H_{eff} commute, i.e. $[H_{\text{eff}}^{(i)}, H_{\text{int}}] = 0$, and thus, the time evolution $U(t)$ can be written in the form

$$U(t) = e^{-iH_{\text{eff}}t} = (U_1(t) \otimes U_2(t))\, U_{12}(t). \tag{6.52}$$

We see that the time evolution comprises two parts. $U_i(t)$ is a single-qubit rotation on nuclear spin i generated by the Hamiltonian $H_{\text{eff}}^{(i)}$, and $U_{12}(t)$ describes a two-qubit operation that is generated by the interaction Hamiltonian H_{int}. In Eq. (6.52), the time evolution of the cavity field has been omitted, since the nuclear spin degree of freedom has been decoupled from the cavity field by the second SW transformation and is not of interest in the following. Furthermore, we only concentrate on the two-qubit interaction part $U_{12}(t)$, and disregard the phase shift on the qubit state $|1\rangle$ for every individual qubit. If necessary, these single-qubit rotations can be undone after the gate implementation and therefore do not affect the two-qubit gate. A fast single-qubit phase gate on a ^{14}N nuclear spin qubit has been demonstrated recently using off-resonant excitation of the ground-state electronic spin transition between the $m_S = 0$ and $m_S = -1$ state [151]. The evolution of the coupled nuclear spin system generated by the Hamiltonian H_{int} [Eq. (6.50)] is

$$U_{12}(t) = |00\rangle\langle 00| + |01\rangle\langle 01| + |10\rangle\langle 10| + e^{-ig_{12}t}\,|11\rangle\langle 11|\,. \tag{6.53}$$

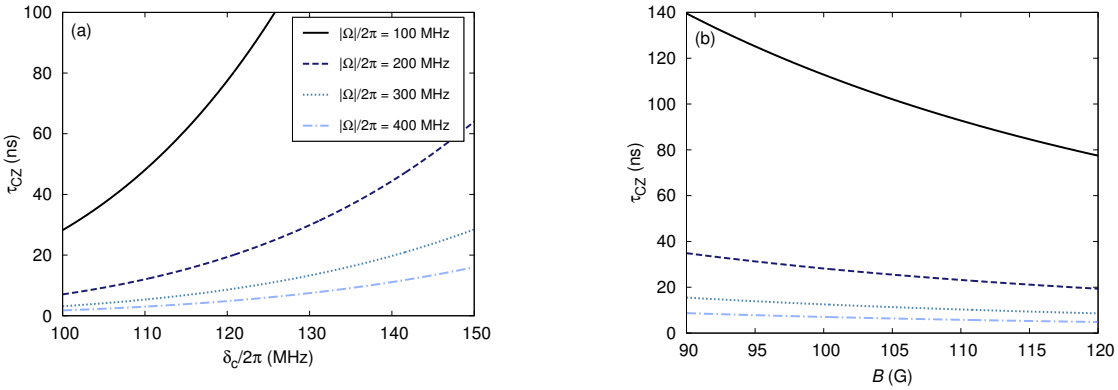

Figure 6.13 – Operation time of cz quantum gate. (a) Time τ_{cz} to generate a cz gate between the two nuclear spin qubits as a function of δ_c for different values of the laser Rabi frequency $\Omega_1 = \Omega_2 \equiv \Omega$ (see legend, valid for both figures) and $g_1/2\pi = g_2/2\pi = 50$ MHz. (b) Time τ_{cz} as a function of the external magnetic field B along the defect axis, for $g_1/2\pi = g_2/2\pi = 50$ MHz and $\delta_c/2\pi = 120$ MHz.

During the laser driving, the nuclear spin system acquires a phase of $g_{12}t$ conditioned on the spin state of both nuclear spins. It is described in Sec. 3.2 that particular conditional two-qubit gates are required to perform universal quantum computation [16]. Depending on the interaction time, different two-qubit gates can be implemented by the derived mechanism. For $t = \tau_{cs}$ with $g_{12}\tau_{cs} = -\pi/2$, a controlled-phase (cs) gate is generated [cf. Eq. (3.7) for the nomenclature],

$$U_{cs} = U_{12}(\tau_{cs}) = |00\rangle\langle 00| + |01\rangle\langle 01| + |10\rangle\langle 10| + i\,|11\rangle\langle 11| = \begin{pmatrix} 1 & 0 & 0 & 0 \\ 0 & 1 & 0 & 0 \\ 0 & 0 & 1 & 0 \\ 0 & 0 & 0 & i \end{pmatrix}, \tag{6.54}$$

where the matrix representation is given in the basis $\{|00\rangle, |01\rangle, |10\rangle, |11\rangle\}$. If the interaction time $t = \tau_{cz}$ with $g_{12}\tau_{cz} = \pi$, the universal controlled-Z gate is generated [Eq. (3.9)],

$$U_{cz} = U_{12}(\tau_{cz}) = |00\rangle\langle 00| + |01\rangle\langle 01| + |10\rangle\langle 10| - |11\rangle\langle 11| = \begin{pmatrix} 1 & 0 & 0 & 0 \\ 0 & 1 & 0 & 0 \\ 0 & 0 & 1 & 0 \\ 0 & 0 & 0 & -1 \end{pmatrix}, \tag{6.55}$$

which equivalent to the cnot gate upon single-qubit rotations [see Eq. (3.10)]. In Figs. 6.13 (a), the value of τ_{cz} is depicted for $g_1/2\pi = g_2/2\pi = 50$ MHz and for different coupling strengths Ω_i. Since τ_{cz} is inversely proportional to g_{12}, larger interaction strengths lead a to faster gate operation. We find operation times for the cz gate that are well below 100 ns for a wide range of parameter values, which is few orders of magnitude smaller than the nuclear spin decoherence time of about 1 ms [49]. Hence, the qubit coherence is well preserved during the gate implementation. Due to

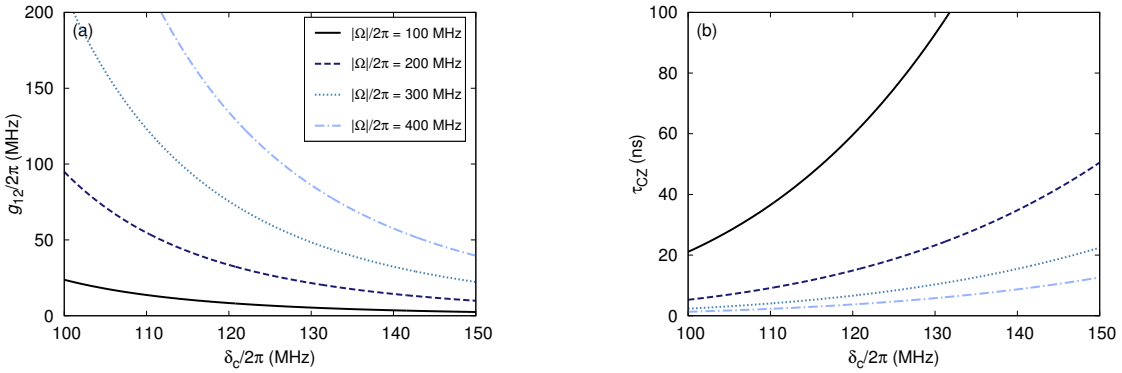

Figure 6.14 – Two-qubit coupling strength and gate operation time for ^{15}N nuclear spins. (a) Effective two-qubit coupling strength g_{12} as a function of cavity detuning δ_c for different values of the laser Rabi frequency $\Omega_1 = \Omega_2 \equiv \Omega$ (see legend, valid for both figures) and $g_1/2\pi = g_2/2\pi = 50$ MHz. (b) Time τ_{CZ} to generate a CZ gate between the two nuclear spins as a function of δ_c for different values of the laser Rabi frequency $\Omega_1 = \Omega_2 \equiv \Omega$ and $g_1/2\pi = g_2/2\pi = 50$ MHz.

the fast gate operation, the proposed scheme is rather insensitive to the exact coupling strengths to the laser field and the cavity, but we need to assure large detunings $|\delta_L - \delta_c| > g$ and $|\delta_L| > |\Omega|$ for validity of the applied SW transformations. Fig. 6.13 (b) shows the dependence of τ_{CZ} on the magnetic field strength B along the defect axis, and one can see that the gate time decreases for larger magnetic fields.

6.5 Conclusions

Nitrogen nuclear spins in diamond have proved to be highly promising candidates to physically realize qubits. We have developed a theoretical proposal for the implementation of a controlled quantum gate between two nitrogen nuclear-spin qubits intrinsic to NV centers in diamond. Gate operation can be achieved within a 100 ns or less, which is well below the nuclear-spin decoherence time $T_2 \approx 1$ ms [49]. The typical time τ for a photon to escape the cavity must be longer than the gate operation time τ_{CZ}. Therefore, the cavity loss rate κ must not exceed values of $\kappa \equiv (g/\delta_c)^2/\tau < 1/\tau_{CZ} \approx 50$ MHz if we assume a gate operation time $\tau_{CZ} \approx 20$ ns [see Fig. 6.13 (a)] and $(g/\delta_c)^2$ is the probability of the cavity mode being excited. Quality (Q) factors of the optical cavity of 10^6–10^7 are thus required [160]. Such values have been reached in high-Q silica microsphere cavities [219] and progress towards photonic crystal cavities in bulk diamond exceeding Q-factors of 10^5 has been recently reported [223].

In addition to the presented derivation for ^{14}N nuclear spins, an equivalent calculation for ^{15}N nuclear spins with $I = 1/2$ demonstrates the feasibility of the proposed scheme also for this isotope. In this case, the computational basis is chosen as the nuclear-spin eigenstates $|0\rangle \equiv |m_S = -1, m_I = -1/2\rangle$ and $|1\rangle \equiv |m_S = -1, m_I = +1/2\rangle$ [Fig. 6.9 (b)]. The effective two-qubit coupling strength g_{12} and the gate time τ_{CZ} show qualitatively the same behavior as for the ^{14}N nuclear

spin, and are depicted in Fig. 6.14. The case of different nitrogen isotopes has not been studied yet. Therefore, the question whether a ^{14}N and a ^{15}N nuclear spin can be coupled via the developed mechanism should be answered in further studies.

During the fast electronic excitation cycles, the nuclear spins are subject to a time-varying hyperfine interaction. However, using a spin-fluctuator model, it has been shown that the nuclear spin state will be unaffected and coherence can be preserved [224]. Together with elementary and experimentally demonstrated single-qubit operations, the realization of a universal CZ gate makes the nitrogen nuclear spin vulnerable for quantum computation in addition to its remarkable quality as quantum memory [49].

7

Optical Readout of a Quantum-Dot Spin

7.1 Introduction

In this chapter, we describe work that originates from a research stay in the group of Prof. Yoshihisa Yamamoto at Stanford University. Optically active, self-assembled quantum dots (QDs) are further solid-state systems that bear the potential to realize qubits [22, 26]. The measurement of a qubit state is a basic procedure in the context of quantum communication and also the verification of entanglement typically involves measurements, i.e. a spin readout in the case of spin qubits. Another crucial component in a quantum network is the interface between the stationary qubits and the flying qubits that transmit quantum information. Whereas pioneering experiments demonstrated entanglement between the spin of an electron in a self-assembled QD and a photon [225, 226], and the teleportation of a photon superposition state onto a QD electron-spin state [227], the readout of the electron spin state in a single shot has not been achieved for most experiments [26]. A theoretical proposal by S. Puri *et al.* [228] describes the single-shot readout of an electron spin in a self-assembled QD by a quantum nondemolition measurement [229], thereby harnessing the interaction with an exciton-polariton in a nearby quantum well. The aim of this work is to derive a fully quantum-mechanical description of the system studied in Ref. 228 in order to characterize the optical readout process more carefully. Therefore, this chapter has more the character of a technical report, in which we focus on the applied theoretical methods.

7.2 Spin Qubits in Self-Assembled Quantum Dots

Self-assembled quantum dots (QDs) are naturally formed during the growth process of a specific semiconductor heterostructure. Prominent examples are InGaAs dots in a GaAs matrix. Small islands of InGaAs that contain about 10^5 atoms are formed if grown on top of a GaAs layer due to the mismatch in lattice constants of both materials, which have about 5 nm in height and 20 nm in diameter. The dots can then be covered by further growing of GaAs layers. Due to a difference in

the valence and conduction band edges between both materials, strong confinement of electrons (and holes) is possible in all three dimensions with quantization energies of a few meV [26]. An important feature is that the charge state of the QDs is controllable and hence, it can be occupied, e.g., with a single electron in the conduction band or a single hole in the valence band. The lowest conduction band level is an s-type orbital, such that the electron angular momentum is simply determined by the electron spin. In the so-called Faraday geometry, a magnetic field is applied along the growth axis, which also determines the quantization axis of the electron spin. Thus, the computational basis is typically chosen by the two spin eigenstates $|0\rangle = |\uparrow\rangle = |m_S = +1/2\rangle$ and $|1\rangle = |\downarrow\rangle = |m_S = -1/2\rangle$. The decoherence time T_2 of a single electron spin in a self-assembled QD has been measured to be around 2.6 μs [230] and relaxation times T_1 of more than 20 ms have been reported [231]. Various ideas of qubit initialization, manipulation, and measurement have been suggested and partially been implemented. An overview regarding these works can be found in Refs. 22, 24, and 26, and the references therein.

7.3 Input-Output Formalism for Optical Spin Readout

7.3.1 Model

The system that has been studied in Ref. 228 shows similarities to the intersubband cavity system studied in Chap. 4 and is schematically depicted in Fig. 7.1. However, we only consider a single quantum well (QW) that is embedded inside a semiconductor microcavity, and the Fermi level of the QW and the cavity resonance are chosen such that the cavity photons can excite *interband* transition, i.e. electronic excitations from the valence band to the conduction band. The Coulomb-bound pair of an excited electron and the hole that is left in the valence band is called an exciton, which is a quasiparticle that can be usually considered as boson [232]. The QW excitons have total angular momentum $J = 1$ and can be excited optically with circularly-polarized light, where σ^+ (σ^-) polarization leads to the excitation of a QW exciton with $J_z = +1(-1)$. Inside the cavity, the excitons can interact with the cavity photons. If the rate of coherent energy exchange between the QW excitons and cavity photons is larger than the loss rates from the cavity, i.e. the system is in the strong coupling regime of cavity QED, the interaction leads to the formation of combined exciton-photon states, known as exciton-polaritons [232] (see also Chap. 4 for a different kind of polariton).

Additionally to the QW, a singly-charged QD is also positioned inside the microcavity, but so close to the QW that the wave function of the QD electron slightly penetrates the QW. If an exciton is present in the QW, this eventually leads to a spin-dependent exchange interaction between the QD electron and the electronic part of the exciton [cf. also Eq. (5.4)]. The principle idea of the optical readout of the QD spin state is the following. The energy of an exciton-polariton changes due to the exchange interaction of the exciton with the QD electron spin. However, the sign of the exchange energy depends on the relative orientations of the QD electron spin and

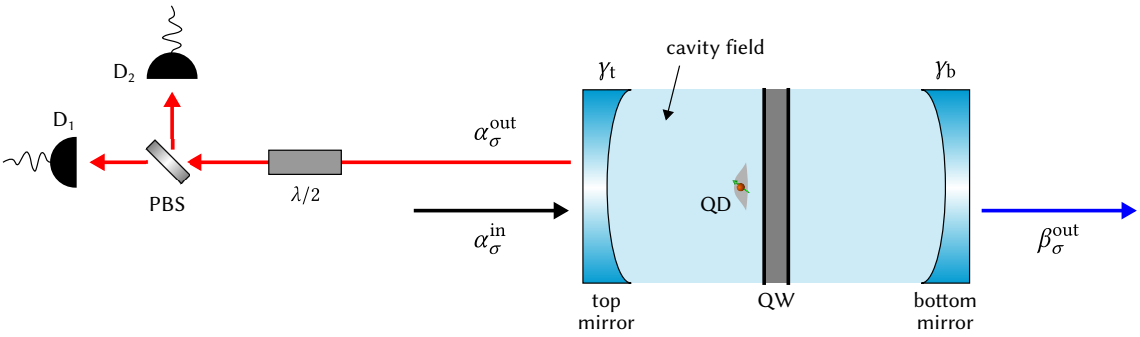

Figure 7.1 – Schematic setup of optical spin readout. Quantum-well (QW) excitons interact with microcavity photons, which leads to the formation of exciton polaritons. A nearby singly-charged quantum dot (QD) interacts with QW excitons via exchange interaction. An incoming light field ($\alpha_\sigma^{\text{in}}$) is reflected from the top mirror of the microcavity. (Decay rates from the cavity are $\gamma_{t(b)}$ for top (bottom) mirror.) The reflected beam ($\alpha_\sigma^{\text{out}}$) acquires a phase shift that depends on the spin state of a QD electron. Information about the QD spin state is obtained by the subsequent measurement setup consisting of a $\lambda/2$ wave plate, a polarizing beam splitter (PBS), and the two photon detectors D_1 and D_2.

the spin of an excited electron in the QW that forms the exciton. As it is shown in the following, the reflected part of an incoming light beam incident on the cavity acquires a different phase shift, depending on whether the spin of the QD electron is state $|\uparrow\rangle$ or $|\downarrow\rangle$. With a measurement setup shown in Fig. 7.1, the difference in phase shifts can be converted into a signal that gives information about the spin state of the electron in the QD.

We model the physical situation using the so-called input-output formalism developed in Refs. 233 and 234, in which the fields of the reflected light can be related to the incoming beam. To describe the setup in Fig. 7.1, we use a Hamiltonian H consisting of three parts,

$$H = H_{\text{sys}} + H_{\text{bath}} + H_{\text{int}}, \tag{7.1}$$

where H_{sys} describes the QW-cavity system, H_{bath} describes the external photonic modes as a collection of harmonic oscillators that constitutes a heat bath, and the coupling of the cavity field to the modes of the heat bath is given by H_{int}. The system Hamiltonian describes the interaction of cavity photons and QW excitons ($\hbar = 1$) [232],

$$H_{\text{sys}} = \sum_{\sigma'=\pm} \omega_c a_{\sigma'}^\dagger a_{\sigma'} + \omega_{\text{ex}} b_{\sigma'}^\dagger b_{\sigma'} + ig\left(a_{\sigma'}^\dagger b_{\sigma'} - b_{\sigma'}^\dagger a_{\sigma'}\right), \tag{7.2}$$

The operator $a_{\sigma'}^{(\dagger)}$ annihilates (creates) a cavity photon with frequency ω_c and polarization σ' that can be either right-handed circular ($\sigma' = +$) or left-handed circular ($\sigma' = -$). The bosonic operators $b_{\sigma'}^{(\dagger)}$ describe the QW excitons of frequency ω_{ex} with total angular momentum $J = 1$ and angular momentum projection $J_z = +1$ ($\sigma' = +$) or $J_z = -1$ ($\sigma' = -$). The last term describes the interaction between cavity photons and QW excitons with Rabi frequency g, where the rotating

wave approximation is made. Furthermore, we only consider the interaction between photons and excitons with zero in-plane momentum, because the cavity is assumed to be excited by a beam perpendicular to the cavity mirrors. We also assume the cavity frequency to be resonant with the exciton transition, i.e. $\omega_c = \omega_{ex}$. Note that so far, the QD has been neglected in the description for the sake of clarity, and will be added later. The extracavity bath modes are modeled by a continuous set of harmonic oscillators [234],

$$H_{\text{bath}} = \sum_{\sigma=\text{H/V}} \int_{-\infty}^{\infty} \mathrm{d}\nu\, \nu \left(\alpha^{\dagger}_{\nu,\sigma} \alpha_{\nu,\sigma} + \beta^{\dagger}_{\nu,\sigma} \beta_{\nu,\sigma} \right), \tag{7.3}$$

where $\alpha_{\nu,\sigma}(\beta_{\nu,\sigma})$ is the annihilation operator of a photon belonging to the top (bottom) bath (see Fig. 7.1) with polarization σ that can be either horizontal (H) or vertical (V). The reason for choosing the basis of linear polarization here is that the cavity is assumed to be pumped with horizontally-polarized light (see Sec. 7.3.2 below) and therefore, the following description is more clear compared to using the circular-polarization basis. Thus, the index σ denotes linear polarization and σ' is the index for circular polarization. The Hamiltonian for the interaction between intracavity modes and external bath modes is assumed to be of the form [234]

$$H_{\text{int}} = i \sum_{\sigma=\text{H/V}} \int_{-\infty}^{\infty} \mathrm{d}\nu \sqrt{\frac{\gamma_t}{2\pi}} \left(\alpha^{\dagger}_{\nu,\sigma} a_{\sigma} - a^{\dagger}_{\sigma} \alpha_{\nu,\sigma} \right) + \sqrt{\frac{\gamma_b}{2\pi}} \left(\beta^{\dagger}_{\nu,\sigma} a_{\sigma} - a^{\dagger}_{\sigma} \beta_{\nu,\sigma} \right). \tag{7.4}$$

For the coupling between the field modes of intra- and extracavity photons, we use real coupling constants γ_t and γ_b that could be different for the top and bottom mirror, and we applied the Markov approximation, i.e. the coupling constants are assumed to be independent of the photon frequency.

So far, we only considered a system comprised of a QW coupled to the cavity and the electron spin of the singly-charged QD has to not been included. Since the energy for exciting an additional electron-hole pair within the QD[1] is far from the cavity resonance, no direct interaction takes place between the QD and the cavity [228]. If an exciton is present in the QW and the wave functions of the exciton and the electron confined to the QD have finite overlap, the spins of both are coupled via an exchange interaction Hamiltonian [228][cf. also Eq. (5.4)]

$$H_{\text{exc}} = -\sum_{\sigma'=\pm} V_{\text{exc}} S_z S_{\text{ex},z} b^{\dagger}_{\sigma'} b_{\sigma'}, \tag{7.5}$$

where V_{exc} is the exchange integral, S_z is the z component of the QD electron-spin operator, and $S_{\text{ex},z}$ is the respective operator of the electron forming the exciton.[2] The exciton energy shifts

[1] The optically excited states of a charged QD consisting of two electrons in the conduction band and a single hole in the valence band are known as trions.

[2] A detailed derivation of the Hamiltonian H_{exc}, including numerical calculations, can be found in the Supplemental

proportional to the exchange interaction and the direction of the shift depends on the exciton spin itself. On can incorporate this in the system Hamiltonian in the following form,

$$H_{\mathrm{sys}} = \sum_{\sigma'=\pm} \omega_{\mathrm{c}} a^{\dagger}_{\sigma'} a_{\sigma'} + \left(\omega_{\mathrm{c}} - \frac{1}{2}\sigma' V_{\mathrm{exc}} S_z\right) b^{\dagger}_{\sigma'} b_{\sigma'} + ig(a^{\dagger}_{\sigma'} b_{\sigma'} - b^{\dagger}_{\sigma'} a_{\sigma'}), \tag{7.6}$$

where we replaced the operator $S_{\mathrm{ex},z}$ by its eigenvalue $\sigma'/2$.

To describe the dynamics of the total system, one can work in the Heisenberg picture and obtain the following stochastic differential equations for the intracavity-field operators $a_{\mathrm{H}}(t)$ and $a_{\mathrm{V}}(t)$,

$$\dot{a}_{\mathrm{H}}(t) = -\left(i\omega_{\mathrm{c}} + \frac{\gamma_{\mathrm{t}} + \gamma_{\mathrm{b}}}{2}\right) a_{\mathrm{H}}(t) + \frac{g}{\sqrt{2}}\Big(b_+(t) + b_-(t)\Big) - \sqrt{\gamma_{\mathrm{t}}}\alpha^{\mathrm{in}}_{\mathrm{H}}(t) - \sqrt{\gamma_{\mathrm{b}}}\beta^{\mathrm{in}}_{\mathrm{H}}(t), \tag{7.7}$$

$$\dot{a}_{\mathrm{V}}(t) = -\left(i\omega_{\mathrm{c}} + \frac{\gamma_{\mathrm{t}} + \gamma_{\mathrm{b}}}{2}\right) a_{\mathrm{V}}(t) + \frac{ig}{\sqrt{2}}\Big(b_+(t) - b_-(t)\Big) - \sqrt{\gamma_{\mathrm{t}}}\alpha^{\mathrm{in}}_{\mathrm{V}}(t) - \sqrt{\gamma_{\mathrm{b}}}\beta^{\mathrm{in}}_{\mathrm{V}}(t), \tag{7.8}$$

which are also known as *quantum Langevin equations*. A detailed derivation of Eqs. (7.7) and (7.8) as well as the definition of the input-field operators $\alpha^{\mathrm{in}}_{\mathrm{H/V}}(t)$ and $\beta^{\mathrm{in}}_{\mathrm{H/V}}(t)$ can be found in Appendix E.1. The quantum Langevin equations can be solved in frequency space, which yields

$$\begin{pmatrix} \tilde{a}_{\mathrm{H}}(\omega) \\ \tilde{a}_{\mathrm{H}}(\omega) \\ \tilde{b}_+(\omega) \\ \tilde{b}_-(\omega) \end{pmatrix} = B(\omega) \begin{pmatrix} \sqrt{\gamma_{\mathrm{t}}}\tilde{\alpha}^{\mathrm{in}}_{\mathrm{H}}(\omega) + \sqrt{\gamma_{\mathrm{b}}}\tilde{\beta}^{\mathrm{in}}_{\mathrm{H}}(\omega) \\ \sqrt{\gamma_{\mathrm{t}}}\tilde{\alpha}^{\mathrm{in}}_{\mathrm{V}}(\omega) + \sqrt{\gamma_{\mathrm{b}}}\tilde{\beta}^{\mathrm{in}}_{\mathrm{V}}(\omega) \\ 0 \\ 0 \end{pmatrix}, \tag{7.9}$$

where the matrix $B(\omega)$ is defined in Eqs. (E.24) and (E.25) of Appendix E.2, and the Fourier transform of an operator $O(t)$ is $\widetilde{O}(\omega) \equiv (2\pi)^{-1/2} \int_{-\infty}^{\infty} \mathrm{d}t \, \exp(i\omega t) O(t)$.

The aim of the model is to describe the cavity output depending on the input field and also incorporate the dynamics within the cavity. Therefore, one can define outgoing field modes [Eqs. (E.28) and (E.29) in Appendix E.3], which describe the reflected part of an incoming beam by the so-called *input-output relations*,

$$\begin{pmatrix} \tilde{\alpha}^{\mathrm{out}}_{\mathrm{H}}(\omega) \\ \tilde{\alpha}^{\mathrm{out}}_{\mathrm{V}}(\omega) \\ \tilde{\beta}^{\mathrm{out}}_{\mathrm{H}}(\omega) \\ \tilde{\beta}^{\mathrm{out}}_{\mathrm{V}}(\omega) \end{pmatrix} = U(\omega) \begin{pmatrix} \tilde{\alpha}^{\mathrm{in}}_{\mathrm{H}}(\omega) \\ \tilde{\alpha}^{\mathrm{in}}_{\mathrm{V}}(\omega) \\ \tilde{\beta}^{\mathrm{in}}_{\mathrm{H}}(\omega) \\ \tilde{\beta}^{\mathrm{in}}_{\mathrm{V}}(\omega) \end{pmatrix}, \tag{7.10}$$

where the unitary matrix specific for the problem described in this chapter is derived in Appendix E.3 [Eq. (E.41)].

Material of Ref. 228 and shall not be the topic of this chapter.

7.3.2 Phase Shift

It was noted in the introduction that light with different circular polarization experiences a different phase shift when being reflected from the cavity, which is shown in this chapter. A difference of phase shifts is an experimentally measurable quantity and the sign of this difference crucially depends on the spin state of the QD electron, as is shown in the subsequent section. As a converse argument, this means that by measuring the difference in phase shifts for both circular polarizations one can obtain information about the spin state of the QD electron. The output fields in the circular-polarization basis are given by

$$\begin{aligned}\tilde{\alpha}^{\text{out}}_{\pm}(\omega) &= \frac{1}{\sqrt{2}}\left(\tilde{\alpha}^{\text{out}}_{\text{H}}(\omega) \mp i\tilde{\alpha}^{\text{out}}_{\text{V}}(\omega)\right)\\ &= \frac{1}{\sqrt{2}}\Big[\left(U_{11}(\omega)\tilde{\alpha}^{\text{in}}_{\text{H}}(\omega) + U_{12}(\omega)\tilde{\alpha}^{\text{in}}_{\text{V}}(\omega) + U_{13}(\omega)\tilde{\beta}^{\text{in}}_{\text{H}}(\omega) + U_{14}(\omega)\tilde{\beta}^{\text{in}}_{\text{V}}(\omega)\right)\\ &\mp i\left(U_{21}(\omega)\tilde{\alpha}^{\text{in}}_{\text{H}}(\omega) + U_{22}(\omega)\tilde{\alpha}^{\text{in}}_{\text{V}}(\omega) + U_{23}(\omega)\tilde{\beta}^{\text{in}}_{\text{H}}(\omega) + U_{24}(\omega)\tilde{\beta}^{\text{in}}_{\text{V}}(\omega)\right)\Big].\end{aligned} \tag{7.11}$$

Hence, if the system is excited by some horizontally-polarized input field only through the top mirror, i.e. $\langle\tilde{\alpha}^{\text{in}}_{\text{H}}(\omega)\rangle \neq 0$ and $\langle\tilde{\alpha}^{\text{in}}_{\text{V}}(\omega)\rangle = \langle\tilde{\beta}^{\text{in}}_{\text{H}}(\omega)\rangle = \langle\tilde{\beta}^{\text{in}}_{\text{V}}(\omega)\rangle = 0$, the expectation value of the output field operators is

$$\begin{aligned}\langle\tilde{\alpha}^{\text{out}}_{\pm}(\omega)\rangle &= \frac{1}{\sqrt{2}}\left(U_{11}(\omega) \mp iU_{21}(\omega)\right)\langle\tilde{\alpha}^{\text{in}}_{\text{H}}(\omega)\rangle\\ &= \frac{1}{\sqrt{2}}\frac{2g^2 \pm \left(i\frac{\gamma_{\text{b}}-\gamma_{\text{t}}}{2} + \omega - \omega_{\text{c}}\right)\left(\frac{1}{2}V_{\text{exc}}\langle S_z\rangle \mp (\omega-\omega_{\text{c}})\right)}{2g^2 \pm \left(i\frac{\gamma_{\text{b}}+\gamma_{\text{t}}}{2} + \omega - \omega_{\text{c}}\right)\left(\frac{1}{2}V_{\text{exc}}\langle S_z\rangle \mp (\omega-\omega_{\text{c}})\right)}\langle\tilde{\alpha}^{\text{in}}_{\text{H}}(\omega)\rangle\\ &\equiv r_{\pm}(\omega)\langle\tilde{\alpha}^{\text{in}}_{\text{H}}(\omega)\rangle,\end{aligned} \tag{7.12}$$

where the phase shift is now defined as the argument of the complex reflection coefficient $r_{\pm}(\omega) = \sqrt{R_{\pm}(\omega)}e^{i\phi_{\pm}(\omega)}$ [235],

$$\phi_{\pm}(\omega) = \arg[r_{\pm}(\omega)] = \arg\left[\frac{1}{\sqrt{2}}\left(U_{11}(\omega) \mp iU_{21}(\omega)\right)\right]. \tag{7.13}$$

7.3.3 Phase Response

From the experimental setup depicted in Fig. 7.1, one can see that the reflected beam is first subjected to a $\lambda/2$ wave plate that rotates the polarizations by ±45° into the diagonal polarization basis, i.e.

$$\tilde{\alpha}^{\text{out}}_{\text{D}}(\omega) = \frac{1}{\sqrt{2}}\left(\tilde{\alpha}^{\text{out}}_{\text{H}}(\omega) + \tilde{\alpha}^{\text{out}}_{\text{V}}(\omega)\right), \tag{7.14}$$

$$\tilde{\alpha}^{\text{out}}_{\text{A}}(\omega) = \frac{1}{\sqrt{2}}\left(\tilde{\alpha}^{\text{out}}_{\text{H}}(\omega) - \tilde{\alpha}^{\text{out}}_{\text{V}}(\omega)\right). \tag{7.15}$$

The photons with diagonal (D) and anti-diagonal (A) polarization are subsequently split by a polarizing beam splitter (PBS), and separately detected by detectors D_1 and D_2, respectively. The difference in the measured intensities of both detectors yields information about the spin state of the QD electron. The measured intensities are proportional to the mean number of impinging photons, i.e.[3]

$$I_{D_1} = \int_{-\infty}^{\infty} d\omega \left\langle \tilde{\alpha}_D^{out\dagger}(\omega)\tilde{\alpha}_D^{out}(\omega)\right\rangle, \tag{7.16}$$

$$I_{D_2} = \int_{-\infty}^{\infty} d\omega \left\langle \tilde{\alpha}_A^{out\dagger}(\omega)\tilde{\alpha}_A^{out}(\omega)\right\rangle. \tag{7.17}$$

Using Eqs. (7.10) and (7.13), it is straightforward to derive the measured intensity difference as a function of the input field,

$$I_{D_1} - I_{D_2} = 2\int_{-\infty}^{\infty} d\omega \sqrt{R_+(\omega)R_-(\omega)}\,\sin\left(\phi_-(\omega) - \phi_+(\omega)\right)\left\langle \tilde{\alpha}_H^{in\dagger}(\omega)\tilde{\alpha}_H^{in}(\omega)\right\rangle, \tag{7.18}$$

where $R_\pm$ is the reflectivity of the cavity for the respective circular polarization. The input-output formalism allows to specify different kinds of input fields via the expectation value $\langle \tilde{\alpha}_H^{in\dagger}(\omega)\tilde{\alpha}_H^{in}(\omega)\rangle$ in Eq. (7.18), which can be, e.g., coherent states, number states, squeezed states, pulsed beams with a defined pulse shape, or noise in the framework of continuum field operators [236].

In the following, we only investigate the case of cavity excitation by a single-mode laser beam of frequency ω_{in}, which can be described by the expectation value

$$\left\langle \tilde{\alpha}_H^{in\dagger}(\omega)\tilde{\alpha}_H^{in}(\omega)\right\rangle = I_{in}\delta(\omega - \omega_{in}), \tag{7.19}$$

where I_{in} is the intensity of the input laser beam. The relative intensity difference on detectors D_1 and D_2, called the phase response, is thus given by

$$\frac{I_{D_1} - I_{D_2}}{I_{in}} = 2\sqrt{R_+(\omega_{in})R_-(\omega_{in})}\,\sin\left(\phi_-(\omega_{in}) - \phi_+(\omega_{in})\right), \tag{7.20}$$

which formally confirms the result obtained in Ref. 228. The phase response derived from the input-output formalism described above is shown in Fig. 7.2 for different Rabi frequencies g. The sign of the phase response very well depends on the spin state of the QD electron, being either $|\uparrow\rangle$ or $|\downarrow\rangle$ [$\langle S_z\rangle = \pm 1/2$, respectively, in Eq. (7.12)]. Qualitative differences compared to Ref. 228 originate from the inclusion of both polariton states that is implicitly done in Eq. (7.6), whereas the upper polariton state has been neglected in Ref. 228. For Rabi frequencies g that are on the

[3] Note that in Eqs. (7.16) and (7.17), the intensities are defined to equal the mean number of photons.

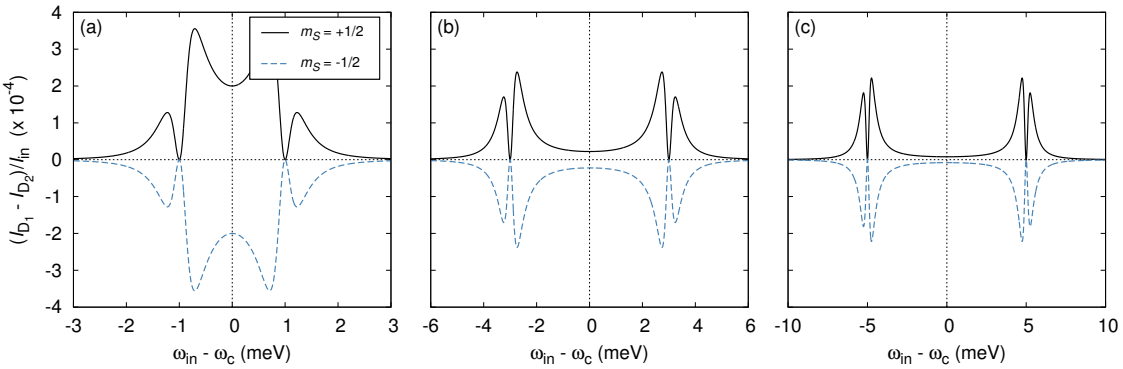

Figure 7.2 – Phase response. Phase response [Eq. (7.20)] for the two QD spin configurations $|\uparrow\rangle$ ($m_S = +1/2$) and $|\downarrow\rangle$ ($m_S = -1/2$) as a function of the laser detuning $\omega_{\mathrm{in}} - \omega_{\mathrm{c}}$ for (a) $g = 1$ meV, (b) $g = 3$ meV, and (c) $g = 5$ meV. Other parameter values are adapted from Ref. 228, i.e. $\gamma_{\mathrm{t}} = \gamma_{\mathrm{b}} = 0.5$ meV, and $V_{\mathrm{exc}} = 8$ μeV.

order of the laser detuning, these states cannot be neglected and lead to significant changes in the phase response.

7.4 Conclusions

An optical spin readout scheme has been proposed in Ref. 228 that harnesses the interaction with exciton polaritons. The aim of the work presented in this chapter was to verify previously obtained results on a more fundamental level. In doing so, we derive a quantum mechanical model to describe the phase response of a reflected light beam that is incident on a semiconductor microcavity, including the dynamics within the cavity. In comparison to Ref. 228, we find qualitative differences, mainly due to the inclusion of the upper polariton states. The input-output formalism applied here allows to calculate the cavity output depending on arbitrary input fields and e.g., offers the possibility to develop a pulse shape that maximizes the phase response in a realistic measurement scenario. Furthermore, the applied formalism allows to include frequency-dependent mirror decay to model, in principle, non-Markovian dynamics, or to include the decoherence of the exciton state as well.

8

Conclusions and Outlook

In this final chapter, we briefly summarize the main results of this dissertation, where we investigated some of the basic hardware components of quantum networks, and try to classify these results in a more general context.

In Chap. 4, we studied the intersubband cavity system with respect to its usefulness as a source of entangled photons. Since the photons that are contained in the polariton vacuum are correlated in their momentum degree of freedom, we tested the photon states for mode entanglement. The entanglement has been quantified analytically by using the concurrence as a measure of entanglement and it is found that the ground state of the intersubband cavity system contains maximally entangled photons. This is one of the prerequisites to be useful as a source of entanglement in quantum information processing. If the polariton vacuum is modulated nonadiabatically, the energy of the emitted photons is expected to be in the mid and far infrared [93]. A method to transfer the entanglement onto photons with energies in technologically relevant frequency domains, such as one of the telecom wavelengths, is necessary for further entanglement distribution, since the absorption in optical fibers would otherwise be too large. The verification of mode entanglement is an open question. One possibility would be to transform mode entanglement into polarization entanglement, for which verification methods exist [30, 31, 54, 71]. The development of a scheme to achieve such a transformation could be a starting point of further studies. We already pointed out that a non-instantaneous switch-off of the Rabi frequency and its effect on the entanglement has still to be modeled. Since a nonadiabatic switch-off of the Rabi frequency was so far not realizable in experiments, the obtained results could also motivate further research and new developments to eventually observe the predicted radiation from the vacuum state in the first place.

By introducing the concept of asymmetric bilateral two-qubit operations in Chap. 5, we developed an entanglement purification protocol for a very broad range of solid-state qubits, e.g. electron spins in quantum dots, NV centers in diamond, or superconducting qubits. Such a protocol is essential for the use of spin qubits as quantum memory, e.g. in quantum repeaters, and further increases their potential for being used in practical quantum information processing. The necessity of inter-

facing flying and stationary qubits in quantum repeaters can therefore stimulate further research on spin-photon interfaces. In addition, we have investigated a new class of recurrence protocols for entanglement purification, i.e. we considered asymmetric bilateral two-qubit operations. The idea of asymmetric operations opens new possibilities to perform entanglement purification and, to the best of our knowledge, has not been considered in the literature before. Since the studies described in this dissertation are special cases of a more general tensorial interaction $\mathbf{S}_i^T \cdot \overleftrightarrow{\mathbf{J}} \cdot \mathbf{S}_j$ with some coupling tensor $\overleftrightarrow{\mathbf{J}}$, we think that further research devoted to this class of operations needs to take place. The applicability of an asymmetric operation might even be extended to multipartite systems [45]. Regarding the experimental realization of entanglement purification with spin qubits, there have been implementations of the required $\sqrt{\text{SWAP}}$ gate [48, 114] and the pairwise coherent coupling of three spin qubits has also been demonstrated [130]. Scaling the system to four qubits should therefore be within reach of current technology.

The third part that was also devoted to entanglement generation and qubit coupling dealt with nitrogen nuclear spins in NV centers in diamond (Chap. 6). The abilities to entangle two nuclear spin qubits and to implement a universal set of quantum gates are essential for quantum communication and computation. In this dissertation, we developed a process to generate a controlled two-qubit quantum gate that creates entanglement and can be used for universal quantum computation. As a proof of principle, we demonstrate the feasibility under perfect conditions. Subsequent studies are necessary to obtain values for achievable gate fidelities and should include, e.g., photon loss from the cavity and qubit decoherence. However, we expect high fidelities due to the very good isolation of nuclear spins from their environment, which manifests itself in the very long decoherence times T_2. Through the possibility of optical control and therefore fast gate operation within 100 nanoseconds and less, we think we could advance the field of practical, nuclear-spin based quantum information processing and also offer possibilities for further interesting research in this direction. The complete understanding of the low-temperature hyperfine structure in the excited-state manifold is an open issue. The potential of harnessing the excited-state hyperfine structure to eventually couple two nuclear spin qubits, which is provided by the developed scheme, should motivate a more careful experimental investigation of the ^{3}E orbital level structure.

The experimental implementation of the optical readout scheme described in Chap. 7 is an ongoing challenge by the time of writing. It seems that additional decoherence channels might play a significant role. This could be the unwanted tunneling of the QD electron into the QW and the subsequent recombination with the hole in there. Furthermore, the effect of a surrounding nuclear-spin bath has not been considered at all so far, although it is known that nuclear spins mainly affect the decoherence time T_2 [24]. The model developed here using the input-output formalism should therefore be extended and include the two decoherence mechanisms mentioned above.

Bibliography

[1] A. Einstein, B. Podolsky, and N. Rosen, *Can Quantum-Mechanical Description of Physical Reality Be Considered Complete?*, Phys. Rev. **47**, 777 (1935).

[2] E. Schrödinger, *Die gegenwärtige Situation in der Quantenmechanik*, Naturwissenschaften **23**, 807; 823; 844 (1935).

[3] M. A. Nielsen and I. L. Chuang, *Quantum Computation and Quantum Information*, Cambridge University Press, Cambridge (2000).

[4] D. Bouwmeester, A. K. Ekert, and A. Zeilinger, *The Physics of Quantum Information: Quantum Cryptography, Quantum Teleportation, Quantum Computation*, Springer, New York (2001).

[5] R. L. Rivest, A. Shamir, and L. Adleman, *A Method for Obtaining Digital Signatures and Public-key Cryptosystems*, Commun. ACM **21**, 120 (1978).

[6] C. H. Bennett and G. Brassard, *Quantum Cryptography: Public key distribution and coin tossing*, in *Proceedings of the IEEE International Conference on Computers, Systems, and Signal Processing, Bangalore, India*, 175–179, IEEE, New York (1984).

[7] A. K. Ekert, *Quantum cryptography based on Bell's theorem*, Phys. Rev. Lett. **67**, 661 (1991).

[8] H.-J. Briegel, W. Dür, J. I. Cirac, and P. Zoller, *Quantum Repeaters: The Role of Imperfect Local Operations in Quantum Communication*, Phys. Rev. Lett. **81**, 5932 (1998).

[9] W. Dür, H.-J. Briegel, J. I. Cirac, and P. Zoller, *Quantum repeaters based on entanglement purification*, Phys. Rev. A **59**, 169 (1999).

[10] C. H. Bennett, G. Brassard, S. Popescu, B. Schumacher, J. A. Smolin, and W. K. Wootters, *Purification of Noisy Entanglement and Faithful Teleportation via Noisy Channels*, Phys. Rev. Lett. **76**, 722 (1996).

[11] D. Deutsch, A. Ekert, R. Jozsa, C. Macchiavello, S. Popescu, and A. Sanpera, *Quantum Privacy Amplification and the Security of Quantum Cryptography over Noisy Channels*, Phys. Rev. Lett. **77**, 2818 (1996).

[12] R. P. Feynman, *Simulating physics with computers*, Int. J. Theor. Phys. **21**, 467 (1982).

[13] D. Deutsch, *Quantum Theory, the Church-Turing Principle and the Universal Quantum Computer*, Proc. R. Soc. A **400**, 97 (1985).

[14] L. K. Grover, *A Fast Quantum Mechanical Algorithm for Database Search*, in *Proceedings of the Twenty-eighth Annual ACM Symposium on Theory of Computing*, 212–219, ACM Press, New York (1996).

[15] P. Shor, *Polynomial-Time Algorithms for Prime Factorization and Discrete Logarithms on a Quantum Computer*, SIAM J. Comput. **26**, 1484 (1997).

[16] A. Barenco, C. H. Bennett, R. Cleve, D. P. DiVincenzo, N. Margolus, P. Shor, T. Sleator, J. A. Smolin, and H. Weinfurter, *Elementary gates for quantum computation*, Phys. Rev. A **52**, 3457 (1995).

[17] D. P. DiVincenzo, *The Physical Implementation of Quantum Computation*, Fortschr. Phys. **48**, 771 (2000).

[18] D. Loss and D. P. DiVincenzo, *Quantum computation with quantum dots*, Phys. Rev. A **57**, 120 (1998).

[19] R. Hanson, L. P. Kouwenhoven, J. R. Petta, S. Tarucha, and L. M. K. Vandersypen, *Spins in few-electron quantum dots*, Rev. Mod. Phys. **79**, 1217 (2007).

[20] R. Hanson and D. D. Awschalom, *Coherent manipulation of single spins in semiconductors*, Nature **453**, 1043 (2008).

[21] T. D. Ladd, F. Jelezko, R. Laflamme, Y. Nakamura, C. Monroe, and J. L. O'Brien, *Quantum computers*, Nature **464**, 45 (2010).

[22] B. Urbaszek, X. Marie, T. Amand, O. Krebs, P. Voisin, P. Maletinsky, A. Högele, and A. Imamoglu, *Nuclear spin physics in quantum dots: An optical investigation*, Rev. Mod. Phys. **85**, 79 (2013).

[23] V. Dobrovitski, G. Fuchs, A. Falk, C. Santori, and D. Awschalom, *Quantum Control over Single Spins in Diamond*, Annu. Rev. Condens. Matter Phys. **4**, 23 (2013).

[24] C. Kloeffel and D. Loss, *Prospects for Spin-Based Quantum Computing in Quantum Dots*, Annu. Rev. Condens. Matter Phys. **4**, 51 (2013).

[25] M. W. Doherty, N. B. Manson, P. Delaney, F. Jelezko, J. Wrachtrup, and L. C. Hollenberg, *The nitrogen-vacancy colour centre in diamond*, Phys. Rep. **528**, 1 (2013).

[26] R. J. Warburton, *Single spins in self-assembled quantum dots*, Nature Mater. **12**, 483 (2013).

[27] R. Ursin, F. Tiefenbacher, T. Schmitt-Manderbach, H. Weier, T. Scheidl, M. Lindenthal, B. Blauensteiner, T. Jennewein, J. Perdigues, P. Trojek, B. Omer, M. Furst, M. Meyenburg, J. Rarity, Z. Sodnik, C. Barbieri, H. Weinfurter, and A. Zeilinger, *Entanglement-based quantum communication over 144 km*, Nature Phys. **3**, 481 (2007).

[28] R. Horodecki, P. Horodecki, M. Horodecki, and K. Horodecki, *Quantum entanglement*, Rev. Mod. Phys. **81**, 865 (2009).

[29] J. S. Bell, *On the Einstein Podolsky Rosen Paradox*, Physics **1**, 195 (1964).

[30] A. Aspect, P. Grangier, and G. Roger, *Experimental Tests of Realistic Local Theories via Bell's Theorem*, Phys. Rev. Lett. **47**, 460 (1981).

[31] A. Aspect, P. Grangier, and G. Roger, *Experimental Realization of Einstein-Podolsky-Rosen-Bohm Gedankenexperiment : A New Violation of Bell's Inequalities*, Phys. Rev. Lett. **49**, 91 (1982).

[32] C. H. Bennett, G. Brassard, C. Crépeau, R. Jozsa, A. Peres, and W. K. Wootters, *Teleporting an unknown quantum state via dual classical and Einstein-Podolsky-Rosen channels*, Phys. Rev. Lett. **70**, 1895 (1993).

[33] R. F. Werner, *Quantum states with Einstein-Podolsky-Rosen correlations admitting a hidden-variable model*, Phys. Rev. A **40**, 4277 (1989).

[34] A. Peres, *Separability Criterion for Density Matrices*, Phys. Rev. Lett. **77**, 1413 (1996).

[35] M. Horodecki, P. Horodecki, and R. Horodecki, *Separability of mixed states: necessary and sufficient conditions*, Phys. Lett. A **223**, 1 (1996).

[36] C. H. Bennett, D. P. DiVincenzo, J. A. Smolin, and W. K. Wootters, *Mixed-state entanglement and quantum error correction*, Phys. Rev. A **54**, 3824 (1996).

[37] W. K. Wootters, *Entanglement of Formation of an Arbitrary State of Two Qubits*, Phys. Rev. Lett. **80**, 2245 (1998).

[38] H. J. Kimble, *The quantum internet*, Nature **453**, 1023 (2008).

[39] C. Simon, M. Afzelius, J. Appel, A. Boyer de la Giroday, S. J. Dewhurst, N. Gisin, C. Y. Hu, F. Jelezko, S. Kröll, J. H. Müller, J. Nunn, E. S. Polzik, J. G. Rarity, H. De Riedmatten, W. Rosenfeld, A. J. Shields, N. Sköld, R. M. Stevenson, R. Thew, I. A. Walmsley, M. C. Weber, H. Weinfurter, J. Wrachtrup, and R. J. Young, *Quantum memories*, Eur. Phys. J. D **58**, 1 (2010).

[40] W. K. Wootters and W. H. Zurek, *A single quantum cannot be cloned*, Nature **299**, 802 (1982).

[41] J. I. Cirac, A. K. Ekert, S. F. Huelga, and C. Macchiavello, *Distributed quantum computation over noisy channels*, Phys. Rev. A **59**, 4249 (1999).

[42] L.-M. Duan and C. Monroe, *Colloquium: Quantum networks with trapped ions*, Rev. Mod. Phys. **82**, 1209 (2010).

[43] M. Żukowski, A. Zeilinger, M. A. Horne, and A. K. Ekert, *"Event-ready-detectors" Bell experiment via entanglement swapping*, Phys. Rev. Lett. **71**, 4287 (1993).

[44] C. H. Bennett, H. J. Bernstein, S. Popescu, and B. Schumacher, *Concentrating partial entanglement by local operations*, Phys. Rev. A **53**, 2046 (1996).

[45] W. Dür and H.-J. Briegel, *Purification and Distillation*, in *Lectures on Quantum Information* (edited by D. Bruß and G. Leuchs), chapter 11, 177–208, Wiley-VCH Verlag GmbH, Weinheim (2008).

[46] A. Auer and G. Burkard, *Entangled photons from the polariton vacuum in a switchable optical cavity*, Phys. Rev. B **85**, 235140 (2012).

[47] P. Neumann, N. Mizuochi, F. Rempp, P. Hemmer, H. Watanabe, S. Yamasaki, V. Jacques, T. Gaebel, F. Jelezko, and J. Wrachtrup, *Multipartite Entanglement Among Single Spins in Diamond*, Science **320**, 1326 (2008).

[48] R. Brunner, Y.-S. Shin, T. Obata, M. Pioro-Ladrière, T. Kubo, K. Yoshida, T. Taniyama, Y. Tokura, and S. Tarucha, *Two-Qubit Gate of Combined Single-Spin Rotation and Inter-dot Spin Exchange in a Double Quantum Dot*, Phys. Rev. Lett. **107**, 146801 (2011).

[49] G. D. Fuchs, G. Burkard, P. V. Klimov, and D. D. Awschalom, *A quantum memory intrinsic to single nitrogen-vacancy centres in diamond*, Nature Phys. **7**, 789 (2011).

[50] W. Pfaff, T. H. Taminiau, L. Robledo, H. Bernien, M. Markham, D. J. Twitchen, and R. Hanson, *Demonstration of entanglement-by-measurement of solid-state qubits*, Nature Phys. **9**, 29 (2013).

[51] H. Bernien, B. Hensen, W. Pfaff, G. Koolstra, M. S. Blok, L. Robledo, T. H. Taminiau, M. Markham, D. J. Twitchen, L. Childress, and R. Hanson, *Heralded entanglement between solid-state qubits separated by three metres*, Nature **497**, 86 (2013).

[52] W. Pfaff, B. J. Hensen, H. Bernien, S. B. van Dam, M. S. Blok, T. H. Taminiau, M. J. Tiggelman, R. N. Schouten, M. Markham, D. J. Twitchen, and R. Hanson, *Unconditional quantum teleportation between distant solid-state quantum bits*, Science **345**, 532 (2014).

[53] K. Edamatsu, *Entangled Photons: Generation, Observation, and Characterization*, Jpn. J. Appl. Phys. **46**, 7175 (2007).

[54] P. G. Kwiat, K. Mattle, H. Weinfurter, A. Zeilinger, A. V. Sergienko, and Y. Shih, *New High-Intensity Source of Polarization-Entangled Photon Pairs*, Phys. Rev. Lett. **75**, 4337 (1995).

[55] O. Benson, C. Santori, M. Pelton, and Y. Yamamoto, *Regulated and Entangled Photons from a Single Quantum Dot*, Phys. Rev. Lett. **84**, 2513 (2000).

[56] C. Ciuti, G. Bastard, and I. Carusotto, *Quantum vacuum properties of the intersubband cavity polariton field*, Phys. Rev. B **72**, 115303 (2005).

[57] H. C. Liu and F. Capasso (Editors), *Intersubband Transitions in Quantum Wells: Physics and Device Applications I*, volume 62 of *Semiconductors and Semimetals*, Academic Press, San Diego (1999).

[58] H. C. Liu and F. Capasso (Editors), *Intersubband Transitions in Quantum Wells: Physics and Device Applications II*, volume 66 of *Semiconductors and Semimetals*, Academic Press, San Diego (1999).

[59] J. Faist, F. Capasso, D. L. Sivco, C. Sirtori, A. L. Hutchinson, and A. Y. Cho, *Quantum Cascade Laser*, Science **264**, 553 (1994).

[60] R. Kohler, A. Tredicucci, F. Beltram, H. E. Beere, E. H. Linfield, A. G. Davies, D. A. Ritchie, R. C. Iotti, and F. Rossi, *Terahertz semiconductor-heterostructure laser*, Nature **417**, 156 (2002).

[61] R. Colombelli, K. Srinivasan, M. Troccoli, O. Painter, C. F. Gmachl, D. M. Tennant, A. M. Sergent, D. L. Sivco, A. Y. Cho, and F. Capasso, *Quantum Cascade Surface-Emitting Photonic Crystal Laser*, Science **302**, 1374 (2003).

[62] G. Günter, A. A. Anappara, J. Hees, A. Sell, G. Biasiol, L. Sorba, S. De Liberato, C. Ciuti, A. Tredicucci, A. Leitenstorfer, and R. Huber, *Sub-cycle switch-on of ultrastrong light-matter interaction*, Nature **458**, 178 (2009).

[63] A. A. Anappara, S. De Liberato, A. Tredicucci, C. Ciuti, G. Biasiol, L. Sorba, and F. Beltram, *Signatures of the ultrastrong light-matter coupling regime*, Phys. Rev. B **79**, 201303 (2009).

[64] Y. Todorov, A. M. Andrews, R. Colombelli, S. De Liberato, C. Ciuti, P. Klang, G. Strasser, and C. Sirtori, *Ultrastrong Light-Matter Coupling Regime with Polariton Dots*, Phys. Rev. Lett. **105**, 196402 (2010).

[65] M. Geiser, F. Castellano, G. Scalari, M. Beck, L. Nevou, and J. Faist, *Ultrastrong Coupling Regime and Plasmon Polaritons in Parabolic Semiconductor Quantum Wells*, Phys. Rev. Lett. **108**, 106402 (2012).

[66] J. Bourassa, J. M. Gambetta, A. A. Abdumalikov, O. Astafiev, Y. Nakamura, and A. Blais, *Ultrastrong coupling regime of cavity QED with phase-biased flux qubits*, Phys. Rev. A **80**, 032109 (2009).

[67] T. Niemczyk, F. Deppe, H. Huebl, E. P. Menzel, F. Hocke, M. J. Schwarz, J. J. Garcia-Ripoll, D. Zueco, T. Hummer, E. Solano, A. Marx, and R. Gross, *Circuit quantum electrodynamics in the ultrastrong-coupling regime*, Nature Phys. **6**, 772 (2010).

[68] P. Forn-Díaz, J. Lisenfeld, D. Marcos, J. J. García-Ripoll, E. Solano, C. J. P. M. Harmans, and J. E. Mooij, *Observation of the Bloch-Siegert Shift in a Qubit-Oscillator System in the Ultrastrong Coupling Regime*, Phys. Rev. Lett. **105**, 237001 (2010).

[69] C. M. Wilson, G. Johansson, A. Pourkabirian, M. Simoen, J. R. Johansson, T. Duty, F. Nori, and P. Delsing, *Observation of the dynamical Casimir effect in a superconducting circuit*, Nature **479**, 376 (2011).

[70] D. Bouwmeester, J.-W. Pan, K. Mattle, M. Eibl, H. Weinfurter, and A. Zeilinger, *Experimental quantum teleportation*, Nature **390**, 575 (1997).

[71] P. G. Kwiat, E. Waks, A. G. White, I. Appelbaum, and P. H. Eberhard, *Ultrabright source of polarization-entangled photons*, Phys. Rev. A **60**, R773 (1999).

[72] R. M. Stevenson, R. J. Young, P. Atkinson, K. Cooper, D. A. Ritchie, and A. J. Shields, *A semiconductor source of triggered entangled photon pairs*, Nature **439**, 179 (2006).

[73] E. Welander, *Spin and Photon Coherence and Entanglement in Semiconductor Quantum Dots*, Ph.D. thesis, Universität Konstanz (2014).

[74] R. J. Young, R. M. Stevenson, P. Atkinson, K. Cooper, D. A. Ritchie, and A. J. Shields, *Improved fidelity of triggered entangled photons from single quantum dots*, New J. Phys. **8**, 29 (2006).

[75] N. Akopian, N. H. Lindner, E. Poem, Y. Berlatzky, J. Avron, D. Gershoni, B. D. Gerardot, and P. M. Petroff, *Entangled Photon Pairs from Semiconductor Quantum Dots*, Phys. Rev. Lett. **96**, 130501 (2006).

[76] A. Muller, W. Fang, J. Lawall, and G. S. Solomon, *Creating Polarization-Entangled Photon Pairs from a Semiconductor Quantum Dot Using the Optical Stark Effect*, Phys. Rev. Lett. **103**, 217402 (2009).

[77] A. Dousse, J. Suffczynski, A. Beveratos, O. Krebs, A. Lemaitre, I. Sagnes, J. Bloch, P. Voisin, and P. Senellart, *Ultrabright source of entangled photon pairs*, Nature **466**, 217 (2010).

[78] A. Liu, *Rabi splitting of the optical intersubband absorption line of multiple quantum wellsinside a Fabry-Pérot microcavity*, Phys. Rev. B **55**, 7101 (1997).

[79] D. E. Nikonov, A. Imamoğlu, L. V. Butov, and H. Schmidt, *Collective Intersubband Excitations in Quantum Wells: Coulomb Interaction versus Subband Dispersion*, Phys. Rev. Lett. **79**, 4633 (1997).

[80] S. De Liberato and C. Ciuti, *Quantum theory of intersubband polarons*, Phys. Rev. B **85**, 125302 (2012).

[81] Y. Todorov and C. Sirtori, *Intersubband polaritons in the electrical dipole gauge*, Phys. Rev. B **85**, 045304 (2012).

[82] S. De Liberato, *Cavity quantum electrodynamics and intersubband polaritonics of a two-dimensional electron gas*, Ph.D. thesis, Université Paris Diderot (Paris 7) (2009).

[83] S. De Liberato and C. Ciuti, *Stimulated Scattering and Lasing of Intersubband Cavity Polaritons*, Phys. Rev. Lett. **102**, 136403 (2009).

[84] D. Hagenmüller, S. De Liberato, and C. Ciuti, *Ultrastrong coupling between a cavity resonator and the cyclotron transition of a two-dimensional electron gas in the case of an integer filling factor*, Phys. Rev. B **81**, 235303 (2010).

[85] J. J. Hopfield, *Theory of the Contribution of Excitons to the Complex Dielectric Constant of Crystals*, Phys. Rev. **112**, 1555 (1958).

[86] D. Dini, R. Köhler, A. Tredicucci, G. Biasiol, and L. Sorba, *Microcavity Polariton Splitting of Intersubband Transitions*, Phys. Rev. Lett. **90**, 116401 (2003).

[87] A. A. Anappara, A. Tredicucci, G. Biasiol, and L. Sorba, *Electrical control of polariton coupling in intersubband microcavities*, Appl. Phys. Lett. **87**, 051105 (2005).

[88] A. A. Anappara, A. Tredicucci, F. Beltram, G. Biasiol, and L. Sorba, *Tunnel-assisted manipulation of intersubband polaritons in asymmetric coupled quantum wells*, Appl. Phys. Lett. **89**, 171109 (2006).

[89] D. Walls and G. Milburn, *Quantum Optics*, Springer, Berlin (2008).

[90] A. Quattropani, L. Andreani, and F. Bassani, *Quantum theory of polaritons with spatial dispersion: Exact solutions*, Nuovo Cimento D **7**, 55 (1986).

[91] A. Auer, *Generation of entangled photon pairs from the polariton vacuum in a switchable optical cavity*, Diploma thesis, Universität Konstanz (2011).

[92] C. Ciuti and I. Carusotto, *Input-output theory of cavities in the ultrastrong coupling regime: The case of time-independent cavity parameters*, Phys. Rev. A **74**, 033811 (2006).

[93] S. D. Liberato, C. Ciuti, and I. Carusotto, *Quantum Vacuum Radiation Spectra from a Semiconductor Microcavity with a Time-Modulated Vacuum Rabi Frequency*, Phys. Rev. Lett. **98**, 103602 (2007).

[94] R. Huber, A. A. Anappara, G. Günter, A. Sell, S. De Liberato, C. Ciuti, G. Biasiol, L. Sorba, A. Tredicucci, and A. Leitenstorfer, *Switching ultrastrong light–matter coupling on a subcycle scale*, J. Appl. Phys. **109**, 102418 (2011).

[95] M. Porer, J.-M. Ménard, A. Leitenstorfer, R. Huber, R. Degl'Innocenti, S. Zanotto, G. Biasiol, L. Sorba, and A. Tredicucci, *Nonadiabatic switching of a photonic band structure: Ultrastrong light-matter coupling and slow-down of light*, Phys. Rev. B **85**, 081302 (2012).

[96] A. Ridolfo, R. Vilardi, O. Di Stefano, S. Portolan, and S. Savasta, *All Optical Switch of Vacuum Rabi Oscillations: The Ultrafast Quantum Eraser*, Phys. Rev. Lett. **106**, 013601 (2011).

[97] C. H. Bennett and S. J. Wiesner, *Communication via one- and two-particle operators on Einstein-Podolsky-Rosen states*, Phys. Rev. Lett. **69**, 2881 (1992).

[98] A. Auer and G. Burkard, *Entanglement purification with the exchange interaction*, Phys. Rev. A **90**, 022320 (2014).

[99] J. Berezovsky, M. H. Mikkelsen, N. G. Stoltz, L. A. Coldren, and D. D. Awschalom, *Picosecond Coherent Optical Manipulation of a Single Electron Spin in a Quantum Dot*, Science **320**, 349 (2008).

[100] R. Vrijen and E. Yablonovitch, *A spin-coherent semiconductor photo-detector for quantum communication*, Physica E **10**, 569 (2001).

[101] P. G. Kwiat, S. Barraza-Lopez, A. Stefanov, and N. Gisin, *Experimental entanglement distillation and 'hidden' non-locality*, Nature **409**, 1014 (2001).

[102] Z. Zhao, T. Yang, Y.-A. Chen, A.-N. Zhang, and J.-W. Pan, *Experimental Realization of Entanglement Concentration and a Quantum Repeater*, Phys. Rev. Lett. **90**, 207901 (2003).

[103] T. Yamamoto, M. Koashi, S. K. Ozdemir, and N. Imoto, *Experimental extraction of an entangled photon pair from two identically decohered pairs*, Nature **421**, 343 (2003).

[104] J.-W. Pan, S. Gasparoni, R. Ursin, G. Weihs, and A. Zeilinger, *Experimental entanglement purification of arbitrary unknown states*, Nature **423**, 417 (2003).

[105] T. Yamamoto, M. Koashi, and N. Imoto, *Concentration and purification scheme for two partially entangled photon pairs*, Phys. Rev. A **64**, 012304 (2001).

[106] R. Reichle, D. Leibfried, E. Knill, J. Britton, R. B. Blakestad, J. D. Jost, C. Langer, R. Ozeri, S. Seidelin, and D. J. Wineland, *Experimental purification of two-atom entanglement*, Nature **443**, 838 (2006).

[107] T. Tanamoto, K. Maruyama, Y.-x. Liu, X. Hu, and F. Nori, *Efficient purification protocols using* iSWAP *gates in solid-state qubits*, Phys. Rev. A **78**, 062313 (2008).

[108] K. Maruyama and F. Nori, *Entanglement purification without controlled-NOT gates by using the natural dynamics of spin chains*, Phys. Rev. A **78**, 022312 (2008).

[109] D. Gonţa and P. van Loock, *Dynamical entanglement purification using chains of atoms and optical cavities*, Phys. Rev. A **84**, 042303 (2011).

[110] D. Gonţa and P. van Loock, *High-fidelity entanglement purification using chains of atoms and optical cavities*, Phys. Rev. A **86**, 052312 (2012).

[111] J. M. Taylor, W. Dür, P. Zoller, A. Yacoby, C. M. Marcus, and M. D. Lukin, *Solid-State Circuit for Spin Entanglement Generation and Purification*, Phys. Rev. Lett. **94**, 236803 (2005).

[112] Y. Makhlin, G. Schön, and A. Shnirman, *Quantum-state engineering with Josephson-junction devices*, Rev. Mod. Phys. **73**, 357 (2001).

[113] A. Imamoğlu, D. D. Awschalom, G. Burkard, D. P. DiVincenzo, D. Loss, M. Sherwin, and A. Small, *Quantum Information Processing Using Quantum Dot Spins and Cavity QED*, Phys. Rev. Lett. **83**, 4204 (1999).

[114] J. R. Petta, A. C. Johnson, J. M. Taylor, E. A. Laird, A. Yacoby, M. D. Lukin, C. M. Marcus, M. P. Hanson, and A. C. Gossard, *Coherent Manipulation of Coupled Electron Spins in Semiconductor Quantum Dots*, Science **309**, 2180 (2005).

[115] J. M. Elzerman, R. Hanson, L. H. Willems van Beveren, B. Witkamp, L. M. K. Vandersypen, and L. P. Kouwenhoven, *Single-shot read-out of an individual electron spin in a quantum dot*, Nature **430**, 431 (2004).

[116] R. Hanson, L. H. W. van Beveren, I. T. Vink, J. M. Elzerman, W. J. M. Naber, F. H. L. Koppens, L. P. Kouwenhoven, and L. M. K. Vandersypen, *Single-Shot Readout of Electron Spin States in a Quantum Dot Using Spin-Dependent Tunnel Rates*, Phys. Rev. Lett. **94**, 196802 (2005).

[117] S. Tarucha, D. G. Austing, T. Honda, R. J. van der Hage, and L. P. Kouwenhoven, *Shell Filling and Spin Effects in a Few Electron Quantum Dot*, Phys. Rev. Lett. **77**, 3613 (1996).

[118] G. Burkard, D. Loss, and D. P. DiVincenzo, *Coupled quantum dots as quantum gates*, Phys. Rev. B **59**, 2070 (1999).

[119] J. Levy, *Universal Quantum Computation with Spin-*1/2 *Pairs and Heisenberg Exchange*, Phys. Rev. Lett. **89**, 147902 (2002).

[120] J. R. Petta, H. Lu, and A. C. Gossard, *A Coherent Beam Splitter for Electronic Spin States*, Science **327**, 669 (2010).

[121] D. P. DiVincenzo, D. Bacon, J. Kempe, G. Burkard, and K. B. Whaley, *Universal quantum computation with the exchange interaction*, Nature **408**, 339 (2000).

[122] T. Hayashi, T. Fujisawa, H. D. Cheong, Y. H. Jeong, and Y. Hirayama, *Coherent Manipulation of Electronic States in a Double Quantum Dot*, Phys. Rev. Lett. **91**, 226804 (2003).

[123] F. H. L. Koppens, C. Buizert, K. J. Tielrooij, I. T. Vink, K. C. Nowack, T. Meunier, L. P. Kouwenhoven, and L. M. K. Vandersypen, *Driven coherent oscillations of a single electron spin in a quantum dot*, Nature **442**, 766 (2006).

[124] K. C. Nowack, F. H. L. Koppens, Y. V. Nazarov, and L. M. K. Vandersypen, *Coherent Control of a Single Electron Spin with Electric Fields*, Science **318**, 1430 (2007).

[125] M. Pioro-Ladriere, T. Obata, Y. Tokura, Y. S. Shin, T. Kubo, K. Yoshida, T. Taniyama, and S. Tarucha, *Electrically driven single-electron spin resonance in a slanting Zeeman field*, Nature Phys. **4**, 776 (2008).

[126] J. M. Elzerman, R. Hanson, J. S. Greidanus, L. H. Willems van Beveren, S. De Franceschi, L. M. K. Vandersypen, S. Tarucha, and L. P. Kouwenhoven, *Few-electron quantum dot circuit with integrated charge read out*, Phys. Rev. B **67**, 161308 (2003).

[127] K. C. Nowack, M. Shafiei, M. Laforest, G. E. D. K. Prawiroatmodjo, L. R. Schreiber, C. Reichl, W. Wegscheider, and L. M. K. Vandersypen, *Single-Shot Correlations and Two-Qubit Gate of Solid-State Spins*, Science **333**, 1269 (2011).

[128] C. B. Simmons, J. R. Prance, B. J. Van Bael, T. S. Koh, Z. Shi, D. E. Savage, M. G. Lagally, R. Joynt, M. Friesen, S. N. Coppersmith, and M. A. Eriksson, *Tunable Spin Loading and T_1 of a Silicon Spin Qubit Measured by Single-Shot Readout*, Phys. Rev. Lett. **106**, 156804 (2011).

[129] I. van Weperen, B. D. Armstrong, E. A. Laird, J. Medford, C. M. Marcus, M. P. Hanson, and A. C. Gossard, *Charge-State Conditional Operation of a Spin Qubit*, Phys. Rev. Lett. **107**, 030506 (2011).

[130] L. Gaudreau, G. Granger, A. Kam, G. C. Aers, S. A. Studenikin, P. Zawadzki, M. Pioro-Ladriere, Z. R. Wasilewski, and A. S. Sachrajda, *Coherent control of three-spin states in a triple quantum dot*, Nature Phys. **8**, 54 (2012).

[131] B. M. Maune, M. G. Borselli, B. Huang, T. D. Ladd, P. W. Deelman, K. S. Holabird, A. A. Kiselev, I. Alvarado-Rodriguez, R. S. Ross, A. E. Schmitz, M. Sokolich, C. A. Watson, M. F. Gyure, and A. T. Hunter, *Coherent singlet-triplet oscillations in a silicon-based double quantum dot*, Nature **481**, 344 (2012).

[132] S. Amasha, K. MacLean, I. P. Radu, D. M. Zumbühl, M. A. Kastner, M. P. Hanson, and A. C. Gossard, *Electrical Control of Spin Relaxation in a Quantum Dot*, Phys. Rev. Lett. **100**, 046803 (2008).

[133] F. H. L. Koppens, K. C. Nowack, and L. M. K. Vandersypen, *Spin Echo of a Single Electron Spin in a Quantum Dot*, Phys. Rev. Lett. **100**, 236802 (2008).

[134] J.-W. Pan, C. Simon, C. Brukner, and A. Zeilinger, *Entanglement purification for quantum communication*, Nature **410**, 1067 (2001).

[135] D. M. Zumbühl, C. M. Marcus, M. P. Hanson, and A. C. Gossard, *Cotunneling Spectroscopy in Few-Electron Quantum Dots*, Phys. Rev. Lett. **93**, 256801 (2004).

[136] A. Abragam, *Principles of Nuclear Magnetism*, Oxford University Press, Oxford (1961).

[137] P. Neumann, R. Kolesov, B. Naydenov, J. Beck, F. Rempp, M. Steiner, V. Jacques, G. Balasubramanian, M. L. Markham, D. J. Twitchen, S. Pezzagna, J. Meijer, J. Twamley, F. Jelezko, and J. Wrachtrup, *Quantum register based on coupled electron spins in a room-temperature solid*, Nature Phys. **6**, 249 (2010).

[138] W. A. Coish and D. Loss, *Exchange-controlled single-electron-spin rotations in quantum dots*, Phys. Rev. B **75**, 161302 (2007).

[139] G. Cao, H.-O. Li, T. Tu, L. Wang, C. Zhou, M. Xiao, G.-C. Guo, H.-W. Jiang, and G.-P. Guo, *Ultrafast universal quantum control of a quantum-dot charge qubit using Landau–Zener–Stückelberg interference*, Nat. Commun. **4**, 1401 (2013).

[140] D. Press, T. D. Ladd, B. Zhang, and Y. Yamamoto, *Complete quantum control of a single quantum dot spin using ultrafast optical pulses*, Nature **456**, 218 (2008).

[141] B. E. Kane, *A silicon-based nuclear spin quantum computer*, Nature **393**, 133 (1998).

[142] J. J. L. Morton, A. M. Tyryshkin, R. M. Brown, S. Shankar, B. W. Lovett, A. Ardavan, T. Schenkel, E. E. Haller, J. W. Ager, and S. A. Lyon, *Solid-state quantum memory using the 31P nuclear spin*, Nature **455**, 1085 (2008).

[143] K. Saeedi, S. Simmons, J. Z. Salvail, P. Dluhy, H. Riemann, N. V. Abrosimov, P. Becker, H.-J. Pohl, J. J. L. Morton, and M. L. W. Thewalt, *Room-Temperature Quantum Bit Storage Exceeding 39 Minutes Using Ionized Donors in Silicon-28*, Science **342**, 830 (2013).

[144] J. R. Weber, W. F. Koehl, J. B. Varley, A. Janotti, B. B. Buckley, C. G. Van de Walle, and D. D. Awschalom, *Quantum computing with defects*, Proc. Nat. Acad. Sci. U.S.A. **107**, 8513 (2010).

[145] D. J. Christle, A. L. Falk, P. Andrich, P. V. Klimov, J. U. Hassan, N. T. Son, E. Janzén, T. Ohshima, and D. D. Awschalom, *Isolated electron spins in silicon carbide with millisecond coherence times*, Nature Mater. **14**, 160 (2015).

[146] C. Kurtsiefer, S. Mayer, P. Zarda, and H. Weinfurter, *Stable Solid-State Source of Single Photons*, Phys. Rev. Lett. **85**, 290 (2000).

[147] J. M. Taylor, P. Cappellaro, L. Childress, L. Jiang, D. Budker, P. R. Hemmer, A. Yacoby, R. Walsworth, and M. D. Lukin, *High-sensitivity diamond magnetometer with nanoscale resolution*, Nature Phys. **4**, 810 (2008).

[148] R. Schirhagl, K. Chang, M. Loretz, and C. L. Degen, *Nitrogen-Vacancy Centers in Diamond: Nanoscale Sensors for Physics and Biology*, Annu. Rev. Phys. Chem. **65**, 83 (2014).

[149] P. C. Maurer, G. Kucsko, C. Latta, L. Jiang, N. Y. Yao, S. D. Bennett, F. Pastawski, D. Hunger, N. Chisholm, M. Markham, D. J. Twitchen, J. I. Cirac, and M. D. Lukin, *Room-Temperature Quantum Bit Memory Exceeding One Second*, Science **336**, 1283 (2012).

[150] B. Smeltzer, J. McIntyre, and L. Childress, *Robust control of individual nuclear spins in diamond*, Phys. Rev. A **80**, 050302 (2009).

[151] S. Sangtawesin, T. O. Brundage, and J. R. Petta, *Fast Room-Temperature Phase Gate on a Single Nuclear Spin in Diamond*, Phys. Rev. Lett. **113**, 020506 (2014).

[152] P. Neumann, J. Beck, M. Steiner, F. Rempp, H. Fedder, P. R. Hemmer, J. Wrachtrup, and F. Jelezko, *Single-Shot Readout of a Single Nuclear Spin*, Science **329**, 542 (2010).

[153] F. Dolde, I. Jakobi, B. Naydenov, N. Zhao, S. Pezzagna, C. Trautmann, J. Meijer, P. Neumann, F. Jelezko, and J. Wrachtrup, *Room-temperature entanglement between single defect spins in diamond*, Nature Phys. **9**, 139 (2013).

[154] F. Dolde, V. Bergholm, Y. Wang, I. Jakobi, B. Naydenov, S. Pezzagna, J. Meijer, F. Jelezko, P. Neumann, T. Schulte-Herbrüggen, J. Biamonte, and J. Wrachtrup, *High-fidelity spin entanglement using optimal control*, Nat. Commun. **5** (2014).

[155] T. H. Taminiau, J. Cramer, T. van der Sar, V. V. Dobrovitski, and R. Hanson, *Universal control and error correction in multi-qubit spin registers in diamond*, Nature Nanotech. **9**, 171 (2014).

[156] L. Childress, J. Taylor, A. Sørensen, and M. Lukin, *Fault-tolerant quantum repeaters with minimal physical resources and implementations based on single-photon emitters*, Phys. Rev. A **72**, 052330 (2005).

[157] L. Childress, J. Taylor, A. Sørensen, and M. Lukin, *Fault-Tolerant Quantum Communication Based on Solid-State Photon Emitters*, Phys. Rev. Lett. **96**, 070504 (2006).

[158] A. Bermudez, F. Jelezko, M. B. Plenio, and A. Retzker, *Electron-Mediated Nuclear-Spin Interactions between Distant Nitrogen-Vacancy Centers*, Phys. Rev. Lett. **107**, 150503 (2011).

[159] K. Nemoto, M. Trupke, S. J. Devitt, A. M. Stephens, B. Scharfenberger, K. Buczak, T. Nöbauer, M. S. Everitt, J. Schmiedmayer, and W. J. Munro, *Photonic Architecture for Scalable Quantum Information Processing in Diamond*, Phys. Rev. X **4**, 031022 (2014).

[160] G. Burkard and D. D. Awschalom, *A cavity-mediated quantum CPHASE gate between NV spin qubits in diamond*, arXiv:1402.6351 (2014).

[161] I. Vlasov, V. Ralchenko, A. Khomich, S. Nistor, D. Shoemaker, and R. Khmelnitskii, *Relative Abundance of Single and Vacancy-Bonded Substitutional Nitrogen in CVD Diamond*, Phys. Status Solidi A **181**, 83 (2000).

[162] J. Meijer, B. Burchard, M. Domhan, C. Wittmann, T. Gaebel, I. Popa, F. Jelezko, and J. Wrachtrup, *Generation of single color centers by focused nitrogen implantation*, Appl. Phys. Lett. **87**, 261909 (2005).

[163] D. D. Awschalom, L. C. Bassett, A. S. Dzurak, E. L. Hu, and J. R. Petta, *Quantum Spintronics: Engineering and Manipulating Atom-Like Spins in Semiconductors*, Science **339**, 1174 (2013).

[164] G. Davies, *Charge states of the vacancy in diamond*, Nature **269**, 498 (1977).

[165] A. Gali, M. Fyta, and E. Kaxiras, *Ab initio supercell calculations on nitrogen-vacancy center in diamond: Electronic structure and hyperfine tensors*, Phys. Rev. B **77**, 155206 (2008).

[166] M. W. Doherty, N. B. Manson, P. Delaney, and L. C. L. Hollenberg, *The negatively charged nitrogen-vacancy centre in diamond: the electronic solution*, New J. Phys. **13**, 025019 (2011).

[167] J. R. Maze, A. Gali, E. Togan, Y. Chu, A. Trifonov, E. Kaxiras, and M. D. Lukin, *Properties of nitrogen-vacancy centers in diamond: the group theoretic approach*, New J. Phys. **13**, 025025 (2011).

[168] J. H. N. Loubser and J. A. van Wyk, *Electron spin resonance in the study of diamond*, Rep. Prog. Phys. **41**, 1201 (1978).

[169] X.-F. He, N. B. Manson, and P. T. H. Fisk, *Paramagnetic resonance of photoexcited N- V defects in diamond. I. Level anticrossing in the* ^{3} *A ground state*, Phys. Rev. B **47**, 8809 (1993).

[170] N. B. Manson, J. P. Harrison, and M. J. Sellars, *Nitrogen-vacancy center in diamond: Model of the electronic structure and associated dynamics*, Phys. Rev. B **74**, 104303 (2006).

[171] G. D. Fuchs, A. L. Falk, V. V. Dobrovitski, and D. D. Awschalom, *Spin Coherence during Optical Excitation of a Single Nitrogen-Vacancy Center in Diamond*, Phys. Rev. Lett. **108**, 157602 (2012).

[172] A. Batalov, C. Zierl, T. Gaebel, P. Neumann, I.-Y. Chan, G. Balasubramanian, P. R. Hemmer, F. Jelezko, and J. Wrachtrup, *Temporal Coherence of Photons Emitted by Single Nitrogen-Vacancy Defect Centers in Diamond Using Optical Rabi-Oscillations*, Phys. Rev. Lett. **100**, 077401 (2008).

[173] J. Harrison, M. Sellars, and N. Manson, *Optical spin polarisation of the N-V centre in diamond*, J. Lumin. **107**, 245 (2004).

[174] G. Balasubramanian, P. Neumann, D. Twitchen, M. Markham, R. Kolesov, N. Mizuochi, J. Isoya, J. Achard, J. Beck, J. Tissler, V. Jacques, P. R. Hemmer, F. Jelezko, and J. Wrachtrup, *Ultralong spin coherence time in isotopically engineered diamond*, Nature Mater. **8**, 383 (2009).

[175] T. Yamamoto, T. Umeda, K. Watanabe, S. Onoda, M. Markham, D. Twitchen, B. Naydenov, L. McGuinness, T. Teraji, S. Koizumi, F. Dolde, H. Fedder, J. Honert, J. Wrachtrup, T. Ohshima, F. Jelezko, and J. Isoya, *Extending spin coherence times of diamond qubits by high-temperature annealing*, Phys. Rev. B **88**, 075206 (2013).

[176] N. Bar-Gill, L. M. Pham, A. Jarmola, D. Budker, and R. L. Walsworth, *Solid-state electronic spin coherence time approaching one second*, Nat. Commun. **4**, 1743 (2013).

[177] A. Jarmola, V. Acosta, K. Jensen, S. Chemerisov, and D. Budker, *Temperature- and Magnetic-Field-Dependent Longitudinal Spin Relaxation in Nitrogen-Vacancy Ensembles in Diamond*, Phys. Rev. Lett. **108**, 197601 (2012).

[178] L. Childress, M. V. Gurudev Dutt, J. M. Taylor, A. S. Zibrov, F. Jelezko, J. Wrachtrup, P. R. Hemmer, and M. D. Lukin, *Coherent Dynamics of Coupled Electron and Nuclear Spin Qubits in Diamond*, Science **314**, 281 (2006).

[179] J. R. Maze, J. M. Taylor, and M. D. Lukin, *Electron spin decoherence of single nitrogen-vacancy defects in diamond*, Phys. Rev. B **78**, 094303 (2008).

[180] R. Hanson, V. V. Dobrovitski, A. E. Feiguin, O. Gywat, and D. D. Awschalom, *Coherent Dynamics of a Single Spin Interacting with an Adjustable Spin Bath*, Science **320**, 352 (2008).

[181] A. Batalov, V. Jacques, F. Kaiser, P. Siyushev, P. Neumann, L. J. Rogers, R. L. McMurtrie, N. B. Manson, F. Jelezko, and J. Wrachtrup, *Low Temperature Studies of the Excited-State Structure of Negatively Charged Nitrogen-Vacancy Color Centers in Diamond*, Phys. Rev. Lett. **102**, 195506 (2009).

[182] L. J. Rogers, R. L. McMurtrie, M. J. Sellars, and N. B. Manson, *Time-averaging within the excited state of the nitrogen-vacancy centre in diamond*, New J. Phys. **11**, 063007 (2009).

[183] P. Tamarat, N. B. Manson, J. P. Harrison, R. L. McMurtrie, A. Nizovtsev, C. Santori, R. G. Beausoleil, P. Neumann, T. Gaebel, F. Jelezko, P. Hemmer, and J. Wrachtrup, *Spin-flip and spin-conserving optical transitions of the nitrogen-vacancy centre in diamond*, New J. Phys. **10**, 045004 (2008).

[184] G. D. Fuchs, V. V. Dobrovitski, R. Hanson, A. Batra, C. D. Weis, T. Schenkel, and D. D. Awschalom, *Excited-State Spectroscopy Using Single Spin Manipulation in Diamond*, Phys. Rev. Lett. **101**, 117601 (2008).

[185] P. Neumann, R. Kolesov, V. Jacques, J. Beck, J. Tisler, A. Batalov, L. Rogers, N. B. Manson, G. Balasubramanian, F. Jelezko, and J. Wrachtrup, *Excited-state spectroscopy of single NV defects in diamond using optically detected magnetic resonance*, New J. Phys. **11**, 013017 (2009).

[186] L. C. Bassett, F. J. Heremans, D. J. Christle, C. G. Yale, G. Burkard, B. B. Buckley, and D. D. Awschalom, *Ultrafast optical control of orbital and spin dynamics in a solid-state defect*, Science **345**, 1333 (2014).

[187] C. P. Slichter, *Principles of Magnetic Resonance*, Springer, Berlin (1990).

[188] S. Felton, A. M. Edmonds, M. E. Newton, P. M. Martineau, D. Fisher, D. J. Twitchen, and J. M. Baker, *Hyperfine interaction in the ground state of the negatively charged nitrogen vacancy center in diamond*, Phys. Rev. B **79**, 075203 (2009).

[189] A. Gali, *Identification of individual ^{13}C isotopes of nitrogen-vacancy center in diamond by combining the polarization studies of nuclear spins and first-principles calculations*, Phys. Rev. B **80**, 241204 (2009).

[190] R. K. Harris, E. D. Becker, S. M. Cabral de Menzes, R. Goodfellow, and P. Granger, *NMR nomenclature. Nuclear spin properties and conventions for chemical shifts(IUPAC Recommendations 2001)*, Pure Appl. Chem. **73**, 1795 (2001).

[191] M. Steiner, P. Neumann, J. Beck, F. Jelezko, and J. Wrachtrup, *Universal enhancement of the optical readout fidelity of single electron spins at nitrogen-vacancy centers in diamond*, Phys. Rev. B **81**, 035205 (2010).

[192] A. Gruber, A. Dräbenstedt, C. Tietz, L. Fleury, J. Wrachtrup, and C. v. Borczyskowski, *Scanning Confocal Optical Microscopy and Magnetic Resonance on Single Defect Centers*, Science **276**, 2012 (1997).

[193] L. Robledo, L. Childress, H. Bernien, B. Hensen, P. F. A. Alkemade, and R. Hanson, *High-fidelity projective read-out of a solid-state spin quantum register*, Nature **477**, 574 (2011).

[194] L. Jiang, J. S. Hodges, J. R. Maze, P. Maurer, J. M. Taylor, D. G. Cory, P. R. Hemmer, R. L. Walsworth, A. Yacoby, A. S. Zibrov, and M. D. Lukin, *Repetitive Readout of a Single Electronic Spin via Quantum Logic with Nuclear Spin Ancillae*, Science **326**, 267 (2009).

[195] F. Jelezko, T. Gaebel, I. Popa, A. Gruber, and J. Wrachtrup, *Observation of Coherent Oscillations in a Single Electron Spin*, Phys. Rev. Lett. **92**, 076401 (2004).

[196] T. Gaebel, M. Domhan, I. Popa, C. Wittmann, P. Neumann, F. Jelezko, J. R. Rabeau, N. Stavrias, A. D. Greentree, S. Prawer, J. Meijer, J. Twamley, P. R. Hemmer, and J. Wrachtrup, *Room-temperature coherent coupling of single spins in diamond*, Nature Phys. **2**, 408 (2006).

[197] M. V. G. Dutt, L. Childress, L. Jiang, E. Togan, J. Maze, F. Jelezko, A. S. Zibrov, P. R. Hemmer, and M. D. Lukin, *Quantum Register Based on Individual Electronic and Nuclear Spin Qubits in Diamond*, Science **316**, 1312 (2007).

[198] T. Kennedy, F. Charnock, J. Colton, J. Butler, R. Linares, and P. Doering, *Single-Qubit Operations with the Nitrogen-Vacancy Center in Diamond*, Phys. Status Solidi B **233**, 416 (2002).

[199] G. D. Fuchs, V. V. Dobrovitski, D. M. Toyli, F. J. Heremans, and D. D. Awschalom, *Gigahertz Dynamics of a Strongly Driven Single Quantum Spin*, Science **326**, 1520 (2009).

[200] F. Shi, X. Rong, N. Xu, Y. Wang, J. Wu, B. Chong, X. Peng, J. Kniepert, R.-S. Schoenfeld, W. Harneit, M. Feng, and J. Du, *Room-Temperature Implementation of the Deutsch-Jozsa Algorithm with a Single Electronic Spin in Diamond*, Phys. Rev. Lett. **105**, 040504 (2010).

[201] B. B. Buckley, G. D. Fuchs, L. C. Bassett, and D. D. Awschalom, *Spin-Light Coherence for Single-Spin Measurement and Control in Diamond*, Science **330**, 1212 (2010).

[202] C. G. Yale, B. B. Buckley, D. J. Christle, G. Burkard, F. J. Heremans, L. C. Bassett, and D. D. Awschalom, *All-optical control of a solid-state spin using coherent dark states*, Proc. Nat. Acad. Sci. U.S.A. **110**, 7595 (2013).

[203] M. Fleischhauer, A. Imamoglu, and J. P. Marangos, *Electromagnetically induced transparency: Optics in coherent media*, Rev. Mod. Phys. **77**, 633 (2005).

[204] S. Arroyo-Camejo, A. Lazariev, S. W. Hell, and G. Balasubramanian, *Room temperature high-fidelity holonomic single-qubit gate on a solid-state spin*, Nat. Commun. **5** (2014).

[205] D. M. Toyli, C. D. Weis, G. D. Fuchs, T. Schenkel, and D. D. Awschalom, *Chip-Scale Nanofabrication of Single Spins and Spin Arrays in Diamond*, Nano Lett. **10**, 3168 (2010).

[206] S. Pezzagna, D. Rogalla, H.-W. Becker, I. Jakobi, F. Dolde, B. Naydenov, J. Wrachtrup, F. Jelezko, C. Trautmann, and J. Meijer, *Creation of colour centres in diamond by collimated ion-implantation through nano-channels in mica*, Phys. Status Solidi A **208**, 2017 (2011).

[207] R. J. Epstein, F. M. Mendoza, Y. K. Kato, and D. D. Awschalom, *Anisotropic interactions of a single spin and dark-spin spectroscopy in diamond*, Nature Phys. **1**, 94 (2005).

[208] R. Hanson, F. Mendoza, R. Epstein, and D. Awschalom, *Polarization and Readout of Coupled Single Spins in Diamond*, Phys. Rev. Lett. **97**, 087601 (2006).

[209] E. Togan, Y. Chu, A. S. Trifonov, L. Jiang, J. Maze, L. Childress, M. V. G. Dutt, A. S. Sorensen, P. R. Hemmer, A. S. Zibrov, and M. D. Lukin, *Quantum entanglement between an optical photon and a solid-state spin qubit*, Nature **466**, 730 (2010).

[210] L. Bassett, F. Heremans, C. Yale, B. Buckley, and D. Awschalom, *Electrical Tuning of Single Nitrogen-Vacancy Center Optical Transitions Enhanced by Photoinduced Fields*, Phys. Rev. Lett. **107**, 266403 (2011).

[211] H. Bernien, L. Childress, L. Robledo, M. Markham, D. Twitchen, and R. Hanson, *Two-Photon Quantum Interference from Separate Nitrogen Vacancy Centers in Diamond*, Phys. Rev. Lett. **108**, 043604 (2012).

[212] A. Sipahigil, M. Goldman, E. Togan, Y. Chu, M. Markham, D. Twitchen, A. Zibrov, A. Kubanek, and M. Lukin, *Quantum Interference of Single Photons from Remote Nitrogen-Vacancy Centers in Diamond*, Phys. Rev. Lett. **108**, 143601 (2012).

[213] T. van der Sar, Z. H. Wang, M. S. Blok, H. Bernien, T. H. Taminiau, D. M. Toyli, D. A. Lidar, D. D. Awschalom, R. Hanson, and V. V. Dobrovitski, *Decoherence-protected quantum gates for a hybrid solid-state spin register*, Nature **484**, 82 (2012).

[214] G. Waldherr, Y. Wang, S. Zaiser, M. Jamali, T. Schulte-Herbruggen, H. Abe, T. Ohshima, J. Isoya, J. F. Du, P. Neumann, and J. Wrachtrup, *Quantum error correction in a solid-state hybrid spin register*, Nature **506**, 204 (2014).

[215] V. Jacques, P. Neumann, J. Beck, M. Markham, D. Twitchen, J. Meijer, F. Kaiser, G. Balasubramanian, F. Jelezko, and J. Wrachtrup, *Dynamic Polarization of Single Nuclear Spins by Optical Pumping of Nitrogen-Vacancy Color Centers in Diamond at Room Temperature*, Phys. Rev. Lett. **102**, 057403 (2009).

[216] A. Dréau, P. Spinicelli, J. R. Maze, J.-F. Roch, and V. Jacques, *Single-Shot Readout of Multiple Nuclear Spin Qubits in Diamond under Ambient Conditions*, Phys. Rev. Lett. **110**, 060502 (2013).

[217] F. Jelezko, T. Gaebel, I. Popa, M. Domhan, A. Gruber, and J. Wrachtrup, *Observation of Coherent Oscillation of a Single Nuclear Spin and Realization of a Two-Qubit Conditional Quantum Gate*, Phys. Rev. Lett. **93**, 130501 (2004).

[218] T. H. Taminiau, J. J. T. Wagenaar, T. van der Sar, F. Jelezko, V. V. Dobrovitski, and R. Hanson, *Detection and Control of Individual Nuclear Spins Using a Weakly Coupled Electron Spin*, Phys. Rev. Lett. **109**, 137602 (2012).

[219] Y.-S. Park, A. K. Cook, and H. Wang, *Cavity QED with Diamond Nanocrystals and Silica Microspheres*, Nano Lett. **6**, 2075 (2006).

[220] J. Riedrich-Moller, L. Kipfstuhl, C. Hepp, E. Neu, C. Pauly, F. Mucklich, A. Baur, M. Wandt, S. Wolff, M. Fischer, S. Gsell, M. Schreck, and C. Becher, *One- and two-dimensional photonic crystal microcavities in single crystal diamond*, Nature Nanotech. **7**, 69 (2012).

[221] J. R. Schrieffer and P. A. Wolff, *Relation between the Anderson and Kondo Hamiltonians*, Phys. Rev. **149**, 491 (1966).

[222] R. Winkler, *Quasi-Degenerate Perturbation Theory*, in *Spin–Orbit Coupling Effects in Two-Dimensional Electron and Hole Systems*, volume 191 of *Springer Tracts in Modern Physics*, 201–206, Springer, Berlin (2003).

[223] M. J. Burek, Y. Chu, M. S. Z. Liddy, P. Patel, J. Rochman, S. Meesala, W. Hong, Q. Quan, M. D. Lukin, and M. Lončar, *High quality-factor optical nanocavities in bulk single-crystal diamond*, Nat. Commun. **5**, 5718 (2014).

[224] L. Jiang, M. V. G. Dutt, E. Togan, L. Childress, P. Cappellaro, J. M. Taylor, and M. D. Lukin, *Coherence of an Optically Illuminated Single Nuclear Spin Qubit*, Phys. Rev. Lett. **100**, 073001 (2008).

[225] K. De Greve, L. Yu, P. L. McMahon, J. S. Pelc, C. M. Natarajan, N. Y. Kim, E. Abe, S. Maier, C. Schneider, M. Kamp, S. Hofling, R. H. Hadfield, A. Forchel, M. M. Fejer, and Y. Yamamoto, *Quantum-dot spin-photon entanglement via frequency downconversion to telecom wavelength*, Nature **491**, 421 (2012).

[226] W. B. Gao, P. Fallahi, E. Togan, J. Miguel-Sanchez, and A. Imamoglu, *Observation of entanglement between a quantum dot spin and a single photon*, Nature **491**, 426 (2012).

[227] W. B. Gao, P. Fallahi, E. Togan, A. Delteil, Y. S. Chin, J. Miguel-Sanchez, and A. Imamoğlu, *Quantum teleportation from a propagating photon to a solid-state spin qubit*, Nat. Commun. **4** (2013).

[228] S. Puri, P. L. McMahon, and Y. Yamamoto, *Single-shot quantum nondemolition measurement of a quantum-dot electron spin using cavity exciton-polaritons*, Phys. Rev. B **90**, 155421 (2014).

[229] V. B. Braginsky and F. Y. Khalili, *Quantum nondemolition measurements: the route from toys to tools*, Rev. Mod. Phys. **68**, 1 (1996).

[230] D. Press, K. De Greve, P. L. McMahon, T. D. Ladd, B. Friess, C. Schneider, M. Kamp, S. Hofling, A. Forchel, and Y. Yamamoto, *Ultrafast optical spin echo in a single quantum dot*, Nature Photon. **4**, 367 (2010).

[231] M. Kroutvar, Y. Ducommun, D. Heiss, M. Bichler, D. Schuh, G. Abstreiter, and J. J. Finley, *Optically programmable electron spin memory using semiconductor quantum dots*, Nature **432**, 81 (2004).

[232] H. Deng, H. Haug, and Y. Yamamoto, *Exciton-polariton Bose-Einstein condensation*, Rev. Mod. Phys. **82**, 1489 (2010).

[233] M. J. Collett and C. W. Gardiner, *Squeezing of intracavity and traveling-wave light fields produced in parametric amplification*, Phys. Rev. A **30**, 1386 (1984).

[234] C. W. Gardiner and M. J. Collett, *Input and output in damped quantum systems: Quantum stochastic differential equations and the master equation*, Phys. Rev. A **31**, 3761 (1985).

[235] E. Waks and J. Vuckovic, *Dispersive properties and large Kerr nonlinearities using dipole-induced transparency in a single-sided cavity*, Phys. Rev. A **73**, 041803 (2006).

[236] K. J. Blow, R. Loudon, S. J. D. Phoenix, and T. J. Shepherd, *Continuum fields in quantum optics*, Phys. Rev. A **42**, 4102 (1990).

Appendix A

Continuum Limit

When taking the sum over all two-dimensional in-plane wave vectors $\mathbf{k}$ in Eq. (4.44), the appearing vectors depend on the boundary conditions. We choose periodic boundary conditions, and hence,

$$k_x = \frac{2\pi}{L_x} n_x \quad (n_x = 0, \pm 1, \dots), \tag{A.1}$$

$$k_y = \frac{2\pi}{L_y} n_y \quad (n_y = 0, \pm 1, \dots), \tag{A.2}$$

where $L_{x(y)}$ is the cavity length in $x(y)$-direction and $n_{x(y)}$ is an integer. Every discrete wave vector $\mathbf{k}$ encloses a volume Δ in $\mathbf{k}$-space,

$$\Delta = \Delta k_x \Delta k_y = \frac{(2\pi)^2}{L_x L_y} = \frac{(2\pi)^2}{A}. \tag{A.3}$$

Here, $\Delta k_{x(y)}$ is the difference between two adjacent wave vectors in $x(y)$-direction, and A the sample area. In the continuum limit, the $\mathbf{k}$ vectors lie close in reciprocal space and the sum can be replaced by an integral,

$$S = \sum_{\mathbf{k}} G^2(k) = \frac{1}{\Delta} \sum_{\mathbf{k}} \Delta G^2(k) \to \frac{1}{\Delta} \int \mathrm{d}^2 k \, G^2(k) = \frac{A}{2\pi} \int_{k=0}^{\infty} \mathrm{d}k \, k \, G^2(k) = \frac{A}{2\pi} \left(\frac{\omega_{12}}{c} \right)^2 \mathcal{I}, \tag{A.4}$$

where we use polar coordinates to evaluate the integral and carry out the polar-angle integration. In the last step, we make a substitution and introduce the dimensionless variable $\tilde{k} := ck/\omega_{12}$ to obtain the dimensionless integral $\mathcal{I}$,

$$\mathcal{I} = \int_{\tilde{k}=0}^{\infty} \mathrm{d}\tilde{k} \, \tilde{k} \, G^2 \left(\frac{c}{\omega_{12}} \tilde{k} \right). \tag{A.5}$$

One can show that the expansion coefficient $G(k)$ decreases like $1/k^2$ for large k. Consequently, the integrand has the asymptotics

$$k \, G^2(k) \overset{k \to \infty}{\approx} \frac{1}{k^3}, \tag{A.6}$$

and hence, the integral converges. We evaluate $\mathcal{I}$ numerically using the same parameters as in Sec. 4.4.2 and find $\mathcal{I} = 4.1 \times 10^{-4}$.

Appendix B

Bilateral Exchange Pulse

Table B.1 – Action of a bilateral exchange pulse $U(\alpha,\beta)$ on the four-qubit Bell-product basis $\{(|\Phi^+\rangle, |\Phi^-\rangle, |\Psi^+\rangle, |\Psi^-\rangle) \otimes (|\Phi^+\rangle, |\Phi^-\rangle, |\Psi^+\rangle, |\Psi^-\rangle)\}$, with $|\Phi^+\Phi^+\rangle \equiv |\Phi^+\rangle_{(12)}|\Phi^+\rangle_{(34)}$, etc. A factor of $(1/4)\exp[-i(\alpha+\beta)/4]$ has been omitted for all transformed states.

Before	After
$\|\Phi^+\Phi^+\rangle$	$\left(3+e^{i(\alpha+\beta)}\right)\|\Phi^+\Phi^+\rangle + \left(1-e^{i(\alpha+\beta)}\right)\|\Phi^-\Phi^-\rangle + \left(1-e^{i(\alpha+\beta)}\right)\|\Psi^+\Psi^+\rangle - \left(1-e^{i(\alpha+\beta)}\right)\|\Psi^-\Psi^-\rangle$
$\|\Phi^-\Phi^+\rangle$	$\left(2-e^{i\alpha}-e^{i\beta}\right)\|\Phi^+\Phi^-\rangle + \left(2+e^{i\alpha}+e^{i\beta}\right)\|\Phi^-\Phi^+\rangle - \left(e^{i\alpha}-e^{i\beta}\right)\|\Psi^+\Psi^-\rangle + \left(e^{i\alpha}-e^{i\beta}\right)\|\Psi^-\Psi^+\rangle$
$\|\Psi^+\Phi^+\rangle$	$\left(2-e^{i\alpha}-e^{i\beta}\right)\|\Phi^+\Psi^+\rangle + \left(e^{i\alpha}-e^{i\beta}\right)\|\Phi^-\Psi^-\rangle + \left(2+e^{i\alpha}+e^{i\beta}\right)\|\Psi^+\Phi^+\rangle - \left(e^{i\alpha}-e^{i\beta}\right)\|\Psi^-\Phi^-\rangle$
$\|\Psi^-\Phi^+\rangle$	$\left(2-e^{i\alpha}-e^{i\beta}\right)\|\Phi^+\Psi^-\rangle + \left(e^{i\alpha}-e^{i\beta}\right)\|\Phi^-\Psi^+\rangle - \left(e^{i\alpha}-e^{i\beta}\right)\|\Psi^+\Phi^-\rangle + \left(2+e^{i\alpha}+e^{i\beta}\right)\|\Psi^-\Phi^+\rangle$
$\|\Psi^+\Psi^+\rangle$	$\left(1-e^{i(\alpha+\beta)}\right)\|\Phi^+\Phi^+\rangle - \left(1-e^{i(\alpha+\beta)}\right)\|\Phi^-\Phi^-\rangle + \left(3+e^{i(\alpha+\beta)}\right)\|\Psi^+\Psi^+\rangle + \left(1-e^{i(\alpha+\beta)}\right)\|\Psi^-\Psi^-\rangle$
$\|\Psi^-\Psi^+\rangle$	$\left(e^{i\beta}-e^{i\alpha}\right)\|\Phi^+\Phi^-\rangle + \left(e^{i\alpha}-e^{i\beta}\right)\|\Phi^-\Phi^+\rangle + \left(2-e^{i\alpha}-e^{i\beta}\right)\|\Psi^+\Psi^-\rangle + \left(2+e^{i\alpha}+e^{i\beta}\right)\|\Psi^-\Psi^+\rangle$
$\|\Phi^+\Psi^+\rangle$	$\left(2+e^{i\alpha}+e^{i\beta}\right)\|\Phi^+\Psi^+\rangle - \left(e^{i\alpha}-e^{i\beta}\right)\|\Phi^-\Psi^-\rangle + \left(2-e^{i\alpha}-e^{i\beta}\right)\|\Psi^+\Phi^+\rangle + \left(e^{i\alpha}-e^{i\beta}\right)\|\Psi^-\Phi^-\rangle$
$\|\Phi^-\Psi^+\rangle$	$\left(e^{i\beta}-e^{i\alpha}\right)\|\Phi^+\Psi^-\rangle + \left(2+e^{i\alpha}+e^{i\beta}\right)\|\Phi^-\Psi^+\rangle + \left(2-e^{i\alpha}-e^{i\beta}\right)\|\Psi^+\Phi^-\rangle + \left(e^{i\alpha}-e^{i\beta}\right)\|\Psi^-\Phi^+\rangle$
$\|\Phi^+\Phi^-\rangle$	$\left(2+e^{i\alpha}+e^{i\beta}\right)\|\Phi^+\Phi^-\rangle + \left(2-e^{i\alpha}-e^{i\beta}\right)\|\Phi^-\Phi^+\rangle + \left(e^{i\alpha}-e^{i\beta}\right)\|\Psi^+\Psi^-\rangle - \left(e^{i\alpha}-e^{i\beta}\right)\|\Psi^-\Psi^+\rangle$
$\|\Phi^-\Phi^-\rangle$	$\left(1-e^{i(\alpha+\beta)}\right)\|\Phi^+\Phi^+\rangle + \left(3+e^{i(\alpha+\beta)}\right)\|\Phi^-\Phi^-\rangle - \left(1-e^{i(\alpha+\beta)}\right)\|\Psi^+\Psi^+\rangle + \left(1-e^{i(\alpha+\beta)}\right)\|\Psi^-\Psi^-\rangle$
$\|\Psi^+\Phi^-\rangle$	$\left(e^{i\alpha}-e^{i\beta}\right)\|\Phi^+\Psi^-\rangle + \left(2-e^{i\alpha}-e^{i\beta}\right)\|\Phi^-\Psi^+\rangle + \left(2+e^{i\alpha}+e^{i\beta}\right)\|\Psi^+\Phi^-\rangle - \left(e^{i\alpha}-e^{i\beta}\right)\|\Psi^-\Phi^+\rangle$
$\|\Psi^-\Phi^-\rangle$	$\left(e^{i\alpha}-e^{i\beta}\right)\|\Phi^+\Psi^+\rangle + \left(2-e^{i\alpha}-e^{i\beta}\right)\|\Phi^-\Psi^-\rangle - \left(e^{i\alpha}-e^{i\beta}\right)\|\Psi^+\Phi^+\rangle + \left(2+e^{i\alpha}+e^{i\beta}\right)\|\Psi^-\Phi^-\rangle$
$\|\Psi^+\Psi^-\rangle$	$\left(e^{i\alpha}-e^{i\beta}\right)\|\Phi^+\Phi^-\rangle - \left(e^{i\alpha}-e^{i\beta}\right)\|\Phi^-\Phi^+\rangle + \left(2+e^{i\alpha}+e^{i\beta}\right)\|\Psi^+\Psi^-\rangle + \left(2-e^{i\alpha}-e^{i\beta}\right)\|\Psi^-\Psi^+\rangle$
$\|\Psi^-\Psi^-\rangle$	$\left(e^{i(\alpha+\beta)}-1\right)\|\Phi^+\Phi^+\rangle + \left(1-e^{i(\alpha+\beta)}\right)\|\Phi^-\Phi^-\rangle + \left(1-e^{i(\alpha+\beta)}\right)\|\Psi^+\Psi^+\rangle + \left(3+e^{i(\alpha+\beta)}\right)\|\Psi^-\Psi^-\rangle$
$\|\Phi^+\Psi^-\rangle$	$\left(2+e^{i\alpha}+e^{i\beta}\right)\|\Phi^+\Psi^-\rangle - \left(e^{i\alpha}-e^{i\beta}\right)\|\Phi^-\Psi^+\rangle + \left(e^{i\alpha}-e^{i\beta}\right)\|\Psi^+\Phi^-\rangle + \left(2-e^{i\alpha}-e^{i\beta}\right)\|\Psi^-\Phi^+\rangle$
$\|\Phi^-\Psi^-\rangle$	$\left(e^{i\beta}-e^{i\alpha}\right)\|\Phi^+\Psi^+\rangle + \left(2+e^{i\alpha}+e^{i\beta}\right)\|\Phi^-\Psi^-\rangle + \left(e^{i\alpha}-e^{i\beta}\right)\|\Psi^+\Phi^+\rangle + \left(2+e^{i\alpha}+e^{i\beta}\right)\|\Psi^-\Phi^-\rangle$

Appendix C

Schrieffer-Wolff Transformation

A method to effectively decouple energetically separated subspaces of a Hamiltonian H is given by the so-called *Schrieffer-Wolff transformation* [221], originally introduced to relate the Anderson and the Kondo model.[1] The two subspaces are denoted as A and B, and we can separate the Hamiltonian H into a block-diagonal part H_0 that only acts within each subspace A and B, respectively, and an off-diagonal part V that connects the two subspaces,

$$H = H_0 + V. \tag{C.1}$$

We assume that the two subspaces only weakly interact, i.e., the matrix elements $\langle\psi_i|V|\phi_j\rangle$ are small compared to the energy separation between A and B. Here, $\{|\psi_i\rangle\}$ are eigenfunctions of H_0 belonging to subspace A, and the $\{|\phi_j\rangle\}$ belong to subspace B. However, we only want to consider the dynamics of the low-energy subspace A. One can construct a unitary transformation $U = \exp(-S)$ with some anti-Hermitian operator S to obtain a new Hamiltonian $\widetilde{H}$,

$$\widetilde{H} = e^{-S} H e^{S}, \tag{C.2}$$

that contains no matrix elements $\langle\psi_i|\widetilde{H}|\phi_j\rangle$ betweeen the two subspaces up to a desired order in V. Using the Baker-Campbell-Hausdorff formula, the transformed Hamiltonian $\widetilde{H}$ is

$$\begin{aligned}\widetilde{H} = e^{-S} H e^{S} = \sum_{k=0}^{\infty} \frac{1}{k!}[-S, H]_k &= H - [S, H] + \frac{1}{2}[S, [S, H]] + \dots \\ &= H_0 + V - [S, H_0 + V] + \frac{1}{2}[S, [S, H_0 + V]] + \dots\end{aligned} \tag{C.3}$$

with $[-S, H]_k = [-S, [-S, H]_{k-1}]$ and $[-S, H]_0 = H$. If the anti-Hermitian matrix S is constructed in such a way that

$$[S, H_0] = V \tag{C.4}$$

holds, the leading order in the interaction V exactly cancels. We obtain the transformed Hamiltonian

$$\widetilde{H} = H_0 - [S, V] + \frac{1}{2}[S, \underbrace{[S, H_0]}_{=V}] + \frac{1}{2}[S, [S, V]] + \dots = H_0 + \frac{1}{2}[V, S] + \frac{1}{2}[S, [S, V]] + \dots, \tag{C.5}$$

in which we only keep the block-diagonal part and continue working with an effective Hamiltonian H_{eff},

$$H_{\text{eff}} \equiv H_0 + \frac{1}{2}[V, S]. \tag{C.6}$$

[1] Equivalent transformations can be applied to a variety of physical problems, see e.g. in Ref. 222.

Appendix D

Transformation into a Rotating Frame

In Sec. 6.4.1, the interaction of a two-level system with a classical radiation field is described by a time-dependent Hamiltonian $H(t)$ of the form

$$H(t) = \Omega e^{-i\omega t}\tau_+ + \Omega^* e^{i\omega t}\tau_-. \tag{D.1}$$

Here, the operators $\tau_\pm$ describe transitions within the two-level system and ω is the frequency of the light field. A time-dependent unitary transformation $U(t) = \exp(i\xi t)$, where ξ is an arbitrary time-independent Hermitian operator, transforms a quantum state $|\psi\rangle$ according to $|\psi'\rangle = U(t)|\psi\rangle$. The time evolution of $|\psi'\rangle$ is

$$i\frac{\mathrm{d}}{\mathrm{d}t}|\psi'\rangle = i\frac{\mathrm{d}}{\mathrm{d}t}U(t)|\psi\rangle = \left(i\frac{\mathrm{d}U(t)}{\mathrm{d}t}U(t)^\dagger + U(t)H(t)U(t)^\dagger\right)|\psi'\rangle \equiv H'(t)|\psi'\rangle, \tag{D.2}$$

where we used the Schrödinger equation $i\mathrm{d}/(\mathrm{d}t)|\psi\rangle = H(t)|\psi\rangle$. Thus, the transformed Hamiltonian $H'(t)$, which is in general still time-dependent, is given by

$$H'(t) = U(t)H(t)U(t)^\dagger - \xi. \tag{D.3}$$

The Hamiltonian in Eq. (D.1) becomes time-independent for $\xi = \omega\tau_z/2$, which can be calculated, e.g., by using the matrix representation of the Pauli operators,

$$e^{i\frac{\omega}{2}\tau_z t}\left(e^{-i\omega t}\tau_+\right)e^{-i\frac{\omega}{2}\tau_z t} = \begin{pmatrix} e^{i\frac{\omega}{2}t} & 0 \\ 0 & e^{-i\frac{\omega}{2}t}\end{pmatrix}\begin{pmatrix} 0 & e^{-i\omega t} \\ 0 & 0\end{pmatrix}\begin{pmatrix} e^{-i\frac{\omega}{2}t} & 0 \\ 0 & e^{i\frac{\omega}{2}t}\end{pmatrix} = \begin{pmatrix} 0 & 1 \\ 0 & 0\end{pmatrix} = \tau_+, \tag{D.4}$$

and respectively for the term $e^{i\omega t}\tau_-$. We also have to transform the cavity operators a and $a^\dagger$ in Sec. 6.4.1, because the unitary transformation in Eq. (6.26) contains a and $a^\dagger$ themselves. The annihilation operator a transforms as

$$e^{i\omega a^\dagger a t}ae^{-i\omega a^\dagger a t} = \sum_{n=0}^{\infty}\frac{1}{n!}[i\omega a^\dagger a t, a]_n = \sum_{n=0}^{\infty}\frac{1}{n!}(i\omega t)^n\underbrace{[a^\dagger a, a]_n}_{=(-1)^n a} = e^{-i\omega t}a, \tag{D.5}$$

using the Baker-Campbell-Haussdorff formula, and $[x,y]_n = [x,[x,y]_{n-1}]$ and $[x,y]_0 = y$. The creation operator $a^\dagger$ is transformed equivalently.

Appendix E

Quantum Langevin Equations

E.1 Derivation

Following the input-output formalism [233, 234], one can calculate the Heisenberg equations of motion for the involved operators from the Hamiltonian H in Eq. (7.1),

$$\dot{\alpha}_{\nu,\sigma} = i[H, \alpha_{\nu,\sigma}] = -i\nu\alpha_{\nu,\sigma} + \sqrt{\frac{\gamma_\mathrm{t}}{2\pi}} a_\sigma, \tag{E.1}$$

$$\dot{\beta}_{\nu,\sigma} = i[H, \beta_{\nu,\sigma}] = -i\nu\beta_{\nu,\sigma} + \sqrt{\frac{\gamma_\mathrm{b}}{2\pi}} a_\sigma, \tag{E.2}$$

$$\dot{a}_\sigma = i[H, a_\sigma] = i[H_\mathrm{sys}, a_\sigma] - \int_{-\infty}^{\infty} \mathrm{d}\nu \sqrt{\frac{\gamma_\mathrm{t}}{2\pi}} \alpha_{\nu,\sigma} - \int_{-\infty}^{\infty} \mathrm{d}\nu \sqrt{\frac{\gamma_\mathrm{b}}{2\pi}} \beta_{\nu,\sigma}, \tag{E.3}$$

$$\dot{b}_{\sigma'} = i[H, b_{\sigma'}] = i[H_\mathrm{sys}, b_{\sigma'}]. \tag{E.4}$$

Evaluation of the commutators $[H_\mathrm{sys}, a_\sigma]$ and $[H_\mathrm{sys}, b_{\sigma'}]$, and using the relation $a_\pm^\dagger = (a_\mathrm{H}^\dagger \pm i a_\mathrm{V}^\dagger)/\sqrt{2}$ between linear and circular polarization, the Heisenberg equations of motion for the cavity-photon and exciton operators are given by

$$\dot{a}_\mathrm{H} = -i\omega_\mathrm{c} a_\mathrm{H} + \frac{g}{\sqrt{2}} (b_+ + b_-) - \int_{-\infty}^{\infty} \mathrm{d}\nu \sqrt{\frac{\gamma_\mathrm{t}}{2\pi}} \alpha_{\nu,\mathrm{H}} - \int_{-\infty}^{\infty} \mathrm{d}\nu \sqrt{\frac{\gamma_\mathrm{b}}{2\pi}} \beta_{\nu,\mathrm{H}}, \tag{E.5}$$

$$\dot{a}_\mathrm{V} = -i\omega_\mathrm{c} a_\mathrm{V} + \frac{ig}{\sqrt{2}} (b_+ - b_-) - \int_{-\infty}^{\infty} \mathrm{d}\nu \sqrt{\frac{\gamma_\mathrm{t}}{2\pi}} \alpha_{\nu,\mathrm{V}} - \int_{-\infty}^{\infty} \mathrm{d}\nu \sqrt{\frac{\gamma_\mathrm{b}}{2\pi}} \beta_{\nu,\mathrm{V}}, \tag{E.6}$$

$$\dot{b}_+ = -i\left(\omega_\mathrm{c} + \frac{1}{2} V_\mathrm{exc} S_z\right) b_+ - \frac{g}{\sqrt{2}} (a_\mathrm{H} - i a_\mathrm{V}), \tag{E.7}$$

$$\dot{b}_- = -i\left(\omega_\mathrm{c} - \frac{1}{2} V_\mathrm{exc} S_z\right) b_- - \frac{g}{\sqrt{2}} (a_\mathrm{H} + i a_\mathrm{V}). \tag{E.8}$$

Eqs. (E.1) and (E.2) can be formally solved as

$$\alpha_{\nu,\sigma}(t) = e^{-i\nu(t-t_0)}\alpha_{\nu,\sigma}(t_0) + \sqrt{\frac{\gamma_\mathrm{t}}{2\pi}}\int_{t_0}^{t} \mathrm{d}t'\, e^{-i\nu(t-t')}a_\sigma(t'), \tag{E.9}$$

$$\beta_{\nu,\sigma}(t) = e^{-i\nu(t-t_0)}\beta_{\nu,\sigma}(t_0) + \sqrt{\frac{\gamma_\mathrm{b}}{2\pi}}\int_{t_0}^{t} \mathrm{d}t'\, e^{-i\nu(t-t')}a_\sigma(t'), \tag{E.10}$$

for $t_0 < t$. Here, the time dependence is explicitly written out. We can define input fields for the limit $t_0 \to -\infty$ like

$$\alpha_\sigma^\mathrm{in}(t) \equiv \lim_{t_0\to-\infty}\frac{1}{\sqrt{2\pi}}\int_{-\infty}^{\infty} \mathrm{d}\nu\, e^{-i\nu(t-t_0)}\alpha_{\nu,\sigma}(t_0), \tag{E.11}$$

$$\beta_\sigma^\mathrm{in}(t) \equiv \lim_{t_0\to-\infty}\frac{1}{\sqrt{2\pi}}\int_{-\infty}^{\infty} \mathrm{d}\nu\, e^{-i\nu(t-t_0)}\beta_{\nu,\sigma}(t_0), \tag{E.12}$$

i.e., for long times in the past. Inserting the formal solutions in Eqs. (E.9) and (E.10) into Eq. (E.5) yields

$$\begin{aligned}\dot{a}_\mathrm{H}(t) = &-i\omega_\mathrm{c}a_\mathrm{H}(t) + \frac{g}{\sqrt{2}}\left(b_+(t) + b_-(t)\right)\\ &-\sqrt{\gamma_\mathrm{t}}\alpha_\mathrm{H}^\mathrm{in}(t) - \frac{\gamma_\mathrm{t}}{2\pi}\int_{-\infty}^{\infty}\mathrm{d}\nu\int_{-\infty}^{t}\mathrm{d}t'\, e^{-i\nu(t-t')}a_\mathrm{H}(t')\\ &-\sqrt{\gamma_\mathrm{b}}\beta_\mathrm{H}^\mathrm{in}(t) - \frac{\gamma_\mathrm{b}}{2\pi}\int_{-\infty}^{\infty}\mathrm{d}\nu\int_{-\infty}^{t}\mathrm{d}t'\, e^{-i\nu(t-t')}a_\mathrm{H}(t'),\end{aligned} \tag{E.13}$$

in the limit $t_0 \to -\infty$. The integration over ν can be performed as well,

$$\int_{-\infty}^{\infty}\mathrm{d}\nu\, e^{-i\nu(t-t')} = 2\pi\delta(t-t'), \tag{E.14}$$

to finally yield the quantum Langevin equations

$$\dot{a}_\mathrm{H}(t) = -\left(i\omega_\mathrm{c} + \frac{\gamma_\mathrm{t}+\gamma_\mathrm{b}}{2}\right)a_\mathrm{H}(t) + \frac{g}{\sqrt{2}}\left(b_+(t)+b_-(t)\right) - \sqrt{\gamma_\mathrm{t}}\alpha_\mathrm{H}^\mathrm{in}(t) - \sqrt{\gamma_\mathrm{b}}\beta_\mathrm{H}^\mathrm{in}(t), \tag{E.15}$$

$$\dot{a}_\mathrm{v}(t) = -\left(i\omega_\mathrm{c} + \frac{\gamma_\mathrm{t}+\gamma_\mathrm{b}}{2}\right)a_\mathrm{v}(t) + \frac{ig}{\sqrt{2}}\left(b_+(t)-b_-(t)\right) - \sqrt{\gamma_\mathrm{t}}\alpha_\mathrm{v}^\mathrm{in}(t) - \sqrt{\gamma_\mathrm{b}}\beta_\mathrm{v}^\mathrm{in}(t), \tag{E.16}$$

where we also used the relation $\int_{-\infty}^{t}\mathrm{d}t' a_\sigma(t')\delta(t-t') = a_\sigma(t)/2$. The operators $\alpha_\sigma^\mathrm{in}(t)$ and $\beta_\sigma^\mathrm{in}(t)$ define the initial state of the corresponding photon bath [234], which can be, e.g., a thermal state and thus, the operators may be interpreted as noise, or it could also be a coherent state, which would correspond to a classical driving field.

E.2 Solutions

We solve Eqs. (E.7), (E.8), (E.15), and (E.16) in frequency space, where we use the Fourier transformation of an operator $O(t)$,

$$\mathrm{FT}[O(t)] = \widetilde{O}(\omega) = \frac{1}{\sqrt{2\pi}} \int_{-\infty}^{\infty} \mathrm{d}t\, e^{i\omega t} O(t), \tag{E.17}$$

$$\mathrm{FT}[\dot{O}(t)] = -i\omega \widetilde{O}(\omega). \tag{E.18}$$

The Fourier transformation of the Langevin equations [Eqs. (E.15) and (E.16)] and the Heisenberg equations of motion of the exciton operators [Eqs. (E.7) and (E.8)] yields a system of linear equations,

$$-i\omega \tilde{a}_{\mathrm{H}}(\omega) = -\left(i\omega_{\mathrm{c}} + \frac{\gamma_{\mathrm{t}} + \gamma_{\mathrm{b}}}{2}\right) \tilde{a}_{\mathrm{H}}(\omega) + \frac{g}{\sqrt{2}} \left(\tilde{b}_{+}(\omega) + \tilde{b}_{-}(\omega)\right) - \sqrt{\gamma_{\mathrm{t}}} \tilde{\alpha}^{\mathrm{in}}_{\mathrm{H}}(\omega) - \sqrt{\gamma_{\mathrm{b}}} \tilde{\beta}^{\mathrm{in}}_{\mathrm{H}}(\omega) \tag{E.19}$$

$$-i\omega \tilde{a}_{\mathrm{V}}(\omega) = -\left(i\omega_{\mathrm{c}} + \frac{\gamma_{\mathrm{t}} + \gamma_{\mathrm{b}}}{2}\right) \tilde{a}_{\mathrm{V}}(\omega) + \frac{ig}{\sqrt{2}} \left(\tilde{b}_{+}(\omega) - \tilde{b}_{-}(\omega)\right) - \sqrt{\gamma_{\mathrm{t}}} \tilde{\alpha}^{\mathrm{in}}_{\mathrm{V}}(\omega) - \sqrt{\gamma_{\mathrm{b}}} \tilde{\beta}^{\mathrm{in}}_{\mathrm{V}}(\omega) \tag{E.20}$$

$$-i\omega \tilde{b}_{+}(\omega) = -i\left(\omega_{\mathrm{c}} + \frac{1}{2} V_{\mathrm{exc}} S_z\right) \tilde{b}_{+}(\omega) - \frac{g}{\sqrt{2}} \left(\tilde{a}_{\mathrm{H}}(\omega) - i\tilde{a}_{\mathrm{V}}(\omega)\right), \tag{E.21}$$

$$-i\omega \tilde{b}_{-}(\omega) = -i\left(\omega_{\mathrm{c}} - \frac{1}{2} V_{\mathrm{exc}} S_z\right) \tilde{b}_{+}(\omega) - \frac{g}{\sqrt{2}} \left(\tilde{a}_{\mathrm{H}}(\omega) + i\tilde{a}_{\mathrm{V}}(\omega)\right), \tag{E.22}$$

or more compactly written in matrix form

$$A(\omega) \begin{pmatrix} \tilde{a}_{\mathrm{H}}(\omega) \\ \tilde{a}_{\mathrm{V}}(\omega) \\ \tilde{b}_{+}(\omega) \\ \tilde{b}_{-}(\omega) \end{pmatrix} = \begin{pmatrix} \sqrt{\gamma_{\mathrm{t}}} \tilde{\alpha}^{\mathrm{in}}_{\mathrm{H}}(\omega) + \sqrt{\gamma_{\mathrm{b}}} \tilde{\beta}^{\mathrm{in}}_{\mathrm{H}}(\omega) \\ \sqrt{\gamma_{\mathrm{t}}} \tilde{\alpha}^{\mathrm{in}}_{\mathrm{V}}(\omega) + \sqrt{\gamma_{\mathrm{b}}} \tilde{\beta}^{\mathrm{in}}_{\mathrm{V}}(\omega) \\ 0 \\ 0 \end{pmatrix}, \tag{E.23}$$

where the matrix $A(\omega)$ is given by

$$A(\omega) = \begin{pmatrix} i\Delta_\omega - \frac{\gamma_{\mathrm{t}}+\gamma_{\mathrm{b}}}{2} & 0 & \frac{g}{\sqrt{2}} & \frac{g}{\sqrt{2}} \\ 0 & i\Delta_\omega - \frac{\gamma_{\mathrm{t}}+\gamma_{\mathrm{b}}}{2} & \frac{ig}{\sqrt{2}} & -\frac{ig}{\sqrt{2}} \\ -\frac{g}{\sqrt{2}} & \frac{ig}{\sqrt{2}} & i\left(\Delta_\omega - \frac{1}{2} V_{\mathrm{exc}} S_z\right) & 0 \\ -\frac{g}{\sqrt{2}} & -\frac{ig}{\sqrt{2}} & 0 & i\left(\Delta_\omega + \frac{1}{2} V_{\mathrm{exc}} S_z\right) \end{pmatrix}. \tag{E.24}$$

Here, we introduced the abbreviation $\Delta_\omega \equiv \omega - \omega_{\mathrm{c}}$. The solutions for the cavity-photon operators and the exciton operators in Fourier space are obtained by inverting the matrix $A(\omega)$,

$$\begin{pmatrix} \tilde{a}_{\mathrm{H}}(\omega) \\ \tilde{a}_{\mathrm{V}}(\omega) \\ \tilde{b}_{+}(\omega) \\ \tilde{b}_{-}(\omega) \end{pmatrix} = B(\omega) \begin{pmatrix} \sqrt{\gamma_{\mathrm{t}}} \tilde{\alpha}^{\mathrm{in}}_{\mathrm{H}}(\omega) + \sqrt{\gamma_{\mathrm{b}}} \tilde{\beta}^{\mathrm{in}}_{\mathrm{H}}(\omega) \\ \sqrt{\gamma_{\mathrm{t}}} \tilde{\alpha}^{\mathrm{in}}_{\mathrm{V}}(\omega) + \sqrt{\gamma_{\mathrm{b}}} \tilde{\beta}^{\mathrm{in}}_{\mathrm{V}}(\omega) \\ 0 \\ 0 \end{pmatrix}, \tag{E.25}$$

with $B(\omega) = [A(\omega)]^{-1}$. The dynamics of the coupled QW-cavity system is thus specified by including internal dynamics and additionally, possible optical input from external field modes.

E.3 Input-Output Relations

We are interested in the output from the cavity depending on a specific input field. For this purpose, one can formally solve (E.1) and (E.2) for $t_1 > t$,

$$\alpha_{\nu,\sigma}(t) = e^{-i\nu(t-t_1)}\alpha_{\nu,\sigma}(t_1) - \sqrt{\frac{\gamma_\mathrm{t}}{2\pi}}\int_t^{t_1} \mathrm{d}t'\, e^{-i\nu(t-t')}a_\sigma(t'), \tag{E.26}$$

$$\beta_{\nu,\sigma}(t) = e^{-i\nu(t-t_1)}\beta_{\nu,\sigma}(t_1) - \sqrt{\frac{\gamma_\mathrm{b}}{2\pi}}\int_t^{t_1} \mathrm{d}t'\, e^{-i\nu(t-t')}a_\sigma(t'), \tag{E.27}$$

and in analogy define operators for the output field like

$$\alpha_\sigma^\mathrm{out}(t) \equiv \lim_{t_1\to\infty}\frac{1}{\sqrt{2\pi}}\int_{-\infty}^{\infty} \mathrm{d}\nu\, e^{-i\nu(t-t_1)}\alpha_{\nu,\sigma}(t_1), \tag{E.28}$$

$$\beta_\sigma^\mathrm{out}(t) \equiv \lim_{t_1\to\infty}\frac{1}{\sqrt{2\pi}}\int_{-\infty}^{\infty} \mathrm{d}\nu\, e^{-i\nu(t-t_1)}\beta_{\nu,\sigma}(t_1), \tag{E.29}$$

Eventually, the goal of the calculation is to obtain a relation between the input and output fields, i.e. given a certain input field, we want to be able to calculate the output from the cavity, which could be a reflected or transmitted signal. We already know how the operators of the internal field depend on the input operators, see Eq. (E.25). In the next step, one can relate both of them to the output fields. Integrating Eqs. (E.9) and (E.10) over the frequency ν yields in the limit $t_0 \to -\infty$

$$\frac{1}{\sqrt{2\pi}}\int_{-\infty}^{\infty} \mathrm{d}\nu\, \alpha_{\nu,\sigma}(t) = \alpha_\sigma^\mathrm{in}(t) + \frac{\sqrt{\gamma_\mathrm{t}}}{2}a_\sigma(t), \tag{E.30}$$

$$\frac{1}{\sqrt{2\pi}}\int_{-\infty}^{\infty} \mathrm{d}\nu\, \beta_{\nu,\sigma}(t) = \beta_\sigma^\mathrm{in}(t) + \frac{\sqrt{\gamma_\mathrm{b}}}{2}a_\sigma(t), \tag{E.31}$$

and from Eqs. (E.26), and (E.27), one obtains in the limit $t_1 \to \infty$

$$\frac{1}{\sqrt{2\pi}}\int_{-\infty}^{\infty} \mathrm{d}\nu\, \alpha_{\nu,\sigma}(t) = \alpha_\sigma^\mathrm{out}(t) - \frac{\sqrt{\gamma_\mathrm{t}}}{2}a_\sigma(t), \tag{E.32}$$

$$\frac{1}{\sqrt{2\pi}}\int_{-\infty}^{\infty} \mathrm{d}\nu\, \beta_{\nu,\sigma}(t) = \beta_\sigma^\mathrm{in}(t) - \frac{\sqrt{\gamma_\mathrm{b}}}{2}a_\sigma(t). \tag{E.33}$$

The combination of these results gives the following relations between input, output, and cavity fields,

$$\alpha_\sigma^\mathrm{out}(t) = \alpha_\sigma^\mathrm{in}(t) + \sqrt{\gamma_\mathrm{t}}a_\sigma(t), \tag{E.34}$$

$$\beta_\sigma^\mathrm{out}(t) = \beta_\sigma^\mathrm{in}(t) + \sqrt{\gamma_\mathrm{b}}a_\sigma(t), \tag{E.35}$$

that are also true for the Fourier transformed operators. Together with Eq. (E.25), we can finally formulate the input-output relations,

$$\tilde{\alpha}_{\mathrm{H}}^{\mathrm{out}}(\omega) = \tilde{\alpha}_{\mathrm{H}}^{\mathrm{in}}(\omega) + \sqrt{\gamma_{\mathrm{t}}}\tilde{a}_{\mathrm{H}}(\omega) = \tilde{\alpha}_{\mathrm{H}}^{\mathrm{in}}(\omega) + \sqrt{\gamma_{\mathrm{t}}}\left[B_{11}(\omega)\left(\sqrt{\gamma_{\mathrm{t}}}\tilde{\alpha}_{\mathrm{H}}^{\mathrm{in}}(\omega) + \sqrt{\gamma_{\mathrm{b}}}\tilde{\beta}_{\mathrm{H}}^{\mathrm{in}}(\omega)\right)\right.$$
$$\left. + B_{12}(\omega)\left(\sqrt{\gamma_{\mathrm{t}}}\tilde{\alpha}_{\mathrm{V}}^{\mathrm{in}}(\omega) + \sqrt{\gamma_{\mathrm{b}}}\tilde{\beta}_{\mathrm{V}}^{\mathrm{in}}(\omega)\right)\right], \tag{E.36}$$

$$\tilde{\alpha}_{\mathrm{V}}^{\mathrm{out}}(\omega) = \tilde{\alpha}_{\mathrm{V}}^{\mathrm{in}}(\omega) + \sqrt{\gamma_{\mathrm{t}}}\tilde{a}_{\mathrm{V}}(\omega) = \tilde{\alpha}_{\mathrm{V}}^{\mathrm{in}}(\omega) + \sqrt{\gamma_{\mathrm{t}}}\left[B_{21}(\omega)\left(\sqrt{\gamma_{\mathrm{t}}}\tilde{\alpha}_{\mathrm{H}}^{\mathrm{in}}(\omega) + \sqrt{\gamma_{\mathrm{b}}}\tilde{\beta}_{\mathrm{H}}^{\mathrm{in}}(\omega)\right)\right.$$
$$\left. + B_{22}(\omega)\left(\sqrt{\gamma_{\mathrm{t}}}\tilde{\alpha}_{\mathrm{V}}^{\mathrm{in}}(\omega) + \sqrt{\gamma_{\mathrm{b}}}\tilde{\beta}_{\mathrm{V}}^{\mathrm{in}}(\omega)\right)\right], \tag{E.37}$$

$$\tilde{\beta}_{\mathrm{H}}^{\mathrm{out}}(\omega) = \tilde{\beta}_{\mathrm{H}}^{\mathrm{in}}(\omega) + \sqrt{\gamma_{\mathrm{b}}}\tilde{a}_{\mathrm{H}}(\omega) = \tilde{\beta}_{\mathrm{H}}^{\mathrm{in}}(\omega) + \sqrt{\gamma_{\mathrm{b}}}\left[B_{11}(\omega)\left(\sqrt{\gamma_{\mathrm{t}}}\tilde{\alpha}_{\mathrm{H}}^{\mathrm{in}}(\omega) + \sqrt{\gamma_{\mathrm{b}}}\tilde{\beta}_{\mathrm{H}}^{\mathrm{in}}(\omega)\right)\right.$$
$$\left. + B_{12}(\omega)\left(\sqrt{\gamma_{\mathrm{t}}}\tilde{\alpha}_{\mathrm{V}}^{\mathrm{in}}(\omega) + \sqrt{\gamma_{\mathrm{b}}}\tilde{\beta}_{\mathrm{V}}^{\mathrm{in}}(\omega)\right)\right], \tag{E.38}$$

$$\tilde{\beta}_{\mathrm{V}}^{\mathrm{out}}(\omega) = \tilde{\beta}_{\mathrm{V}}^{\mathrm{in}}(\omega) + \sqrt{\gamma_{\mathrm{b}}}\tilde{a}_{\mathrm{V}}(\omega) = \tilde{\beta}_{\mathrm{V}}^{\mathrm{in}}(\omega) + \sqrt{\gamma_{\mathrm{b}}}\left[B_{21}(\omega)\left(\sqrt{\gamma_{\mathrm{t}}}\tilde{\alpha}_{\mathrm{H}}^{\mathrm{in}}(\omega) + \sqrt{\gamma_{\mathrm{b}}}\tilde{\beta}_{\mathrm{H}}^{\mathrm{in}}(\omega)\right)\right.$$
$$\left. + B_{22}(\omega)\left(\sqrt{\gamma_{\mathrm{t}}}\tilde{\alpha}_{\mathrm{V}}^{\mathrm{in}}(\omega) + \sqrt{\gamma_{\mathrm{b}}}\tilde{\beta}_{\mathrm{V}}^{\mathrm{in}}(\omega)\right)\right], \tag{E.39}$$

where the $B_{ij}(\omega)$ are the matrix elements of $B(\omega)$, or in a more compact form

$$\begin{pmatrix} \tilde{\alpha}_{\mathrm{H}}^{\mathrm{out}}(\omega) \\ \tilde{\alpha}_{\mathrm{V}}^{\mathrm{out}}(\omega) \\ \tilde{\beta}_{\mathrm{H}}^{\mathrm{out}}(\omega) \\ \tilde{\beta}_{\mathrm{V}}^{\mathrm{out}}(\omega) \end{pmatrix} = U(\omega) \begin{pmatrix} \tilde{\alpha}_{\mathrm{H}}^{\mathrm{in}}(\omega) \\ \tilde{\alpha}_{\mathrm{V}}^{\mathrm{in}}(\omega) \\ \tilde{\beta}_{\mathrm{H}}^{\mathrm{in}}(\omega) \\ \tilde{\beta}_{\mathrm{V}}^{\mathrm{in}}(\omega) \end{pmatrix}, \tag{E.40}$$

with the unitary matrix $U(\omega)$,

$$U(\omega) = \begin{pmatrix} 1+\gamma_{\mathrm{t}}B_{11}(\omega) & \gamma_{\mathrm{t}}B_{12}(\omega) & \sqrt{\gamma_{\mathrm{t}}\gamma_{\mathrm{b}}}B_{11}(\omega) & \sqrt{\gamma_{\mathrm{t}}\gamma_{\mathrm{b}}}B_{12}(\omega) \\ \gamma_{\mathrm{t}}B_{21}(\omega) & 1+\gamma_{\mathrm{t}}B_{22}(\omega) & \sqrt{\gamma_{\mathrm{t}}\gamma_{\mathrm{b}}}B_{21}(\omega) & \sqrt{\gamma_{\mathrm{t}}\gamma_{\mathrm{b}}}B_{22}(\omega) \\ \sqrt{\gamma_{\mathrm{t}}\gamma_{\mathrm{b}}}B_{11}(\omega) & \sqrt{\gamma_{\mathrm{t}}\gamma_{\mathrm{b}}}B_{12}(\omega) & 1+\gamma_{\mathrm{b}}B_{11}(\omega) & \gamma_{\mathrm{b}}B_{12}(\omega) \\ \sqrt{\gamma_{\mathrm{t}}\gamma_{\mathrm{b}}}B_{21}(\omega) & \sqrt{\gamma_{\mathrm{t}}\gamma_{\mathrm{b}}}B_{22}(\omega) & \gamma_{\mathrm{b}}B_{21}(\omega) & 1+\gamma_{\mathrm{b}}B_{22}(\omega) \end{pmatrix}. \tag{E.41}$$